THE ROLE OF DISKS IN THE ANGULAR MOMENTUM EVOLUTION OF YOUNG, LOW-MASS STARS

By

Thompson S. Le Blanc

Dissertation

Submitted to the Faculty of the

Graduate School of Vanderbilt University

in partial fulfillment of the requirements

for the degree of

DOCTOR OF PHILOSOPHY

in

PHYSICS

August, 2012

Nashville, Tennessee

Approved:

Dr. Keivan G. Stassun

Dr. David A. Weintraub

Dr. Andreas Berlind

Dr. David Ersnt

Dr. Antonella Nota

DEDICATION

Dedicated to my two Suns; my wife Sonia, and my daughter Elena.

ACKNOWLEDGEMENTS

I am most thankful to Dr. Keivan Stassun, whose patience and supervision made it possible to conduct this thesis. Without his encouragement and subtle nudges to keep going, I would not have made it this far. I also thank the rest of the members of my committee; your roles, though different, has contributed incredibly to my development as an able scientist. I also thank Dr. Kevin Covey, whose expertise has helped me expand the base of my knowledge.

I extremely grateful to my colleagues; they have answered my countless questions with patience, especially Drs. Saurav Dhital, Alicia Aarnio, Phil Cargile, and Billy Teets. And to those before me, for showing me that your goals can be indeed be attained through blood, sweat and tears.

I would like to acknowledge and thank Sean Matt for helpful and insightful discussions of angular momentum transfer via star-disk interactions. This research has made use of NASA's Astrophysics Data System Bibliographic Services, the SIMBAD database, operated at CDS, Strasbourg, France, and photometry acquired as part of the Two Micron All Sky Survey. The Two Micron All Sky Survey was a joint project of the University of Massachusetts and the Infrared Processing and Analysis Center (California Institute of Technology). The University of Massachusetts was responsible for the overall management of the project, the observing facilities and the data acquisition. The Infrared Processing and Analysis Center was responsible for data processing, data distribution and data archiving.

I also gratefully acknowledge the support provided for this work by NASA through the Jenkins PreDoctoral Fellowship Program (JPFP) and NASA Graduate Student Research Program (GSRP). I acknowledge support provided for this work by NASA through Hubble Fellowship grant HST-HF-51253.01-A awarded by the STScI, which is operated by the AURA, Inc., for NASA, under contract NAS 5-26555, and by

the Spitzer Space Telescope Fellowship Program, through a contract issued by the Jet Propulsion Laboratory, California Institute of Technology under a contract with NASA.

Last, but not least, I am most grateful to my family; my wife and daughter to whom this thesis is dedicated. Without their support and understanding, I would have never made it this far. To my wife, whose patience and encouragement has kept me going, and to my daughter, who smiles even when the sky is grey!

Table of Contents

List of Tables

List of Figures

Chapter I

INTRODUCTION

Stars are born from the gravitational collapse of dense cores within giant molecular clouds. Conservation of angular momentum would imply that this collapse should produce a star spinning at or near breakup velocity. Actual observations, however, show that young stars rotate much slower than breakup ($\leqslant 10\%$ $v_{breakup}$, Hartmann et al., 1986; Bouvier et al., 1986). Where the rest of the angular momentum goes is an important outstanding question.

Circumstellar disks are one important angular momentum reservoir for young stars. During the process of protostellar collapse, a dense core's highest specific angular momentum material forms a flattened disk which persists for ∼2-3 Myr (e.g. Lada et al., 2006) to ∼6 Myr (e.g. Haisch et al., 2001), before it is depleted by accretion onto the star (Bertout et al., 1988; Hartigan et al., 1995), planet formation (Mordasini et al., 2009a,b), outflows (Reipurth et al., 1999; Hartigan et al., 2005), or photoevaporation (Bertoldi, 1989).

Theory suggests that magnetic star-disk interactions could play an important role in the star's early angular momentum evolution (Königl, 1991; Shu et al., 1994; Hartmann, 2001, 2002). Ghosh & Lamb (1979a,b) and Königl (1991) provided the first analytic descriptions of this process, assuming steady state accretion and a star

with a strong magnetic field. In this 'disk-locking' picture, angular momentum is transferred from a star to its circumstellar disk via torques arising from interactions between the star's magnetic field and ionized gas in its circumstellar disk. As the star's magnetic field weakens with distance, the field couples most strongly to the inner edge of the disk, "locking" the star's rotation to the Keplerian orbital period at the inner edge of the disk. Shu et al. (1994) extended this theoretical framework by developing the 'X-wind' model, in which a magnetically driven wind carries angular momentum away from the "X-point", where the star and disk's magnetic fields pinch at the disk's co-rotation radius. This model, originally assuming a dipolar configuration for the star's magnetic field, has been generalized by Mohanty & Shu (2008) to include more complex field geometries.

Edwards et al. (1993) and Edwards (1994) provided some of the first observational evidence in support of the disk-locking picture. Analyzing rotation periods measured from stellar light curves, these studies found that stars possessing close-in circumstellar disks (diagnosed via their $H - K$ color excess) were mostly slow rotators, and that stars without $H - K$ excess were fast rotators.

Following these initial findings, many observational studies have searched for signatures of the disk-locking effect by seeking to detect differences between the characteristic rotation rates of stars that possess and lack circumstellar disks, under the assumption that star-disk interactions will force stars with disks to rotate more slowly than those stars that lack disks (e.g. Herbst et al., 2002; Rebull et al., 2004; Covey

et al., 2005; Cieza & Baliber, 2007). The portrait of a star's angular momentum evolution that has emerged from these efforts suggests that star-disk interactions lock a star to a slow rotation period (P$\sim$8 d) matched to the angular velocity of the disk's inner edge; in this picture stars spin up to become fast rotators (P $\sim$1–2 d) only once their disks have begun to dissipate. This picture suggests that slowly rotating young stars should possess disks with smaller inner holes than their faster rotating contemporaries, whose disks have presumably evolved such that star-disk interactions are no longer able to govern the star's rotation rate.

While most of these observational studies have tested mainly for a statistical correlation between a young star's rotation period and the presence or absence of a circumstellar disk, a key, generic prediction of disk-locking theories is that disk-locked stars should possess circumstellar disks with inner truncation radii (R_{trunc}) very nearly coincident with their co-rotation radus (R_{co}), the location where a Keplerian orbit within the disk possesses the same angular velocity as the star's surface. A few studies have attempted detailed comparisons of R_{trunc} vs. R_{co} for samples of young stars where these quantities could be measured or inferred (see Carr, 2007, and references therein). For example, Najita et al. (2003) spectroscopically measured R_{trunc} for six stars in Taurus-Auriga, finding that on average $R_{trunc} \approx 0.7 \times R_{co}$. In the context of magnetic star-disk interaction models, this result would suggest that these stars are in fact experiencing active *spin-up* torque from their disks, since the stars would then be coupled to disk material with higher specific angular momentum than the stars'.

However, the sample sizes remain too small to draw robust conclusions. Perhaps most importantly, the range of important parameters—especially stellar rotation period—remains to be fully probed by such analyses. Indeed, the Najita et al. (2003) sample includes only slowly rotating stars with P_{rot} = 5–12 d. Thus, the role of star-disk interaction for more rapidly rotating stars remains an important question.

There are also open questions concerning the universality of the disk locking mechanism. Stassun et al. (1999), Herbst et al. (2002), and Cieza & Baliber (2007), for example, found that the lowest mass stars lack the bimodal rotation period distribution traditionally interpreted as another signature of disk-locking. Additionally, Stassun et al. (2001) investigated the structure of circumstellar disks as a function of rotation period and questioned the idea of a simple dichotomy between disked slow rotators and diskless rapid rotators. From a theoretical standpoint, Matt et al. (2010), also found that models of star-disk interactions incorporating the impact of open field lines were unable to reproduce the observed population of slow rotators. They moreover found that, while the bulk of the stars in their models possessed disks truncated at R_{co}, that did not necessarily imply a zero-torque configuration where the star is "locked" at a constant rotation rate.

In this dissertation, we analyze the properties of two star forming regions (IC 348 and the Orion Nebular Cluster (ONC)) for which we have large samples of stars, to test the agreement between their rotational periods and the Keplerian orbital periods at the inner edges of their stellar disks. In particular, we seek to test two implications

of the commonly presented picture of the disk-locking phenomena: (1) how do R_{trunc} and R_{co} compare for well-populated ensembles of circumstellar disks and (2) do fast rotators possess disks with $R_{trunc} \gg R_{co}$, as expected if the disks around fast rotators have evolved to the point that star-disk interactions no longer govern their host star's rotation rate?

The IC 348 star-forming region is located in the Perseus molecular cloud complex, and is one of the closest laboratories for young (∼2-3 Myr for IC 348) pre main-sequence stars (PMS) at a distance of ∼ 315 - 320pc (Cieza & Baliber, 2006; Lada et al., 2006). This region is only partially embedded, which allows for observing in a low-extinction environment ($A_v < 4$, Luhman et al., 2003). This cluster has a confirmed, fairly large membership of ∼ 400 (Cieza & Baliber, 2006), with a wide range in mass determined (from 0.02 - $5M_{\odot}$). The ONC is also fairly close ∼ 414pc (Da Rio et al., 2009), and very young ∼ 1Myr (Hillenbrand, 1997), with a mass range including the entire initial mass function (IMF) of ∼ $25M_{\odot}$ down to $0.01M_{\odot}$ (or ∼ $10M_{Jup}$, Robberto et al., 2005). This region has had its prenatal environment cleared by the expansion of an HII region produced by its brightest members: the resulting large confirmed membership (> 2000, Ali & Depoy, 1995) makes it possible to observe very young stars that would otherwise be veiled in prenatal material. The ONC has been extensively studied in the visible (e.g., Hillenbrand, 1997; Robberto et al., 2004), near-IR (e.g., Hillenbrand & Hartmann, 1998; Hillenbrand & Carpenter, 2000; Luhman et al., 2000), and far-IR (e.g. Robberto et al., 2005), allowing the assembly

of near-complete spectral energy distributions (SEDs) for identified members.

In Chapters II (for IC 348) and III (for Orion), we describe the fundamentals of the test, as well as the parameters needed (stellar properties, disk properties inferred from photometry, and the model grid). We then apply the test and report the findings. We present a discussion and summarize in Chapter IV.

Chapter II

IC348:
THE PERSEUS STAR-FORMING REGION

2.1 Introduction

In this chapter, we analyze the properties of 33 stars in IC 348 to test the predictions of the disk-locking phenomena, i.e., how well do the stellar rotation periods match the Keplerian orbital period at the inner edge of their circumstellar disk. As described in Chapter I, we want to test the implications of this theory: for a well-populated set of stars with circumstellar disks, how do their inferred R_{trunc} and calculated R_{co} compare? And do disks with $R_{trunc} \gg R_{co}$ correspond to stars with evolved disks to the point at which the magnetic star-disk interaction is no longer feasible, and thus resulting in rapidly rotating stars?

2.2 Methods

We aim to conduct a quantitative test of a central prediction of disk locking theories: Does a young star rotate with a period equal to the Keplerian orbital period of its inner disk? To perform this test, we define two characteristic locations within the circumstellar disk: the distance from the star to the disk's inner edge, R_{trunc}, and R_{co}, the radius at which the Keplerian angular velocity in the disk equals the star's angular velocity (Ghosh & Lamb, 1979b; Shu et al., 1994). R_{co} is calculated for each

star as:

$$R_{co} = (GM_{\star}P_{rot}^2/4\pi^2)^{1/3} \tag{2.1}$$

where $M_{\star}$ and P_{rot} are the star's mass and rotation period, respectively.

To measure the truncation radius of each young star's circumstellar disk, we analyze the amount of excess emission detected from each star at near- and mid-infrared wavelengths, arising from warm dust in the inner circumstellar disk. Specifically, we compare mid-infrared photometry from the Spitzer Space Telescope, as well as ground-based optical and near-infrared observations, to synthetic spectral energy distributions (SEDs) computed from a grid of 200,000 Monte-Carlo models covering a wide range of parameter space. We conduct this analysis on young stars in IC 348, a nearby, young cluster in the Perseus star forming region. This compact, optically visible region is amenable to photometric surveys at optical wavelengths, enabling efficient measurements of stellar rotation via star-spot modulation of stellar light curves, and the construction of SEDs sampling the short wavelengths dominated by the stellar photosphere, as well as the longer wavelengths dominated by the circumstellar disk.

2.2.1 Photometry from the Literature

In this study, we make use of the SED measurements compiled by Lada et al. (2006) (L06) in their study of circumstellar disks in IC 348. L06 combined ground-based broadband RIJHK measurements with mid-IR photometry from the Infrared

Table II.1. Photometric Calibration Data

Filter(Type)	$\lambda_{eff}(\mu m)$	Zeropoint (Jy)	Refs.
Johnson[R]	0.64	3072.0	[1]
Johnson[I]	0.79	2496.4	[1]
2MASS[J]	1.24	1594.0	[2]
2MASS[H]	1.65	1024.0	[2]
2MASS[K]	2.17	666.7	[2]
IRAC[3.6]	3.6	277.3	[3]
IRAC[4.5]	4.5	179.6	[3]
IRAC[5.8]	5.8	116.6	[3]
IRAC[8.0]	8.0	63.1	[3]
MIPS[24]	24.0	7.14	[3]

Note. — Calibration data used in converting photometric measurements into flux.

[1]Cousins (1976)

[2]Cohen et al. (2003)

[3]Fazio et al. (2004)

Array Camera (IRAC) and Multiband Imaging Photometer (MIPS) on the Spitzer Space Telescope to produce SEDs for ∼300 stars previously identified as cluster members by Luhman et al. (2003). The L06 SEDs span 0.5–24 μm, providing good sensitivity to emission from the stellar photosphere as well as the inner circumstellar disk. L06 reported the broadband photometry in magnitudes; we converted these into flux units using standard passband zeropoints (Cousins, 1976; Cohen et al., 2003; Fazio et al., 2004), which are summarized in Table II.1.

2.2.2 Stellar Properties

Calculating R_{co} for each star in our sample requires measurements of P_{rot}, $M_\star$, and $R_\star$ (see Eq. 2.1 above). To infer each star's mass and radius, we adopt the T_{eff}, L_{bol} and A_V values determined for these stars by Luhman et al. (2003). Stellar masses were inferred for each star by comparing the measured T_{eff}s and L_{bol}s to pre-main sequence evolutionary models calculated by D'Antona & Mazzitelli (1997)(DM97). We calculate stellar radii using the fundamental Stephan-Boltzmann law, which relates the star's luminosity ($L_\star$) to a given radius ($R_\star$) and T_{eff}: $L_\star = 4\pi R_\star^2 \sigma T_{eff}^4$, where σ is the Stefan-Boltzmann constant. The full set of adopted and inferred parameters for each star are presented in Table II.2. Typical errors in $M_\star$ and $R_\star$ are derived from errors in T_{eff} and $L_\star$, with typical T_{eff} errors of half a spectral subtype ($\pm$82.5 K for M-type, $\pm$140 K for K-type), and typical errors of $\approx$0.3 in $\log L_\star$ (e.g. Hartmann, 2001). We adopt rotation periods from the catalog presented by Cieza & Baliber (2006), who measured $P_{\rm rot}$ due to starspot modulation of each star's light curve, from their multi-epoch I_C photometry of IC 348. To identify stars with circumstellar disks, we applied a $[3.6]-[8.0] > 0.7$ color cut as adopted by Cieza & Baliber (2006) to the stars in the L06 catalog (see Fig. 2.1).

For the low-mass stars under consideration here, this color cut ensures that dusty disk material is present within $\sim$1 AU of our sample stars.

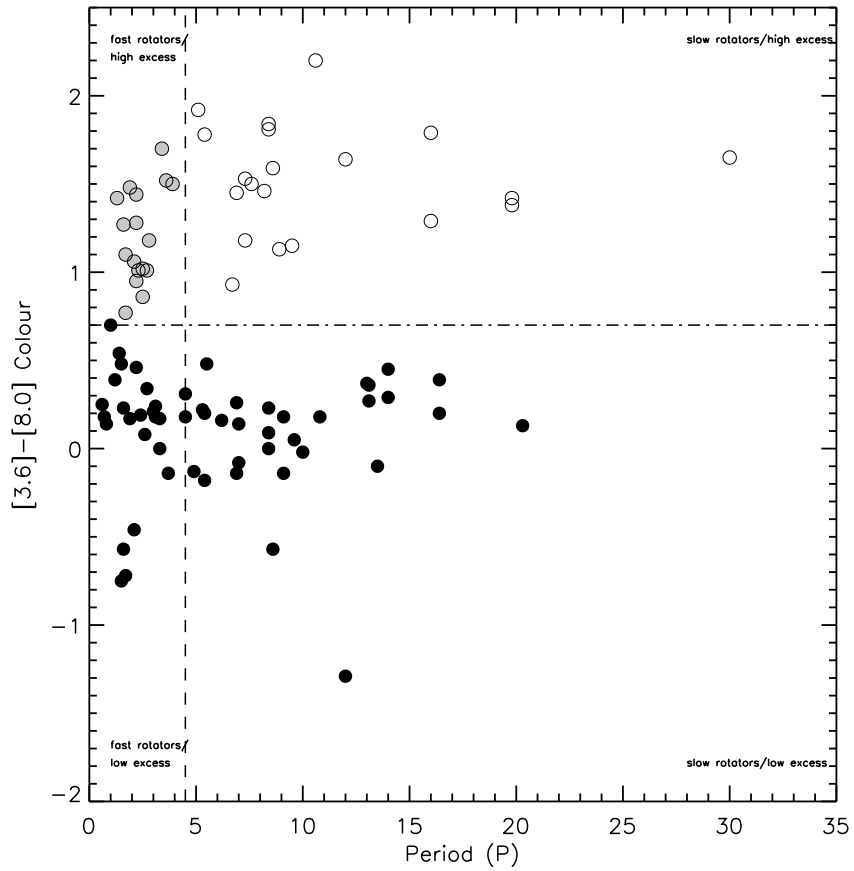

Figure 2.1: IRAC [3.6]-[8.0] color vs. rotation period for IC 348 members. The horizontal dashed line shows the IRAC color cut ([3.6]-[8.0] > 0.7) used to identify IC 348 members with substantial circumstellar disks. Periods are taken from the Lada et al. (2006); Cieza & Baliber (2006); Luhman et al. (2003) catalogues: the vertical dashed line indicates a period of 4.5 days, used to separate the sample of stars with disks into subsets of fast rotators ($P_{rot} < 4.5$ days; light grey filled circles) and slow rotators ($P_{rot} > 4.5$ days; empty circles). See electronic edition of the journal for a coloured version of this figure.

This leaves 33 stars with the requisite data for our study. For 27 of these we are able to determine the disk properties via SED fitting (see below). These are summarized in Table II.2.

Table II.2. Derived Stellar and Disk Parameters of IC 348 Sample

Star ID	Stellar Parameters from the literature						Disk Radii		
	P_{rot} (d)	T_{eff} (K)	L_{bol} ($L_\odot$)	M † ($M_\odot$)	R † ($R_\odot$)	A_V (mag)	R_{sub} ‡ (AU)	R_{co} (AU)	R_{trunc} (AU)
32	8.2	4060	1.4	0.48	2.39	5.79	0.08	0.06	0.11
36	5.1	4205	1.5	0.56	2.31	2.91	0.08	0.05	0.51
37	8.6	4205	0.99	0.64	1.87	2.88	0.07	0.07	0.27
58	7.3	3669	0.72	0.31	2.1	2.59	0.06	0.05	0.04
71	6.7	3415	0.47	0.24	1.96	2.14	0.04	0.04	2.66
75	10.6	3669	0.28	0.44	1.31	2.94	0.03	0.07	0.71
76	9.5	3306	0.39	0.19	1.9	2.13	0.04	0.05	0.04
83	8.4	3705	0.51	0.37	1.73	3.43	0.05	0.06	0.04
91	3.9	3560	0.39	0.32	1.64	2.01	0.04	0.03	0.03
97	7.3	3524	0.54	0.28	1.97	4.63	0.05	0.05	1.06
99	7.6	3306	0.26	0.21	1.55	1.91	0.03	0.04	0.04
100	8.4	3705	0.33	0.44	1.39	2.23	0.04	0.06	0.04
110	19.8	3560	0.34	0.34	1.53	4.66	0.04	0.10	2.18
128	2.2	3560	0.32	0.34	1.49	1.73	0.04	0.02	0.03
133	2.1	3125	0.17	0.16	1.41	4.79	0.03	0.02	2.16
149	2.5	3161	0.18	0.17	1.41	3.04	0.03	0.02	0.03
156	1.3	3234	0.17	0.21	1.31	2.04	0.03	0.01	0.02
165	1.9	3091	0.16	0.16	1.39	3.58	0.03	0.02	0.13

Table II.2 (cont'd)

Star ID	Stellar Parameters from the literature						Disk Radii		
	P_{rot} (d)	T_{eff} (K)	L_{bol} ($L_\odot$)	M † ($M_\odot$)	R † ($R_\odot$)	A_V (mag)	R_{sub} ‡ (AU)	R_{co} (AU)	R_{trunc} (AU)
166	3.6	3234	0.24	0.18	1.56	5.24	0.03	0.03	0.03
173	2.2	3024	0.12	0.15	1.26	2.57	0.02	0.02	0.02
213	2.3	3161	0.07	0.19	0.9	1.87	0.02	0.02	0.02
237	1.7	3125	0.07	0.18	0.93	2.23	0.02	0.02	1.16
336	1.6	3058	0.03	0.16	0.6	3.6	0.01	0.01	0.01
8042	16	3234	0.37	0.17	1.94	3.97	0.04	0.07	0.06
8078	8.9	3778	0.53	0.42	1.7	6.37	0.05	0.06	0.05
9024	4.5	3850	0.69	0.41	1.87	3.82	0.05	0.04	0.06
10352	6.9	3705	1.4	0.28	2.87	3.7	0.08	0.05	0.10
LB06-100	19.8	3560	0.34	0.34	1.53	4.86	0.04	0.10	0.04

Note. — Derived stellar properties. The radius and mass measurements were derived as described in § 2.2.2, while temperature, extinction, and luminosity values are from (Luhman et al., 2003), and rotation periods from (Cieza & Baliber, 2006). Typical fractional errors for the following parameters are; $T_{eff} \sim 3\%$, $L_{bol} \sim 81\%$, $M_\odot \sim 61\%$, and $R_\odot \sim 41\%$.

*These extinction values are the original estimates from L03. Our matches in this study for these stars did not yield enough information to make a judgement on the best fit extinction, and are excluded from the final analysis.

†Masses and radii were estimated using DM97(D'Antona & Mazzitelli, 1997) pre-main sequence evolutionary models (see §2.2.2), and the Stefan-Boltzmann law, respectively.

‡Sublimation radii were estimated using the stellar effective temperature and the sublimation temperature at which the dust in a protoplanetary disk is expected to be destroyed (see §2.3.1).

2.2.3 SED Models

We make use of a pre-computed grid of models, generated by Robitaille et al. (2006) (henceforth R06), to compare with photometry for stars in this study. This grid builds upon previous work done by Whitney et al. (2003a,b) (hereafter W03a, W03b), by calculating the temperature structure of circumstellar disks of young stellar objects (YSOs). W03a generated two-dimensional radiative transfer models of Class I YSOs,

while W03b presented model SEDs, polarizations, and images for an evolutionary sequence of YSOs from Class 0 to Class III. The W03a/W03b code uses Monte Carlo radiative equilibrium to generate model SEDs for YSOs, following the trajectory of photon packets emitted from a central stellar source into a disk and modeling their absorption, re-emission, and/or scattering (Bjorkman & Wood, 2001). This method yields a model temperature structure specific to the parameters describing the star (e.g., T_{eff} and R_*) and its disk (e.g., R_{trunc}, $M_\star$, and scale-height).

The R06 model grid consists of SED models calculated using the W03a algorithm, and covering a wide range of masses (from 0.1 to 50 $M_\odot$) and stages of YSO evolution. R06 characterized each model using 16 stellar, disk, and envelope parameters; the most pertinent to this study include stellar mass, temperature, and radius, as well as disk mass and R_{trunc}. The grid consists of 200,000 SEDs computed at ten different angles (ranging from near face-on at 18°, to near edge-on at 87°), resulting in a comprehensive set of SEDs suitable to comparing with actual YSO photometry. By comparing these synthetic SEDs with the observed SEDs we have assembled for our sample, we can infer the physical properties of each star's disk.

We used the R06 model grid to identify those models which reproduce each IC 348 member's observed SED. We limit each star's acceptable fits, however, to those models with distances (315 ± 30 pc) comparable to those measured for most IC 348 members. The initial matches were further screened on the basis of goodness of fit with the observed SED, agreement with the T_{eff} value reported in the literature for

each star, the implied A_V and disk mass:

- **T_{eff} filter** — We retain only those models with T_{eff} within $\pm$500 K of the value reported in the literature from previous spectroscopy-based determinations.;

- **χ^2 filter** — A χ^2 metric is applied to ensure goodness-of-fit, such that the models selected possessed $\chi^2 \leq \chi^2_{best} + 9.21$. This value corresponds to a 99% confidence level for two model parameters of interest in our SED fitting (Press et al., 1992), R_{trunc} and M_{disk} (see below).

- **A_V filter** — Previous work generally found A_V for IC 348 members to be modest, rarely larger than $\sim$5 mag (e.g. L06). Therefore, our SED fitting results with $A_V \geq 10$ were eliminated to remove models with excessive combined interstellar and stellar extinction. In most cases, models with artificially large A_V were already eliminated by the T_{eff} filter above.

- **M_{disk} filter** — Models lacking sufficiently massive disks ($M_{disk} \leq 10^{-4} M_\odot$) are also removed. Such low-mass disks are rarely seen in sub-mm surveys (Andrews & Williams, 2005), and are unlikely to be capable of sustaining significant star-disk interaction.

Of the 33 stars initially in our sample, six could not be matched to models in the R06 grid which satisfy all of the above criteria (star IDs 6, 21, 41, 61, 140, and 182; refer to Table II.3). In most cases this was because the best-fit SED models required very low disk masses ($M_{disk} < 10^{-4} M_\odot$). We therefore exclude these stars from our

Table II.3. Discarded IC 348 Sample

Star ID	Stellar Parameters from the literature						Disk Radii		
	P_{rot} (d)	T_{eff} (K)	L_{bol} ($L_\odot$)	M † ($M_\odot$)	R † ($R_\odot$)	A_V (mag)	R_{sub} ‡ (AU)	R_{co} (AU)	R_{trunc} (AU)
6	1.7	5830	17	2.86	4.04	3.56	0.28	0.04	0.04
21	2.5	5250	3.9	1.48	2.39	5.83	0.13	0.04	0.04
41	2.8	4060	0.79	0.55	1.8	5.76	0.06	0.03	0.03
61	30	3955	0.54	0.55	1.56	4.53	0.05	0.15	0.15
140	12	3379	0.13	0.28	1.05	3.41	0.02	0.07	0.07
182	2.7	3234	0.15	0.2	1.23	3.43	0.03	0.02	0.02

Note. — Derived stellar properties of the discarded sample. Refer to Table II.2 for notes.

†‡Refer to Table II.2 for notes on masses, radii, and sublimation radii of our sample.

subsequent analysis. The results of the model vs. observed SED comparisons for the remaining 27 stars are discussed in §2.3, with summaries of the SED fitting results for three representative stars shown in Figs. 2.2–2.4. The entire atlas of SED fittings for the IC 348 sample can be accessed in Appendix A at the end of this document.

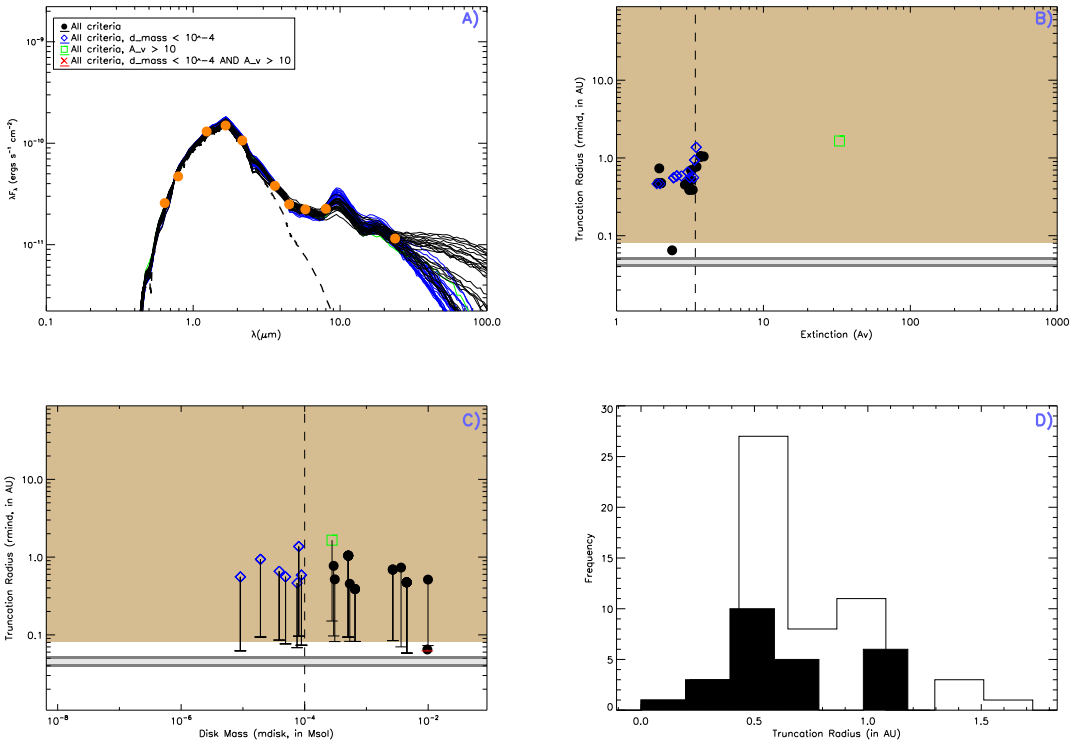

Figure 2.2: SED fitting results for IC 348 36, an example of a star whose model fit predicts $R_{trunc} \gg R_{co}$, and $R_{trunc} \gg R_{sub}$. **Panel A)** Photometric SED (detections shown as yellow filled circles; upper limits as yellow arrows) compared to an artificially reddened Phoenix stellar atmosphere with the same T_{eff} (dashed line) and SED fits from the R06 model grid: black lines show R06 model SEDs meeting all criteria outlined in §2.2.3, with colored lines showing models that fail one of those criteria (see legend in panel). **Panels B and C)** Location of model fits in R_{trunc} vs. M_{disk} or A_V parameter space. Black points indicate models meeting all criteria in § 2.2.3. Models failing the limits on M_{disk} & A_v are shown as blue diamonds and green squares, respectively, with models failing both criteria shown as red crosses. Lower "error" bars indicate the distance between R_{trunc} and R_{sub} (at each model's T_{eff}). Vertical dashed lines in panels B & C show the M_{disk} limit and the A_V value reported for this star in the literature, respectively. The domain where $R > R_{sub}$ is indicated with a mocha background; light grey bars show the range of possible R_{co}s assuming a 50% uncertainty in M_*, with dark grey bands indicating the range of possible R_{co}s assuming a conservative 100% uncertainty in M_*. **Panel D)** Distribution of R_{trunc} values for all R06 models satisfying the basic χ^2 criteria (open histogram), and for models meeting all criteria (filled histogram).

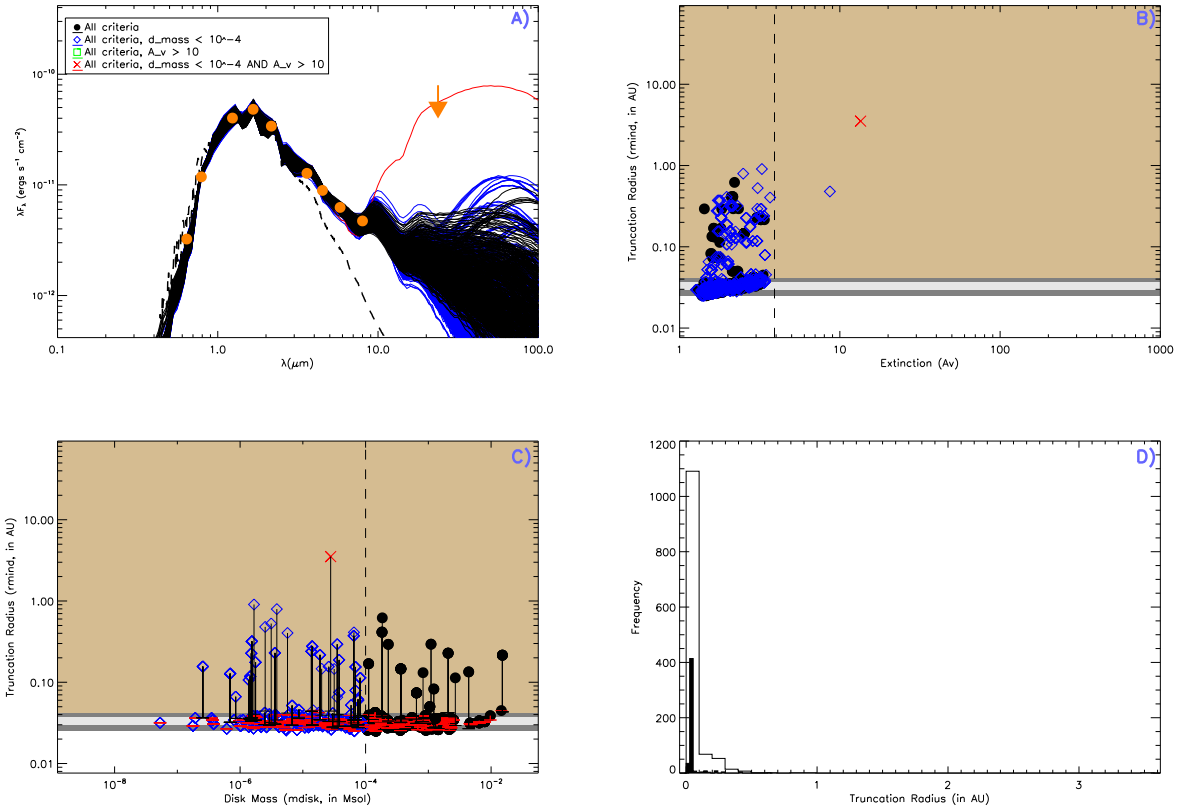

Figure 2.3: IC 348 91. This sample SED and accompanying panels represent a star for which the model grid predicts $R_{trunc} = R_{co}$. Refer to Figure 2.2 for further explanation of each of the above panels.

2.3 Results

2.3.1 Inferred Disk Truncation, Co-rotation, and Dust Sublimation Radii

We have inferred R_{trunc} for each star by computing the mean R_{trunc} of the full suite of R06 models which acceptably reproduce that star's SED and meet each of the criteria outlined above. To provide context for these mean $R_{\rm trunc}$ values, we calculated the ratio between each star's $R_{\rm trunc}$ and its co-rotation and dust-sublimation radii (R_{co} and R_{sub}, respectively). The first of these ratios, $R_{\rm trunc}/R_{\rm co}$, is of course the principal

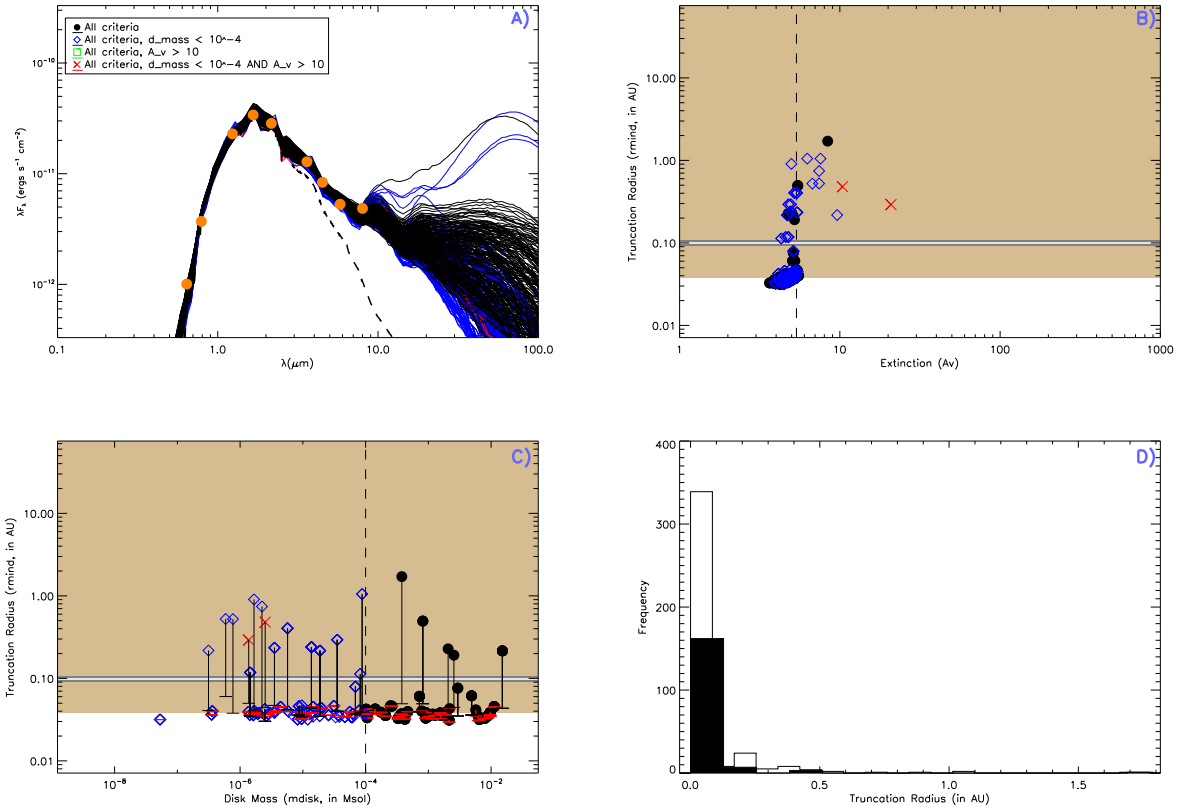

Figure 2.4: IC 348 LB06-100. This sample SED and accompanying panels represent a star for which the model grid predicts $R_{trunc} = R_{sub}$. Refer to Figure 2.2 for further explanation of each of the above panels.

quantity that we seek to test, as $R_{trunc}/R_{co} \approx 1$ is predicted by most disk-locking theories (see Chapter I).

We also compute $R_{\rm trunc}/R_{\rm sub}$, which indicates if the $R_{\rm trunc}$ value returned by the SED model fits corresponds to the true inner edge of the circumstellar disk. Magnetic star-disk interaction requires the stellar magnetic field lines to connect to ionized gas in the circumstellar disk. It is therefore important to note that the observed SEDs used here, based on broadband fluxes, strictly speaking trace only the spatial extent of

a disk's dust. However, dust that is sufficiently close to the stellar surface is expected to be destroyed via sublimation. This effect is included in the R06 SED model grid; if a disk would otherwise extend inward of R_{sub}, the disk is forced to have $R_{trunc} = R_{sub}$. R_{sub} is given by (Tuthill et al., 2001; D'Alessio et al., 2004; Whitney et al., 2003a,b): $R_{sub} = R_{\star} \times (T_{sub}/T_{eff})^{-2.1}$ where T_{sub} is the temperature at which dust is destroyed by photoevaporation (the R06 grid assumes $T_{sub} = 1600$ K).

In cases for which we find $R_{trunc} = R_{sub}$, we assume that the dust has been truncated by sublimation, a process which would not remove the gas (e.g. Najita et al., 2003; Eisner et al., 2005). Therefore, in these cases we assume that the gas in the disk in fact extends closer to the star than inferred from the observed SED; the inferred R_{trunc} in these cases is therefore an upper limit. Conversely, in cases for which we find $R_{trunc} > R_{sub}$, some other process may be responsible for clearing out the inner portion of the disk, and therefore we assume that the inner gas is cleared out as well (e.g. Isella et al., 2009).

Fig. 2.5 shows the $R_{\rm trunc}/R_{\rm co}$ and $R_{\rm trunc}/R_{\rm sub}$ ratios for our entire sample. We immediately identify two distinct populations of stars: One group with $R_{trunc} \gg R_{co}$ and $R_{trunc} \gg R_{sub}$ (32% of the final sample), and a second group with $R_{trunc} \approx R_{co}$ (68% of the sample).

Since $R_{\rm co}$ is generally the location of "action" in most magnetic star-disk interaction models (Shu et al., 1994; Mohanty & Shu, 2008; Matt et al., 2010), the first group represents stars for which a magnetic star-disk interaction is most likely not

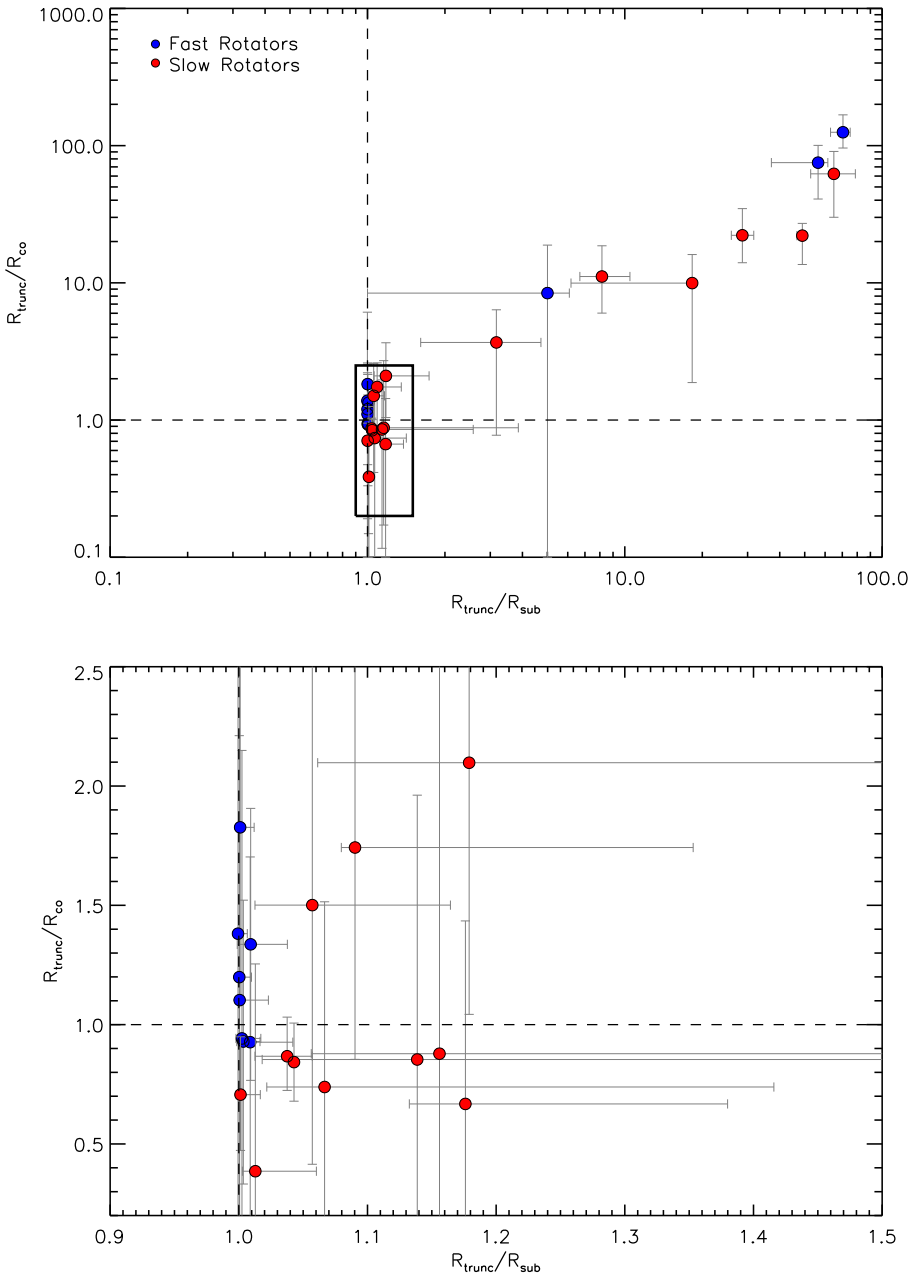

Figure 2.5: Truncation with Corotation and sublimation radii ratio plot. The plot shows the ratios of the corotation and sublimation radii in relation to the mean truncation radii for all acceptable models in the R06 grid for the entire sample (top panel). The targets within the solid box are stars with potential disks (top panel, zoomed in bottom panel), while those outside are stars that are effectively diskless. Errors in the truncation/sublimation radius ratio (x-axis) are represented as interquartile range errors, with 25% on the left and 75% on the right of each data point. Truncation/corotation radius ratio errors are represented as 1 σ.

important. With physically very large R_{trunc}, far beyond R_{co}, these stars evidently harbor disks that have evolved significantly and no longer present substantial disk material within reach of the stellar magnetosphere; we refer to these stars as "effectively diskless". In contrast, the latter group represents stars with substantial disk material situated at or very near to the location of potential star-disk interaction. While the precise location of the inner-disk edge relative to R_{co} requires a detailed examination of possible dust sublimation effects (which we do below), as discussed above the effect of such dust sublimation will be to imply a true R_{trunc} that is even closer to the star that what we have inferred, and for which we might expect active interaction between the disk and the stellar magnetosphere to be even more likely. Therefore, we refer to this group of stars as "potentially disk-locked". We discuss the implications of these two groups in more detail below.

2.3.2 Comparison of Potentially Disk-Locked and Effectively Diskless Stars

Figure 2.6 shows the location of these IC 348 members within the HR diagram, with tracks and isochrones calculated by DM97 overlaid for comparison. The IC 348 members analyzed here possess HR diagram locations consistent with 1–2 Myr isochrones, with implied masses of 0.7 $M_{\odot}$ or below. There is no clear difference between the ages and masses of the members of the potentially disk-locked and effectively diskless groups: this visual conclusion is supported by 1D and 2D two sided K-S tests, which indicate that the ages and masses of the stars in the two groups are

consistent with shared parent populations at 94% and 74% confidence levels (1D) and 52% (2D). We also applied a two-sided K-S test on the rotation period distributions for the potentially disk-locked and effectively diskless groups (see Fig. 2.7). The K-S test in this case returns a probability of 0.74, and as such we cannot reject the null hypothesis that the two distributions are drawn from the same parent distribution.

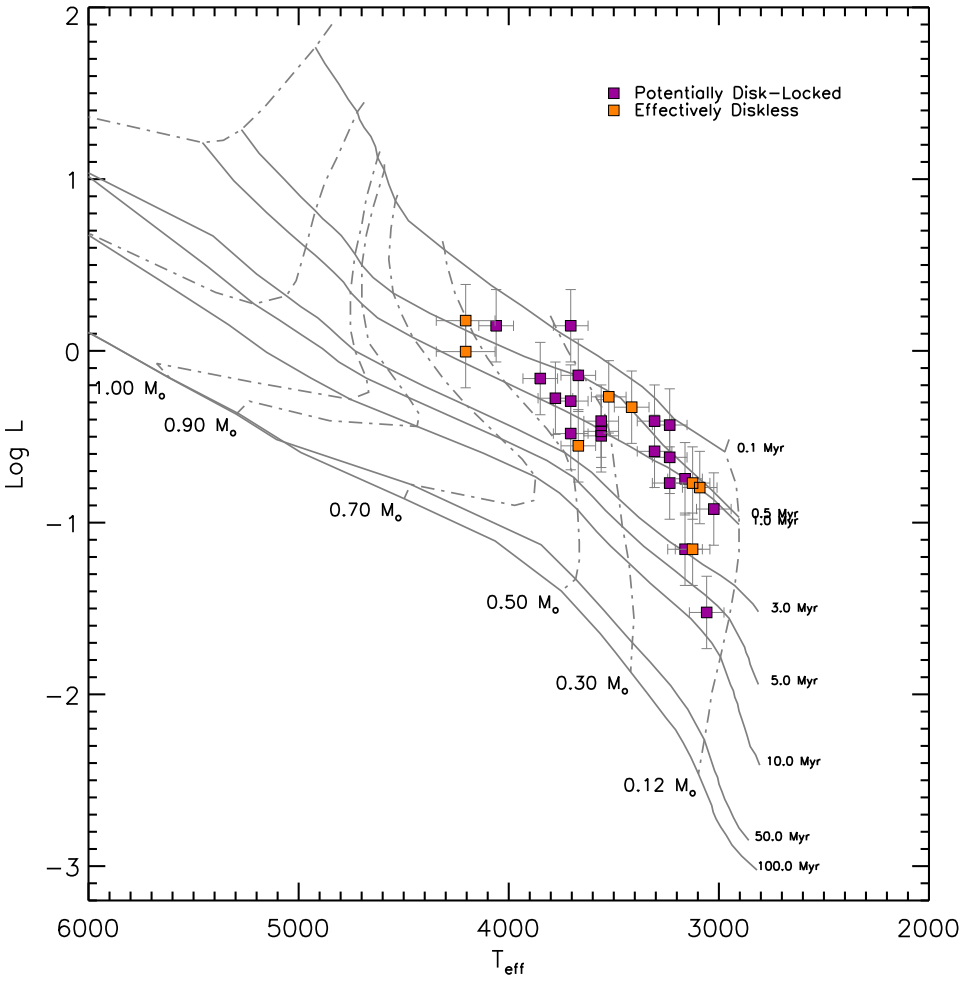

Figure 2.6: HR Diagram with over plotted tracks and isochrones using DM97. All errors represented in both log L & log T are 1 σ.

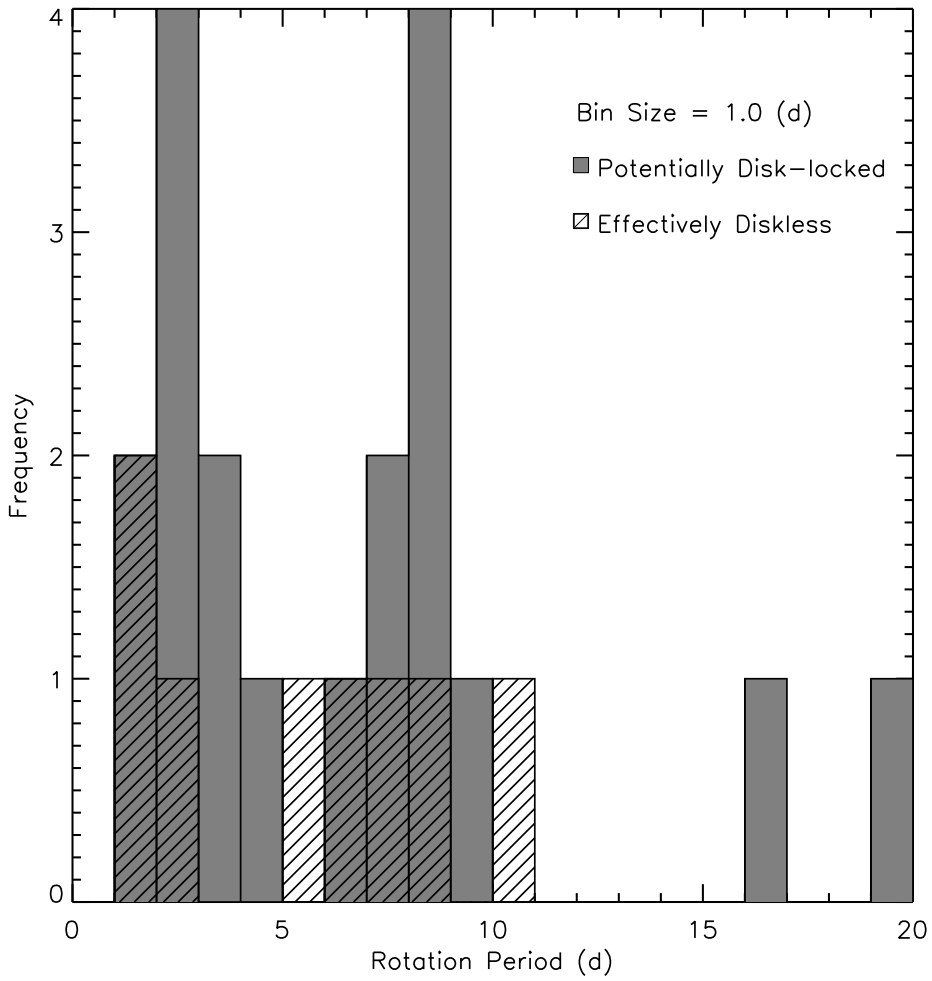

Figure 2.7: Rotation period histogram of potentially disk-locked (gray) and effectively diskless stars (empty hatched). Though the potentially disk-locked stars are greater in number than the effectively diskless stars, this histogram supports the null hypothesis that both distributions are from the same parent distribution.

Chapter III

ORION:
THE ONC STAR-FORMING REGION

3.1 Introduction

In this chapter, analyze the properties of 106 stars in the ONC, which is $\sim$3$\times$ that of the IC 348 sample (refer to Chapter II), to test the predictions of the disk-locking phenomena as described in Chapter I and outlined in §2.2. The parameters needed to conduct this test (such as the stellar properties, the inferred disk properties, and the model grid), are described in §3.2, and the results of our analysis are presented in §3.3.

3.2 Methods

As in our previous paper (Le Blanc et al., 2011, henceforth LB2011), we continue to conduct the quantitative test of the central prediction of the disk-locking theories: does a young star rotate with a period equal to the Keplerian orbital period of its inner disk? And is this an indication that the young star's early rotation history is dependent on the presence of a disk?

The methods used to answer these questions are the same as in LB2011; we continue to use the definitions of the two most important characteristics of the circumstellar disk: the distance from the star the the disk's inner edge, R_{trunc}, as well

as the radius at which the disk rotates at the same Keplarian angular velocity as the star's angular velocity at its surface, R_{co}. Just as before, we compare mid-infrared photometry from the *Spitzer* Space Telescope, as well as various ground-based optical and near-infrared observations, to the synthetic spectral energy distributions (SEDs) computed by Robitaille et al. (2007, henceforth R07) from a grid of 200,000 Monte-Carlo models covering a wide range of parameter space. As opposed to the study outlined in LB2011, however, we conduct this analysis on young stars in the Orion Nebula Cluster (ONC), a relatively close and dense star forming region. The purpose is to perform the same test as we did in IC 348; to analyze the inferred R_{trunc} and measured R_{co} to determine if they indeed agree with the predictions of disk-locking. Just as in IC 348, observation of the ONC is sensitive to optical and near IR wavelengths of the young star and inner disk regions, as well as the far IR signatures of the circumstellar disk as observed by *Spitzer* studies.

3.2.1 Photometry from the Literature

We make use of the *Spitzer* Infrared Array Camera (IRAC) and Multiband Imaging Photometer (MIPS) data from Megeath, T.: 2011 (private communication), covering the IRAC wavelength range of 3.6 - 8.0μm, as well as MIPS 24μm. This wavelength coverage provides good sensitivity to emission from the inner edge region of the circumstellar disk; to cover the stellar photosphere emission, we use photometry in the 0.3-2.5μm range. We supplement the regions probing the stellar emission using

the *Hubble* Space Telescope Advanced Camera for Surveys (ACS) and ESO Wide Field Imager (WFI), covering a wavelength range of 0.3-0.9μm obtained from Robberto et al. (2005). Additionally, we include observations in V and I by Hillenbrand (1997), and 2MASS JHK from the NASA/IPAC Infrared Science Archive [1] (covering wavelengths of 1.1-2.5μm). All photometry were reported in magnitudes; they were converted into flux units in the same manner as in LB2011, using standard passband zeropoints (refer to Table 1 in LB2001).

3.2.2 Stellar Properties

Calculating R_{co} for each star in our sample follows the same procedures as outlined in LB2011, requiring measurements of P_{rot}, $M_\star$, and $R_\star$ (see Eq.1 from LB2011). We adopt the T_{eff} and L_{bol} values determined for these stars by Da Rio et al. (2009), and supplemented by Hillenbrand (1997) where available, to infer each star's mass and radius, while A_V estimates are from Hillenbrand (1997). Stellar masses were inferred for each star by comparing the measured T_{eff}s and L_{bol}s to pre-main sequence evolutionary models calculated by D'Antona & Mazzitelli (1997)(DM97), while we calculate stellar radii using the fundamental Stephan-Boltzmann law, which relates the star's luminosity ($L_\star$) to a given radius ($R_\star$) and T_{eff}: $L_\star = 4\pi R_\star^2 \sigma T_{eff}^4$, where σ is the Stefan-Boltzmann constant. The full set of adopted and inferred parameters for each star are presented in Table III.1. Typical errors in $M_\star$ and $R_\star$ are derived from

[1] http://irsa.caltech.edu/applications/Gator/

errors in T_{eff} and $L_\star$, with typical T_{eff} errors of half a spectral subtype ($\pm$82.5 K for M-type, $\pm$140 K for K-type), and typical errors of ≈ 0.3 in $\log L_\star$ (e.g., Hartmann, 2001). We adopt rotation periods from the catalog presented by Herbst et al. (2002), who measured $P_{\rm rot}$ using Monte Carlo simulations to find the relationship between calculated normalized power (P_N) of stellar periodogram and the false alarm probability (FAP) of their sample. To identify stars with circumstellar disks, we continue to use a $[3.6]-[8.0] > 0.7$ color cut as adopted by Cieza & Baliber (2006) to the stars in our compiled catalogue (see Fig. 3.1). This color cut increases the chances of identifying dusty disk material within $\sim$1 AU of our sample stars for the low-mass stars considered in this study.

This leaves 106 stars with the requisite data for our study; $\sim 3\times$ the amount in the compiled list of our LB2011 study. We are able to determine the disk properties via SED fitting for 82 of these (see §2.2.3). These are summarized in Table III.1.

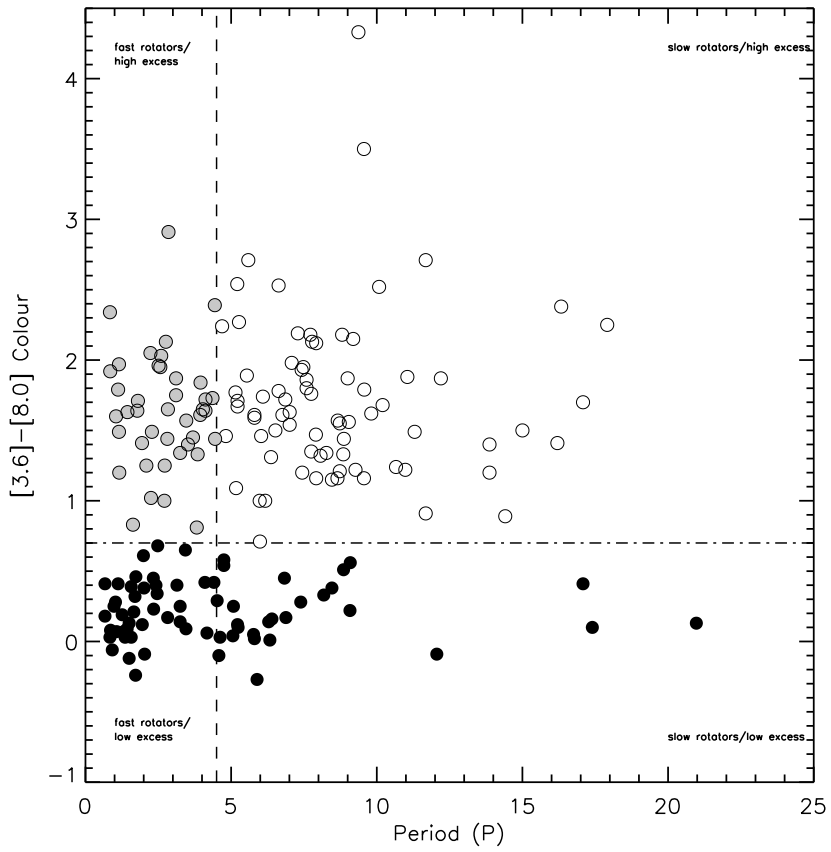

Figure 3.1: IRAC [3.6]-[8.0] color vs. rotation period for IC 348 members. The horizontal dashed line shows the IRAC color cut ([3.6]-[8.0] > 0.7) used to identify IC 348 members with substantial circumstellar disks. Periods are taken from the Herbst et al. (2002) catalogue: the vertical dashed line indicates a period of 4.5 days, used to separate the sample of stars with disks into subsets of fast rotators ($P_{rot} < 4.5$ days; light grey filled circles) and slow rotators ($P_{rot} > 4.5$ days; empty circles).

Table III.1. Derived Stellar and Disk Parameters of ONC Sample

Star ID	Stellar Parameters from the literature						Disk Radii		
	P_{rot} (d)	T_{eff} (K)	L_{bol} ($L_\odot$)	M † ($M_\odot$)	R † ($R_\odot$)	A_V (mag)	R_{sub} ‡ (AU)	R_{co} (AU)	R_{trunc} (AU)
10	8.66	4275	1.00	0.70	2.92	3.01	0.11	0.07	0.21
15	9.56	3706	0.36	0.42	1.87	1.75	0.05	0.07	0.10
25	2.28	3198	0.33	0.17	3.07	0.00	0.06	0.02	0.23
35	5.99	3411	0.56	0.22	4.04	0.00	0.09	0.04	0.13
36	2.72	3411	0.59	0.22	4.24	1.36	0.10	0.02	0.58
91	17.08	3273	0.34	0.18	2.89	0.00	0.06	0.07	0.01
100	2.09	3483	0.21	0.32	1.41	2.21	0.03	0.02	0.21
104	1.78	3411	0.19	0.29	1.40	0.13	0.03	0.02	0.06
114	8.73	3706	0.23	0.49	1.17	0.42	0.03	0.07	0.10
117	8.87	3845	0.58	0.44	2.57	0.86	0.08	0.06	0.14
121	5.54	3411	0.45	0.24	3.23	2.98	0.07	0.04	0.16
123	6.63	4897	1.31	1.22	2.23	3.06	0.11	0.07	0.29
135	3.69	3411	0.44	0.24	3.17	0.98	0.07	0.03	0.42
136	8.65	3775	0.53	0.42	2.53	0.00	0.07	0.06	0.42
138	4.44	3341	0.21	0.24	1.67	0.00	0.04	0.03	0.01
149	2.83	3411	0.09	0.31	0.65	1.80	0.01	0.03	0.42
156	7.92	3775	0.43	0.44	2.08	3.91	0.06	0.06	0.15
164	6.52	3556	0.28	0.35	1.72	0.39	0.04	0.05	0.64
169	3.85	3411	0.17	0.29	1.21	0.00	0.03	0.03	0.28
175	9.19	3411	0.23	0.26	1.66	0.00	0.04	0.05	1.03
186	5.80	3483	0.75	0.24	4.95	4.90	0.12	0.04	0.43
187	14.41	4355	0.96	0.72	2.62	3.95	0.10	0.10	0.26
203	7.29	3845	0.43	0.49	1.93	1.76	0.06	0.06	0.91
222	5.17	3556	0.26	0.36	1.58	1.59	0.04	0.04	0.36

Table III.1 (cont'd)

Star ID	Stellar Parameters from the literature						Disk Radii		
	P_{rot} (d)	T_{eff} (K)	L_{bol} ($L_\odot$)	M † ($M_\odot$)	R † ($R_\odot$)	A_V (mag)	R_{sub} ‡ (AU)	R_{co} (AU)	R_{trunc} (AU)
237	5.22	3273	0.21	0.19	1.82	0.80	0.04	0.03	0.60
243	10.20	3556	0.32	0.33	1.93	0.34	0.05	0.06	0.42
245	8.73	3556	0.45	0.30	2.77	1.21	0.07	0.06	0.14
248	6.86	3775	0.50	0.42	2.40	0.75	0.07	0.05	0.01
249	3.82	4897	2.07	1.25	3.50	3.47	0.17	0.05	0.29
250	2.71	3411	0.37	0.24	2.69	1.16	0.06	0.02	0.12
253	8.46	4355	1.17	0.65	3.17	4.66	0.12	0.07	0.01
254	3.52	3411	0.46	0.24	3.31	1.70	0.08	0.03	0.12
257	5.22	3198	0.17	0.19	1.58	0.00	0.03	0.03	0.62
258	10.98	3775	0.43	0.45	2.05	1.29	0.06	0.07	0.70
278	6.76	4355	0.42	0.85	1.14	1.61	0.04	0.07	0.01
283	7.01	3953	0.55	0.54	2.18	3.48	0.07	0.06	0.15
284	3.11	3411	0.70	0.21	5.08	1.44	0.12	0.02	0.15
301	7.92	4345	1.12	0.68	3.07	0.00	0.12	0.07	0.21
321	7.44	3845	0.53	0.47	2.36	0.76	0.07	0.06	0.26
334	5.27	3706	0.59	0.35	3.07	0.95	0.08	0.04	0.01
356	4.69	3411	0.63	0.22	4.54	0.00	0.10	0.03	0.02
358	4.03	3706	0.82	0.32	4.22	3.34	0.11	0.03	0.17
373	9.81	4731	3.30	1.02	6.43	5.85	0.29	0.09	0.33
379	11.30	3054	0.28	0.14	3.14	0.75	0.06	0.05	0.38
402	15.00	3054	0.16	0.14	1.79	0.39	0.03	0.06	0.43
422	6.37	3491	0.54	0.26	3.52	0.00	0.08	0.04	0.42
466	6.17	3341	0.23	0.22	1.82	0.44	0.04	0.04	0.09
498	7.42	3706	0.22	0.50	1.13	0.00	0.03	0.06	0.01

Table III.1 (cont'd)

Star ID	Stellar Parameters from the literature						Disk Radii		
	P_{rot} (d)	T_{eff} (K)	L_{bol} ($L_\odot$)	M † ($M_\odot$)	R † ($R_\odot$)	A_V (mag)	R_{sub} ‡ (AU)	R_{co} (AU)	R_{trunc} (AU)
579	2.81	3411	0.39	0.24	2.81	1.42	0.06	0.02	0.49
626	1.63	3126	0.07	0.17	0.70	0.00	0.01	0.02	0.03
635	4.12	3198	0.64	0.35	5.96	2.50	0.12	0.04	0.21
646	1.94	3411	0.27	0.25	1.97	2.06	0.04	0.02	0.31
649	1.80	2992	0.22	0.13	2.67	0.00	0.05	0.01	0.40
673	1.44	4355	0.13	0.68	0.35	1.33	0.01	0.02	0.34
677	4.12	3258	0.18	0.21	1.53	0.19	0.03	0.03	0.01
727	6.03	3556	0.28	0.36	1.68	0.54	0.04	0.05	0.42
728	13.87	3706	0.47	0.38	2.44	0.88	0.07	0.08	0.58
735	5.21	3341	0.24	0.23	1.91	0.92	0.04	0.04	3.30
758	2.51	3273	0.77	0.39	6.54	1.39	0.14	0.03	0.17
783	1.15	3556	0.20	0.37	1.21	0.00	0.03	0.02	1.00
787	9.00	3775	0.62	0.38	2.96	0.00	0.08	0.06	0.20
788	4.82	3273	0.58	0.17	4.91	1.46	0.10	0.03	0.57
789	3.25	3341	0.31	0.22	2.41	3.72	0.05	0.03	0.36
826	9.57	4064	0.75	0.55	2.68	0.00	0.09	0.07	0.01
834	7.01	3810	0.91	0.35	4.21	0.00	0.12	0.05	0.21
835	8.85	3411	0.22	0.27	1.61	0.00	0.04	0.05	0.43
850	7.78	3953	0.52	0.53	2.06	1.10	0.06	0.06	0.26
855	7.08	3556	0.44	0.31	2.67	0.28	0.07	0.05	0.35
863	7.91	3341	0.27	0.22	2.11	0.00	0.05	0.05	0.01
867	10.66	3953	1.16	0.42	4.63	0.56	0.14	0.07	0.56
923	1.15	3706	0.55	0.36	2.85	0.37	0.08	0.02	0.21
925	11.68	3411	0.26	0.27	1.90	0.00	0.04	0.07	0.20

Table III.1 (cont'd)

Star ID	Stellar Parameters from the literature						Disk Radii		
	P_{rot} (d)	T_{eff} (K)	L_{bol} ($L_\odot$)	M † ($M_\odot$)	R † ($R_\odot$)	A_V (mag)	R_{sub} ‡ (AU)	R_{co} (AU)	R_{trunc} (AU)
933	5.98	3273	0.30	0.18	2.59	0.00	0.05	0.04	0.28
938	5.15	4897	4.76	1.40	8.08	4.36	0.39	0.07	2.26
972	8.07	3706	0.37	0.42	1.92	0.11	0.05	0.06	0.71
1000	7.48	3556	0.18	0.37	1.11	1.75	0.03	0.05	0.93
1008	9.27	3775	0.55	0.41	2.63	0.00	0.07	0.06	0.44
1021	7.75	4275	0.66	0.69	1.92	1.37	0.07	0.07	0.77
1051	2.25	3411	0.38	0.24	2.73	3.49	0.06	0.02	0.12
1053	1.05	3126	0.09	0.17	0.90	0.00	0.02	0.01	0.04
3130	3.46	3198	0.15	0.19	1.39	0.91	0.03	0.03	0.21
3148	1.16	3126	0.11	0.17	1.09	0.00	0.02	0.01	0.05

Note. — Derived stellar properties. The radius and mass measurements were derived as described in § **??**, while temperature and luminosity values are from Da Rio et al. (2009) (supplemented by Hillenbrand (1997) when not availble), extinction values are from Hillenbrand (1997) and rotation periods from Herbst et al. (2002). Typical fractional errors for the following parameters are; $T_{eff} \sim 3\%$, $L_{bol} \sim 81\%$, $M_\odot \sim 61\%$, and $R_\odot \sim 41\%$.

*These extinction values are the original estimates from L03. Our matches in this study for these stars did not yield enough information to make a judgement on the best fit extinction, and are excluded from the final analysis.

†Masses and radii were estimated using DM97(D'Antona & Mazzitelli, 1997) pre-main sequence evolutionary models (see §**??**), and the Stefan-Boltzmann law, respectively.

‡Sublimation radii were estimated using the stellar effective temperature and the sublimation temperature at which the dust in a protoplanetary disk is expected to be destroyed (see §2.3.1).

3.2.3 SED Models

As in LB2011, we make use of a pre-computed grid of 200,000 models, generated by Robitaille et al. (2006, henceforth R06) for comparison with the obtained photometry for our sample. This grid builds upon previous work done by Whitney et al. (2003a,b, henceforth W03a, W03b); and a proof-of-concept of comparing photometry to synthetic models to correctly identify the evolutionary stage and physical parameters was conducted by Robitaille et al. (2007)[2].

[2]Note that an overview of these studies was presented in LB2011 and will not be covered in this paper; please refer to the aforementioned studies and references therein for details.

Similar to LB2011, we used the R06 model grid to identify those models which reproduce each of the ONC member's observed SED. We limit each star's acceptable fits, however, to those models with distances 414±100 pc, to encompass an acceptable range within the adopted distance to the ONC (e.g., Da Rio et al., 2009). The initial matches were further screened on the basis of goodness of fit with the observed SED, agreement with the T_{eff} value reported in the literature for each star, and the implied A_V and disk mass:

- **T_{eff} filter** — Similar to LB2011, we retain only those models with T_{eff} within ±500 K of the value reported in the literature from previous spectroscopy-based determinations.

- **χ^2 filter** — Alternately from LB2011, a different χ^2 metric is applied to ensure goodness-of-fit, such that the models selected possessed $\chi^2 \leq \chi^2_{best} + 3 \times N$, where N is the total number of photometry available for each member in the ONC. The previous screening for the goodness-of-fit results in a more restricted set of fits from the R06 fitter, and hence impeded the proper analysis needed for this study. This new χ^2 metric was chosen due to the increase in available photometry for the ONC (18, ∼2× greater) compared to IC 348 (10), and allows for a better representation of the best fits for a given number of photometric measurements for each star.

- **A_V filter** — Previous work (Hillenbrand, 1997, Fig.10) found that A_V for ONC members, in particular, the M- type stars in question here, to be modest, (∼6

mag). Therefore, our SED fitting results with $A_V \geq 10$ were eliminated to remove models with excessive combined interstellar and stellar extinction. In most cases, models with artificially large A_V were already eliminated by the T_{eff} filter above.

- **M_{disk} filter** — Models lacking sufficiently massive disks ($M_{disk} \leq 10^{-4} M_{\odot}$) are also removed. Such low-mass disks are rarely seen in sub-mm surveys (Andrews & Williams, 2005), and are unlikely to be capable of sustaining significant star-disk interaction.

Of the 106 stars initially in our sample, 24 could not be matched to models in the R06 grid which satisfy all of the above criteria (refer to Table III.2 for the complete list of discarded models). As before, in most cases this was because the best-fit SED models required very low disk masses ($M_{disk} < 10^{-4} M_{\odot}$). We again exclude these stars from our subsequent analysis. The results of the model vs. observed SED comparisons for the remaining 82 stars are discussed in §3.3, with summaries of the SED fitting results for two representative stars shown in Figs. 3.2–3.3. The entire atlas of SED fittings for the ONC sample can be accessed in Appendix B at the end of this document.

Table III.2. Discarded ONC Sample

Star ID	Stellar Parameters from the literature						Disk Radii		
	P_{rot} (d)	T_{eff} (K)	L_{bol} ($L_\odot$)	M † ($M_\odot$)	R † ($R_\odot$)	A_V (mag)	R_{sub} ‡ (AU)	R_{co} (AU)	R_{trunc} (AU)
37	8.27	4731	0.68	0.98	1.33	1.51	0.06	0.08	0.01
73	2.23	3706	0.53	0.37	2.73	0.00	0.07	0.02	0.01
83	7.72	3556	0.40	0.31	2.46	2.28	0.06	0.05	0.01
192	9.04	3556	0.33	0.33	2.02	0.18	0.05	0.06	0.01
194	13.87	2844	0.18	0.11	2.74	0.00	0.04	0.05	0.01
200	3.11	3483	0.53	0.26	3.50	3.67	0.08	0.03	0.02
239	4.45	3630	0.73	0.30	4.09	0.47	0.11	0.04	0.02
263	7.75	3198	0.26	0.17	2.39	0.04	0.05	0.04	0.01
294	2.57	3198	0.24	0.17	2.28	0.96	0.05	0.02	0.01
295	2.85	3775	1.71	0.34	8.21	0.00	0.23	0.03	0.04
299	2.76	3169	0.09	0.18	0.87	0.00	0.02	0.02	0.00
381	16.20	3775	0.47	0.42	2.26	0.60	0.06	0.09	0.01
391	16.33	3706	0.65	0.34	3.36	0.00	0.09	0.09	0.02
401	17.91	5272	6.19	1.91	7.83	4.42	0.45	0.17	0.04
413	10.08	4275	4.07	0.49	11.90	0.00	0.44	0.07	0.06
447	2.60	3273	0.26	0.19	2.24	0.00	0.05	0.02	0.01
636	5.59	3819	0.64	0.39	2.95	1.60	0.09	0.05	0.01
676	6.63	4395	0.13	0.68	0.34	0.72	0.01	0.06	0.00

Table III.2 (cont'd)

Star ID	Stellar Parameters from the literature						Disk Radii		
	P_{rot} (d)	T_{eff} (K)	L_{bol} ($L_\odot$)	M † ($M_\odot$)	R † ($R_\odot$)	A_V (mag)	R_{sub} ‡ (AU)	R_{co} (AU)	R_{trunc} (AU)
716	3.95	3198	0.50	0.16	4.67	0.00	0.09	0.03	0.02
786	8.81	3775	0.33	0.48	1.61	1.31	0.05	0.07	0.01
836	12.20	3845	0.62	0.42	2.74	1.04	0.08	0.08	0.01
913	9.56	4731	0.02	99.99	0.05	1.28	0.00	0.41	0.00
3110	0.84	4207	0.59	0.69	1.85	2.12	0.07	0.02	0.01
3115	0.85	3411	0.13	0.28	0.96	2.90	0.02	0.01	0.00

Note. — Derived stellar properties of the discarded sample. Refer to Table III.1 for notes.

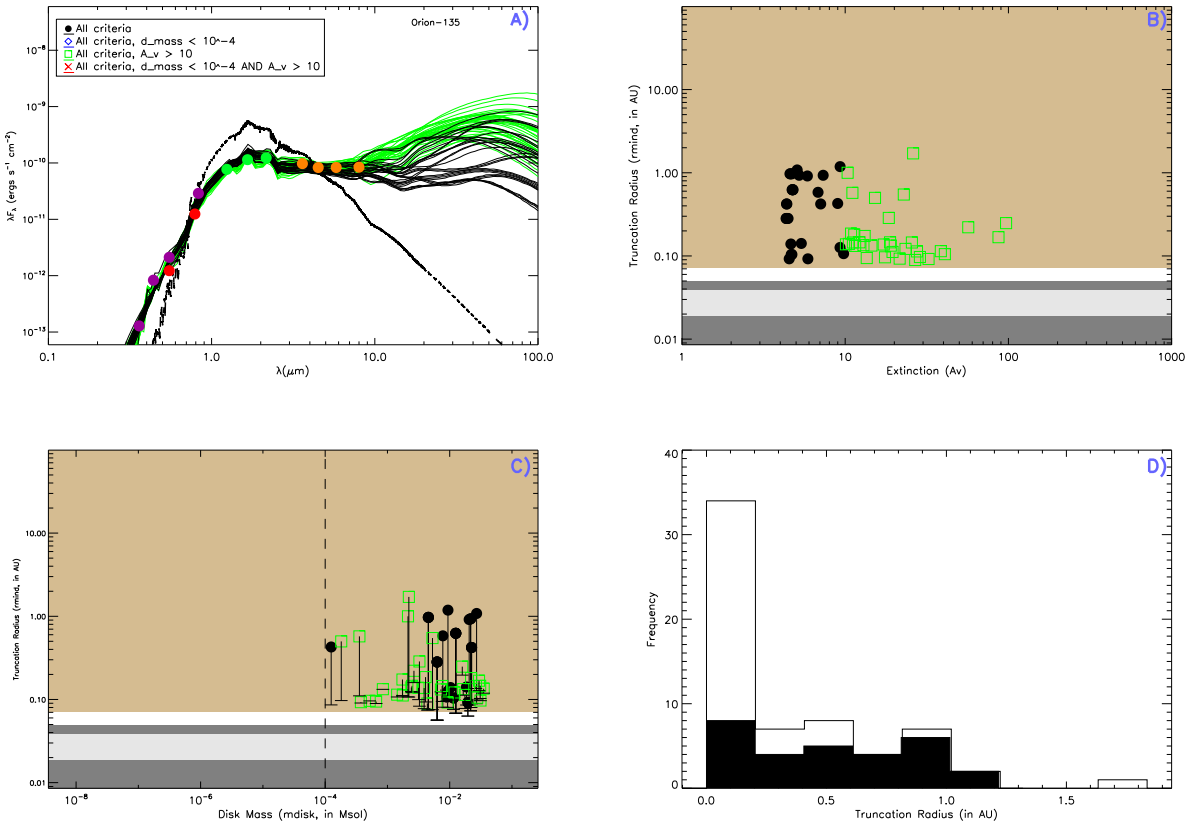

Figure 3.2: SED fitting results for ONC #135, an example of a star whose model fit predicts $R_{trunc} \gg R_{co}$, and $R_{trunc} \gg R_{sub}$. **Panel A)** Photometric SED (detections shown as yellow filled circles; upper limits as yellow arrows) compared to an artificially reddened Phoenix stellar atmosphere with the same T_{eff} (dashed line) and SED fits from the R06 model grid: black lines show R06 model SEDs meeting all criteria outlined in § 3.2.3, with colored lines showing models that fail one of those criteria (see legend in panel). **Panels B and C)** Location of model fits in R_{trunc} vs. M_{disk} or A_V parameter space. Black points indicate models meeting all criteria in §3.2.3. Models failing the limits on M_{disk} & A_v are shown as blue diamonds and green squares, respectively, with models failing both criteria shown as red crosses. Lower "error" bars indicate the distance between R_{trunc} and R_{sub} (at each model's T_{eff}). Vertical dashed lines in panels B & C show the M_{disk} limit and the A_V value reported for this star in the literature, respectively. The domain where $R > R_{sub}$ is indicated with a mocha background; light grey bars show the range of possible R_{co}s assuming a 50% uncertainty in M_*, with dark grey bands indicating the range of possible R_{co}s assuming a conservative 100% uncertainty in M_*. **Panel D)** Distribution of R_{trunc} values for all R06 models satisfying the basic χ^2 criteria (open histogram), and for models meeting all criteria (filled histogram).

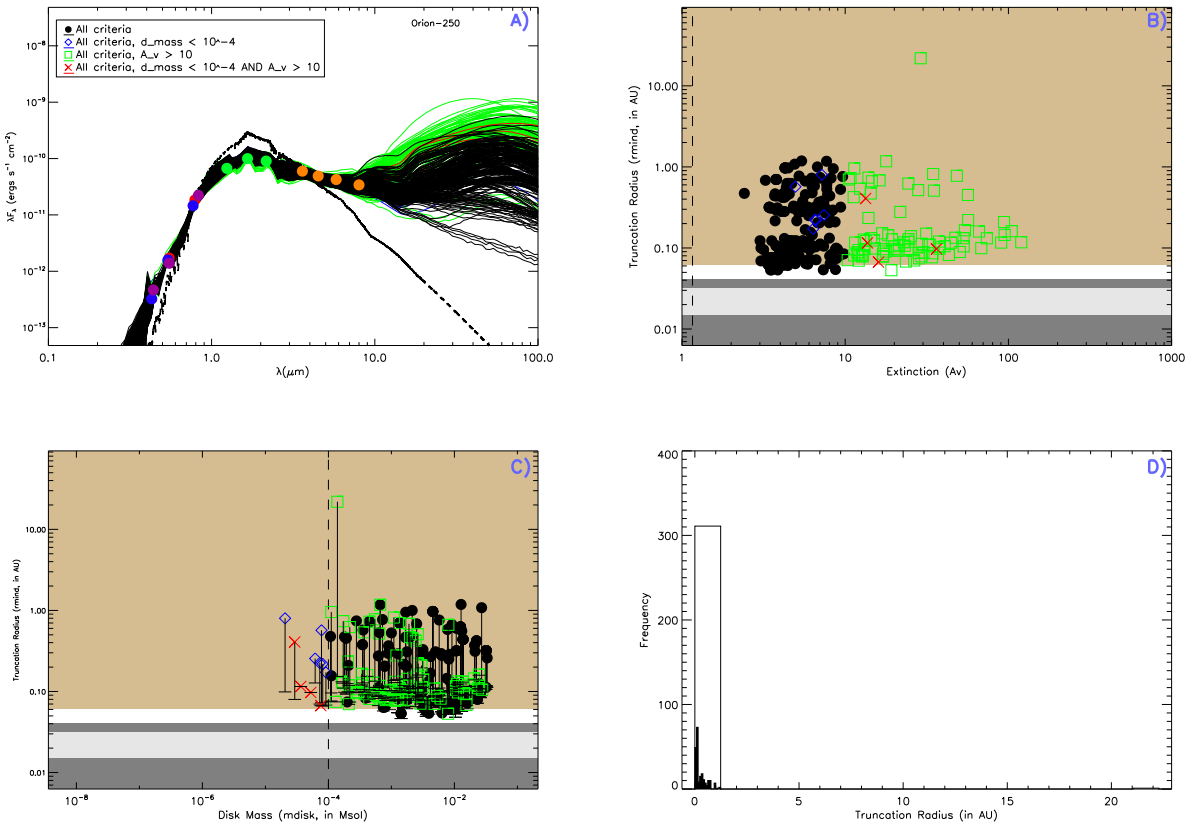

Figure 3.3: SED fitting results for ONC #250, an example star for which the model grid predicts $R_{trunc} = R_{sub}$. Refer to Figure 3.2 for further explanation of each of the above panels.

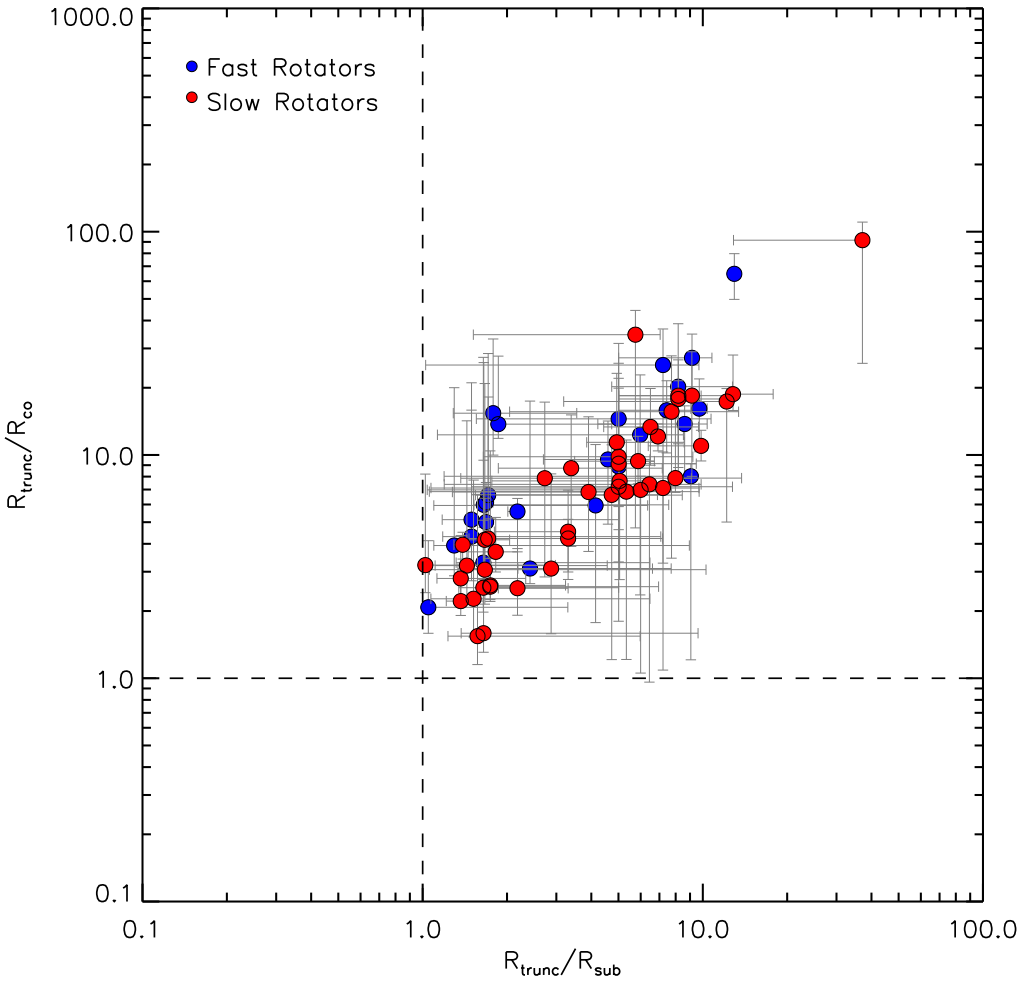

Figure 3.4: Truncation with Corotation and sublimation radii ratio plot for the ONC members. The plot shows the ratios of the corotation and sublimation radii (R_{trunc}/R_{co} & R_{trunc}/R_{sub}) in relation to the mean truncation radii for all acceptable models in the R06 grid for the entire sample. Errors in the truncation/sublimation radius ratio (x-axis) are represented as interquartile range errors, with 25% on the left and 75% on the right of each data point. Truncation/corotation radius ratio errors are represented as 1 σ.

3.3 Results

3.3.1 Inferred Disk Truncation, Co-rotation, and Dust Sublimation Radii

We use similar procedures to infer R_{trunc}, as well as calculate the ratios of a star's R_{trunc} to its co-rotation and sublimation radii (R_{co} and R_{sub}, respectively, refer to LB2011, §3). As before, R_{trunc}/R_{co} is still the principal quantity that we seek to test; $R_{trunc}/R_{co} \approx 1$ is predicted by most disk-locking theories (as outlined in LB2011, §1, and references therein). The other ratio, R_{trunc}/R_{sub}, is also of interest as well, as it indicates how close the inferred R_{trunc} is to the true inner edge of the disk. All the analyses conducted on R_{trunc}, R_{co}, and R_{sub} and their ratios in our previous work are represented in this work as well; this includes our assumptions of the mechanics behind the disk-clearing process for cases where $R_{trunc} = R_{sub}$ and $R_{trunc} > R_{sub}$.

Figure 3.4 shows the R_{trunc}/R_{co} and R_{trunc}/R_{sub} ratios for our usable sample listed in Table III.1. For the usable ONC sample, we identify two populations of stars; one group at R_{trunc}/R_{sub} vs. $R_{trunc}/R_{co} \sim$ [1.5, 3] ($\sim$ 59% of the final sample), and another group $\sim$ [6, 15] ($\sim$ 41% of the usable sample).

As in LB2011, we consider R_{co} to be the region of "action" in the magnetic star-disk interaction that we have defined (see also Shu et al., 1994; Mohanty & Shu, 2008; Matt et al., 2010). Both groups show a progression of the evolution of the circumstellar disk consistent with decreasing magnetic star-disk interaction, where both R_{trunc}/R_{co} and $R_{trunc}/R_{sub} > 1$, and thus the disk-locking mechanic becomes less important as $R_{trunc}/R_{co} \gg 1$. This is as a consequence of the magnetic field weakening

with distance from the star (with increasing R_{co}), coupled with the evacuation of gas capable of supporting the aforementioned interaction (with increasing T_{eff}, and thus increasing R_{sub}). The first group of stars (those centered around [6, 15]) can be considered as "effectively diskless" stars: physically large R_{trunc} beyond R_{co} indicates that the evolved circumstellar disk has material beyond the star's magnetic influence, and hence the star's rotation period is not governed by the disk locking paradigm postulated previously. In contrast, the latter group of stars (centered $\sim$[1.5, 3]) are considered to be "potentially disk-locked": these represent stars that have substantial circumstellar material very near the potential star-disk magnetic interaction. The precise location of R_{co} requires including possible dust sublimation effects (tied to T_{eff}); as such, this effect will be to imply a true R_{trunc} that is even closer to the star than inferred, for which we might expect a more active star-disk magnetic interaction dynamic. We discuss the implications of these two groups in more detail in the following section.

3.3.2 Comparison of Potentially Disk-Locked and Effectively Diskless Stars

The location of the ONC members within the HR diagram are shown on Fig 3.5, with DM97 calculated tracks and isochrones overlaid for comparison. The ONC members analyzed here possess HR diagram locations consistent with 0.1 - 3 Myr isochrones, and with implied masses ranging from 0.12 - 1.5 $M_{\odot}$, consistent with the range found in previous studies. There seems to be a difference between the

potentially disk-locked stars and the effectively diskless in terms of their masses: the effectively diskless stars tend to occupy the lower mass regime in the HR diagram (0.12 - 0.5 $M_{\odot}$, centered at $0.3M_{\odot}$), while the potentially disk-locked stars are spread throughout the aforementioned mass range. Unlike the masses, however, there is no clear difference between the ages of the ONC member analyzed (supported by 1D (ages and masses) and 2D (both) two-sided K-S tests, at 98% and 14% confidence levels respectively (1D) and 31 %(2D)). We also applied a two-sided K-S test on the rotation period distributions for the potentially disk-locked and effectively diskless populations (see Fig. 3.6). The K-S test returns a probability of 0.59, and just as in IC 348 (LB2011), we cannot reject the null hypothesis that the two distributions are drawn from the same parent distribution.

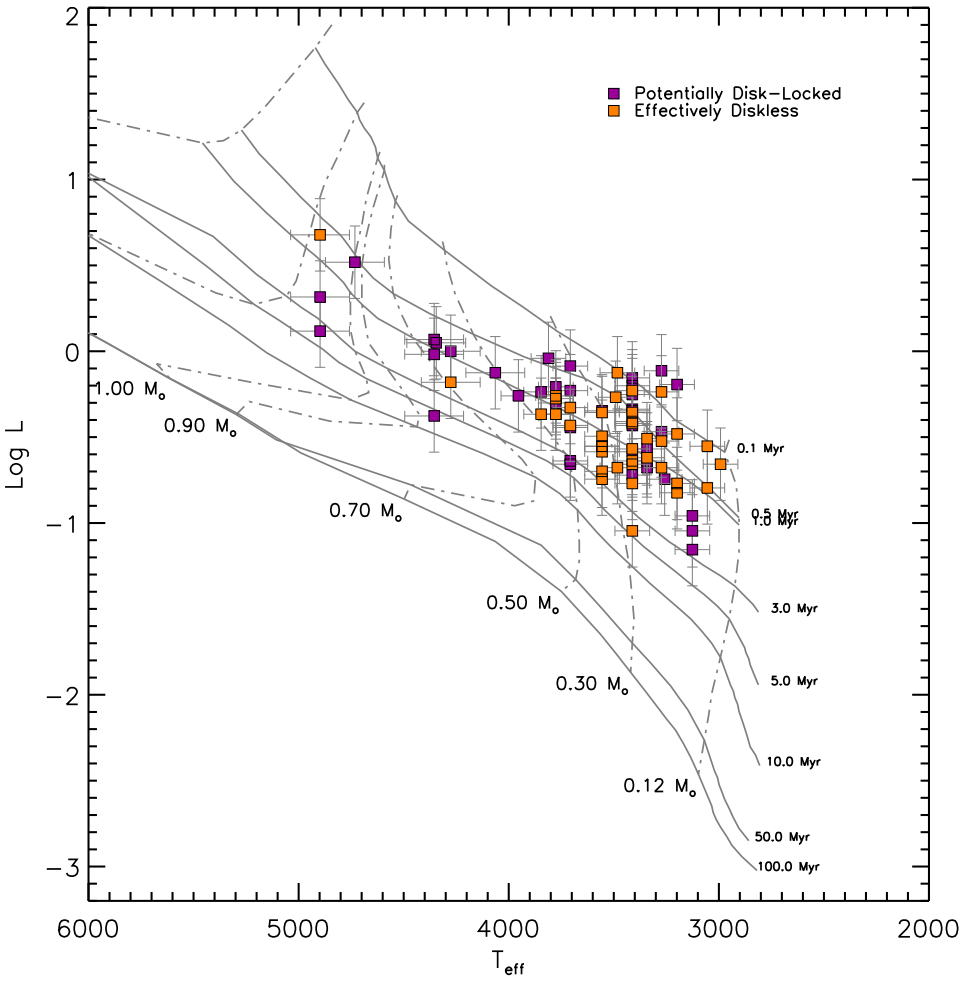

Figure 3.5: HR diagram with over plotted tracks and isochrones using DM97. All errors represented in both log L and T_{eff} are 1σ.

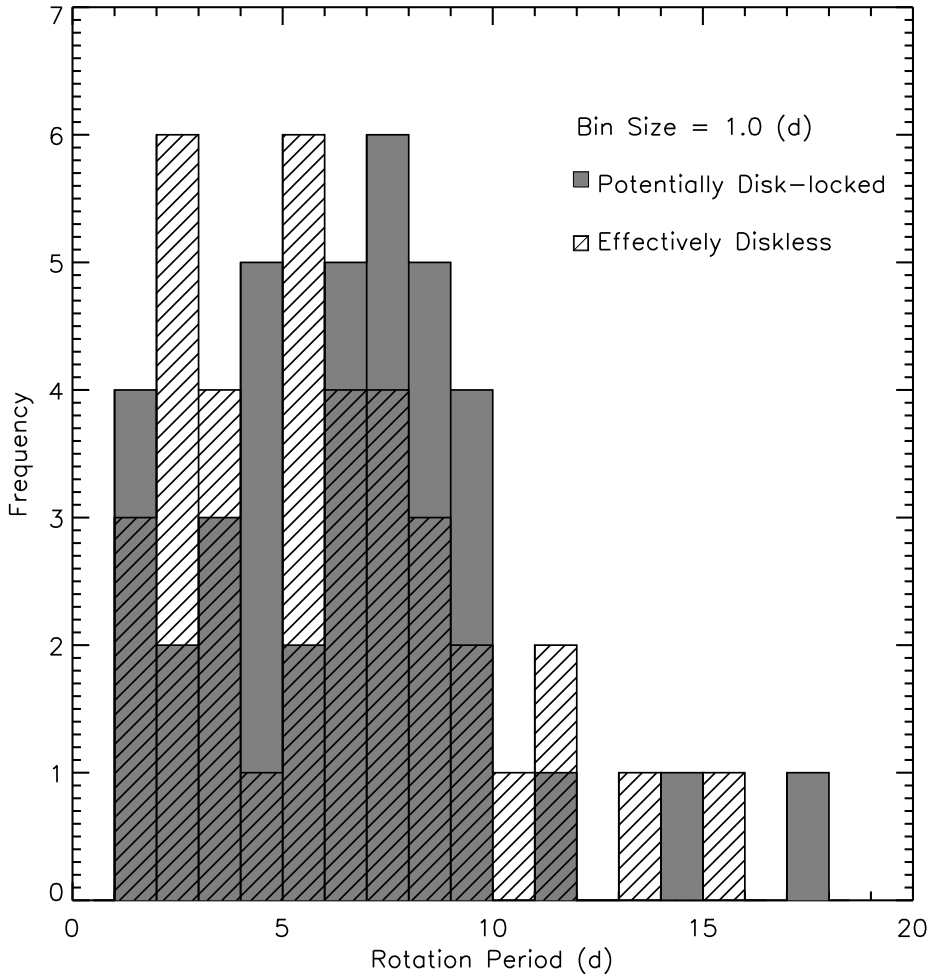

Figure 3.6: Rotation period histogram of potentially disk-locked (gray) and effectively diskless stars (empty hatched). Though the potentially disk-locked stars are greater in number than the effectively diskless stars, this histogram supports the null hypothesis that both distributions are from the same parent distribution.

Chapter IV

DISCUSSION AND SUMMARY

In this chapter we discuss and summarize the implications of the findings presented in the previous chapters. Our analysis has been completed and published for the IC 348 sample, whereas the Orion analysis is preliminary. Therefore, the following discussion will be principally focused based on the IC 348 sample results.

Our SED modeling provides the first detailed investigation of how the structure of circumstellar disks around IC 348 members does or does not influence the star's rotation rate. Specifically, these measurements provide leverage to address the two questions motivating this study: 1) how do the inner truncation radii and co-rotation radii compare for a well populated ensemble of circumstellar disks, and 2) do fast rotators possess circumstellar disks with inner radii larger than co-rotation, as expected if the disks around fast rotators have evolved to the point that star-disk interactions no longer govern their host star's rotation rate? We address each of these questions in turn.

4.1 Are circumstellar disks truncated at co-rotation?

Traditionally, the condition $R_{\rm trunc} \approx R_{\rm co}$ has been assumed as a fundamental requirement for a star to be in a fully disk-locked state, where a quasi-steady-state

configuration of the star-disk interaction exerts a braking torque on the star that counter-balances the star's tendency to spin up as it contracts, and thus maintains a roughly constant stellar rotation period for the lifetime of the disk. For example, in the context of the bimodal distribution of rotation periods reported by Herbst and collaborators in the ONC (e.g. Herbst et al., 2002), the slow rotators have been interpreted as those in an actively "disk-locked" state while the rapid rotators have been interpreted as "disk-released," presumably due to the loss of their disks. These interpretations have generally been made on the basis of near- and mid-IR colors as functions of stellar rotation period, not on an assessment of the $R_{\rm trunc}/R_{\rm co}$ condition on a star by star basis.

Our detailed SED analysis reveals that the majority (70%) of the stars in our sample have clear evidence for $R_{\rm trunc} \approx R_{\rm co}$ (Fig. 2.5). As these potentially disk-locked stars constitute the majority of our sample, it does appear that most stars in IC 348 are consistent with the zeroth order prediction of theoretical models of angular momentum transfer via star-disk interactions.

However, assessing whether the potentially disk-locked stars are experiencing a *braking* torque from any presumed star-disk interaction is made more subtle by the complicating effects of dust sublimation on the determination of the disk's true R_{trunc}. As shown in Fig. 2.5, while both the slow and rapid rotators in the potentially disk-locked group are similarly distributed along the vertical axis (i.e., both the slow and rapid rotators have disks consistent with $R_{\rm trunc} = R_{\rm co}$, within error), their distribu-

tions along the horizontal axis are detectably different. The rapid rotators are very strongly clustered at precisely $R_{\rm trunc}/R_{\rm sub} = 1$ (scatter in $R_{\rm trunc}/R_{\rm sub}$ of less than 1%), which is the hard minimum that any of our SED models can attain because (by definition) dust is destroyed by sublimation interior to this radius. In contrast, the slow rotators show a larger spread of $\sim$15% in $R_{\rm trunc}/R_{\rm sub}$. Moreover, most of the slow rotators' disks are mildly inconsistent with $R_{\rm trunc} = R_{\rm sub}$, requiring $R_{\rm trunc} > R_{\rm sub}$ with greater than 1σ confidence. Taken as a group, the rapid rotators show a high likelihood of possessing a mean $R_{\rm trunc}/R_{\rm sub} = 1$, while the likelihood that the slow rotators possess a mean $R_{\rm trunc}/R_{\rm sub} = 1$ is less than 0.1%.

We interpret the uniform pile-up of fast rotators at $R_{\rm trunc}/R_{\rm sub} = 1$ to mean that our SED modeling is not sensitive to the true inner edge of the fast rotators' disks, which likely extend inward of R_{sub} and perhaps significantly inward of R_{co} as well (though we cannot verify the latter). In contrast, the $R_{\rm trunc}/R_{\rm sub}$ ratios that we observe for the slow rotators are significantly larger than 1. Therefore we regard the $R_{\rm trunc}$ for the slow rotators in general to correspond to true R_{trunc} measurements, and thus we can conclude with greater confidence that these stars truly have disks consistent with $R_{trunc}/R_{co} = 1$.

If the potentially disk-locked stars in our sample are in fact experiencing angular momentum interactions with their disks, the above findings could imply that the slow rotators are slow precisely because they satisfy the $R_{trunc}/R_{co} = 1$ condition, while the fast rotators are fast because they tend to possess disks with $R_{trunc}/R_{co} < 1$. (To

be clear, our results do not demonstrate that $R_{trunc}/R_{co} < 1$ for the rapid rotators in the potentially disk-locked group, but such an interpretation would be consistent with our findings above.) Recent theoretical work complicates such a straightforward interpretation, however. Matt et al. (2010) have demonstrated that the condition $R_{\rm trunc}/R_{\rm co} \approx 1$ can in fact transpire for a very wide range of star/disk parameters and a wide range of star-disk torque configurations. Indeed, in those calculations, relatively small deviations from $R_{\rm trunc}/R_{\rm co} = 1$ can result in large differences in the magnitude and/or the sign of the torque experienced by the star. For example, in the case of strong magnetic coupling to the disk (e.g., $\beta = 0.01$), significant field twisting occurs for $R_{\rm trunc}$ deviations of less than 1% from $R_{\rm co}$. The $R_{\rm trunc}/R_{\rm co}$ that we have determined for potentially disk-locked stars are not sufficiently precise to make such distinctions.

Nonetheless, the findings of Matt et al. (2010) do still predict that disks with smaller R_{trunc}/R_{co} will in general result in more positive stellar torques. Thus, if the potentially disk-locked stars in our sample are in fact disk-locked, the implication is that the rapid rotators are likely experiencing systematically more positive torques. More generally, under the disk-locking hypothesis, our results are most consistent with an interpretation in which the stars are currently experiencing disk torques spanning a large range of magnitude, and perhaps in sign.

4.2 Do fast rotators possess (dust) disks with larger inner holes?

As commonly envisaged, magnetic star-disk interactions force the star to rotate at the Keplerian velocity of the close-in inner disk. Over time, however, the disk's inner hole grows[1] as the disk evolves and begins to dissipate; eventually star-disk interactions are too weak to couple the star to the anemic inner disk, and the star spins up as it completes its pre-main sequence contraction. This picture would predict that slowly rotating stars will be locked to disks with $R_{trunc} \approx R_{co}$, while rapidly rotating stars would be associated with disks with $R_{trunc} \gg R_{co}$ (Edwards et al., 1993; Edwards, 1994; Rebull et al., 2006; Cieza & Baliber, 2007). To test this picture, we can compare the P_{rot} distributions for the potentially disk-locked and effectively diskless stars in our sample.

Interestingly, we find slow and rapid rotators in roughly equal numbers among the potentially disk-locked stars. This suggests that the common interpretation, wherein fast rotators result from stellar spin-up following the cessation of disk-locking, may need to be modified to allow for the existence of rapidly rotating stars with close-in disks. Indeed, both slow and rapid rotators amongst the potentially disk-locked stars in our sample at least approximately satisfy the condition $R_{\rm trunc} \approx R_{\rm co}$. As discussed above, the rapid rotators in the potentially disk-locked group may in fact possess disks with $R_{trunc} < R_{co}$, however this only strengthens the conclusion that

[1]While other models of disk evolution that do not predict a widening inner-disk hole do exist (e.g., homologous depletion; (Currie et al., 2009; Currie & Sicilia-Aguilar, 2011), 'inside-out' disk evolution is the most commonly invoked (e.g. Barsony et al., 2005).

rapid rotators do not possess disks with systematically larger inner holes compared to the slow rotators.

The effectively diskless stars in our sample are very unlikely to be experiencing significant torques from their disks. Interestingly, however, the rotation period distribution of these stars is nonetheless very similar to that of the potentially disk-locked stars (see §2.3.2). Presuming that the effectively diskless stars formerly possessed robust inner disks like their present-day potentially disk-locked counterparts, this implies that their disk properties have evolved significantly while their rotational properties have remained unchanged. If the currently effectively diskless stars are furthermore presumed to have formerly been in a disk-locked state, then the timescale for transitioning from the disk-locked to the disk-released state must be shorter than the timescale on which the stars would spin up due to pre-main-sequence contraction. This conclusion is consistent with previous estimates of disk evolution timescales, which find timescales of ∼0.1-1 Myr for disk evolution processes (Currie & Sicilia-Aguilar, 2011; Muzerolle et al., 2010), compared to the ∼3 Myr spin-up timescale predicted by the DM97 PMS evolutionary models for $0.4 M_{\odot}$ stars (the average mass of our sample) at 1 Myr. This is also consistent with the statistics of our sample: 1/3 of our sample are "effectively diskless", implying a disk evolution timescale (assuming the nominal age of 1 Myr typically adopted for IC 348) of ∼1/3 × 1 Myr = ∼0.3 Myr, in agreement with aforementioned timescale estimates.

Our SED modeling provides a detailed investigation of how the structure of the

circumstellar disks in the ONC influences (or not) the stars rotation rate. In particular, we can address the two motivating questions in this continuing study: (1) do the truncation and co-rotation radii compare such that $R_{trunc} = R_{co}$ as predicted by disk-locking, and (2) does the fact that a no-longer interacting disk with magnetic influence from the star manifest in a rapidly rotating star as expected? Our results show that for the ONC sample, there are no models with the predicted $R_{trunc} \approx R_{co}$; this suggest that the current sample in this analysis contain stars for which disks are truncated outside of co-rotation. As in LB2006, we also have both slow and fast rotators in this aforementioned group; as such, our previous conclusions hold that for the disk-locking theory to work, it must work to speed up stars (where $R_{trunc} < R_{co}$), as well as to slow them down ($R_{trunc} \geq$R$_{co}$).

4.3 Summary and Conclusions

We have analyzed the circumstellar disks around a sample of 33 stars in IC 348 with known rotation periods, in order to assess in detail whether the inner edge of each star's circumstellar disk (R_{trunc}) is consistent with being at the co-rotation radius from the star (R_{co}), as predicted by disk-locking theory. We compare stellar photometry from the Spitzer Space Telescope to a grid of 200,000 pre-computed star+disk radiative transfer models, and compare the implied R_{trunc} of the best fitting SED models to each star's calculated R_{co}. The principal findings of this study are as follows:

- We find two populations of stars: a "potentially disk-locked group" with inner-disk radii located at $R_{\rm trunc}/R_{\rm co} \approx 1$ (68% of the sample), and an "effectively diskless" group whose inner-disk radii are significantly larger, with $R_{\rm trunc}/R_{\rm co} \gg 1$ and thus beyond the reach of disk-locking (32% of the sample).

- Both fast and slow rotators in the potentially disk-locked group possess dust disks with R_{trunc}/R_{co} values consistent with 1. This finding is contrary to previous suggestions that slowly-rotating stars will possess close-in disks that facilitate strong star-disk interactions, while fast rotators will possess more evolved disks with inner radii that are sufficiently large so that they are no longer amenable to significant star-disk interactions. The general agreement between the each star's R_{trunc} and R_{co} may be taken to suggest that star disk-interactions do indeed play a role in these stars' angular momentum evolution. However, under this hypothesis, the lack of a clear distinction between the R_{trunc} inferred for the disks around fast and slow rotators would imply that star-disk interactions influence the rotation rate of the fast rotators as well, not only the slow rotators whose periods disk locking is most commonly invoked to explain.

- Stars in both the potentially disk-locked and effectively diskless groups, whose disks we interpret as being in significantly different evolutionary states, possess statistically identical rotation period distributions. If the potentially disk-locked stars are presumed to currently be in a disk-locked state, and if the effectively diskless stars are presumed to previously have been in a similarly

disk-locked state, this suggests that disks evolve more quickly than the stellar spin-up timescale resulting from pre-main-sequence contraction.

In summary, while our findings may be interpreted within the context of a presumed disk-locking mechanism, invoking the disk-locking hypothesis is not necessitated by the stars in our IC 348 study sample. We do not find obvious differences in the disk truncation radii of slow rotators vs. rapid rotators. This holds true both at the level of whether close-in disk material is present at all, and in analyzing the precise location of the inner disk edge relative to the co-rotation radius amongst the subset of stars with close-in disk material. These results may therefore imply that the disk-locking phenomenon is not operative in these stars. Alternatively, if disk-locking does operate, then our findings imply that (a) its observational signature is more complex than the simple portrait of slowly rotating disk-locked stars and rapidly rotating non-disk-locked stars, and (b) the transition from the disk-locked state to the disk-released state must occur more rapidly than the stellar contraction timescale.

Appendix A

ATLAS OF IC 348 SED FITTINGS

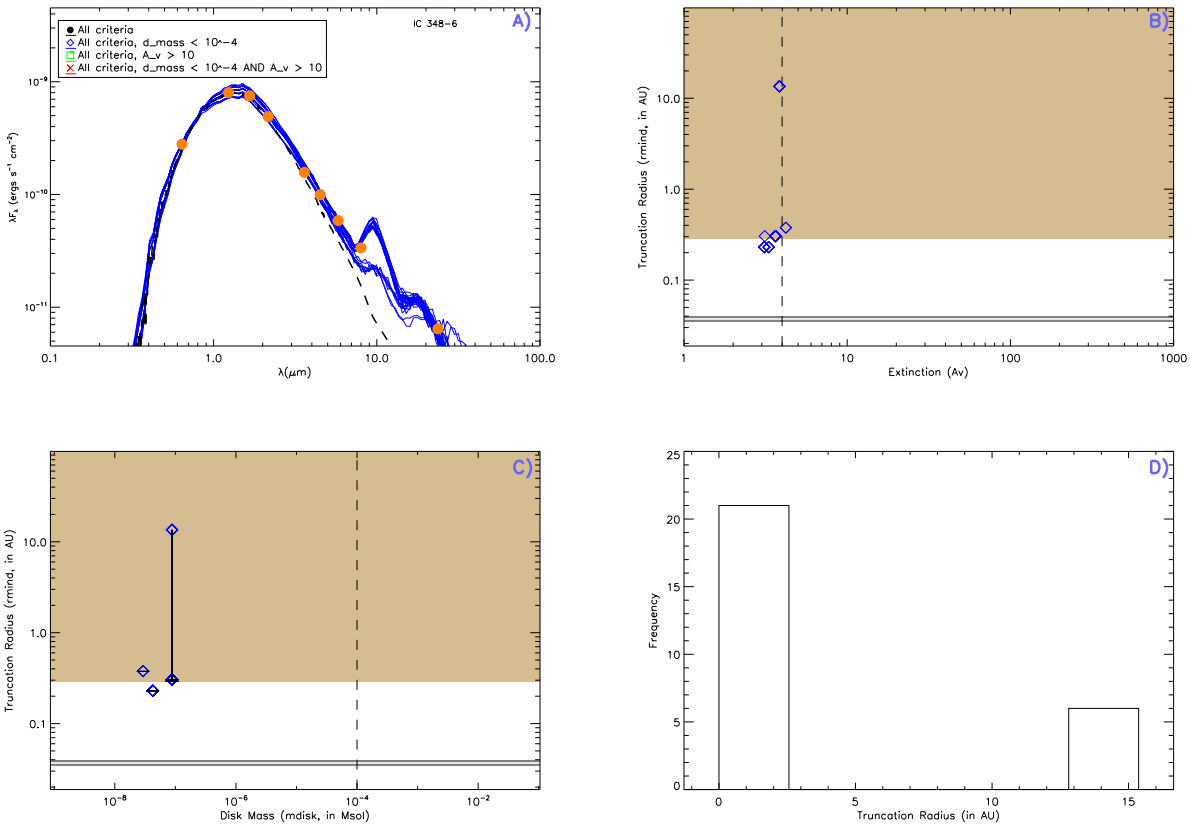

Figure A.1: SED fitting results for IC 348 #6

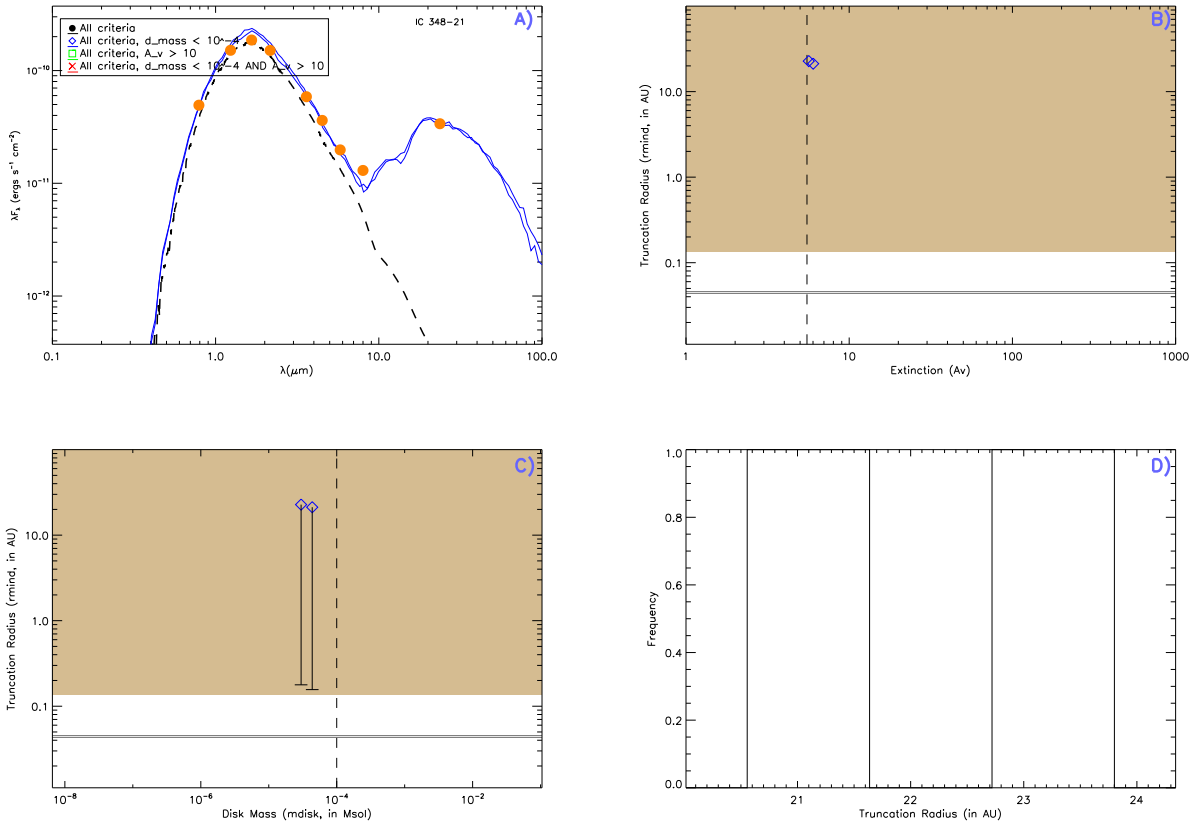

Figure A.2: SED fitting results for IC 348 #21

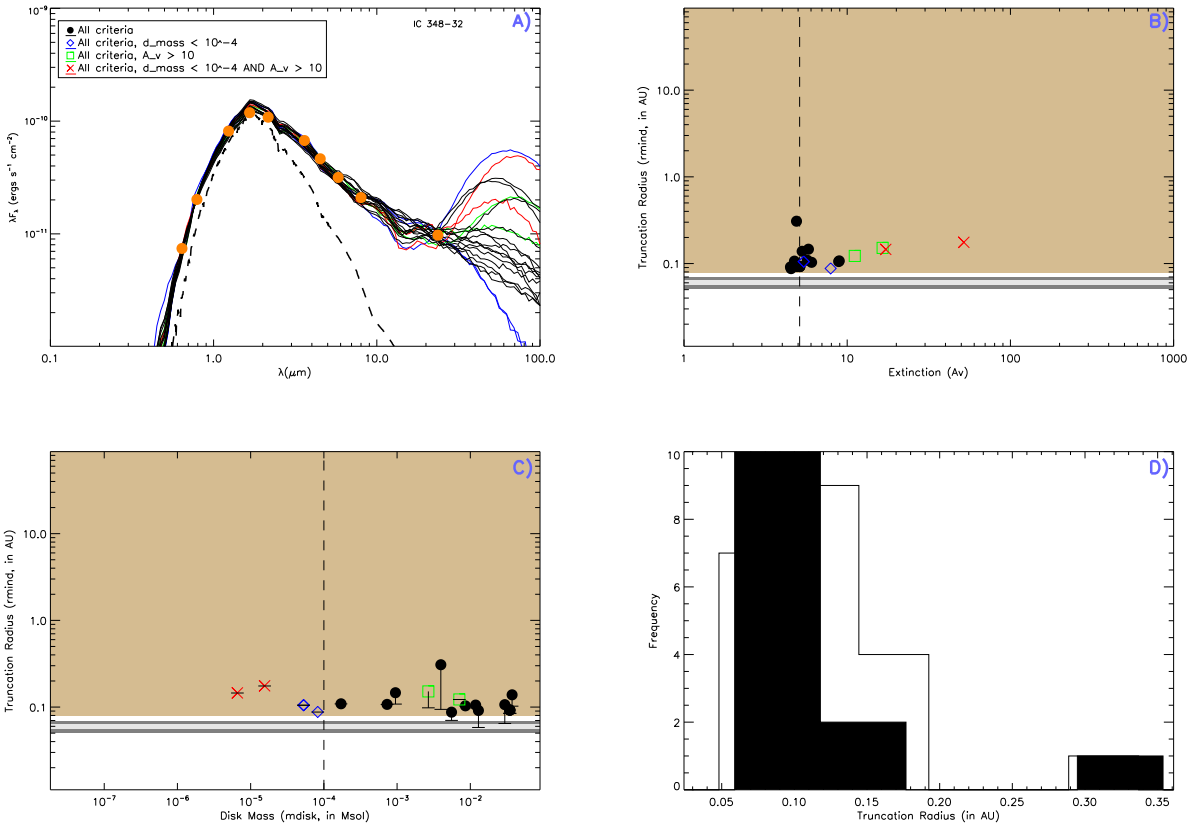

Figure A.3: SED fitting results for IC 348 #32

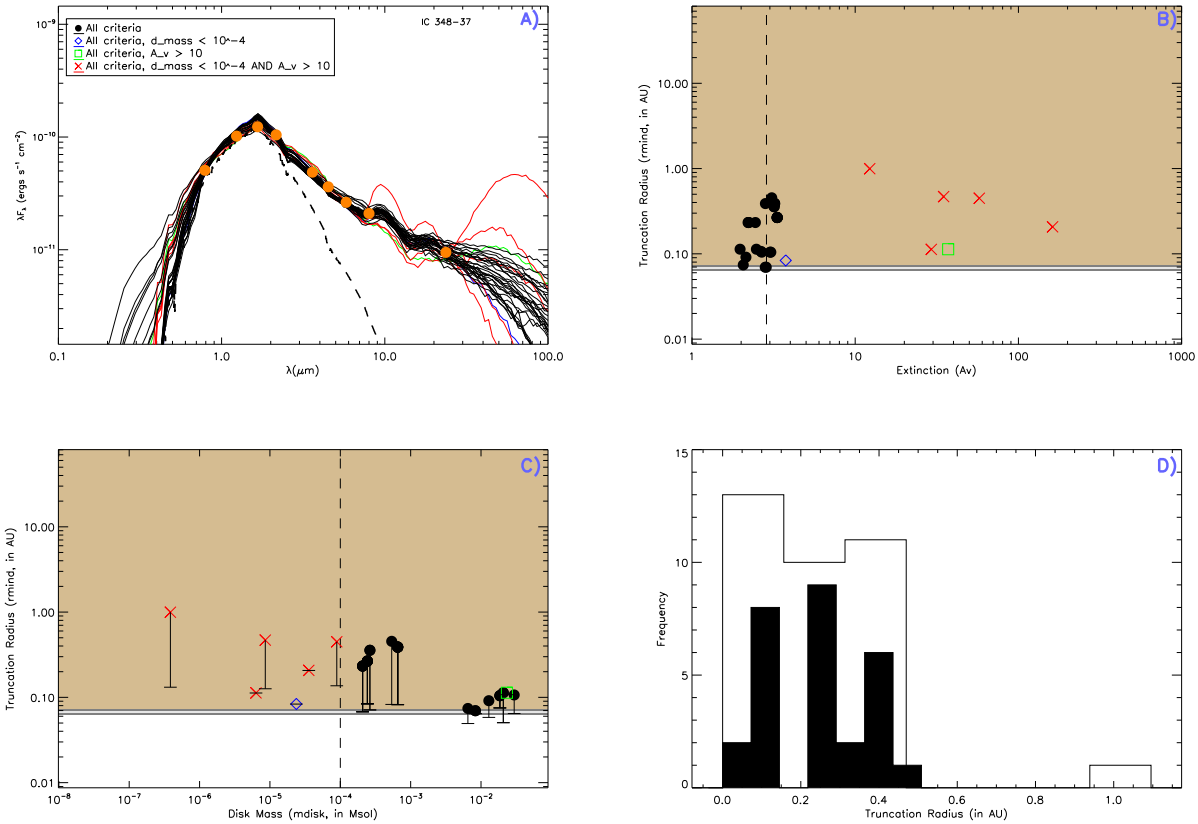

Figure A.4: SED fitting results for IC 348 #37

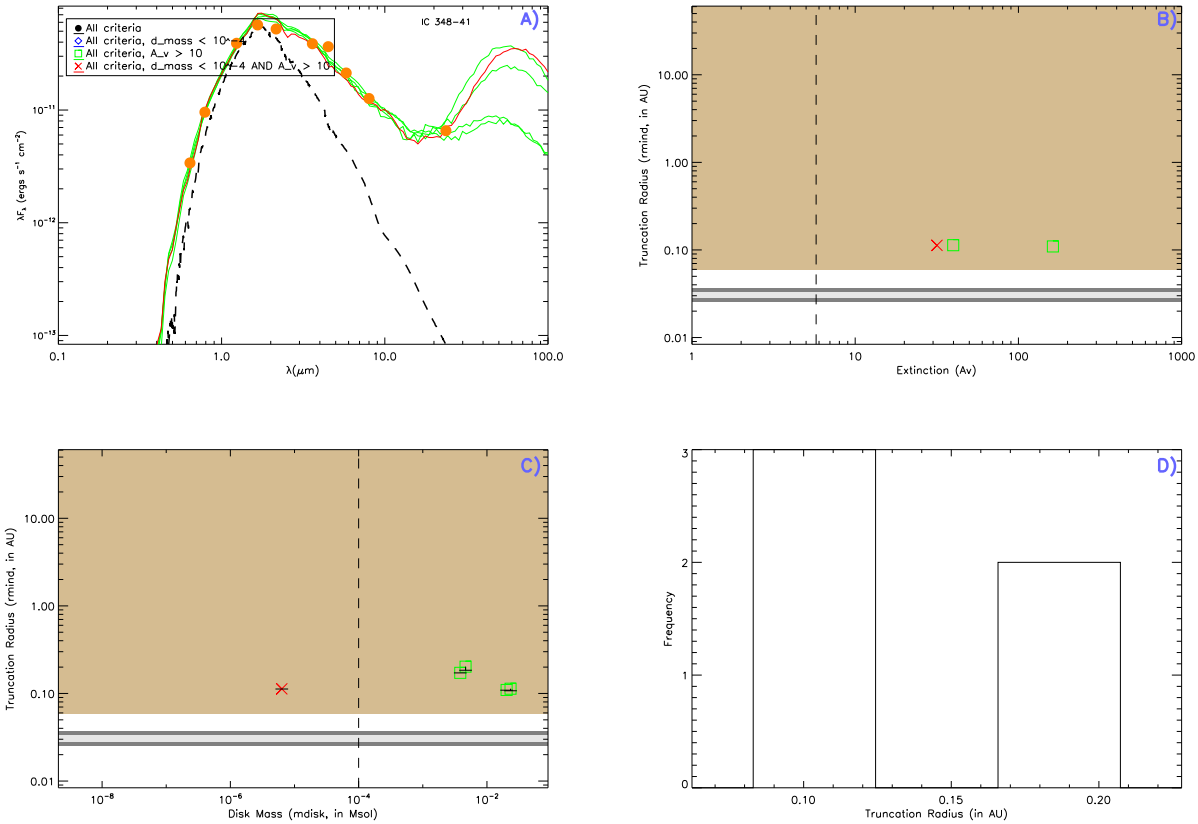

Figure A.5: SED fitting results for IC 348 #41

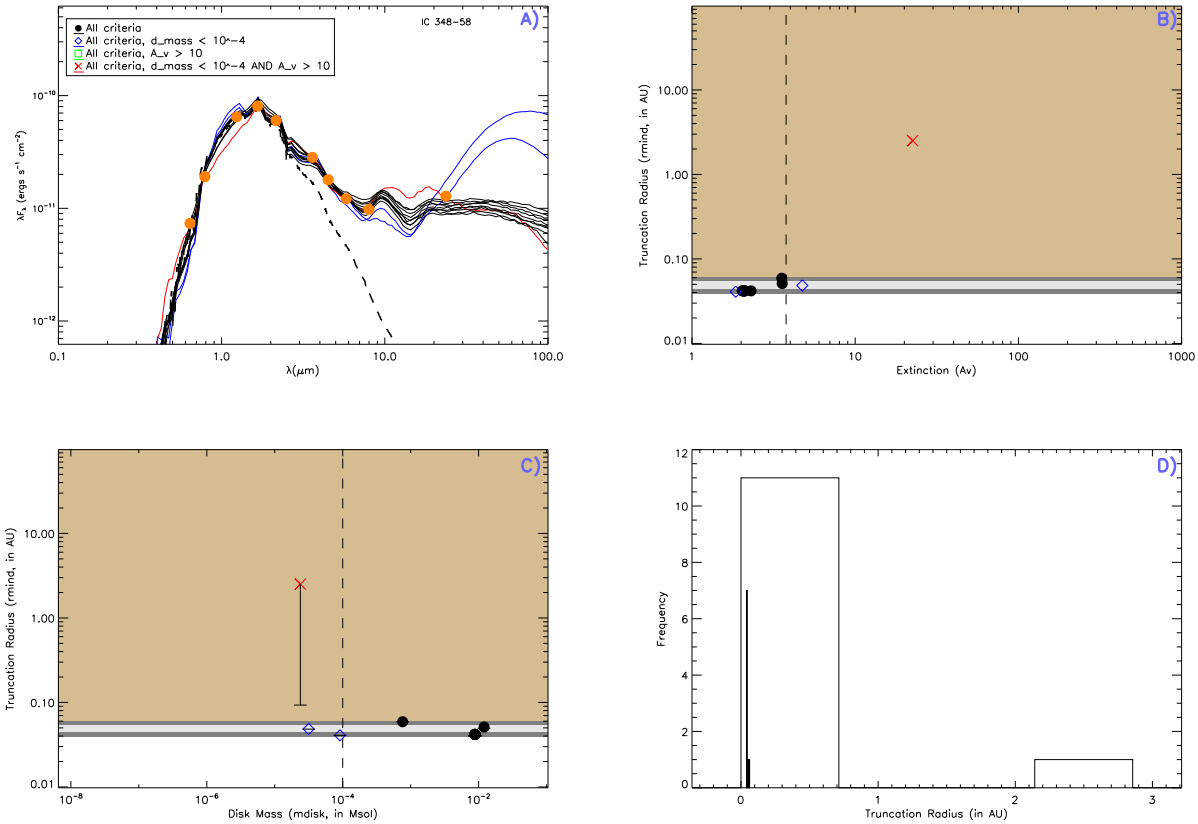

Figure A.6: SED fitting results for IC 348 #58

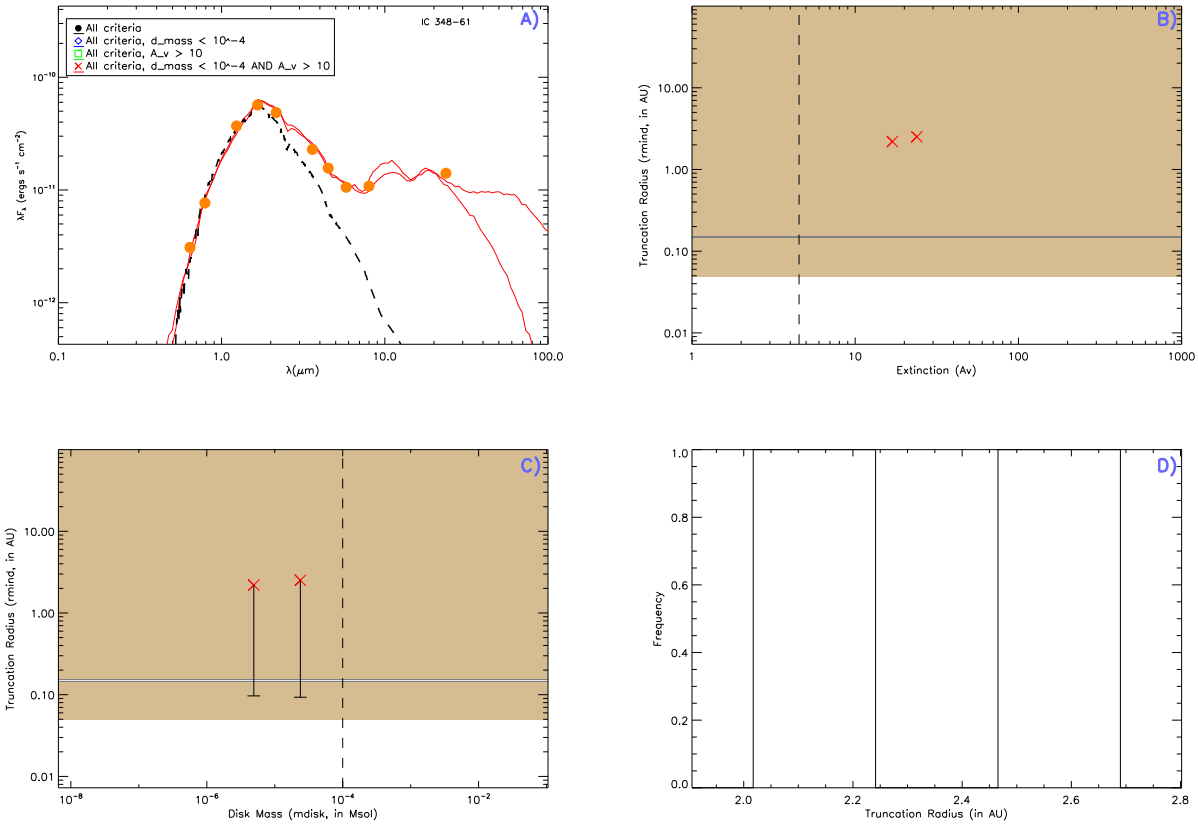

Figure A.7: SED fitting results for IC 348 #61

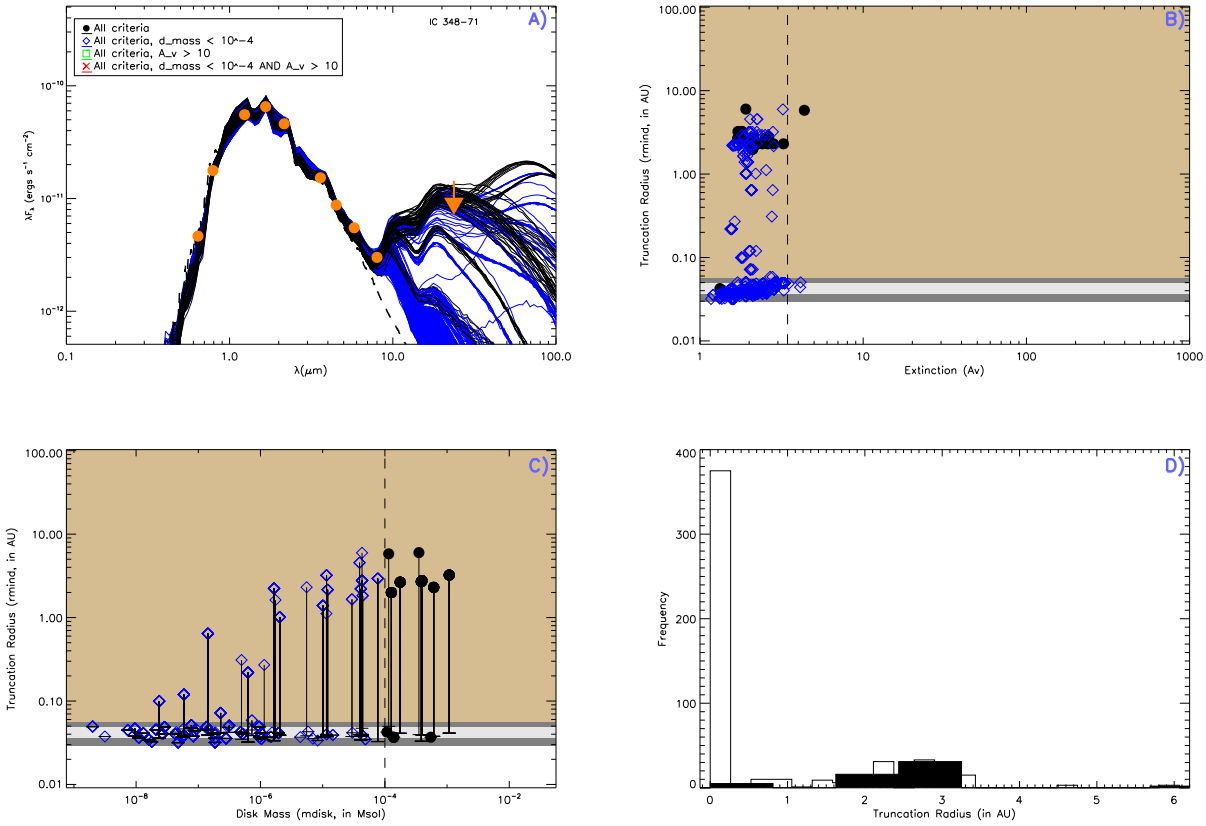

Figure A.8: SED fitting results for IC 348 #71

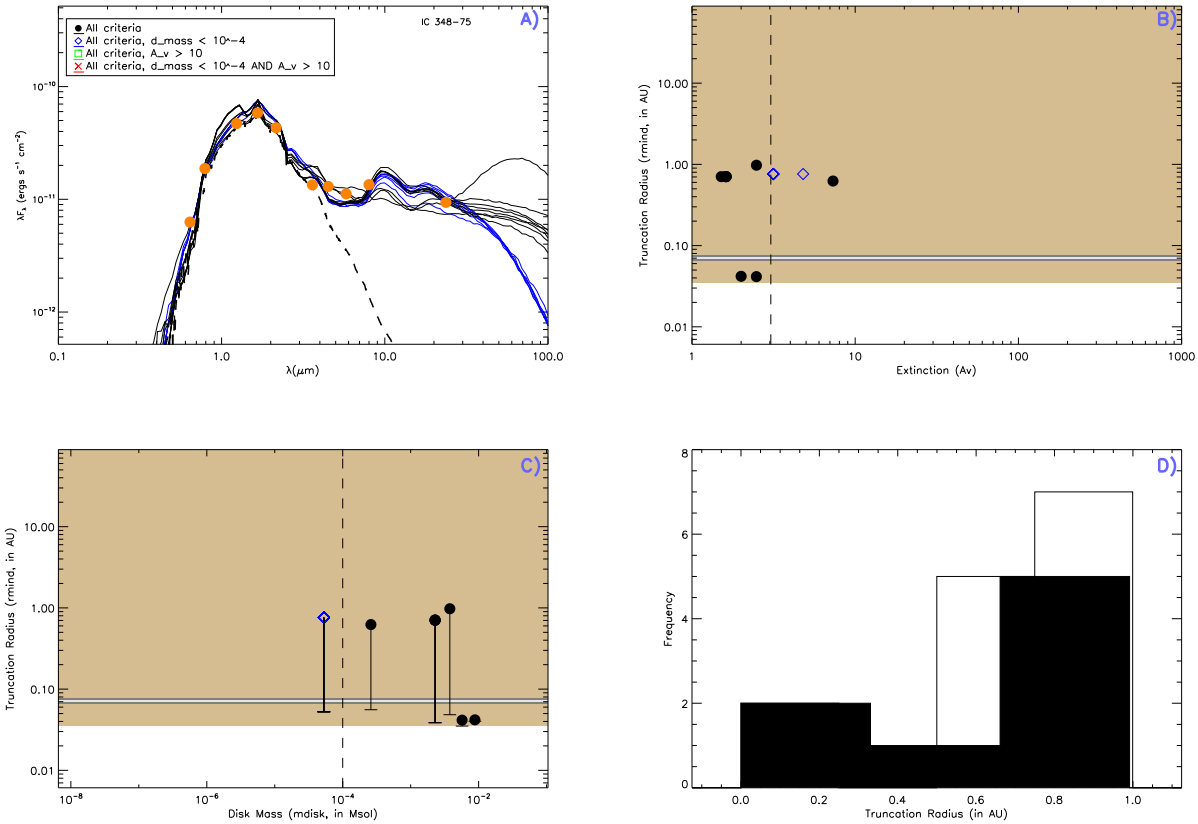

Figure A.9: SED fitting results for IC 348 #75

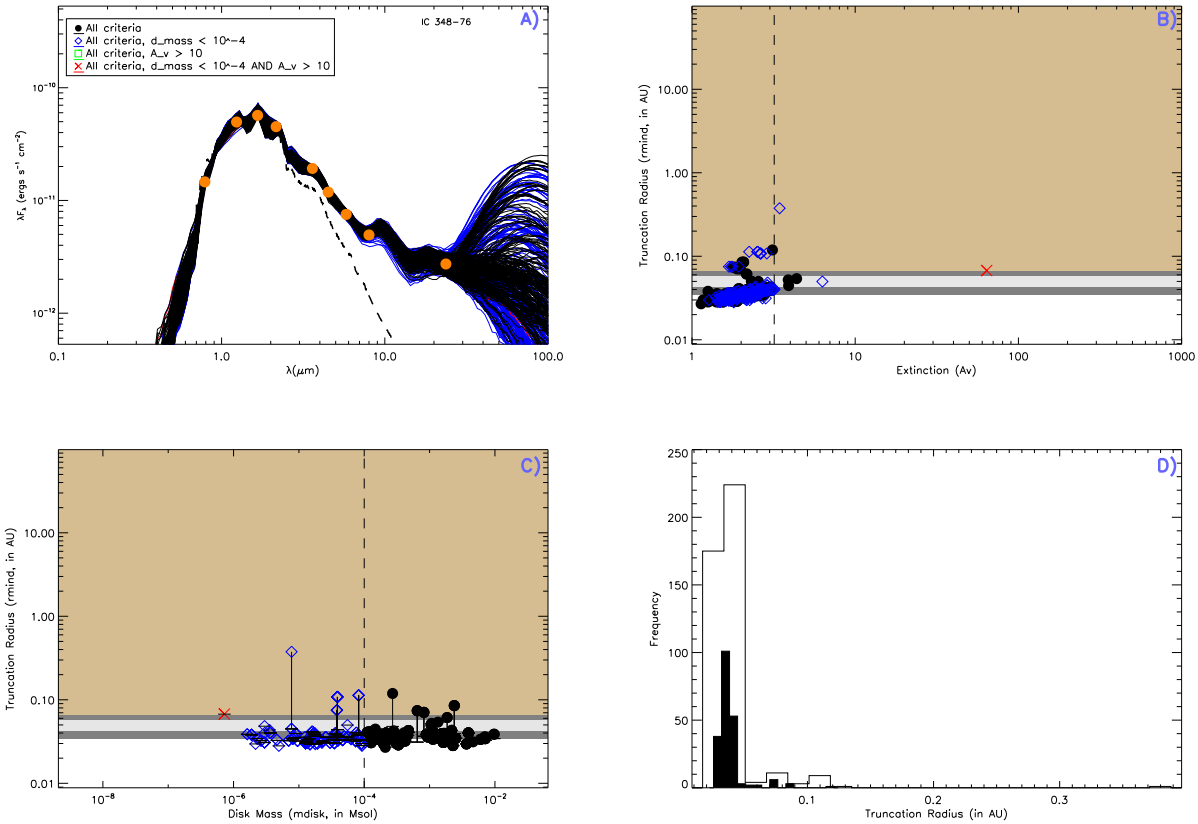

Figure A.10: SED fitting results for IC 348 #76

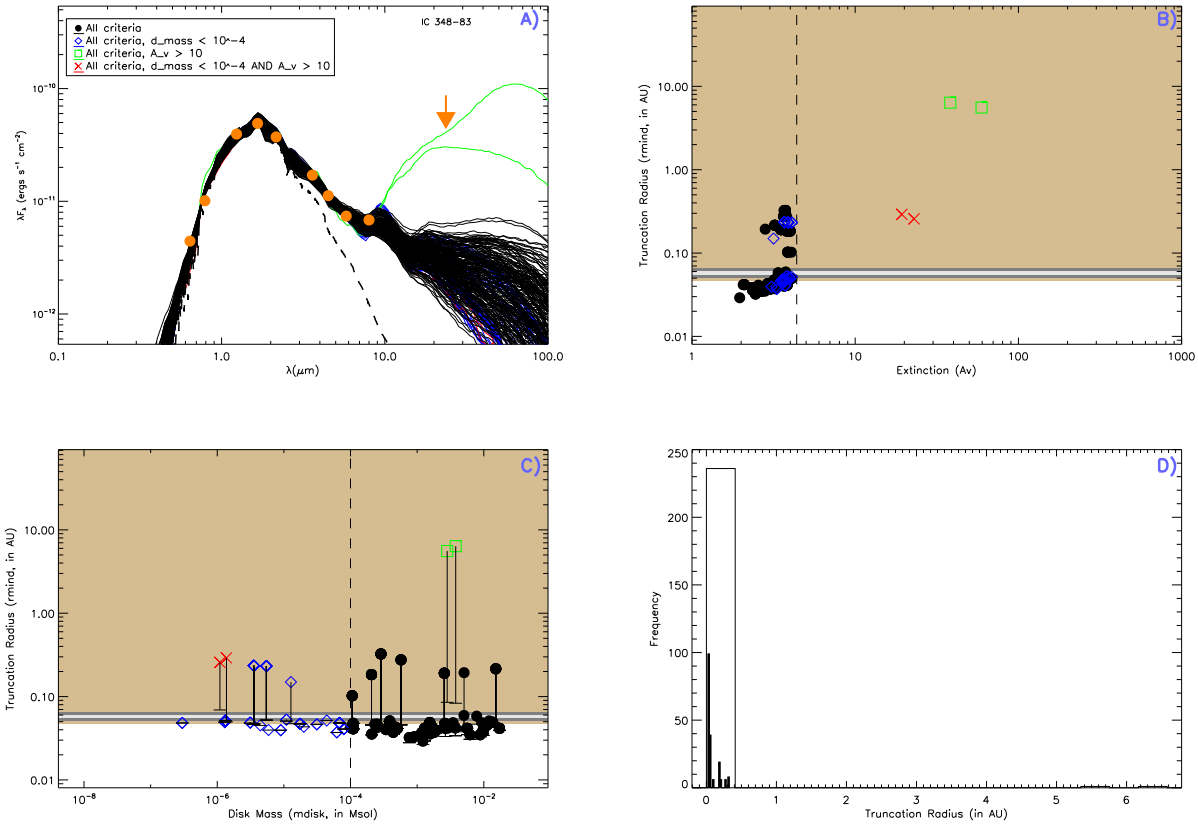

Figure A.11: SED fitting results for IC 348 #83

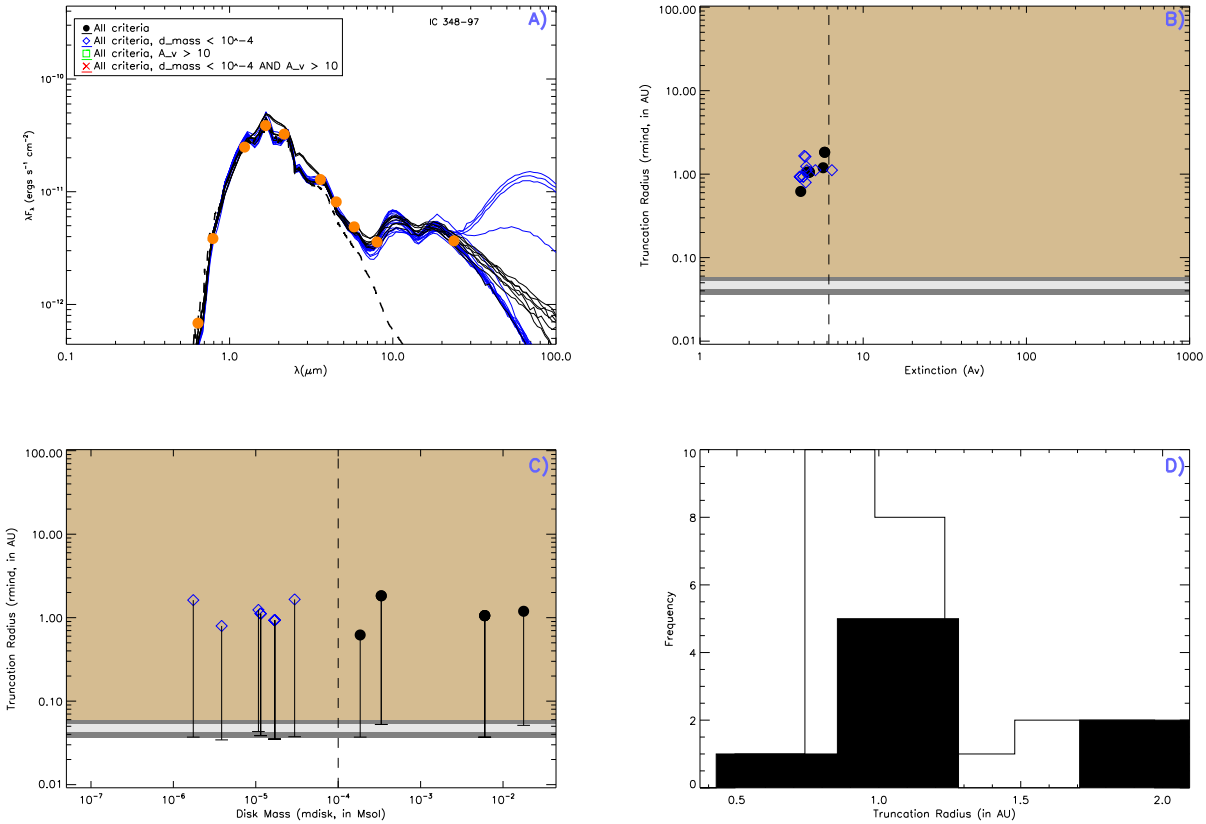

Figure A.12: SED fitting results for IC 348 #97

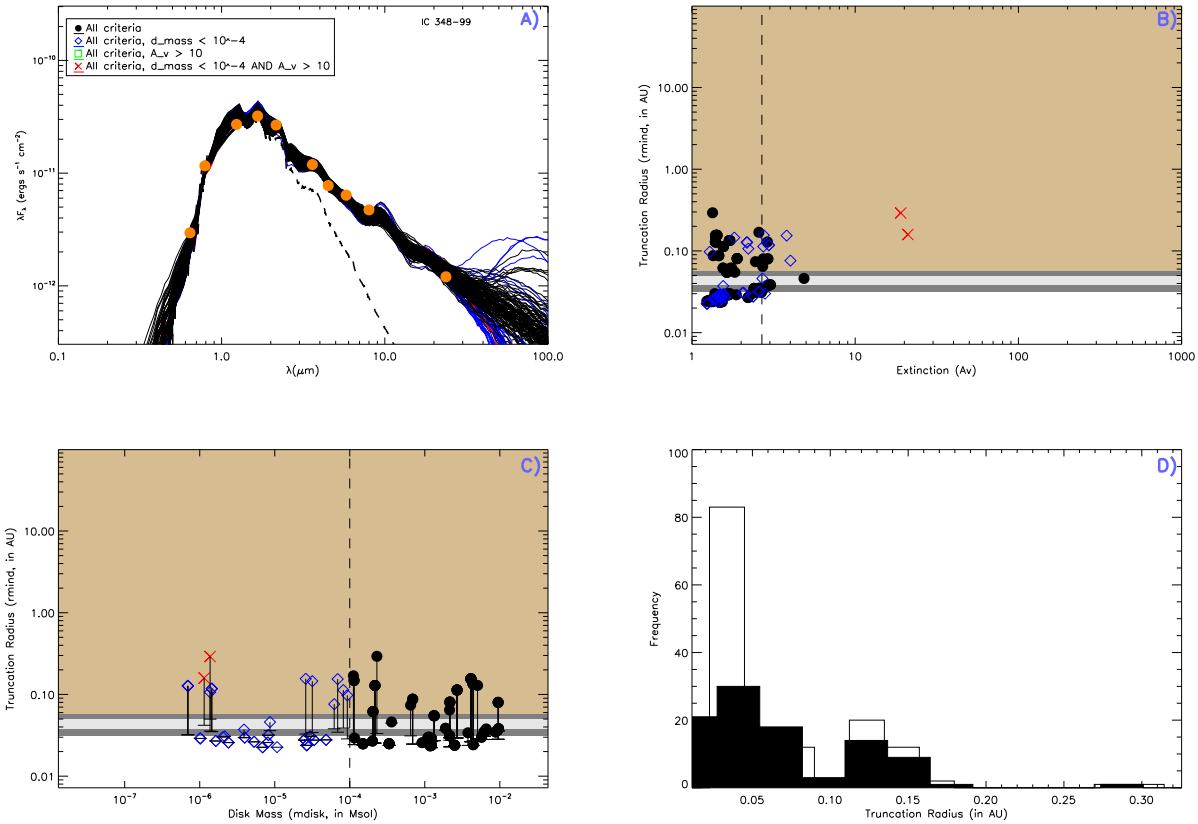

Figure A.13: SED fitting results for IC 348 #99

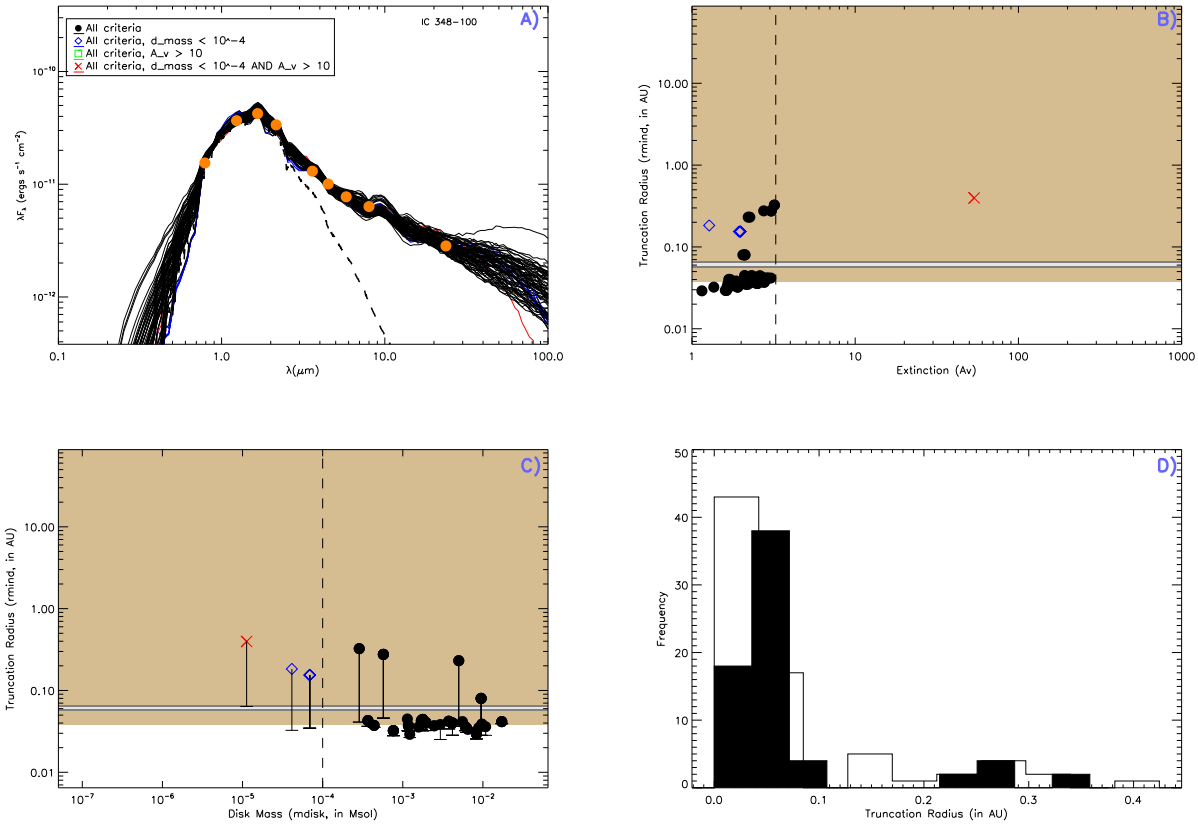

Figure A.14: SED fitting results for IC 348 #100

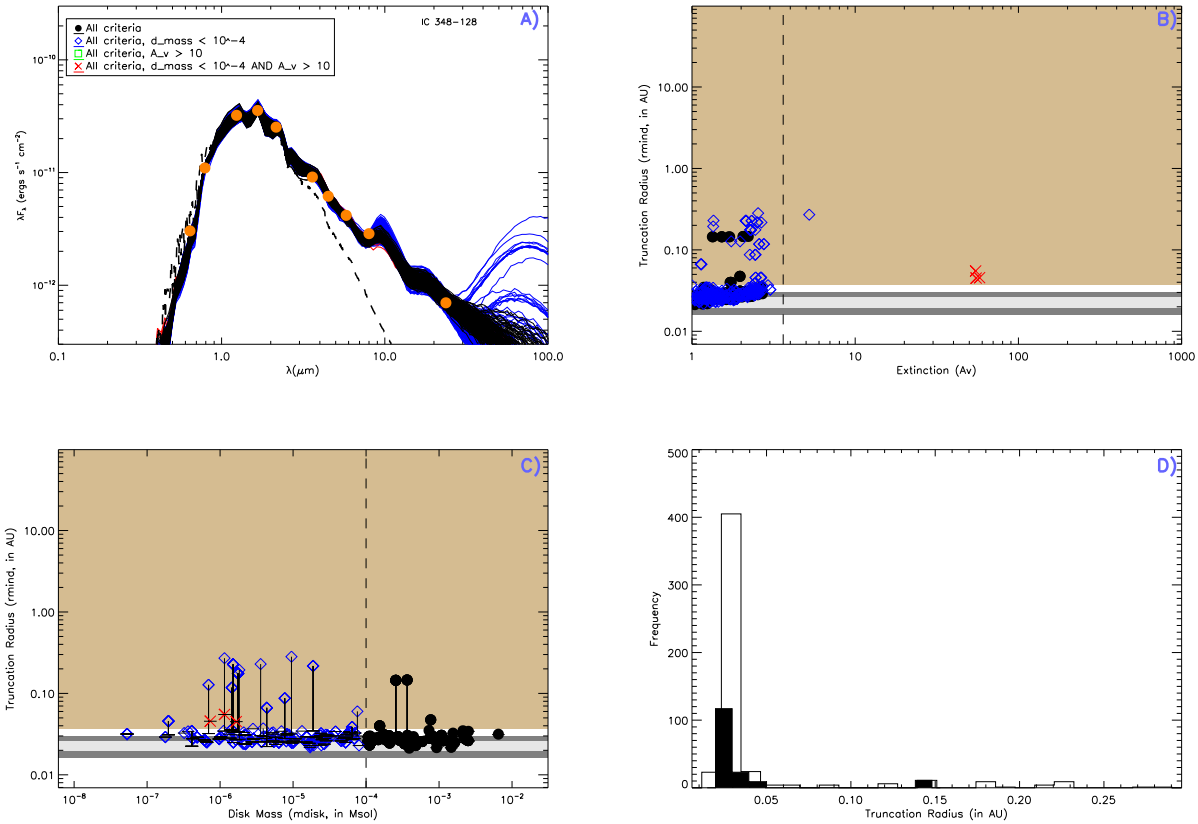

Figure A.15: SED fitting results for IC 348 #128

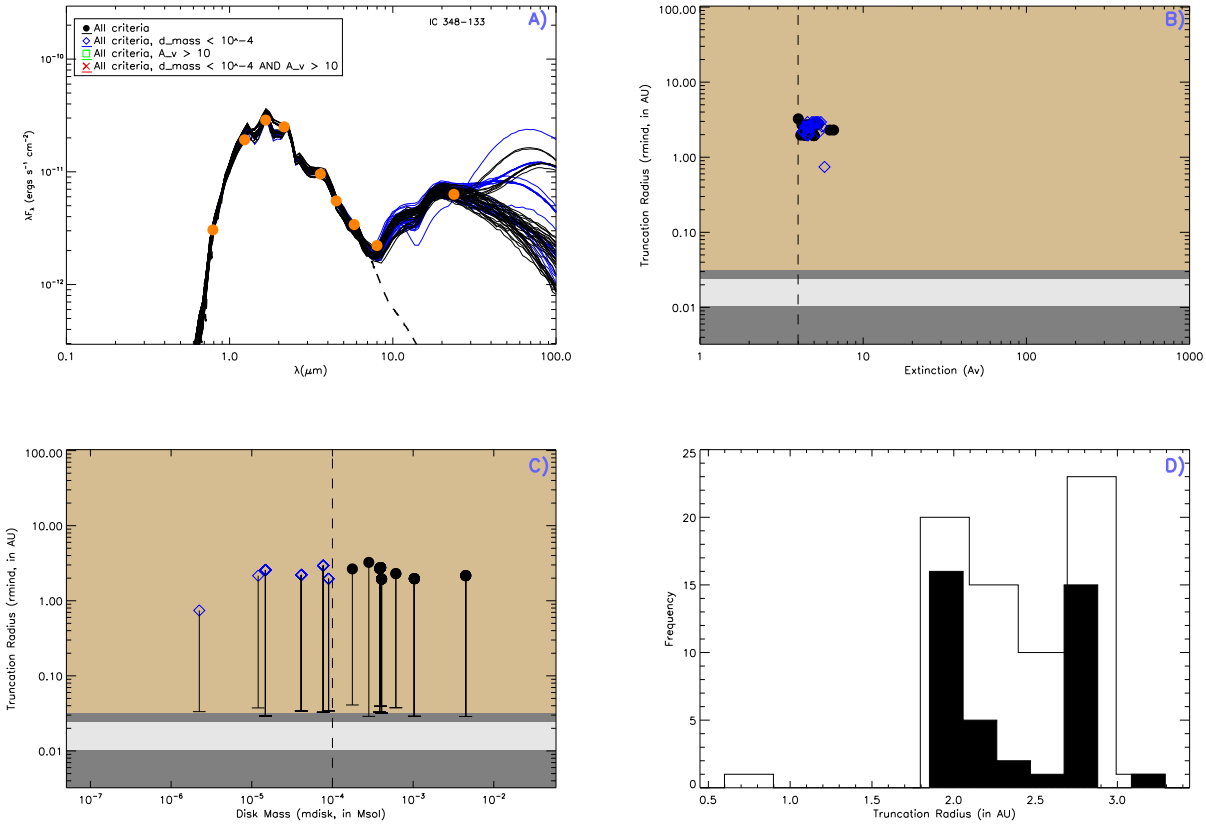

Figure A.16: SED fitting results for IC 348 #133

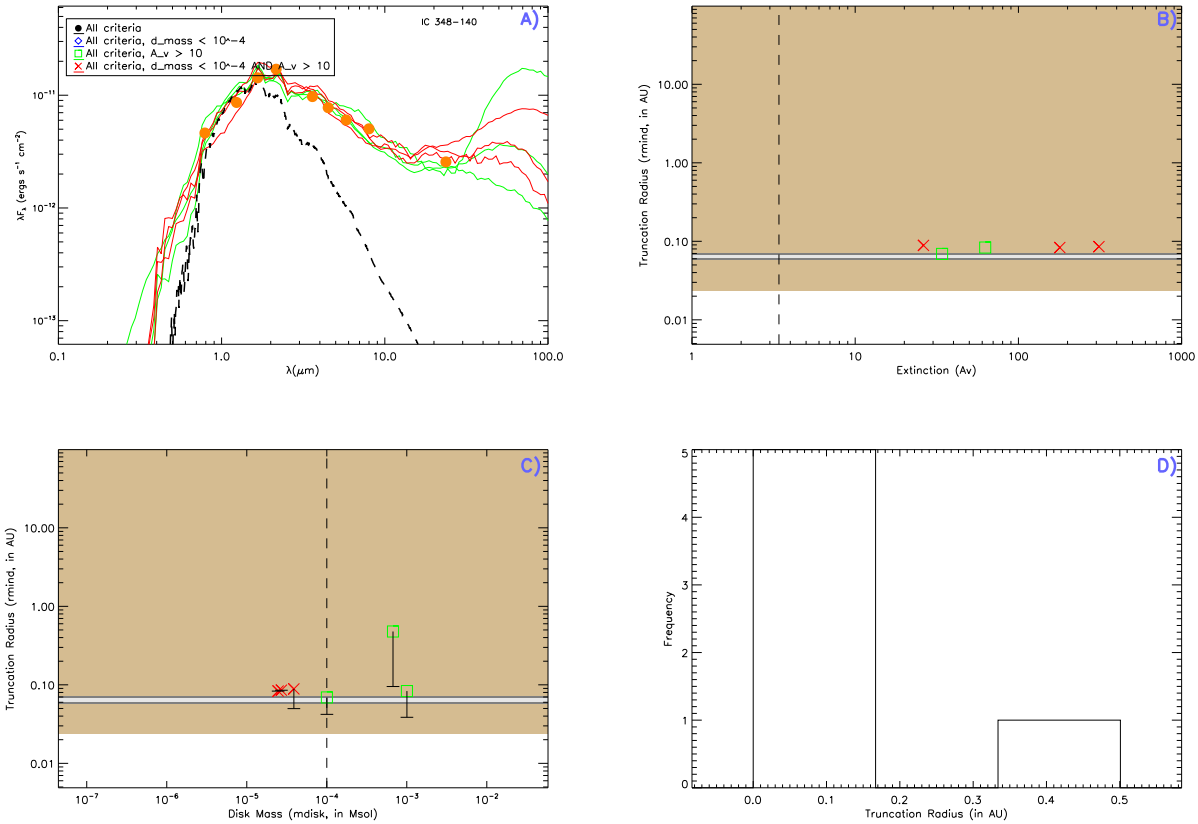

Figure A.17: SED fitting results for IC 348 #140

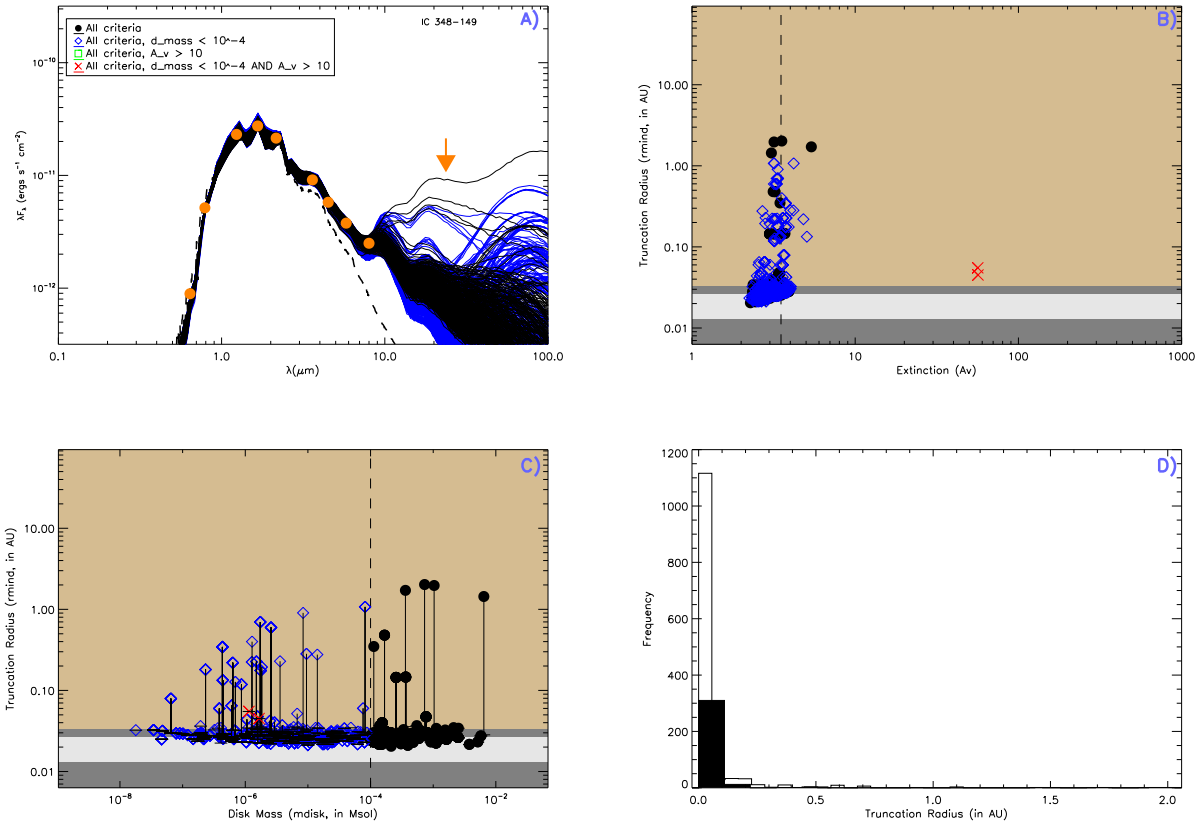

Figure A.18: SED fitting results for IC 348 #149

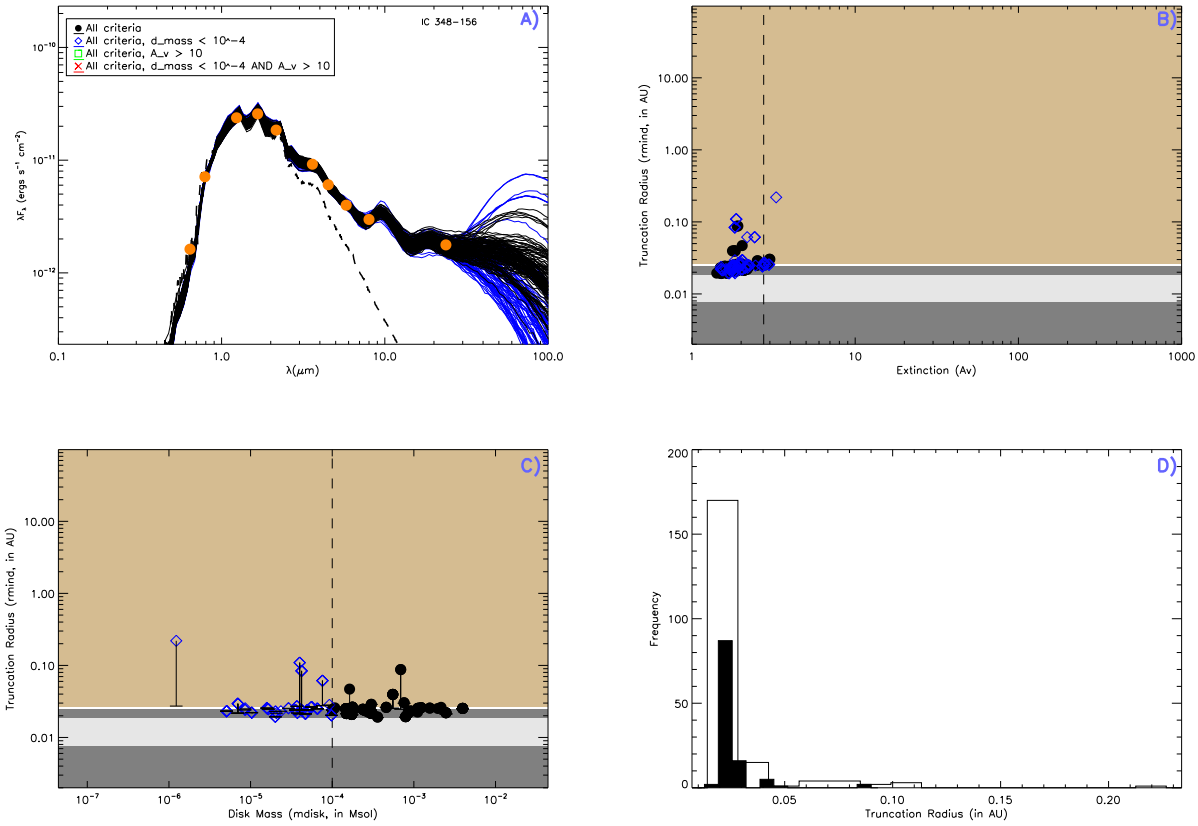

Figure A.19: SED fitting results for IC 348 #156

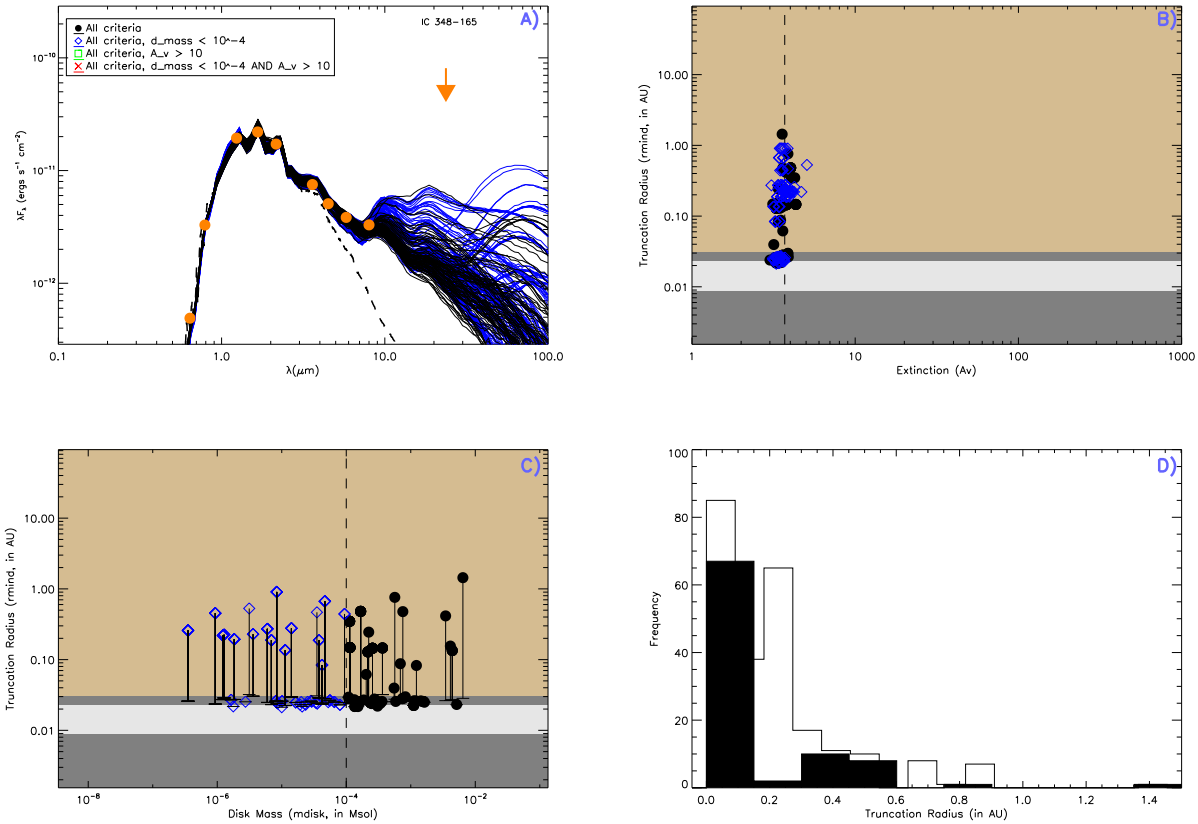

Figure A.20: SED fitting results for IC 348 #165

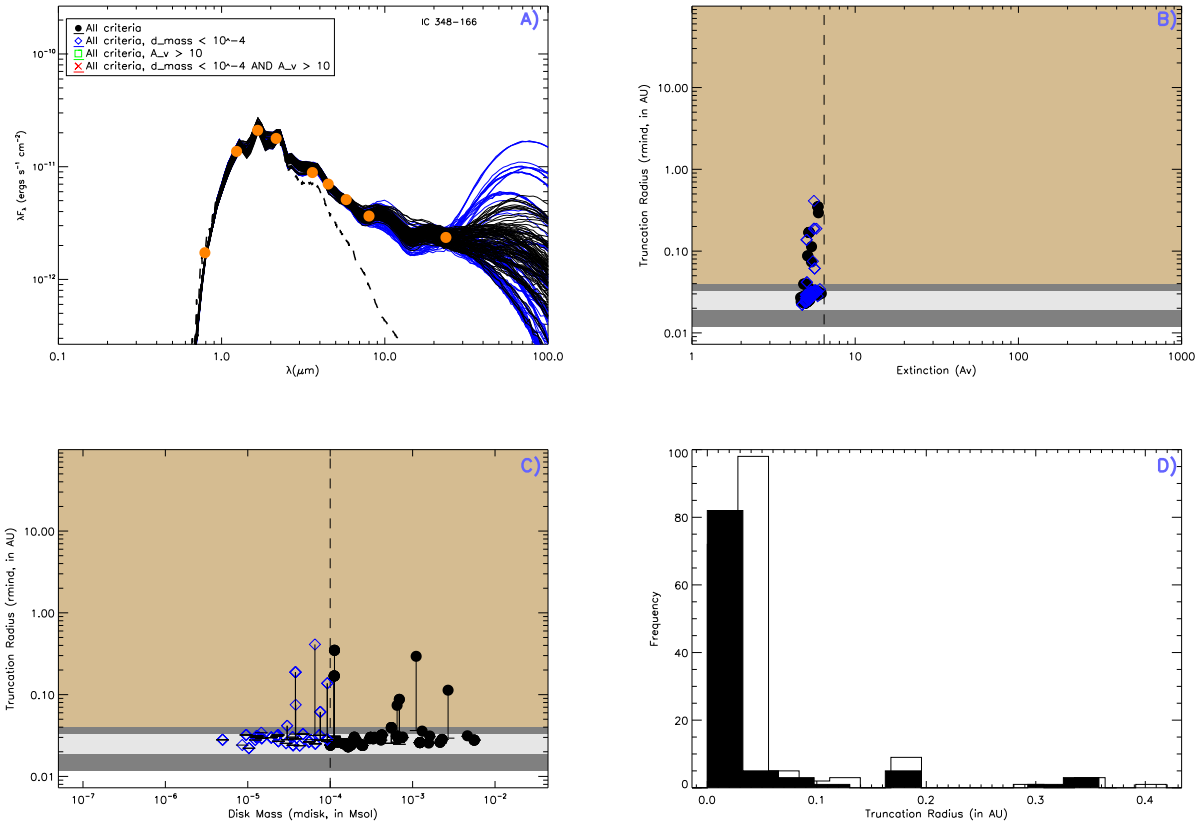

Figure A.21: SED fitting results for IC 348 #166

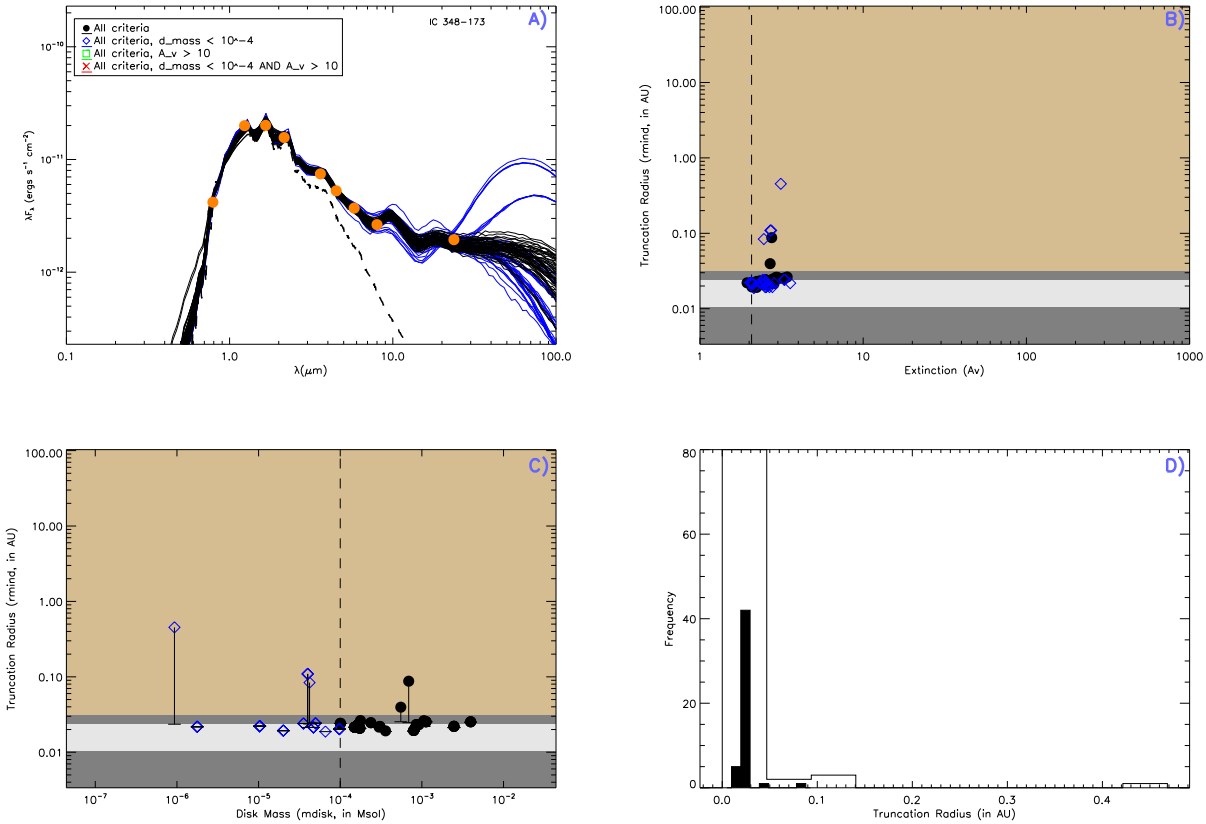

Figure A.22: SED fitting results for IC 348 #173

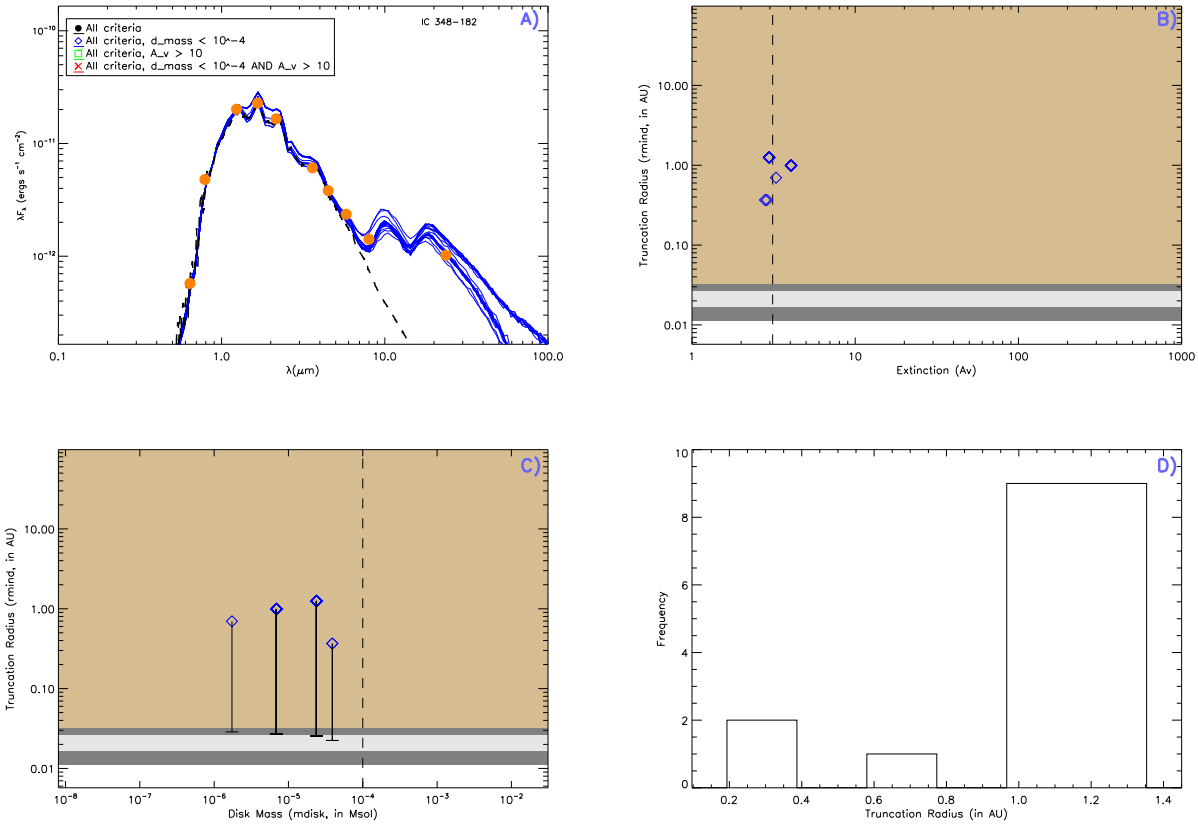

Figure A.23: SED fitting results for IC 348 #182

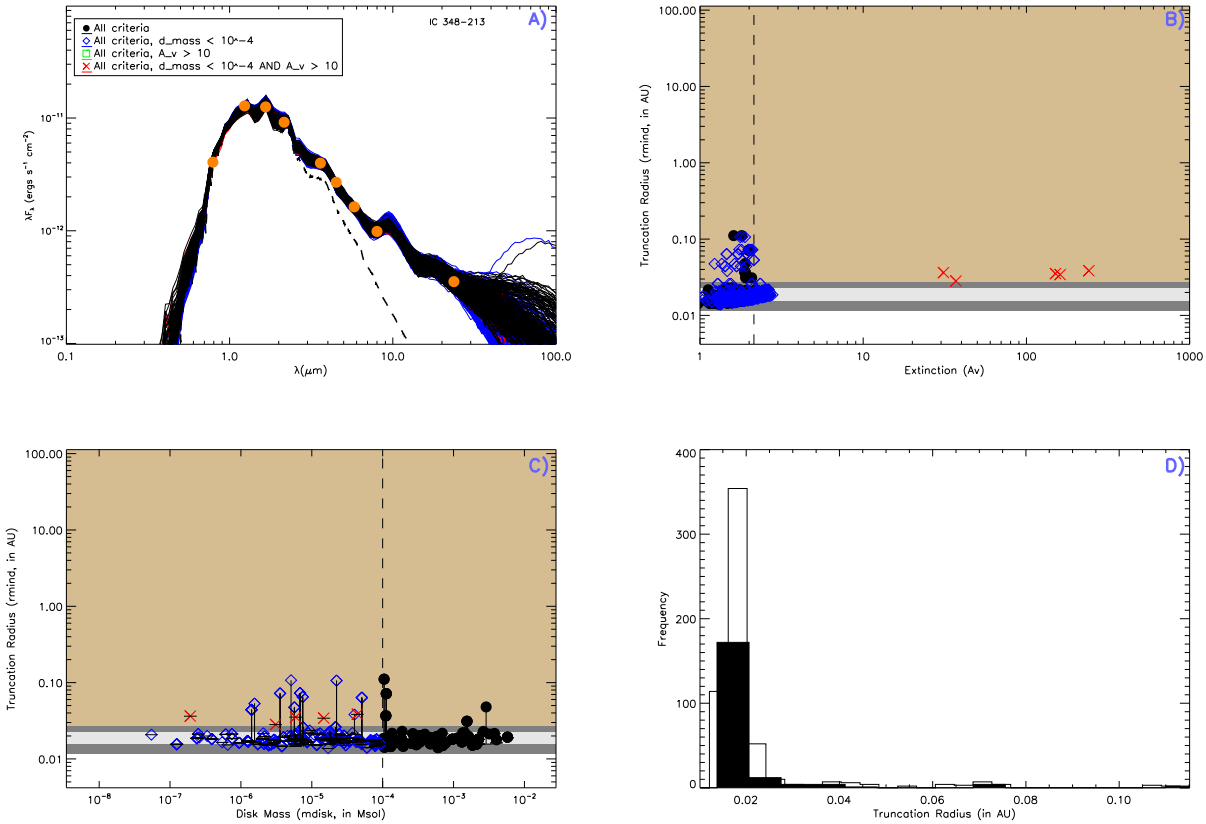

Figure A.24: SED fitting results for IC 348 #213

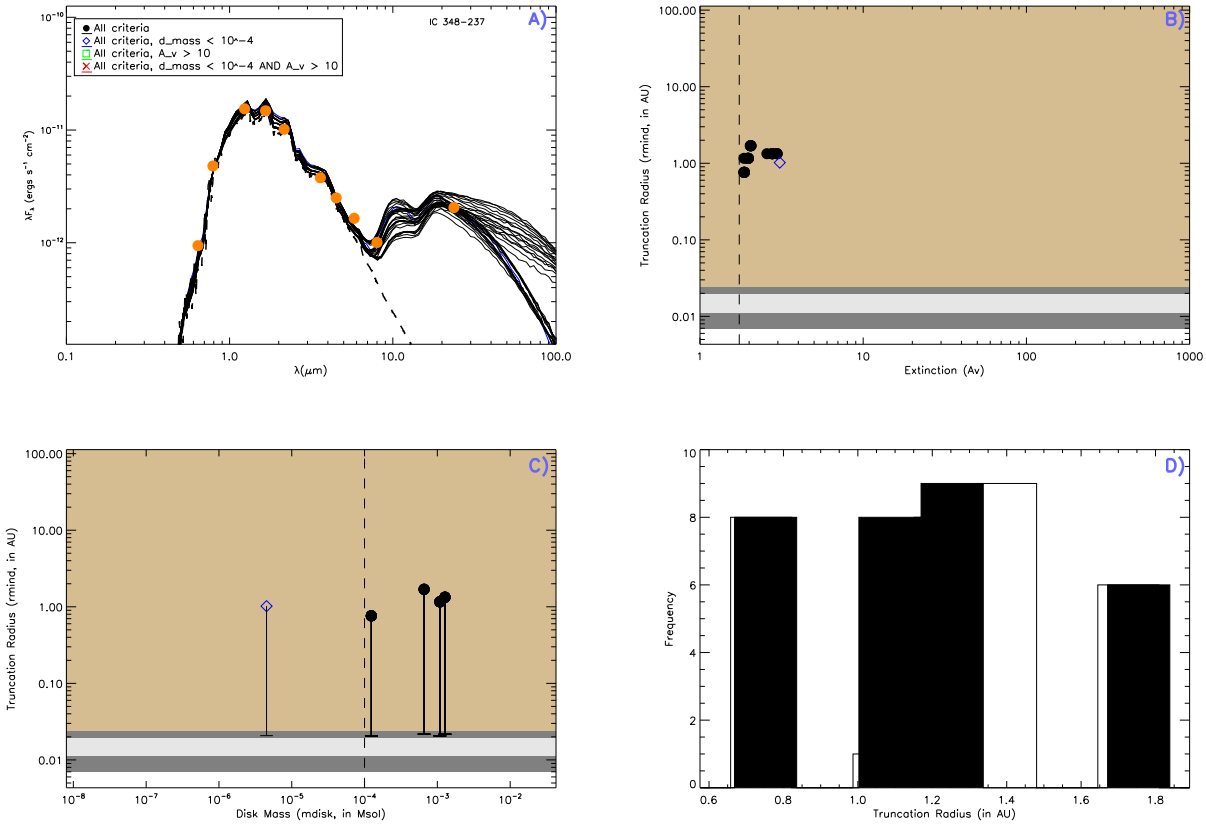

Figure A.25: SED fitting results for IC 348 #237

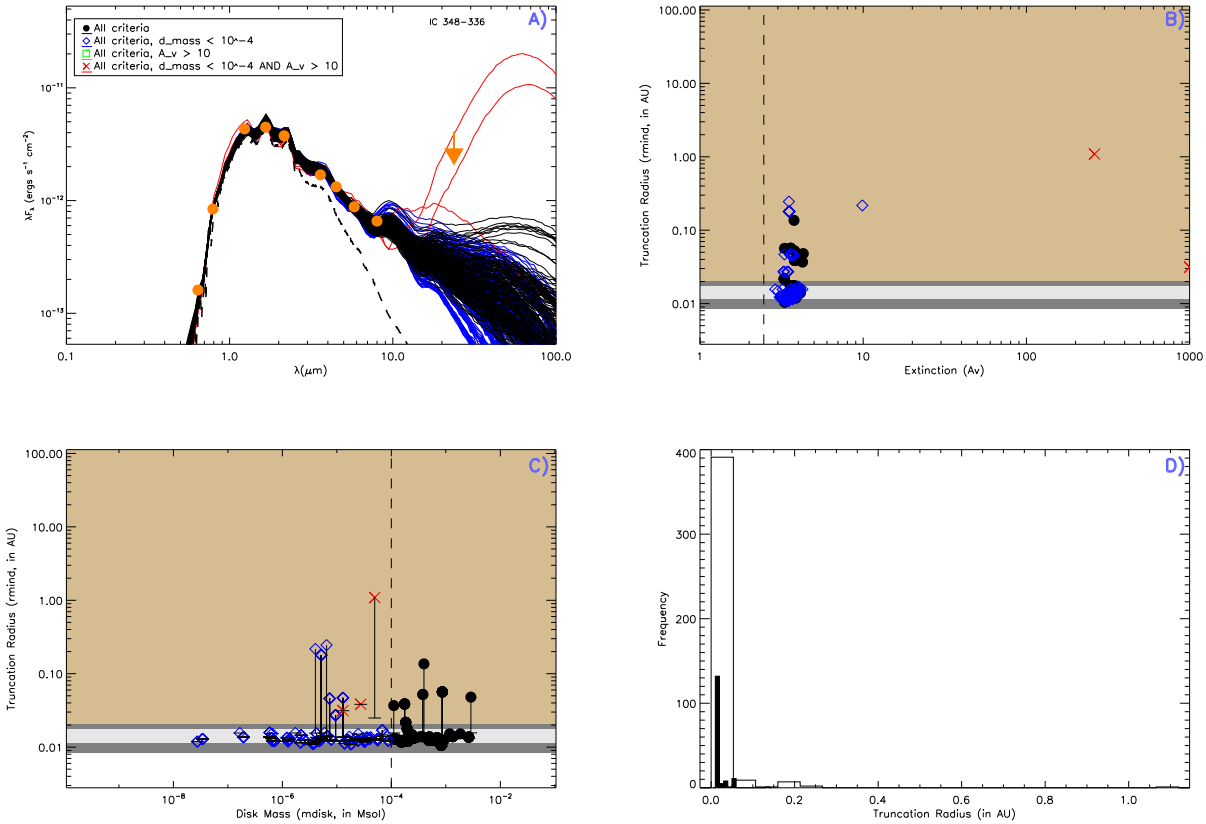

Figure A.26: SED fitting results for IC 348 #336

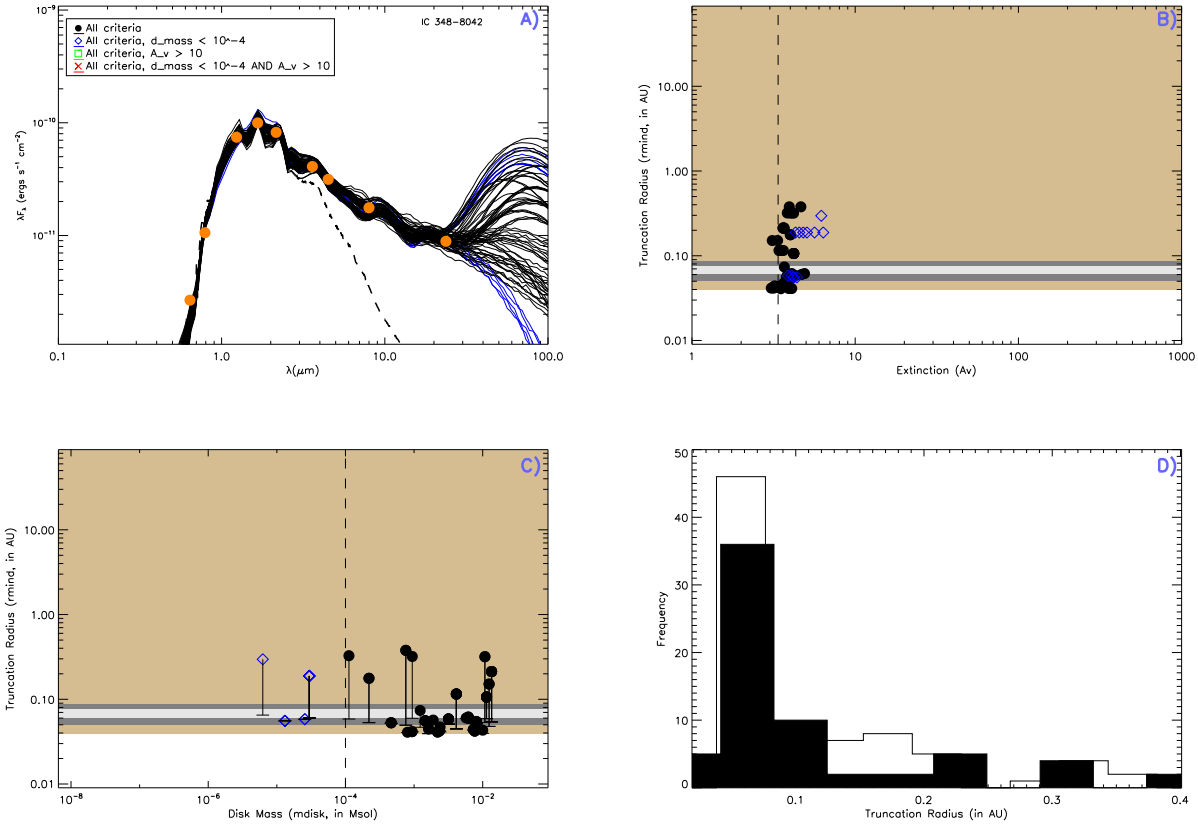

Figure A.27: SED fitting results for IC 348 #8042

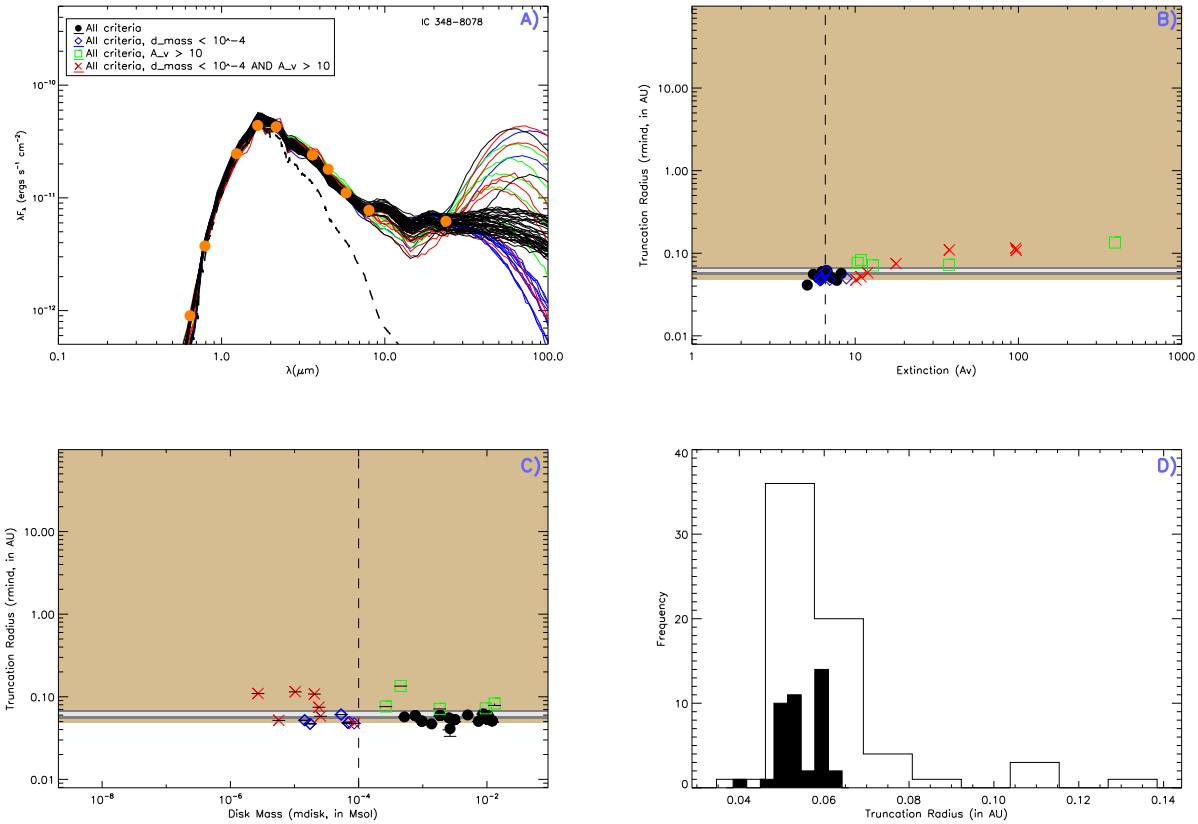

Figure A.28: SED fitting results for IC 348 #8078

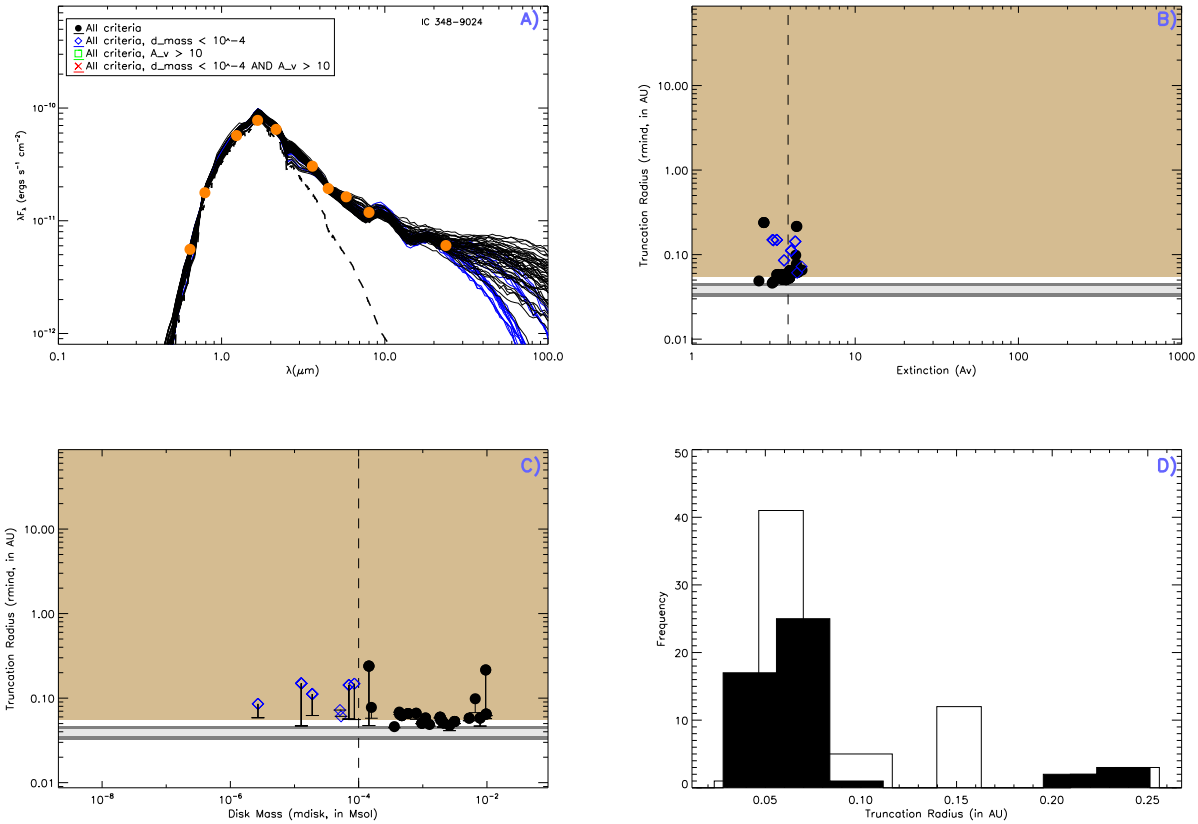

Figure A.29: SED fitting results for IC 348 #9024

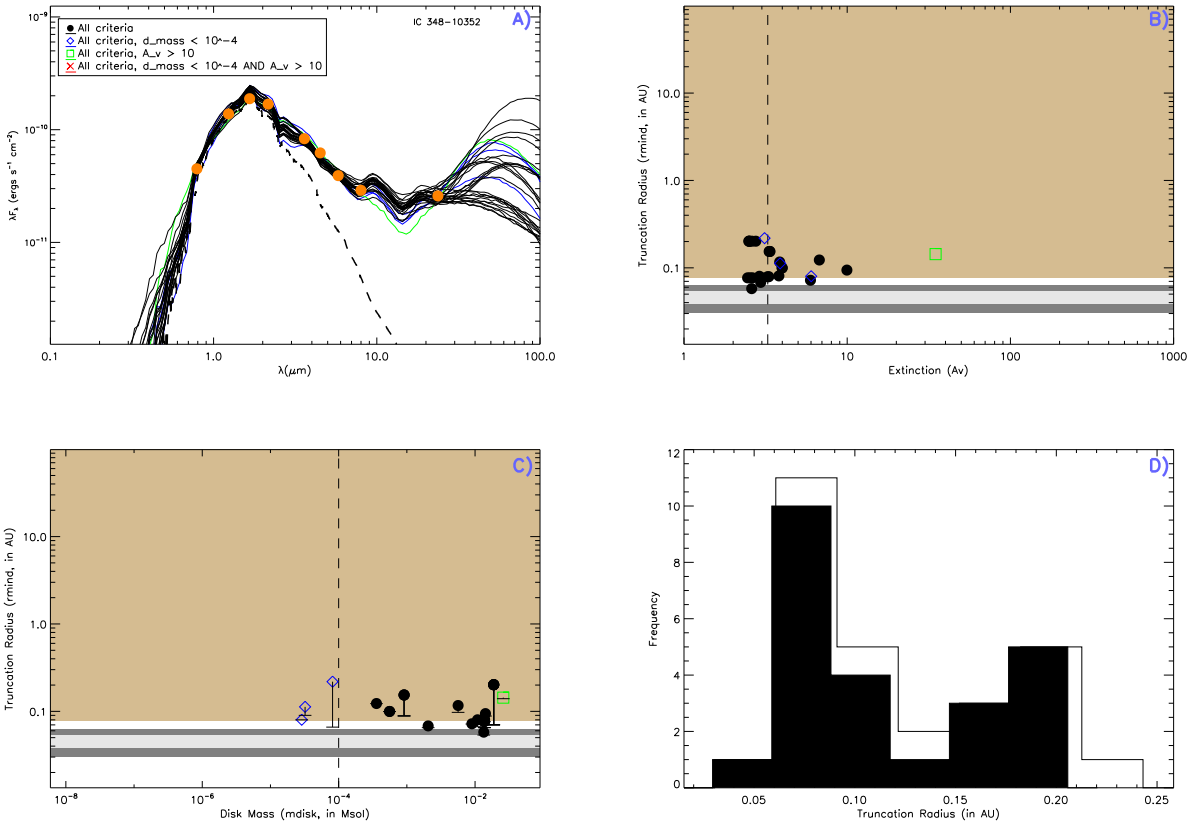

Figure A.30: SED fitting results for IC 348 #10352

Appendix B

ATLAS OF ONC SED FITTINGS

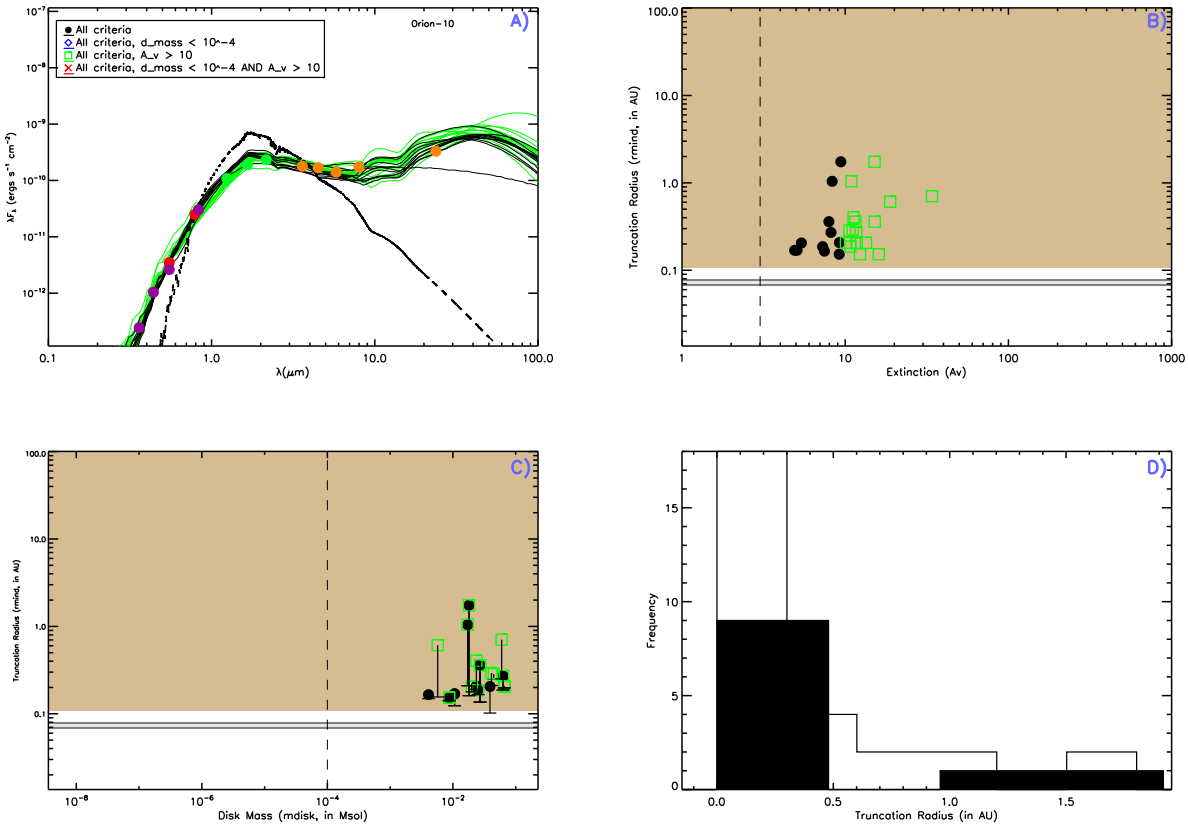

Figure B.1: SED fitting results for ONC #10

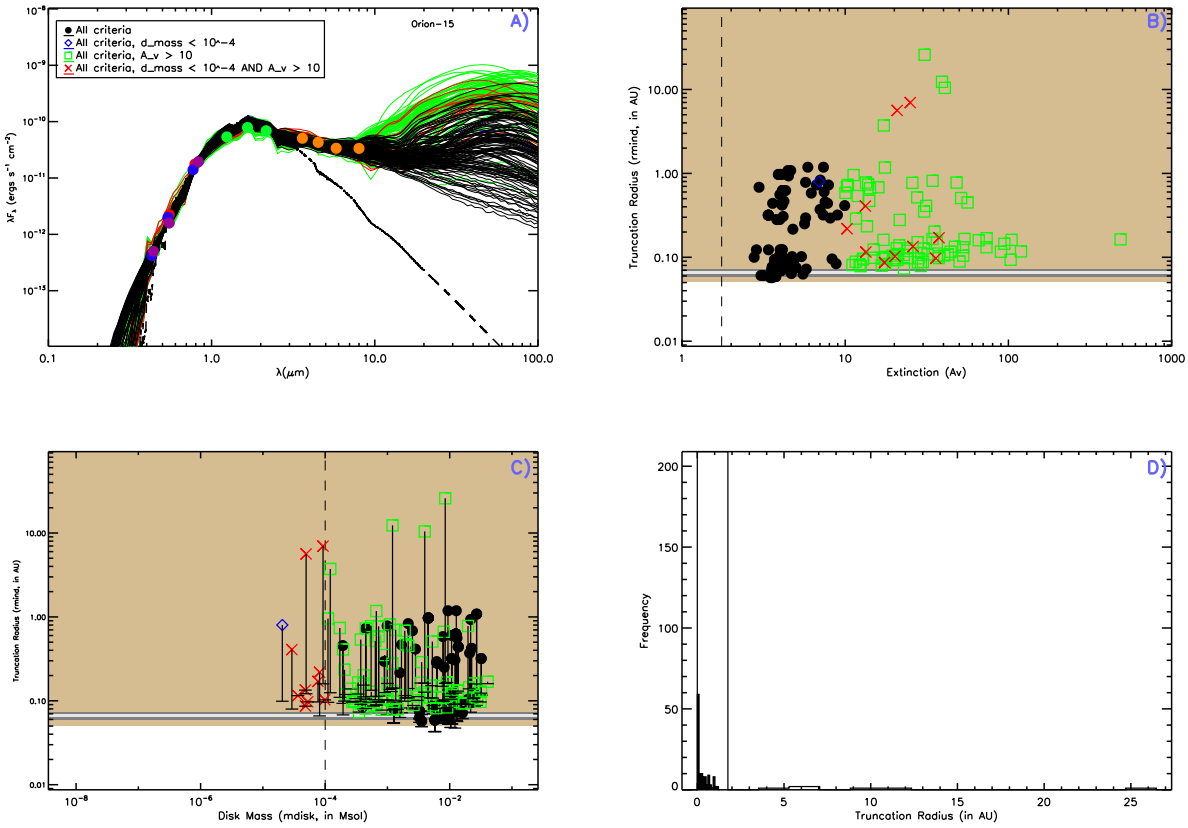

Figure B.2: SED fitting results for ONC #15

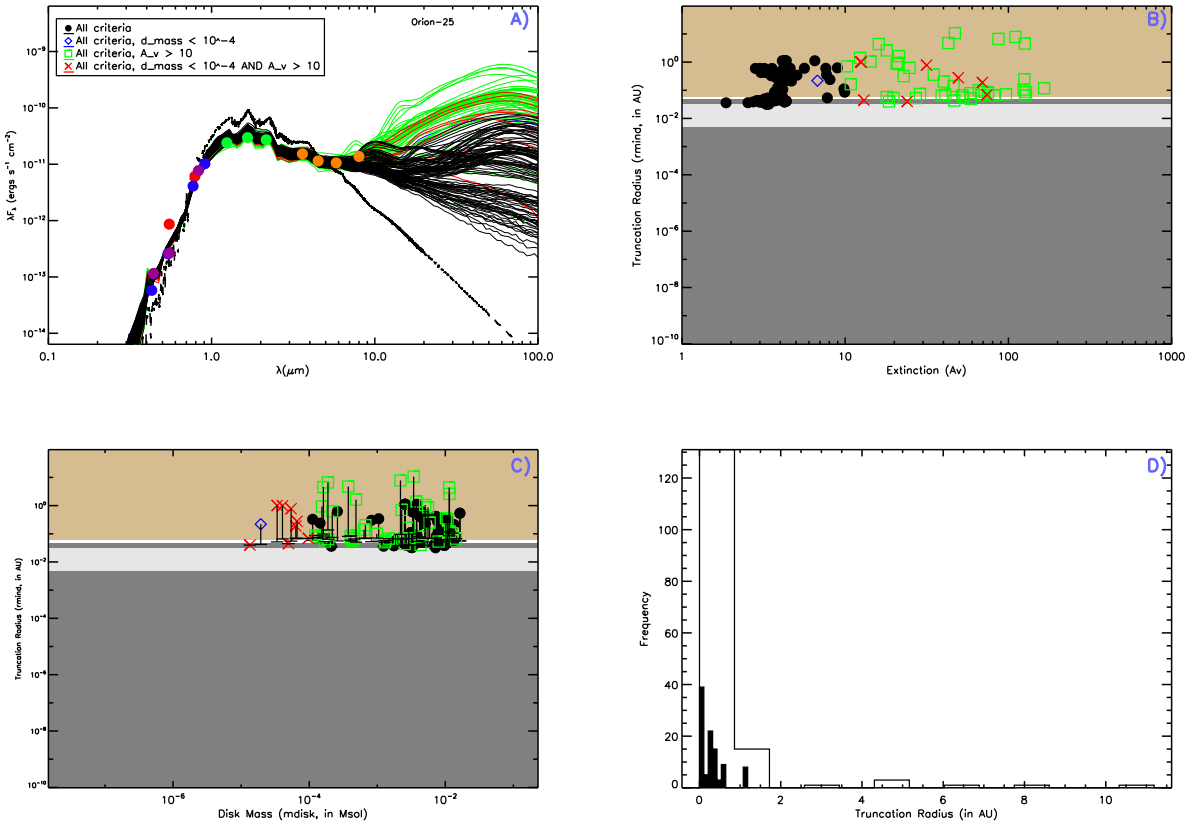

Figure B.3: SED fitting results for ONC #25

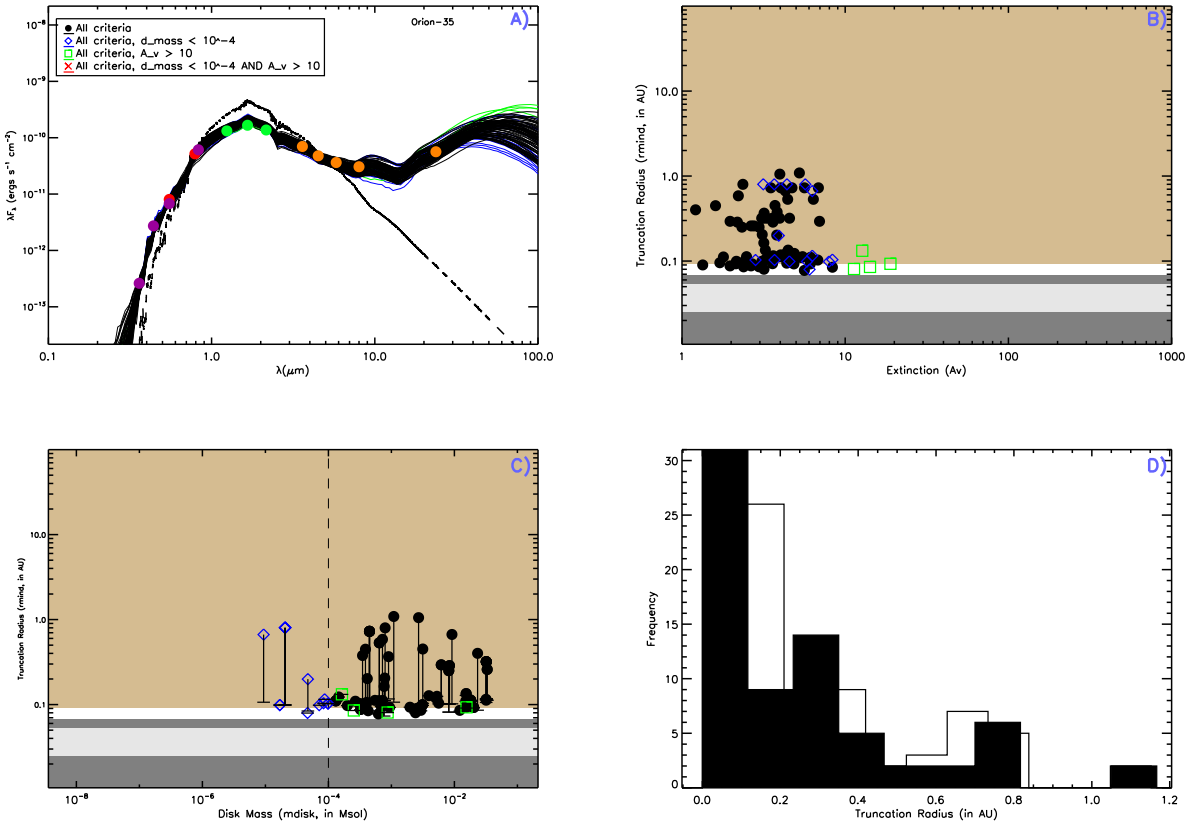

Figure B.4: SED fitting results for ONC #35

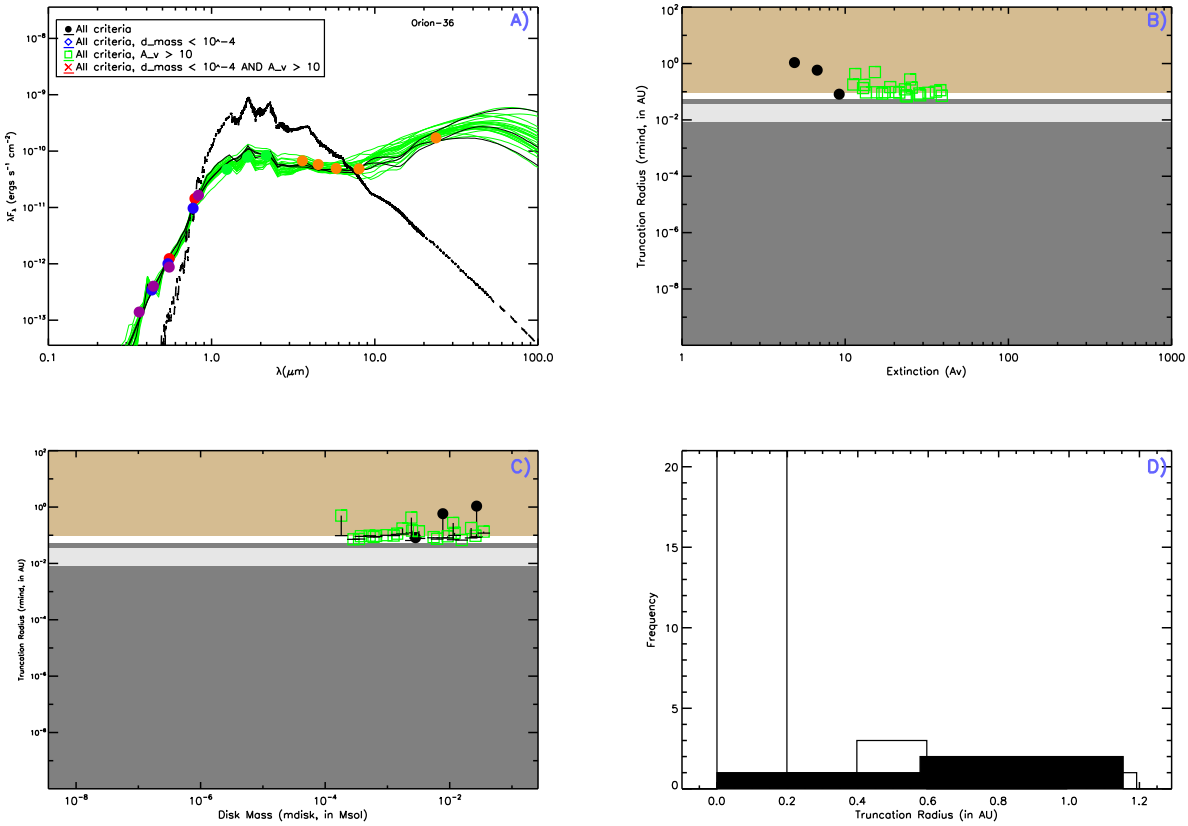

Figure B.5: SED fitting results for ONC #36

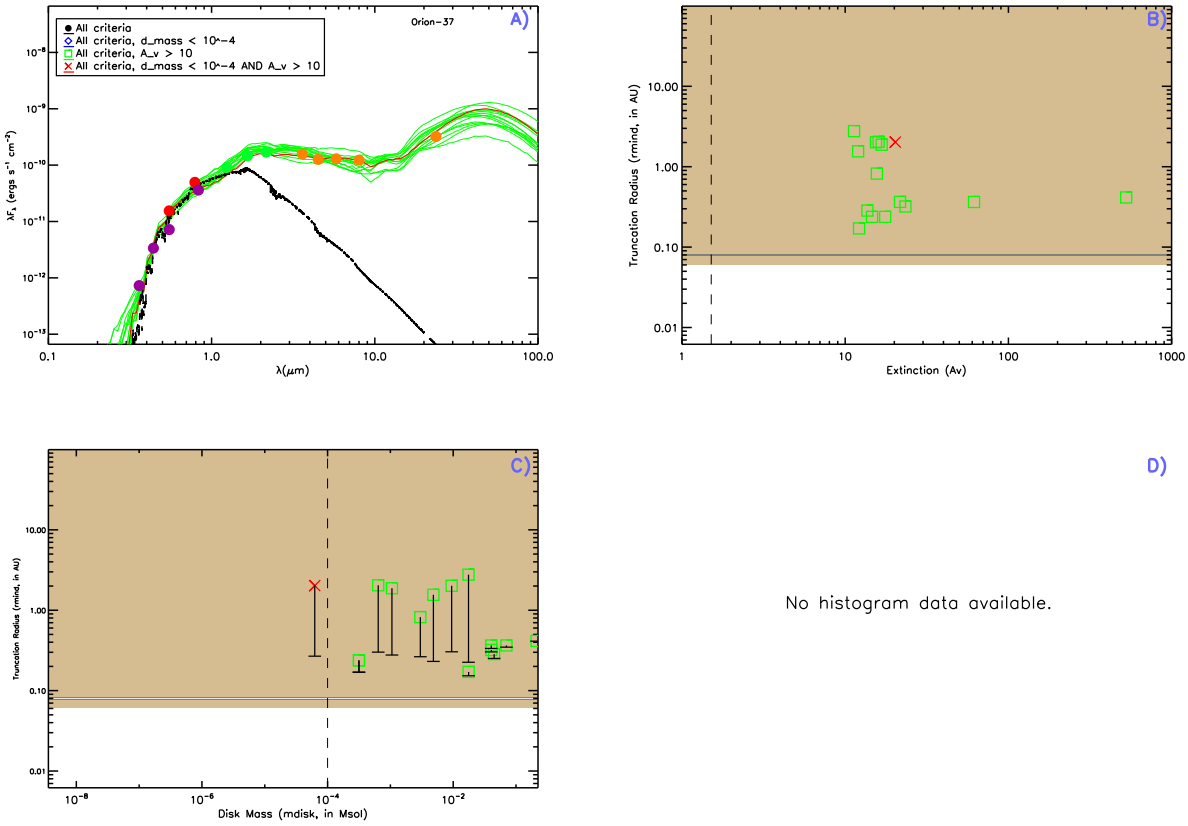

Figure B.6: SED fitting results for ONC #37

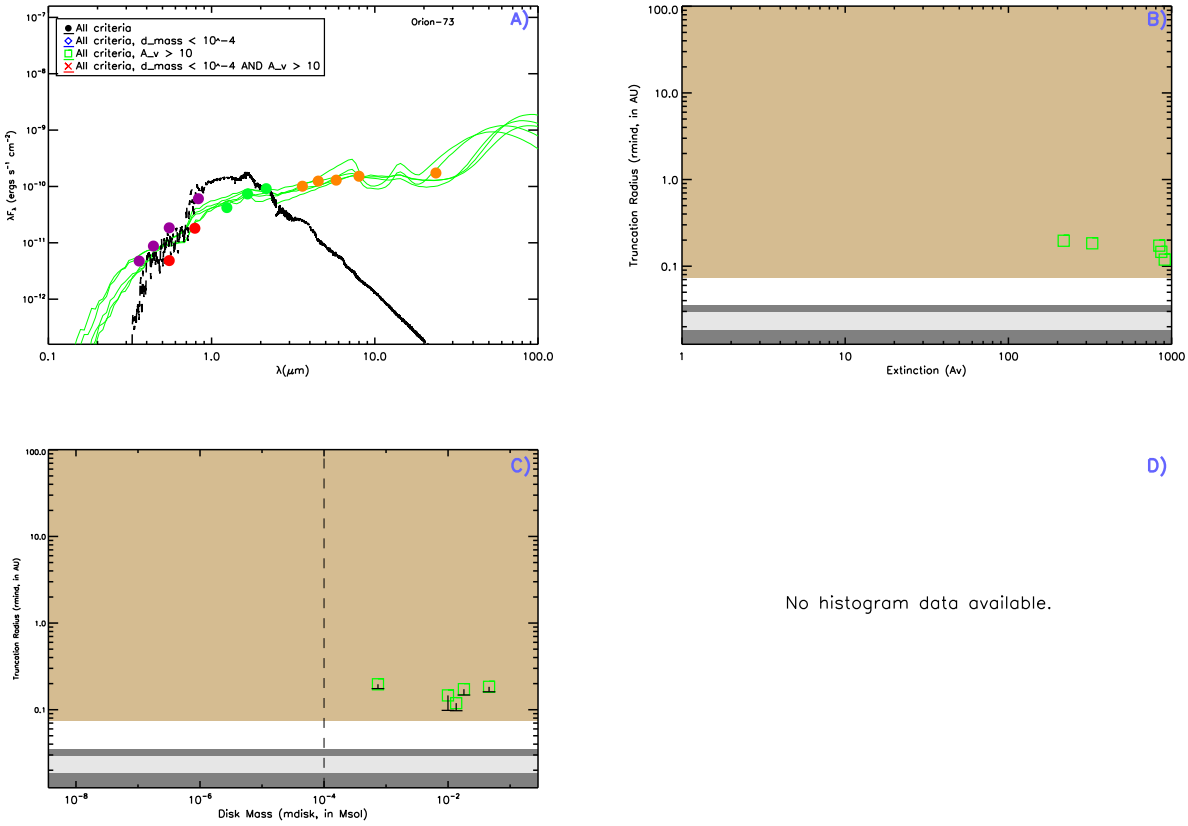

Figure B.7: SED fitting results for ONC #73

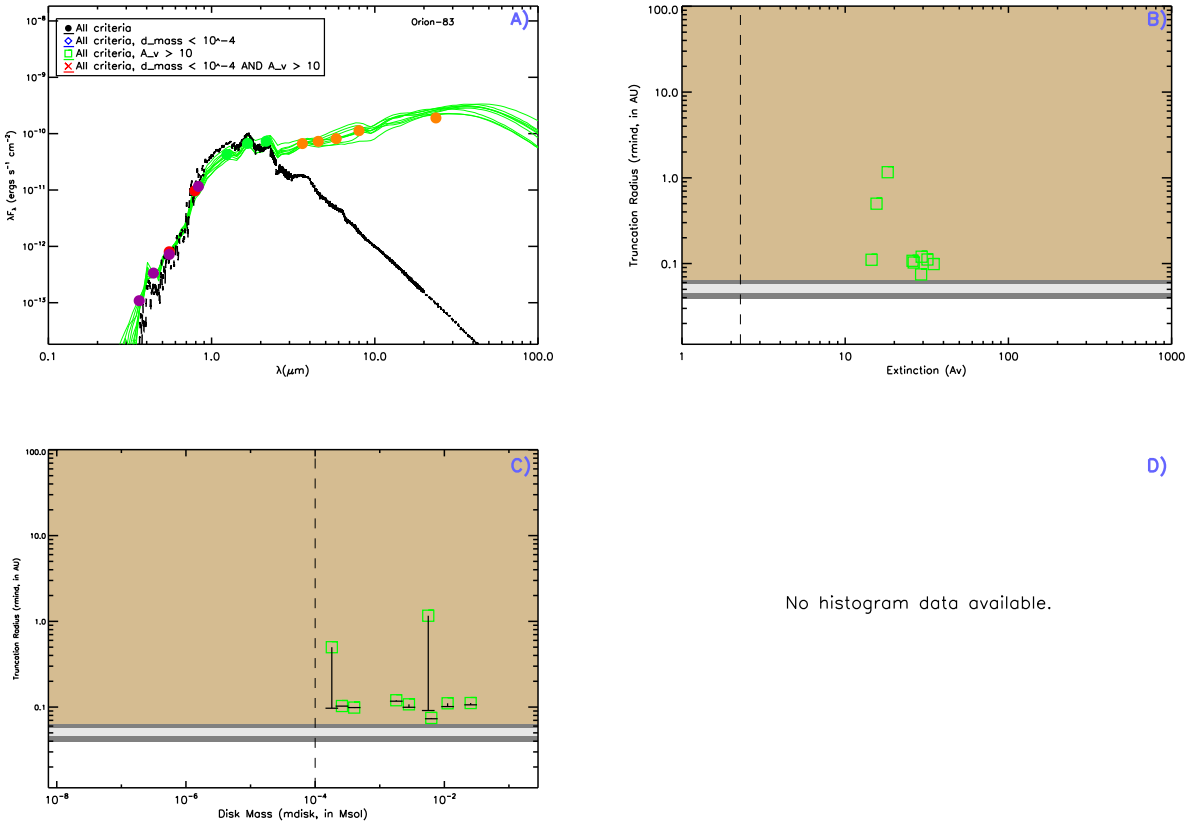

Figure B.8: SED fitting results for ONC #83

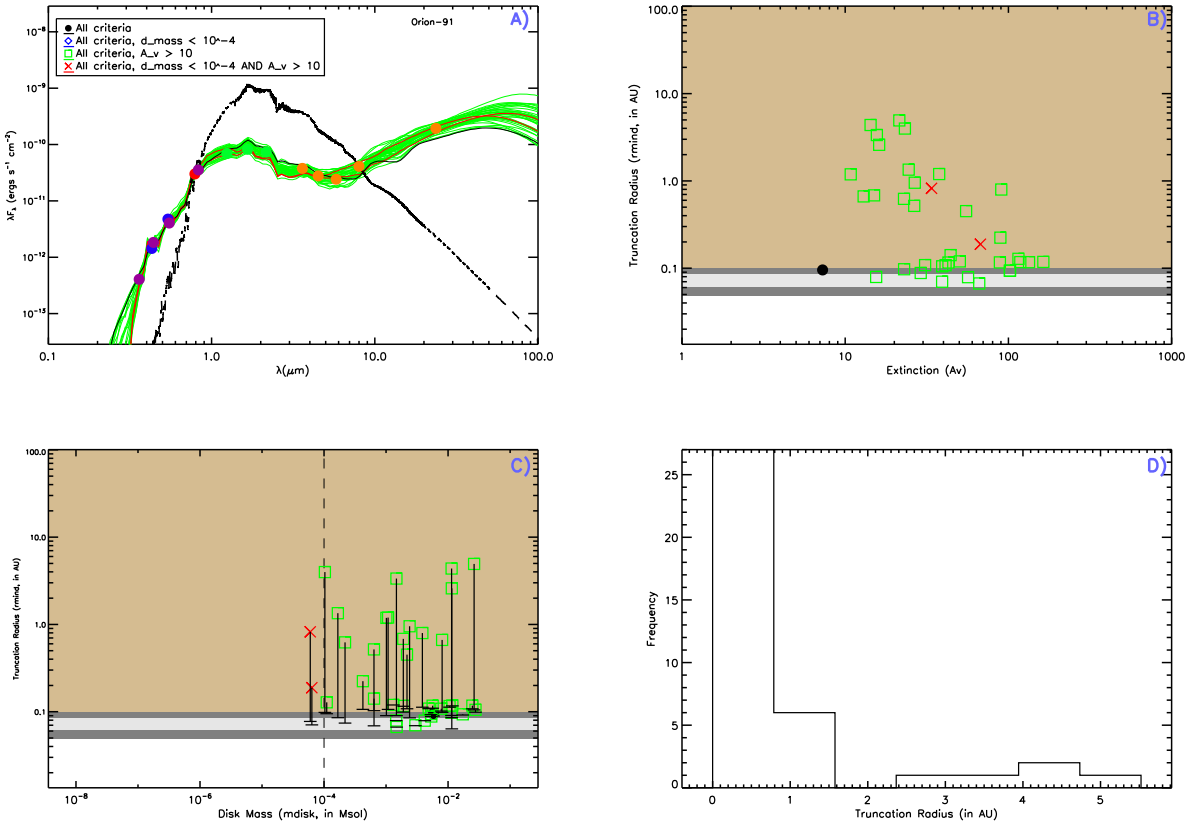

Figure B.9: SED fitting results for ONC #91

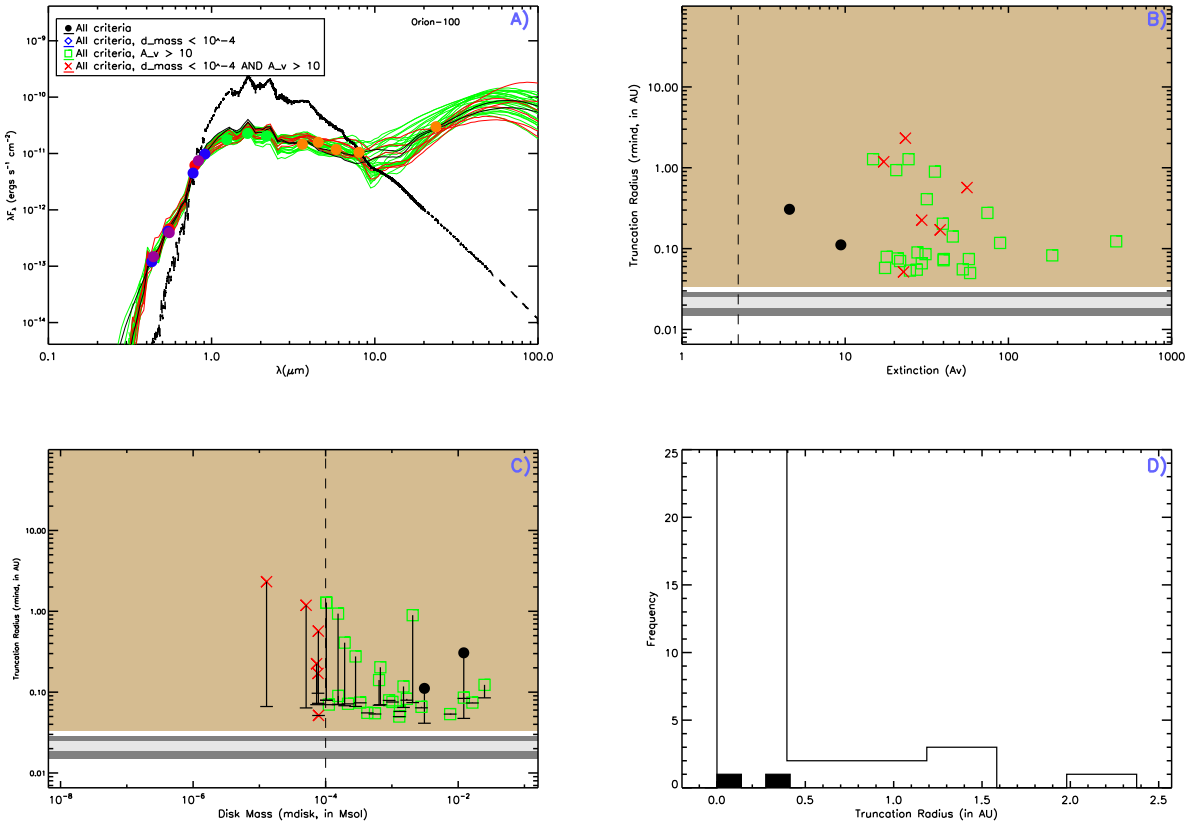

Figure B.10: SED fitting results for ONC #100

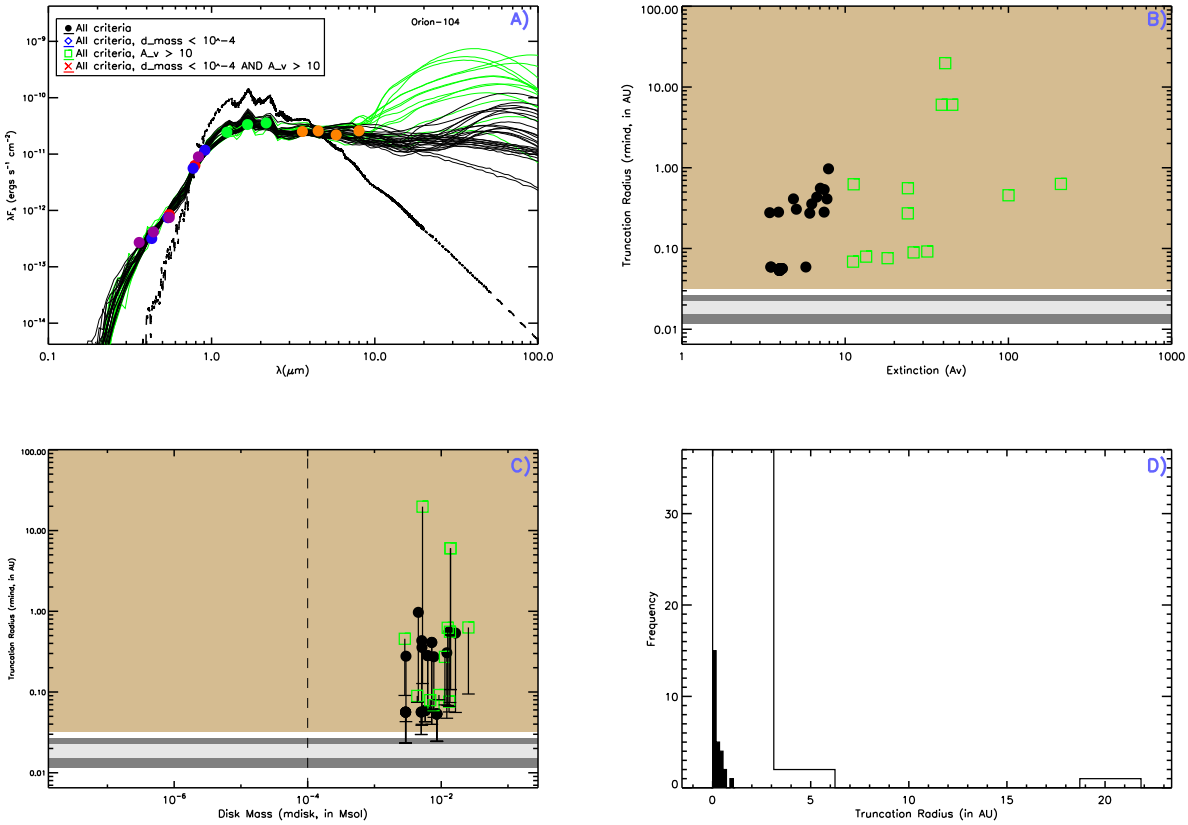

Figure B.11: SED fitting results for ONC #104

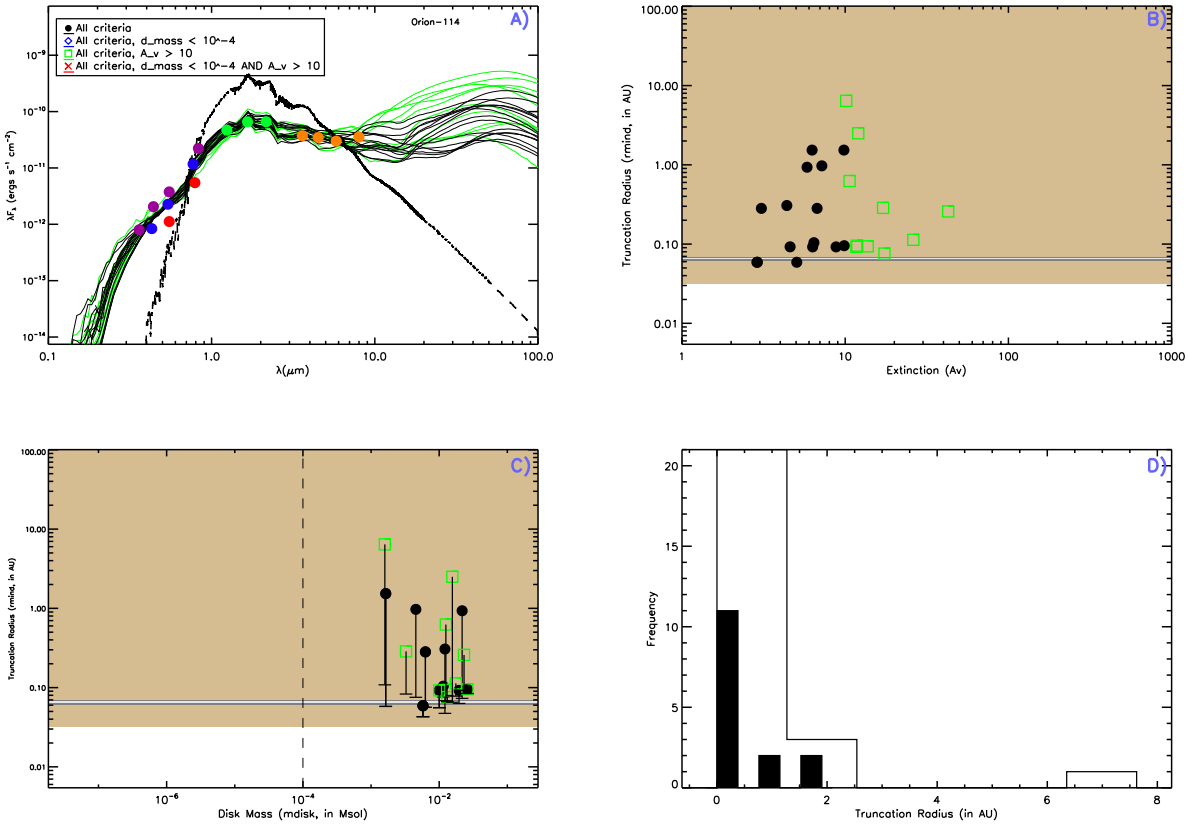

Figure B.12: SED fitting results for ONC #114

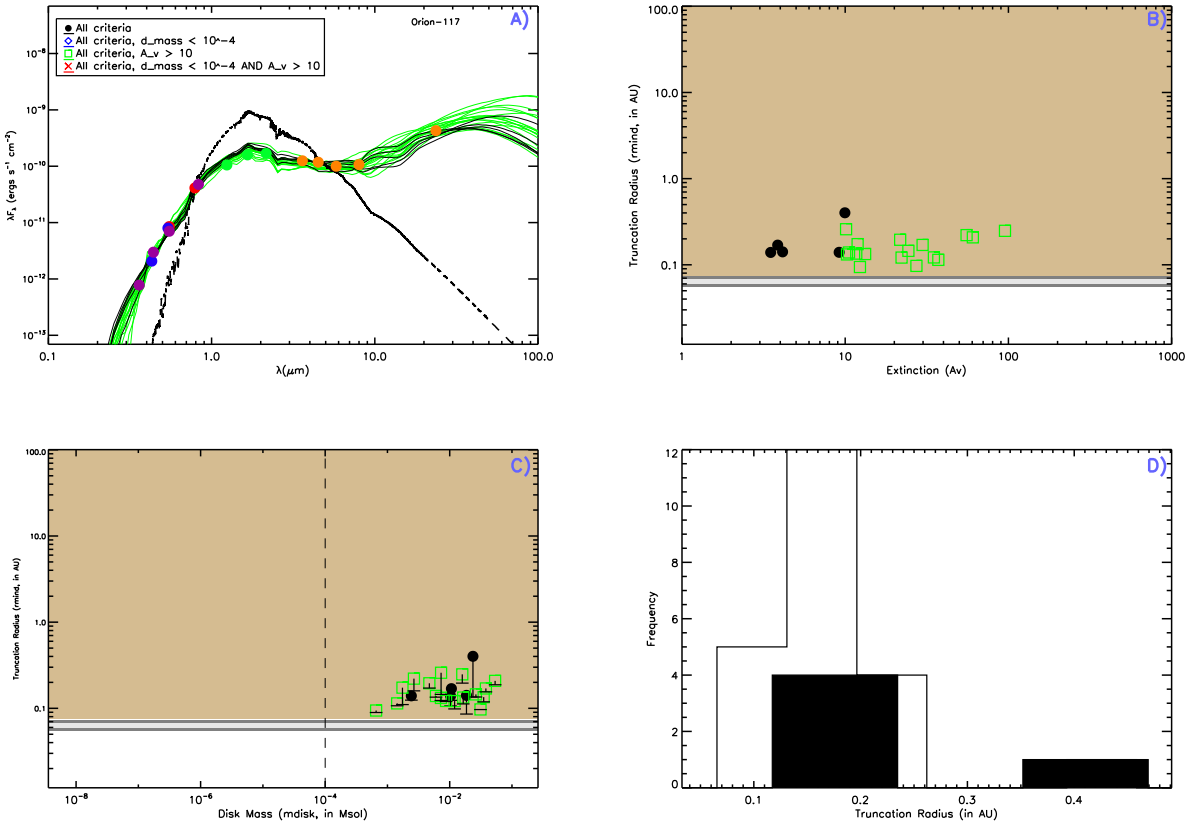

Figure B.13: SED fitting results for ONC #117

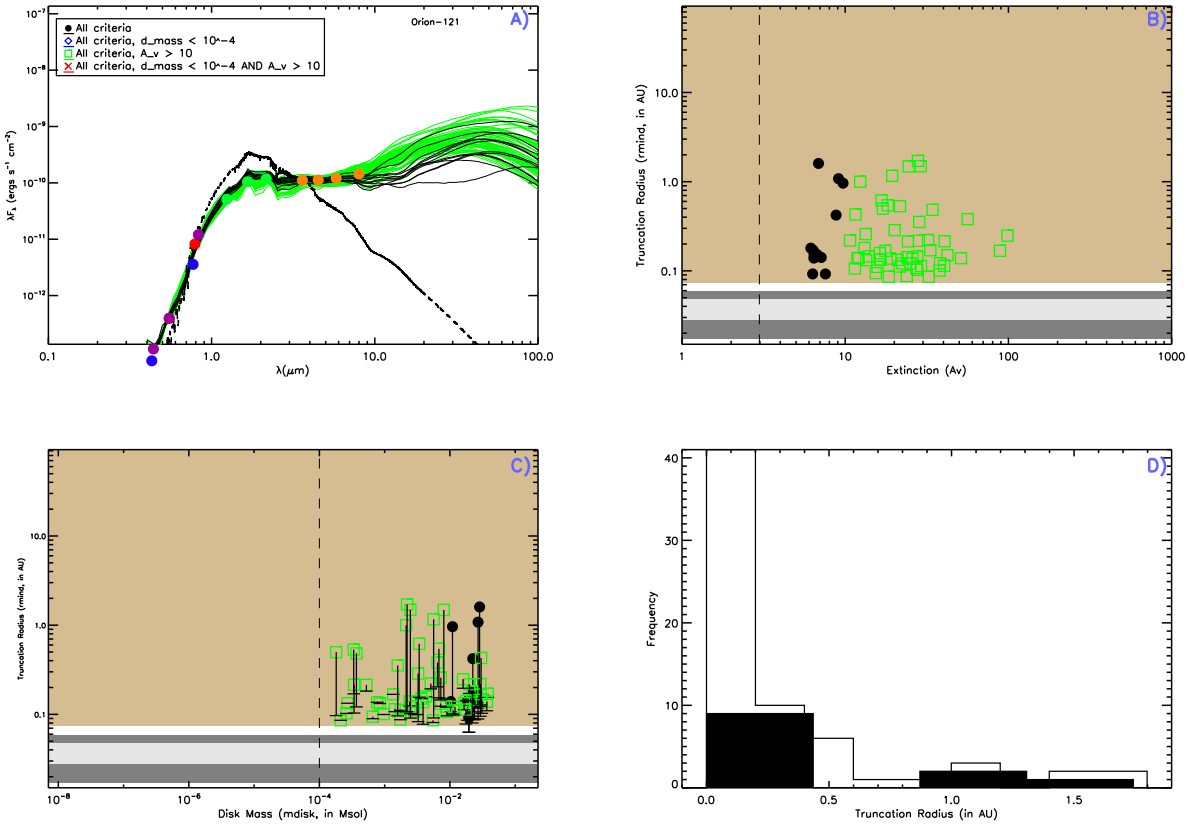

Figure B.14: SED fitting results for ONC #121

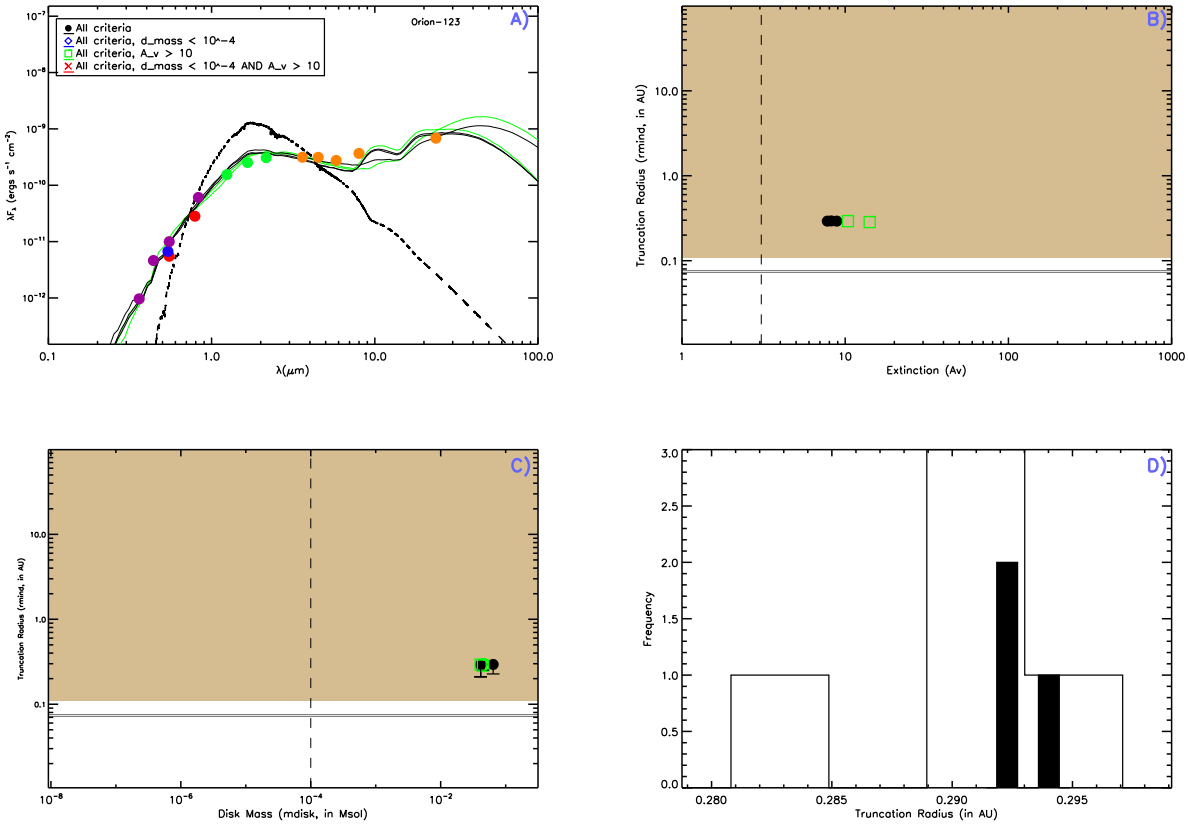

Figure B.15: SED fitting results for ONC #123

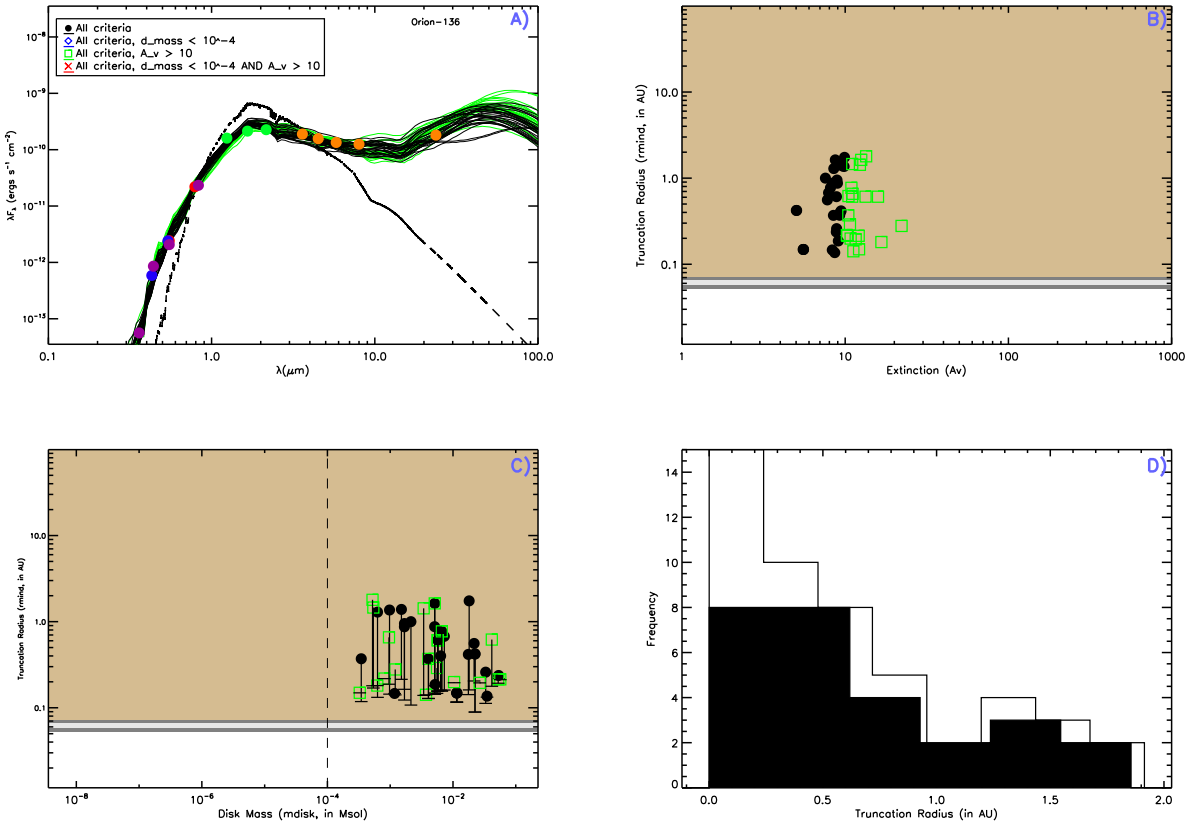

Figure B.16: SED fitting results for ONC #136

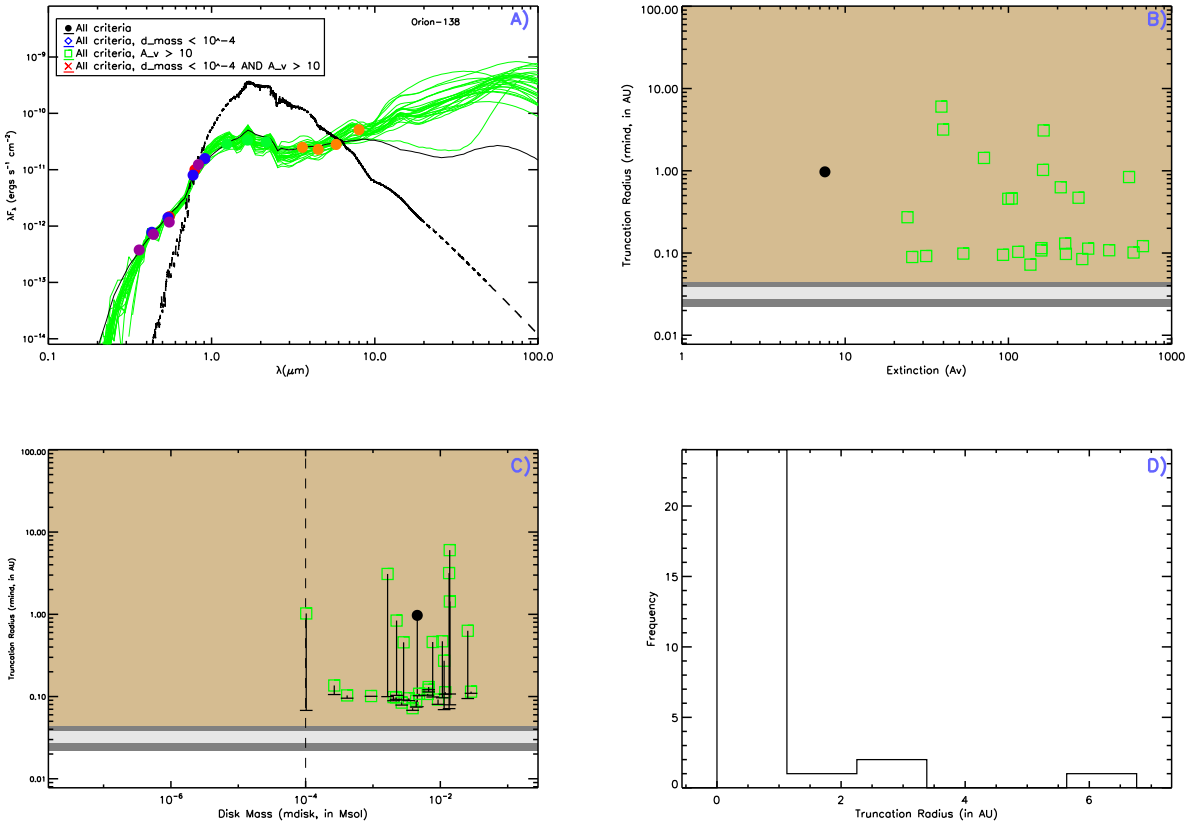

Figure B.17: SED fitting results for ONC #138

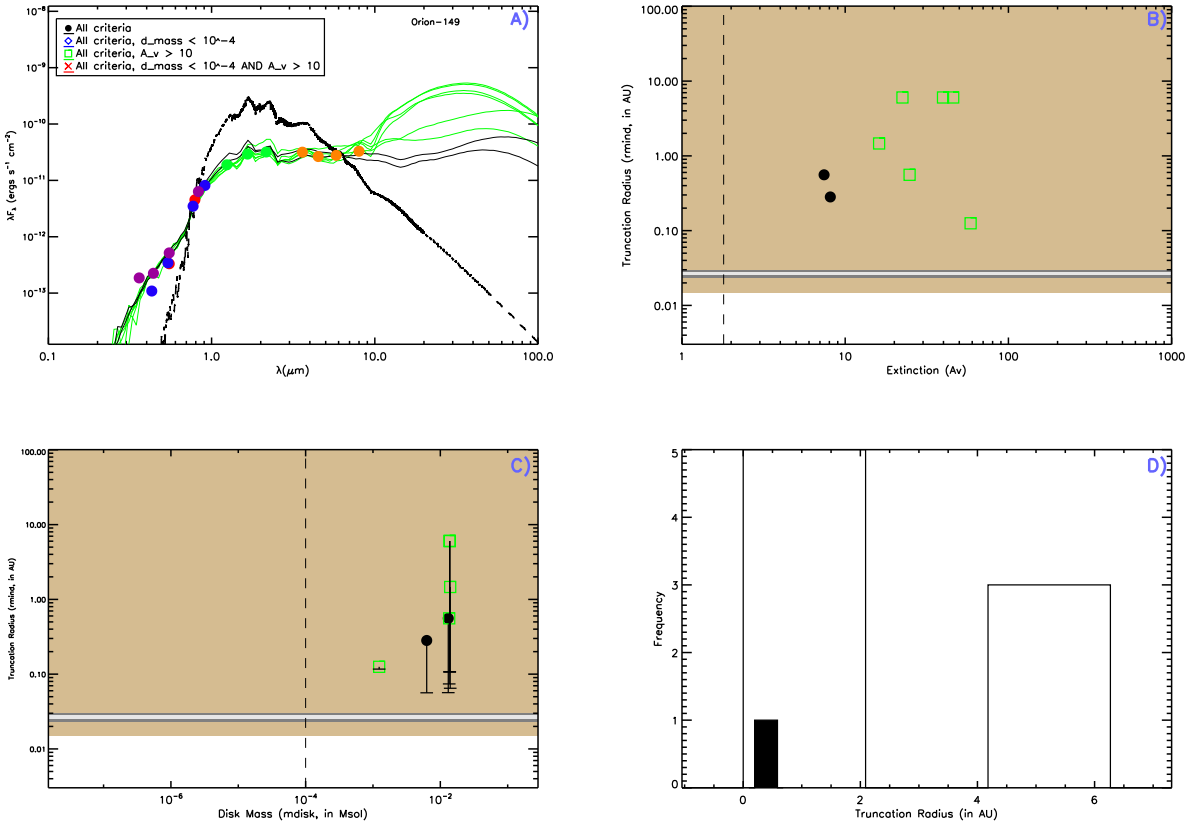

Figure B.18: SED fitting results for ONC #149

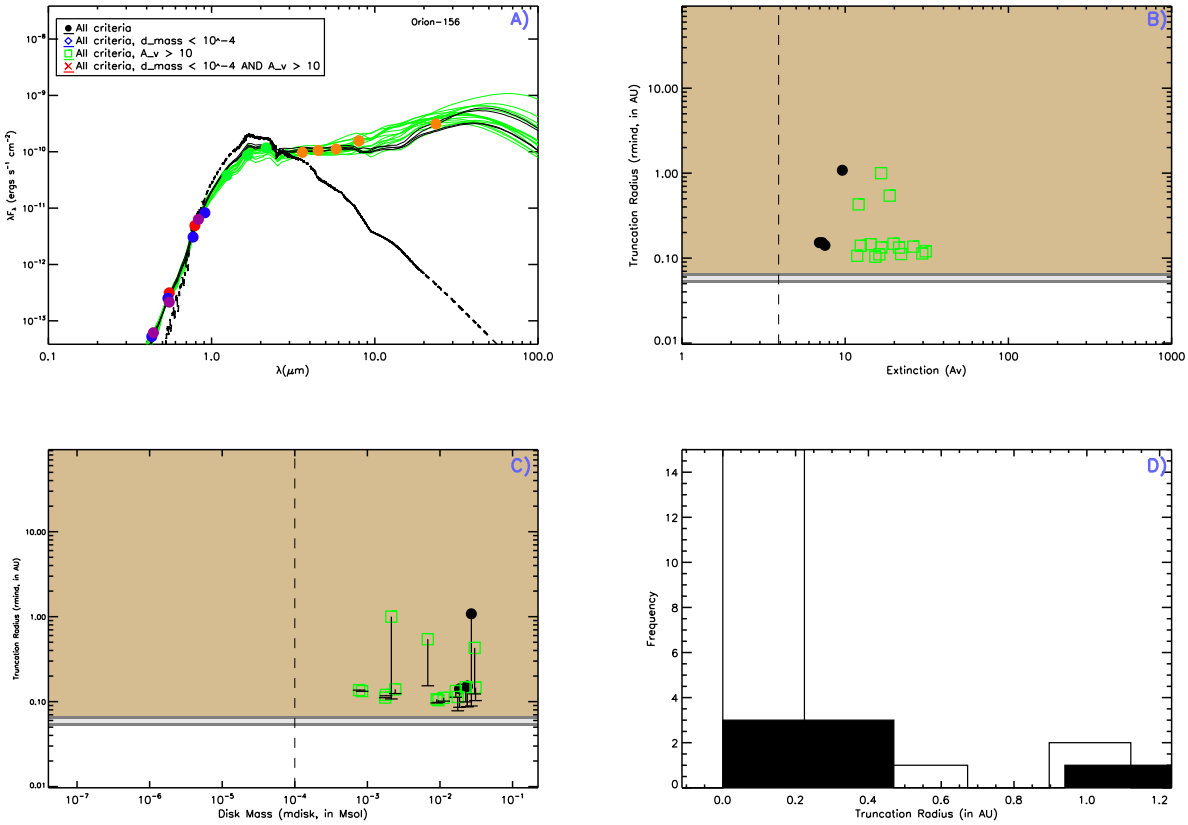

Figure B.19: SED fitting results for ONC #156

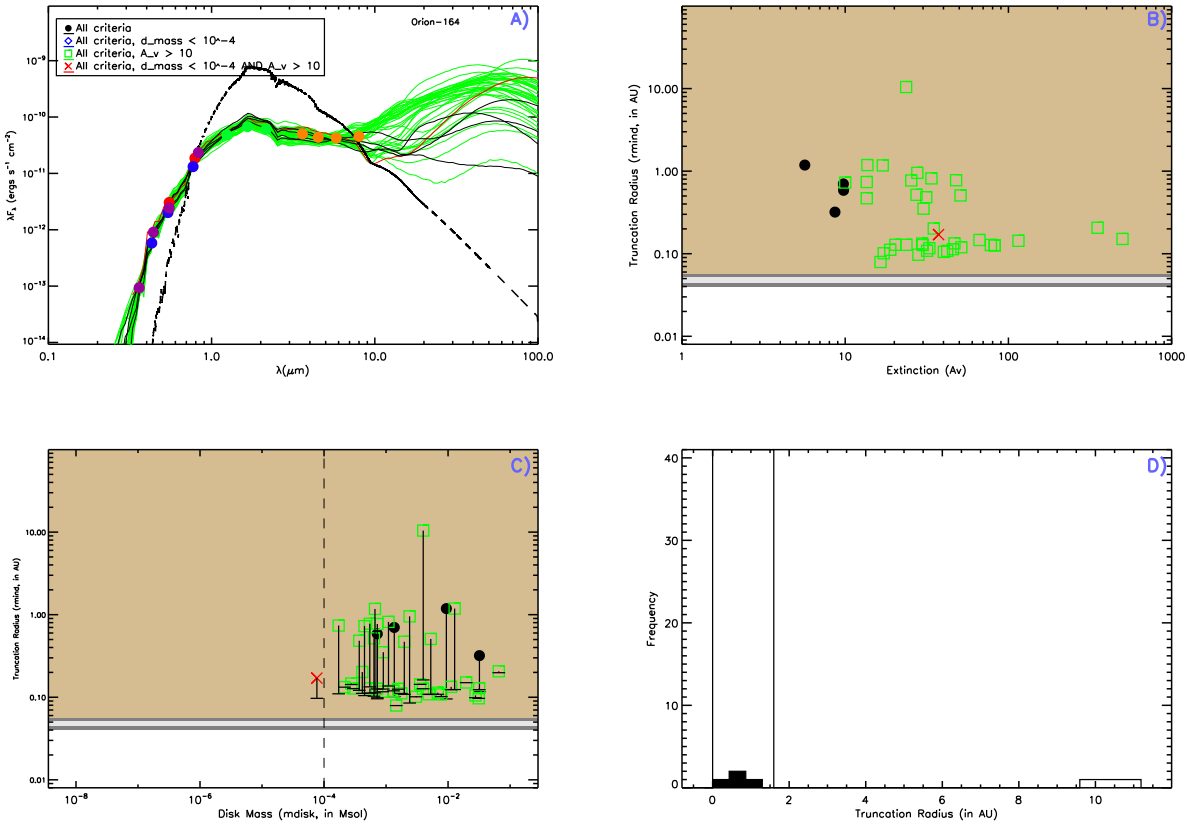

Figure B.20: SED fitting results for ONC #164

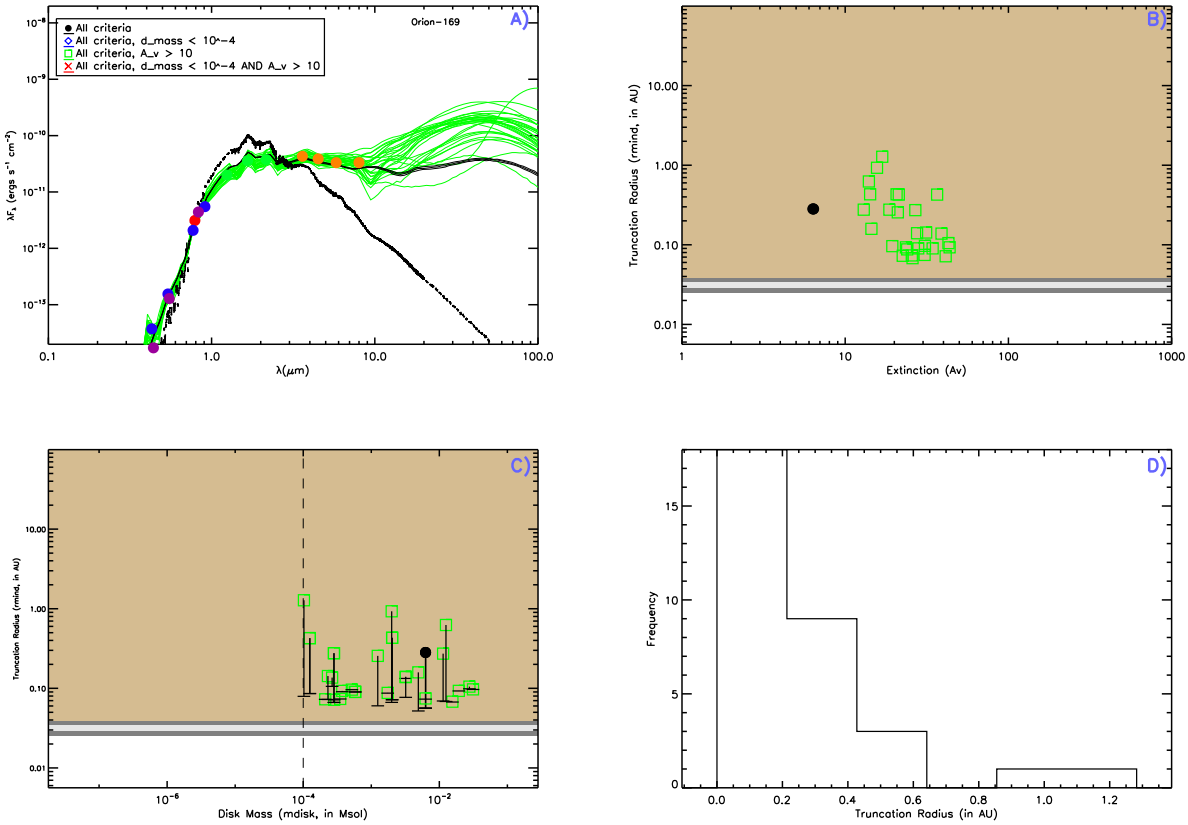

Figure B.21: SED fitting results for ONC #169

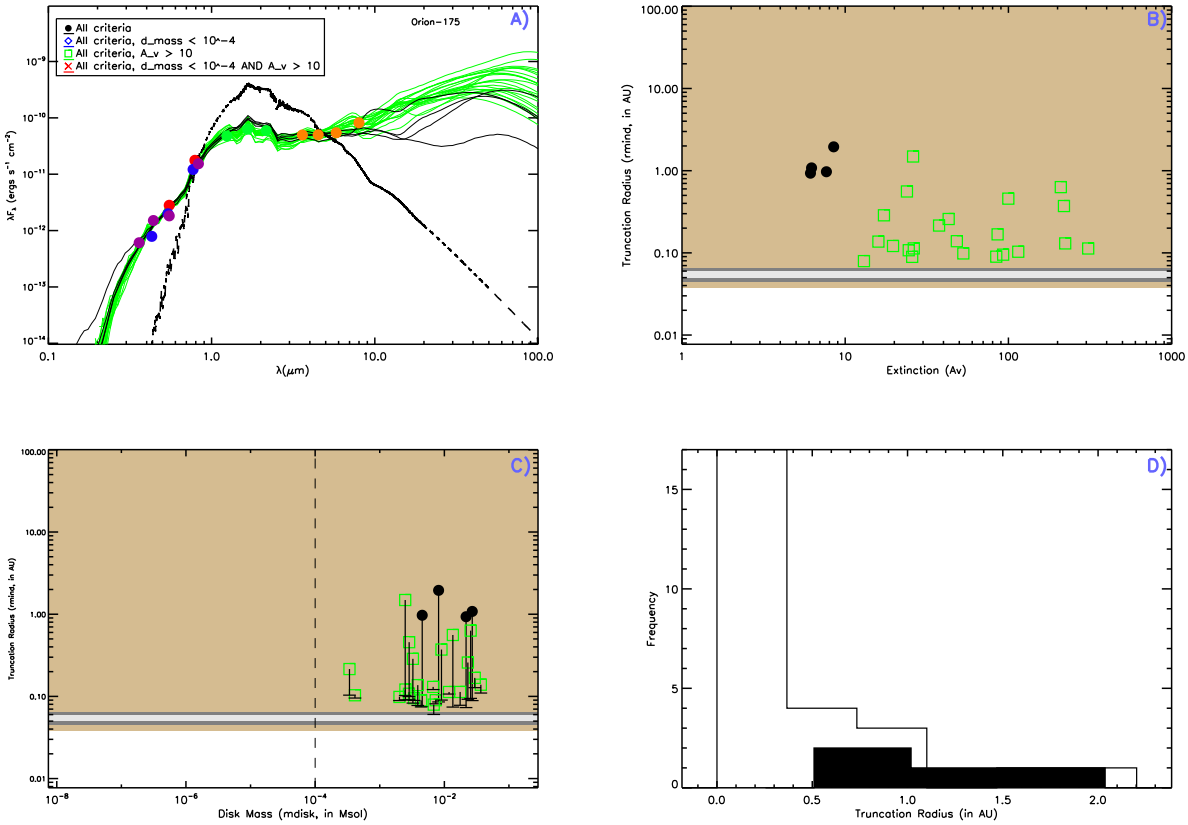

Figure B.22: SED fitting results for ONC #175

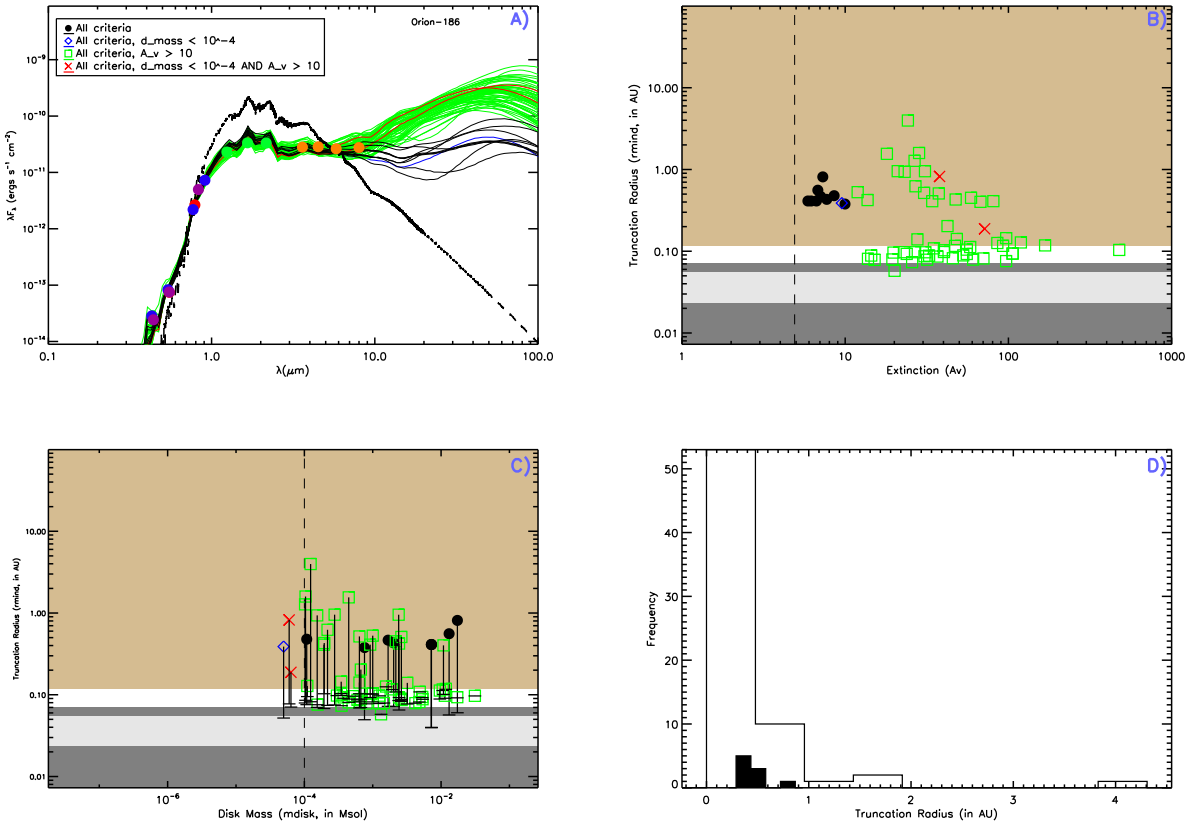

Figure B.23: SED fitting results for ONC #186

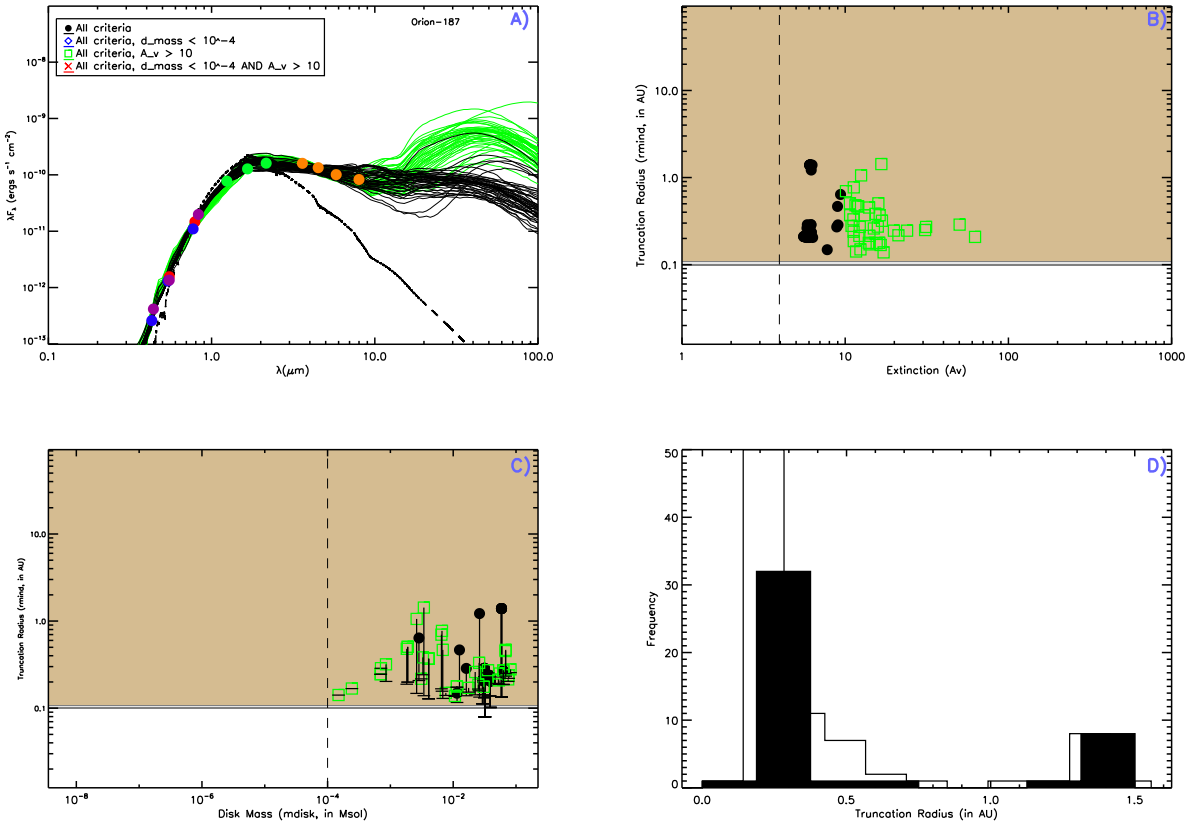

Figure B.24: SED fitting results for ONC #187

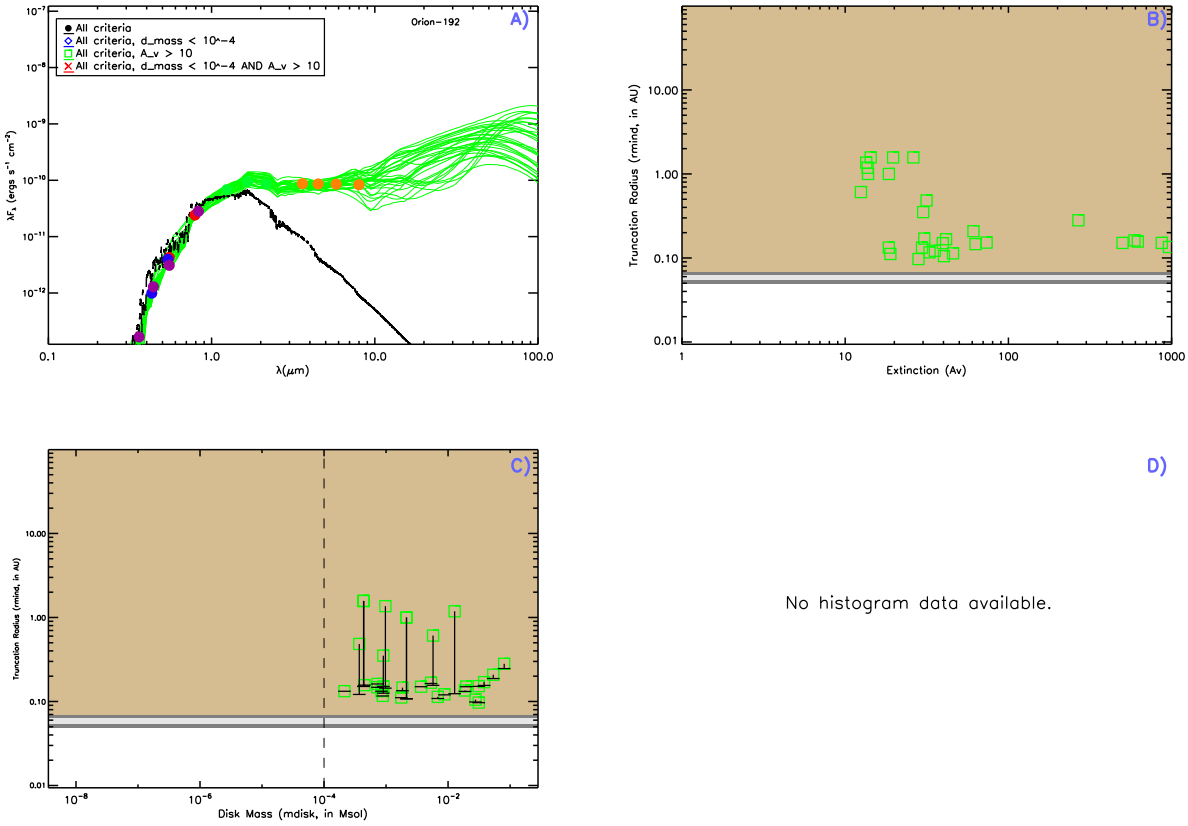

Figure B.25: SED fitting results for ONC #192

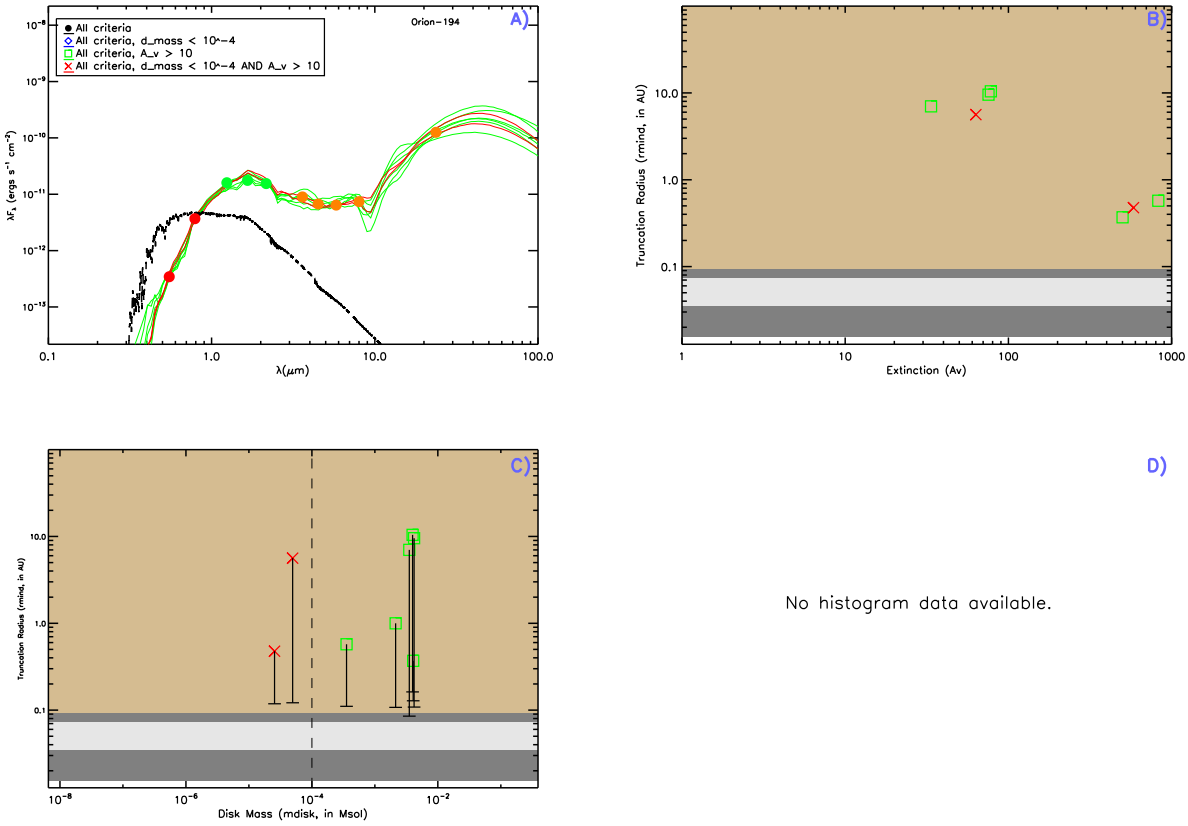

Figure B.26: SED fitting results for ONC #194

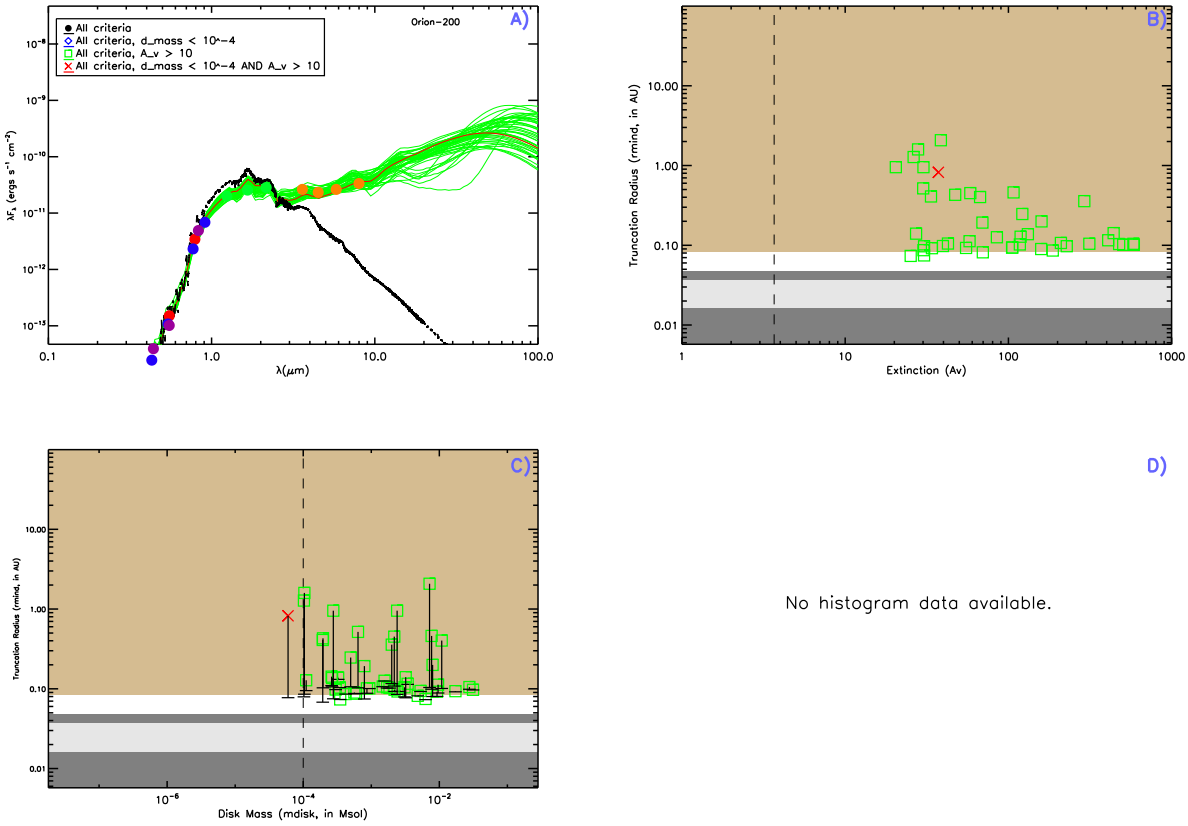

Figure B.27: SED fitting results for ONC #200

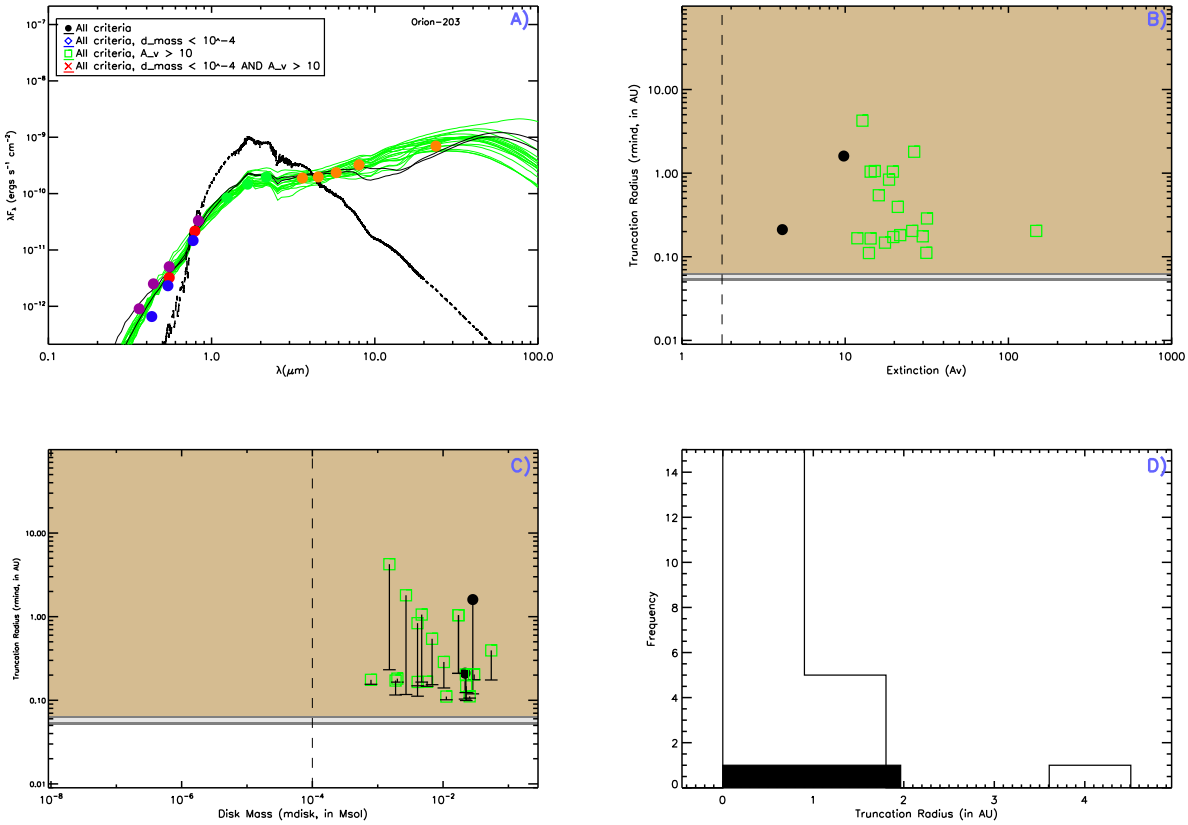

Figure B.28: SED fitting results for ONC #203

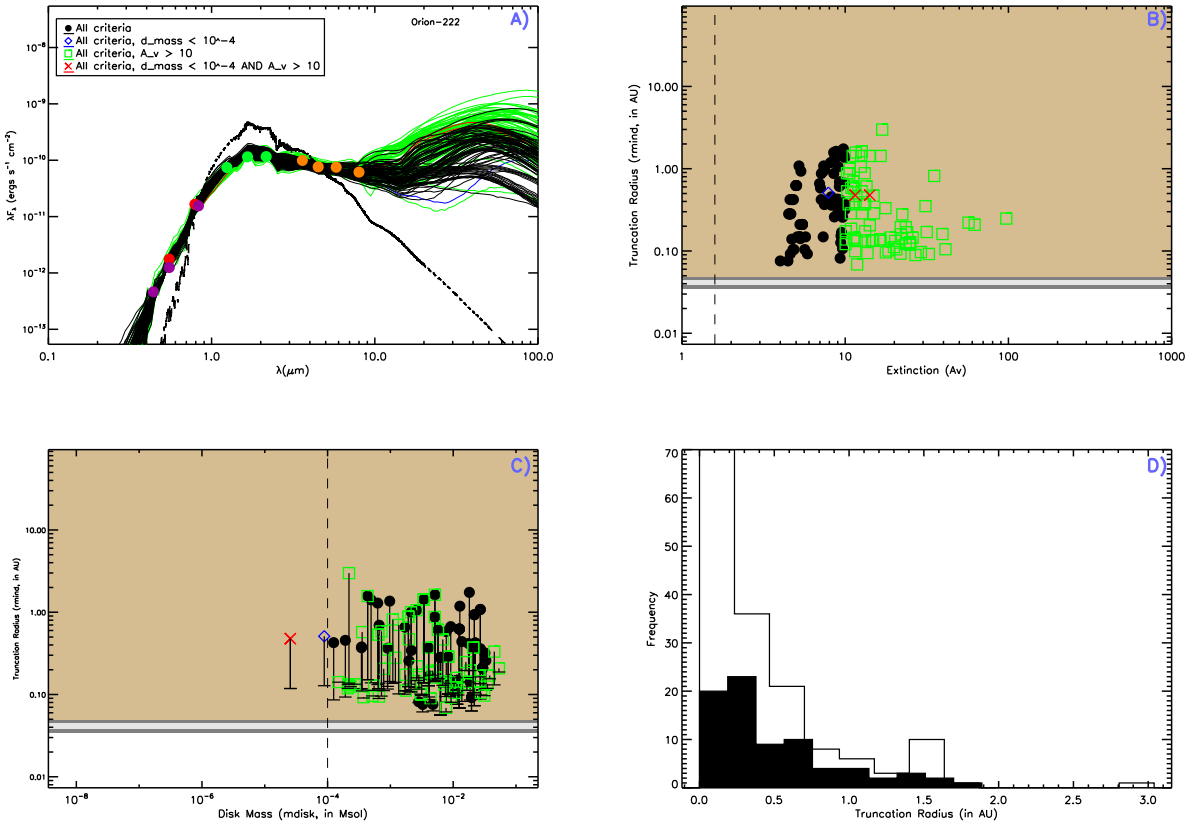

Figure B.29: SED fitting results for ONC #222

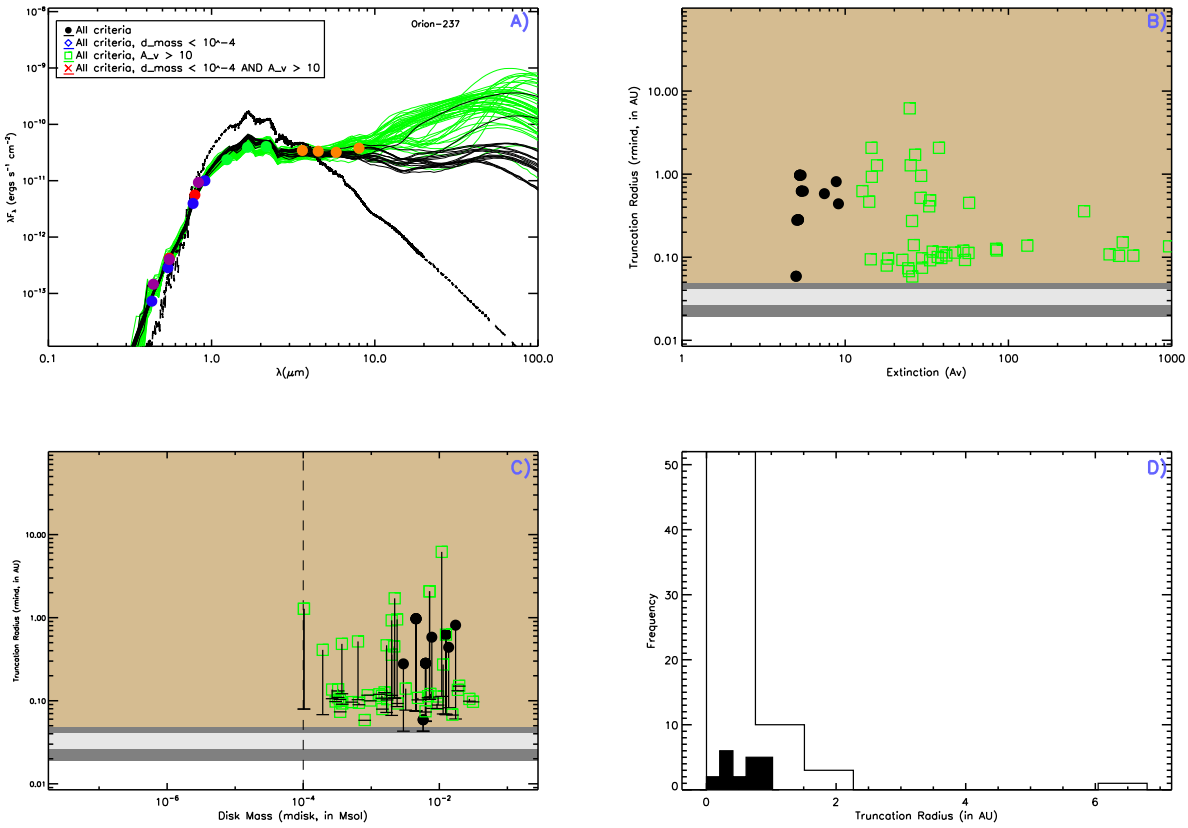

Figure B.30: SED fitting results for ONC #237

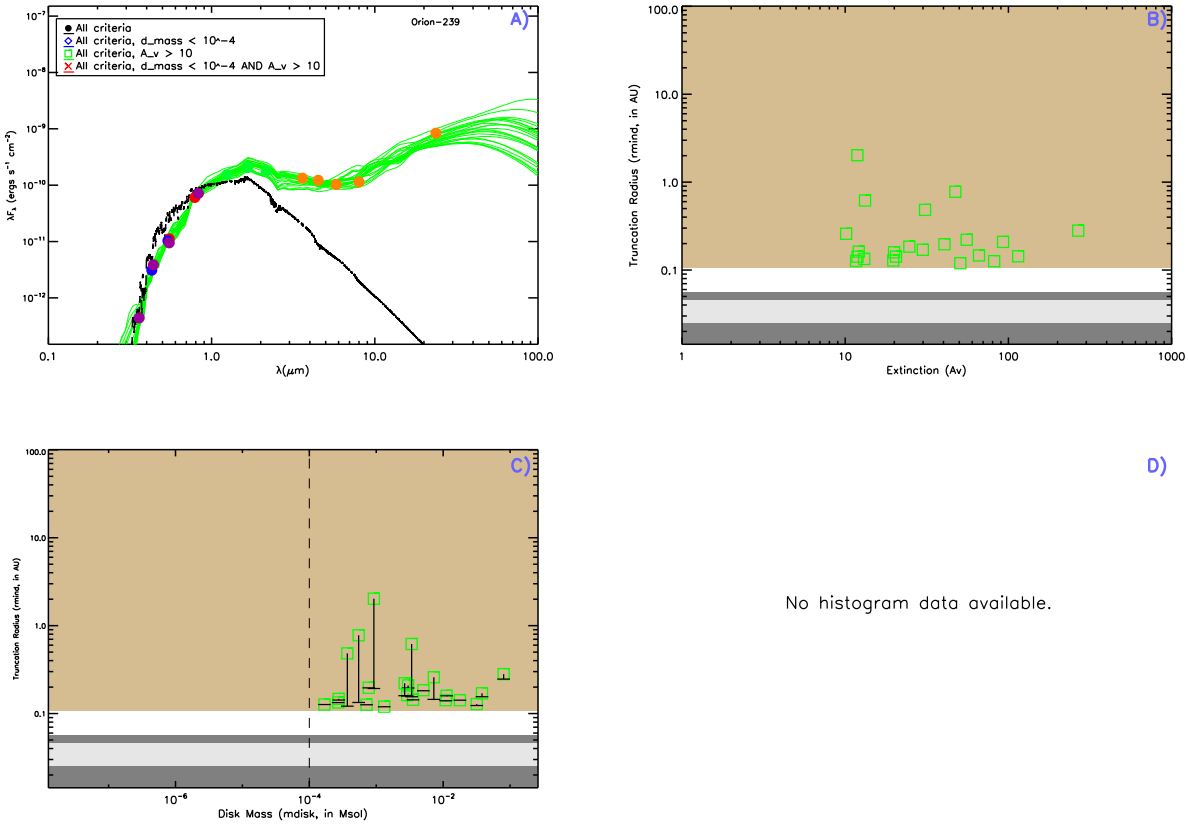

Figure B.31: SED fitting results for ONC #239

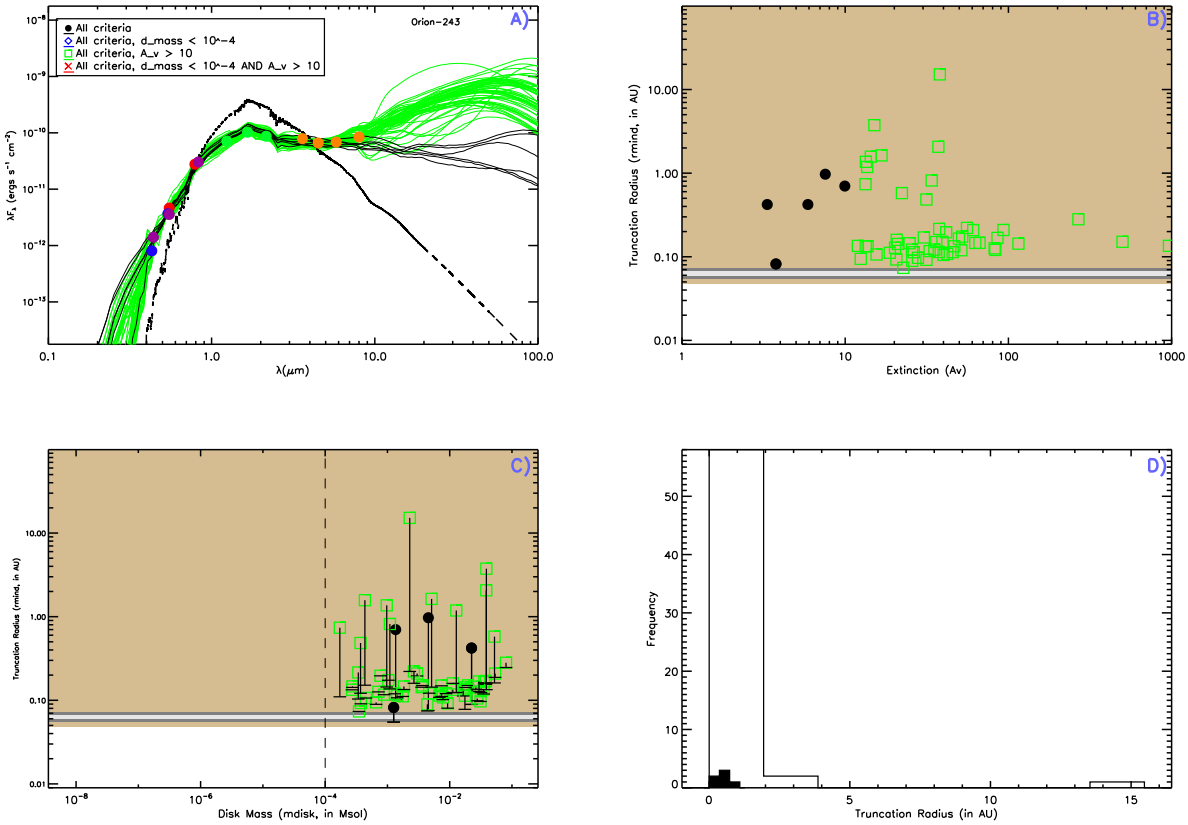

Figure B.32: SED fitting results for ONC #243

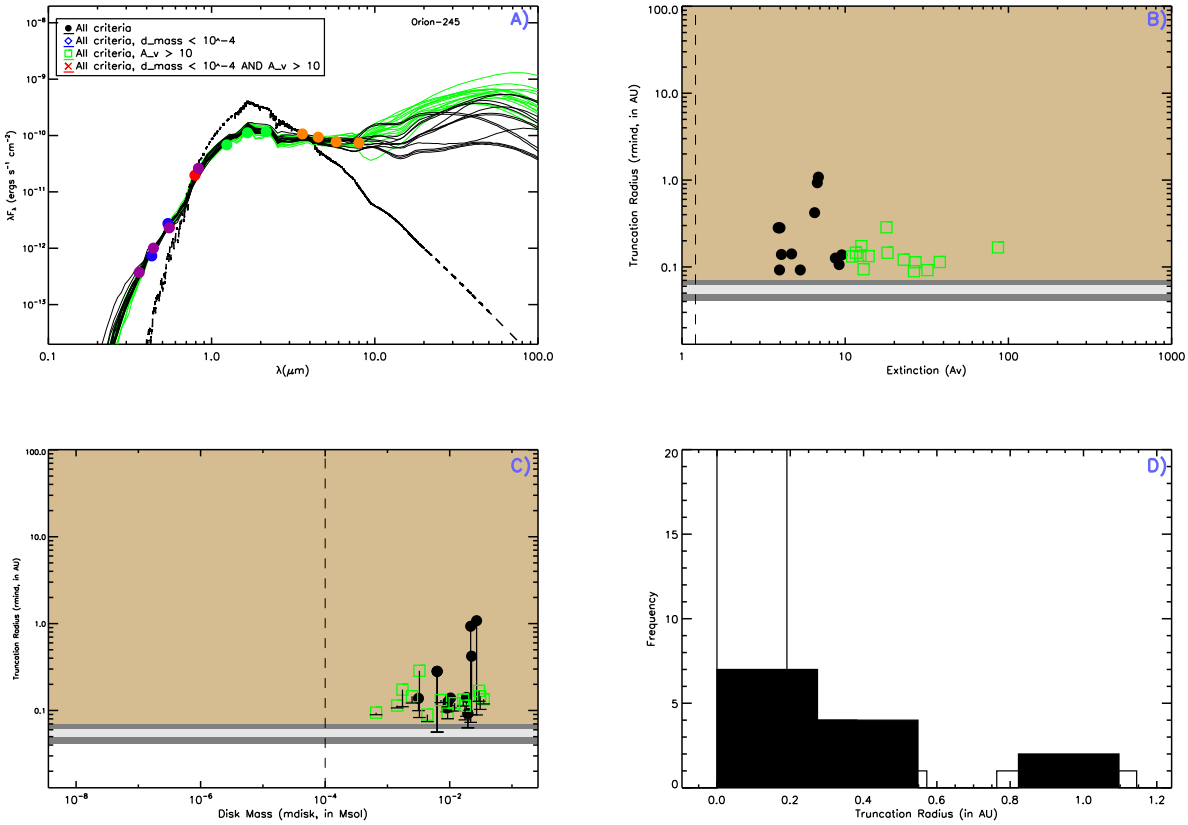

Figure B.33: SED fitting results for ONC #245

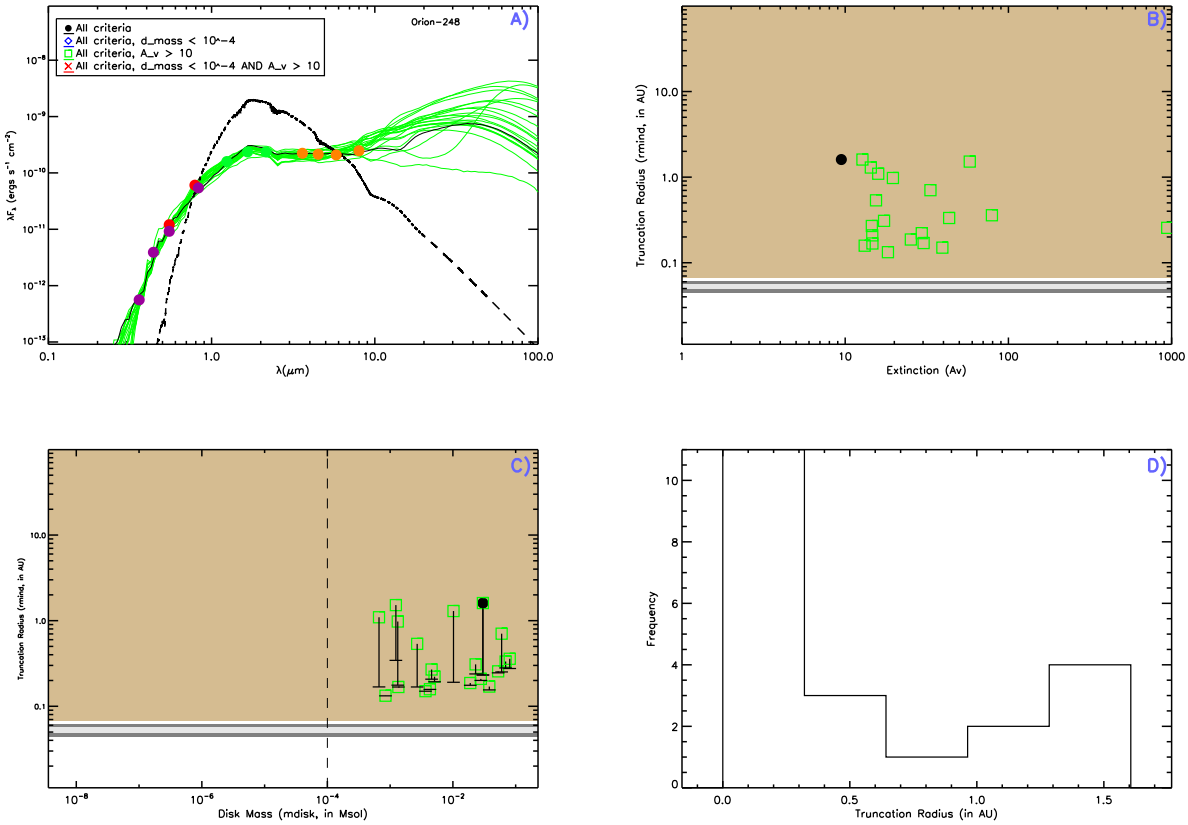

Figure B.34: SED fitting results for ONC #248

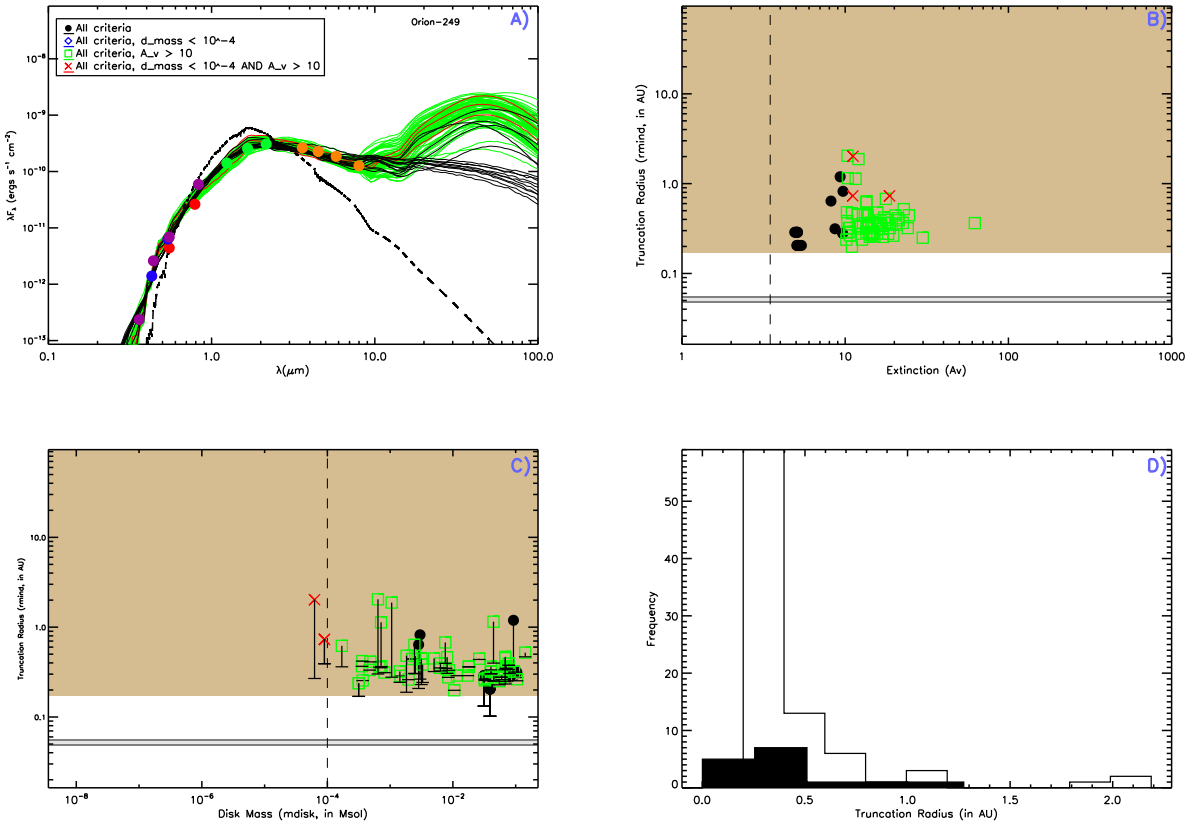

Figure B.35: SED fitting results for ONC #249

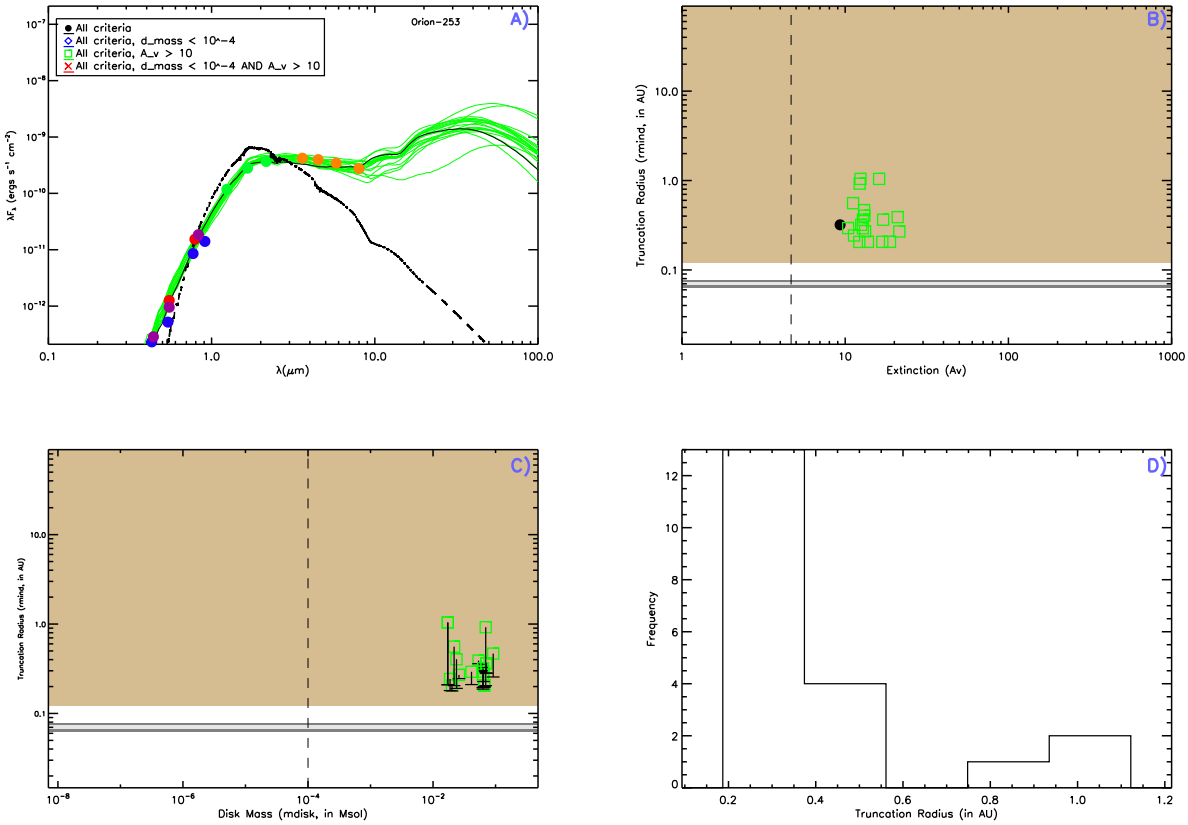

Figure B.36: SED fitting results for ONC #253

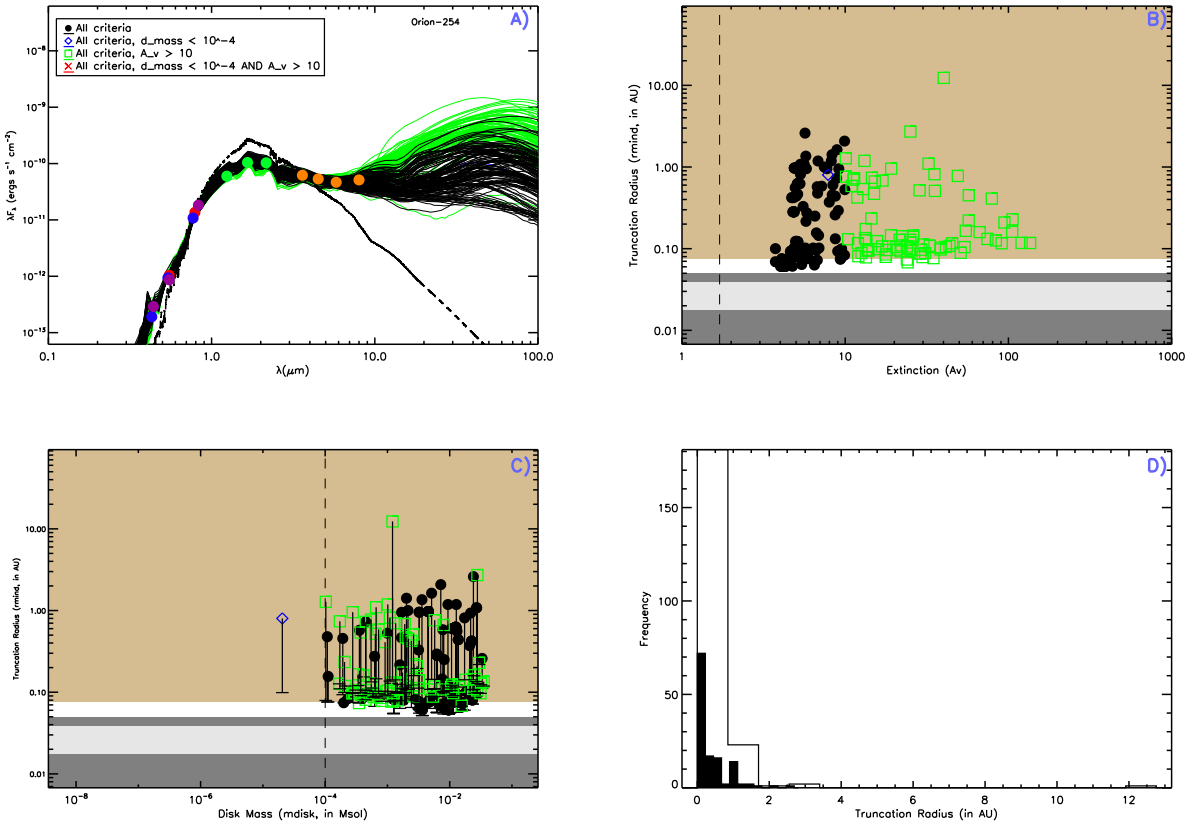

Figure B.37: SED fitting results for ONC #254

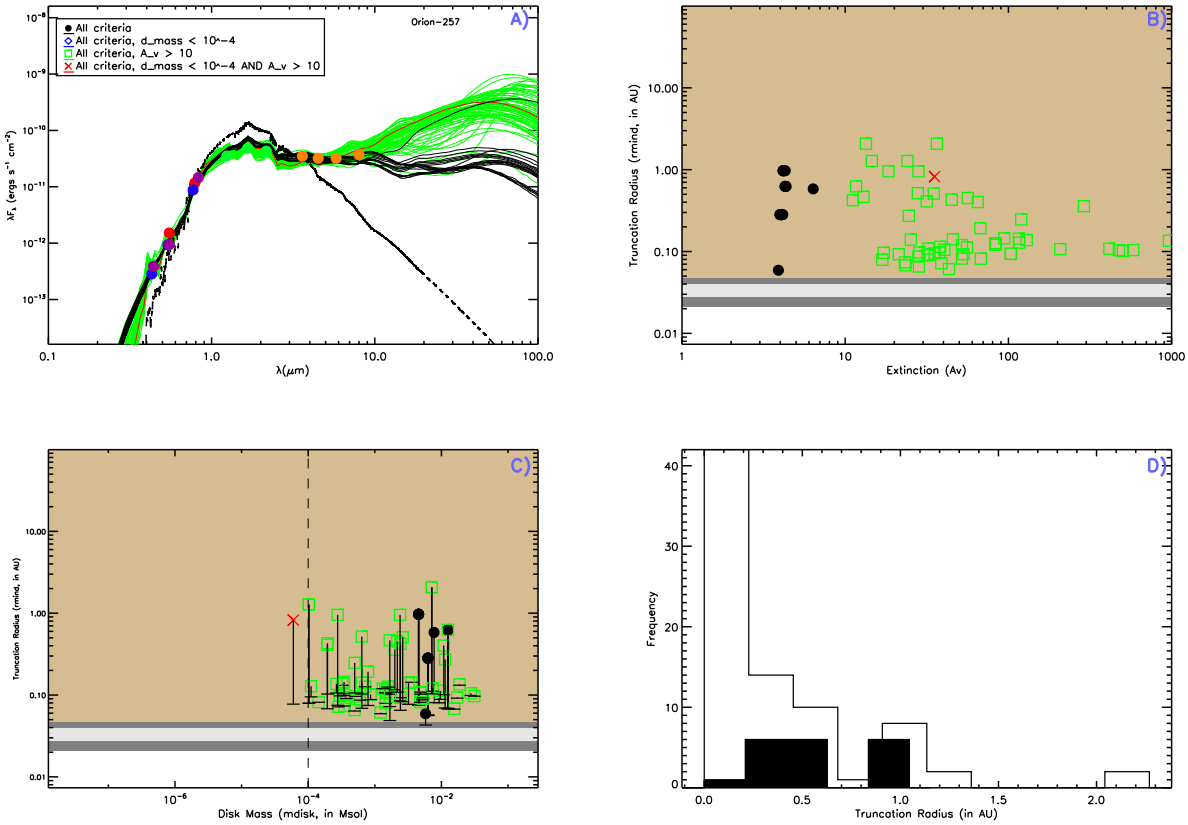

Figure B.38: SED fitting results for ONC #257

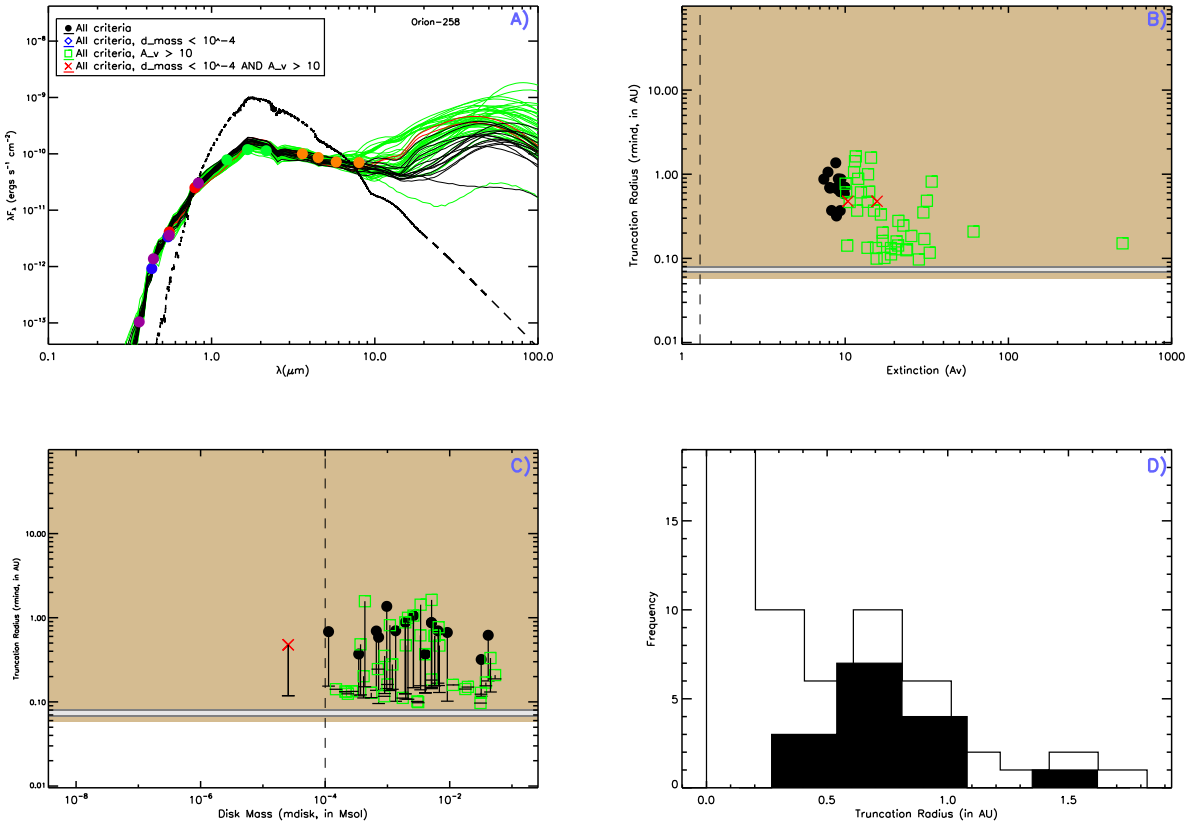

Figure B.39: SED fitting results for ONC #258

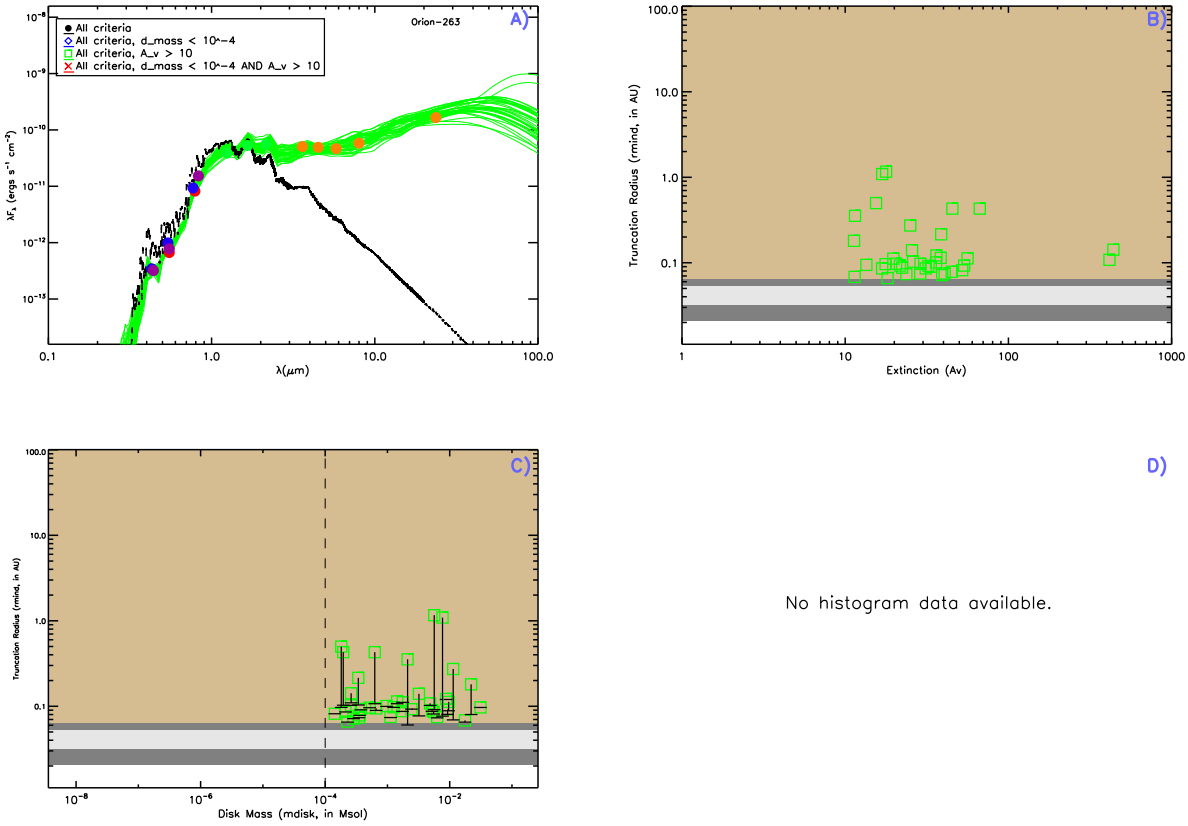

Figure B.40: SED fitting results for ONC #263

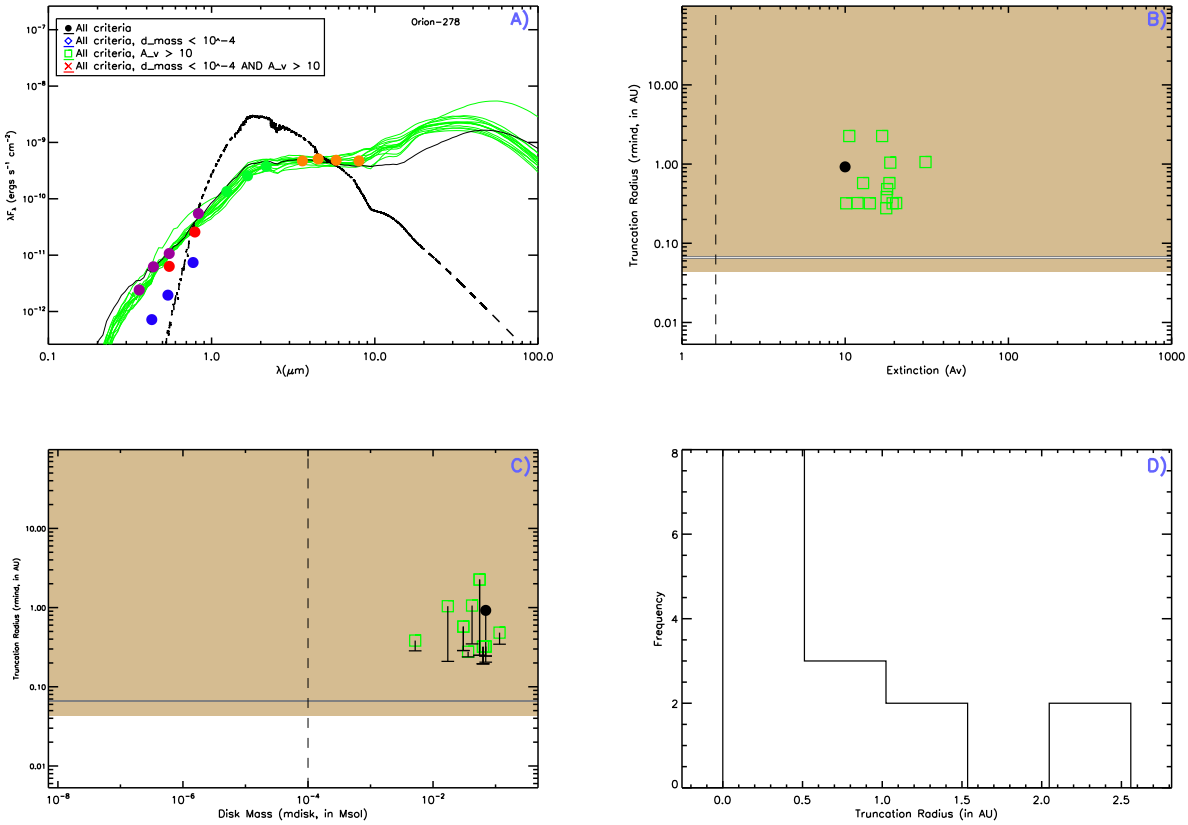

Figure B.41: SED fitting results for ONC #278

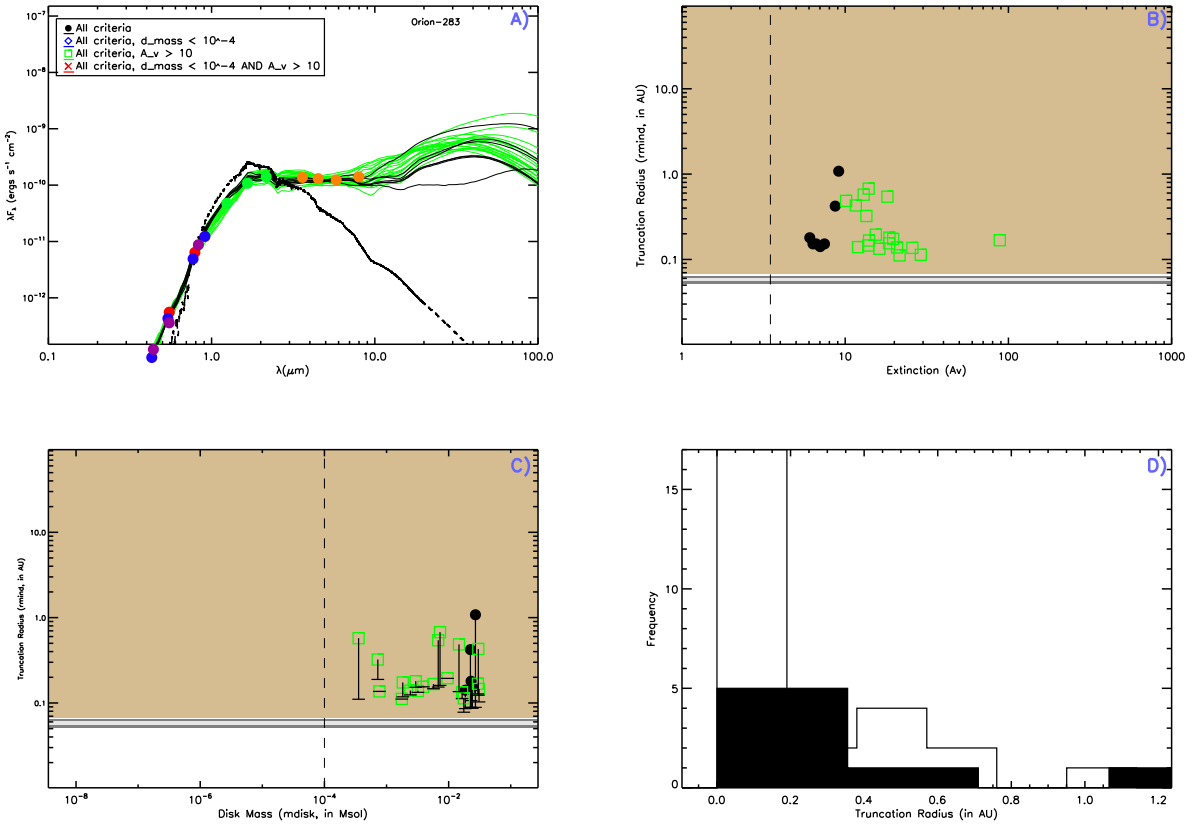

Figure B.42: SED fitting results for ONC #283

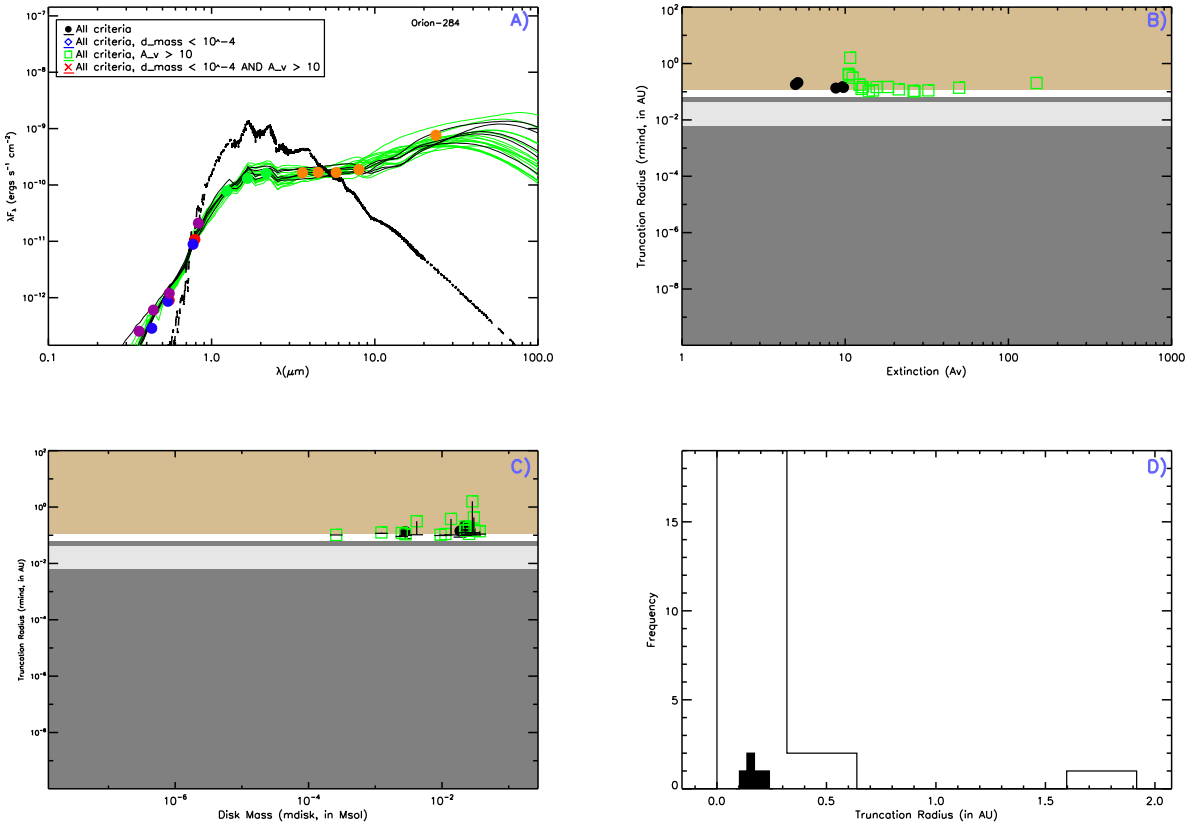

Figure B.43: SED fitting results for ONC #284

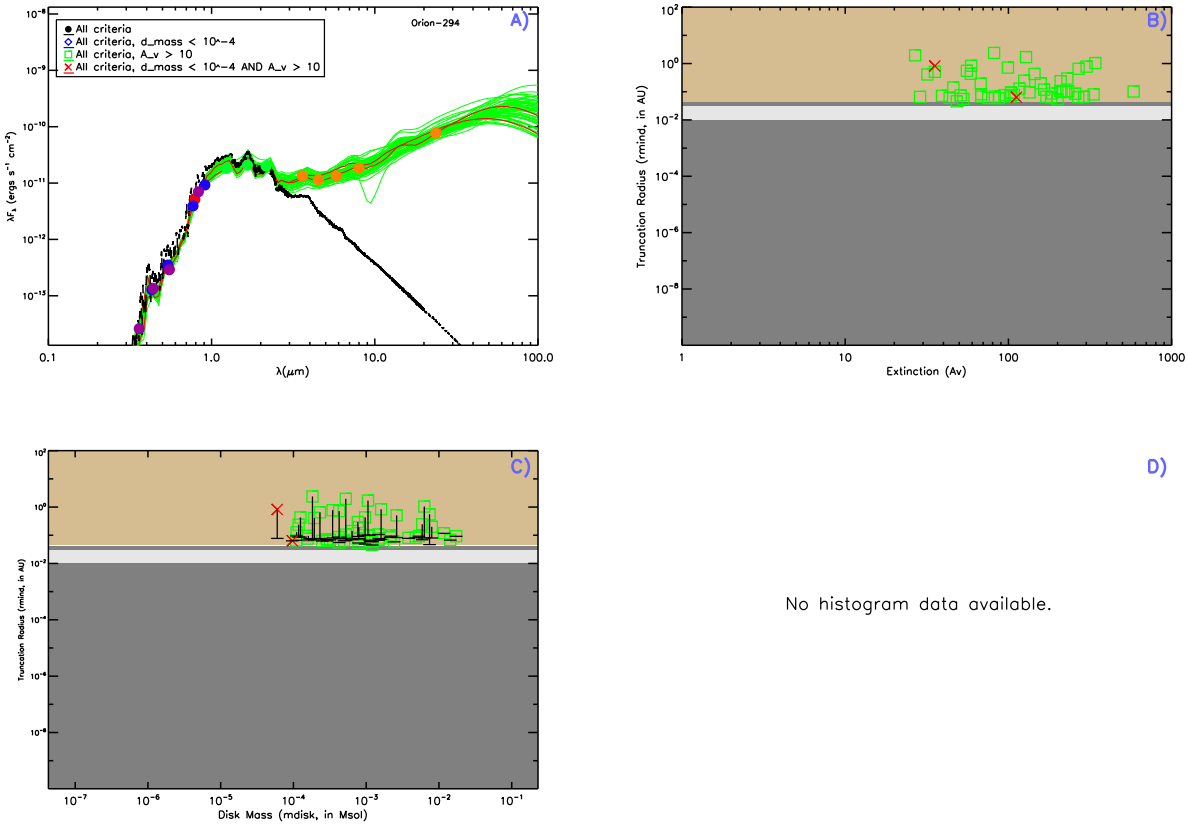

Figure B.44: SED fitting results for ONC #294

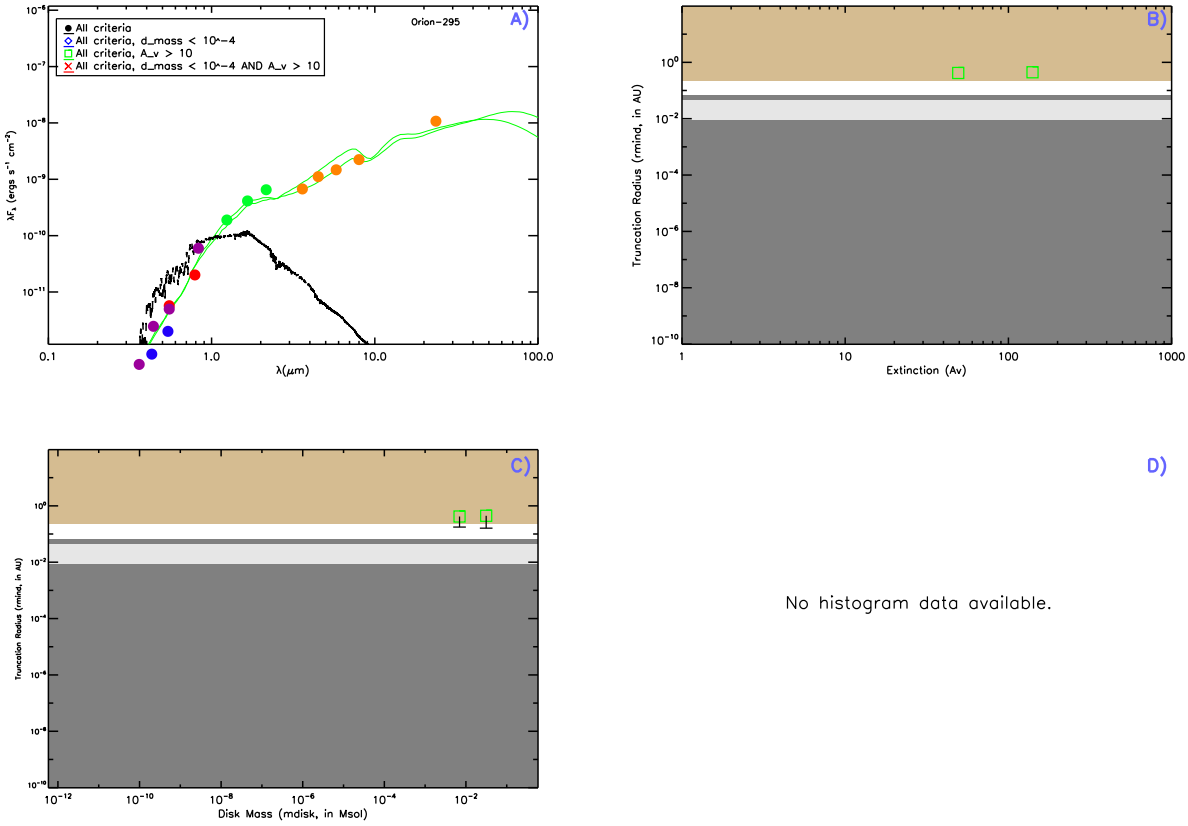

Figure B.45: SED fitting results for ONC #295

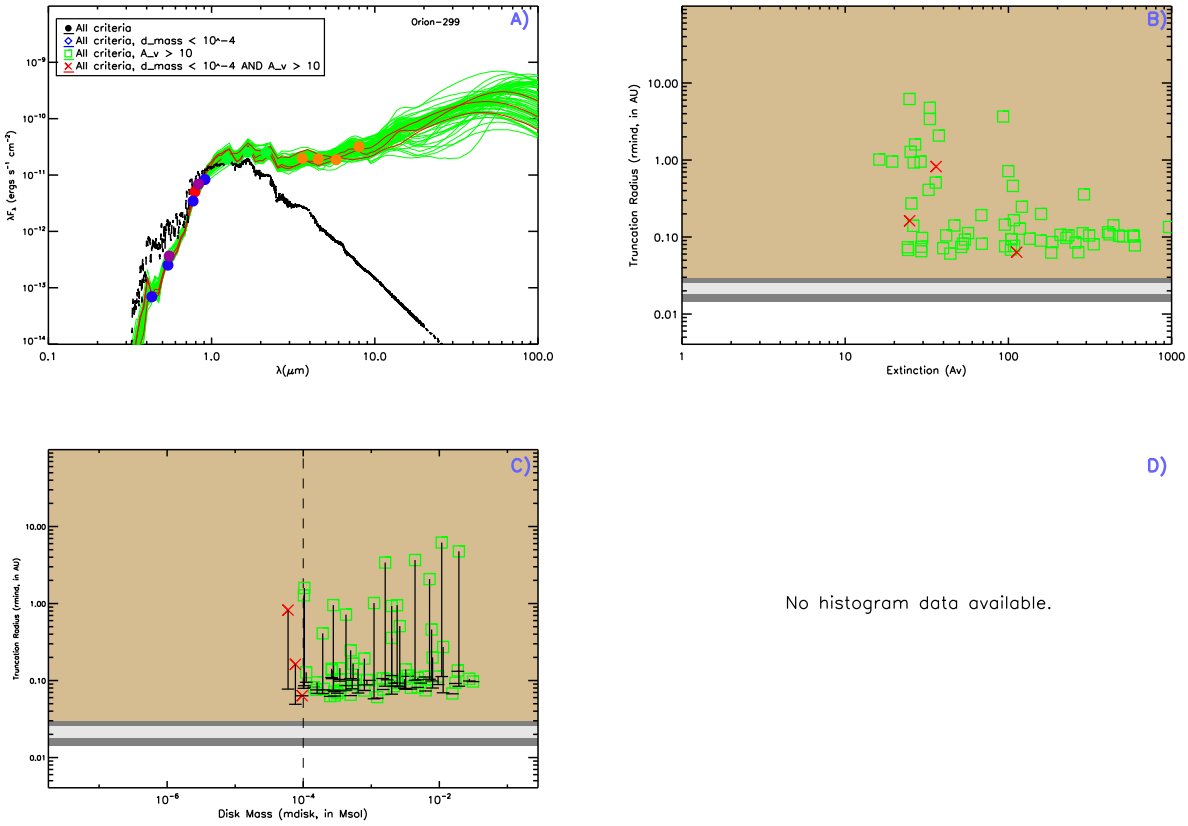

Figure B.46: SED fitting results for ONC #299

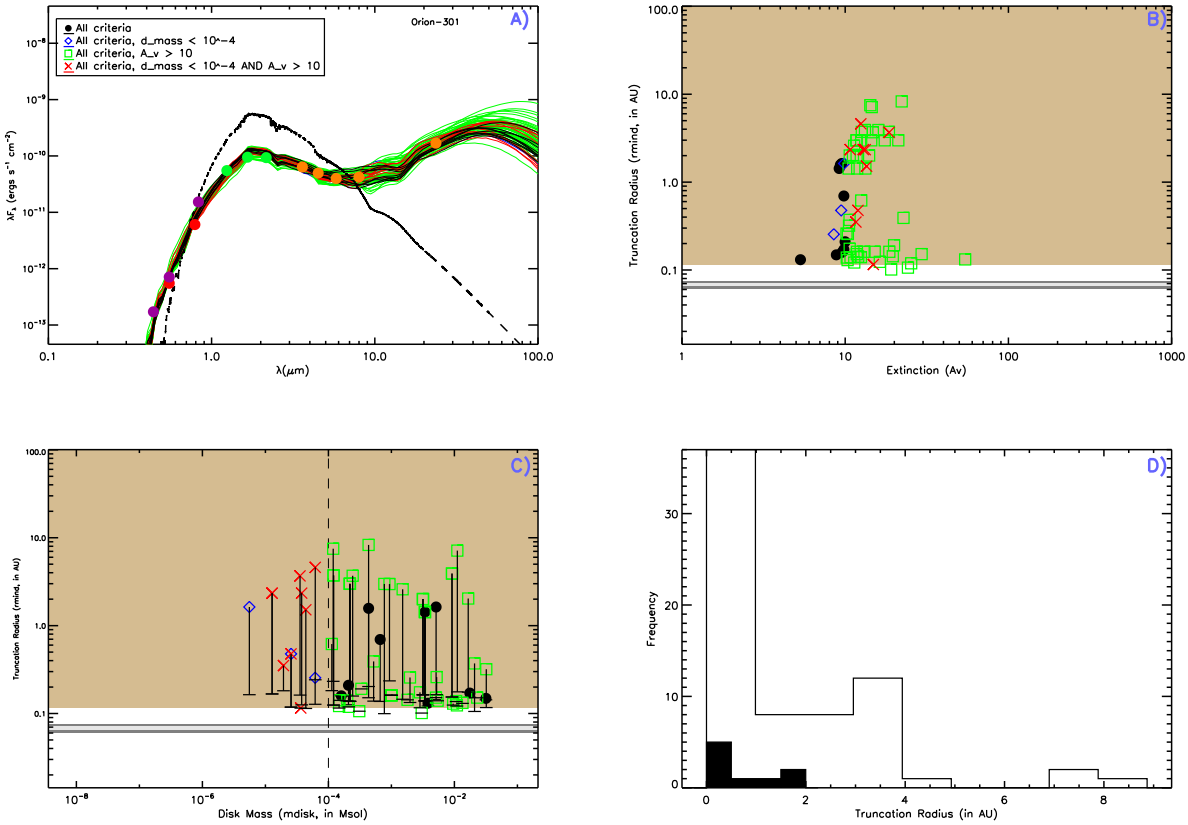

Figure B.47: SED fitting results for ONC #301

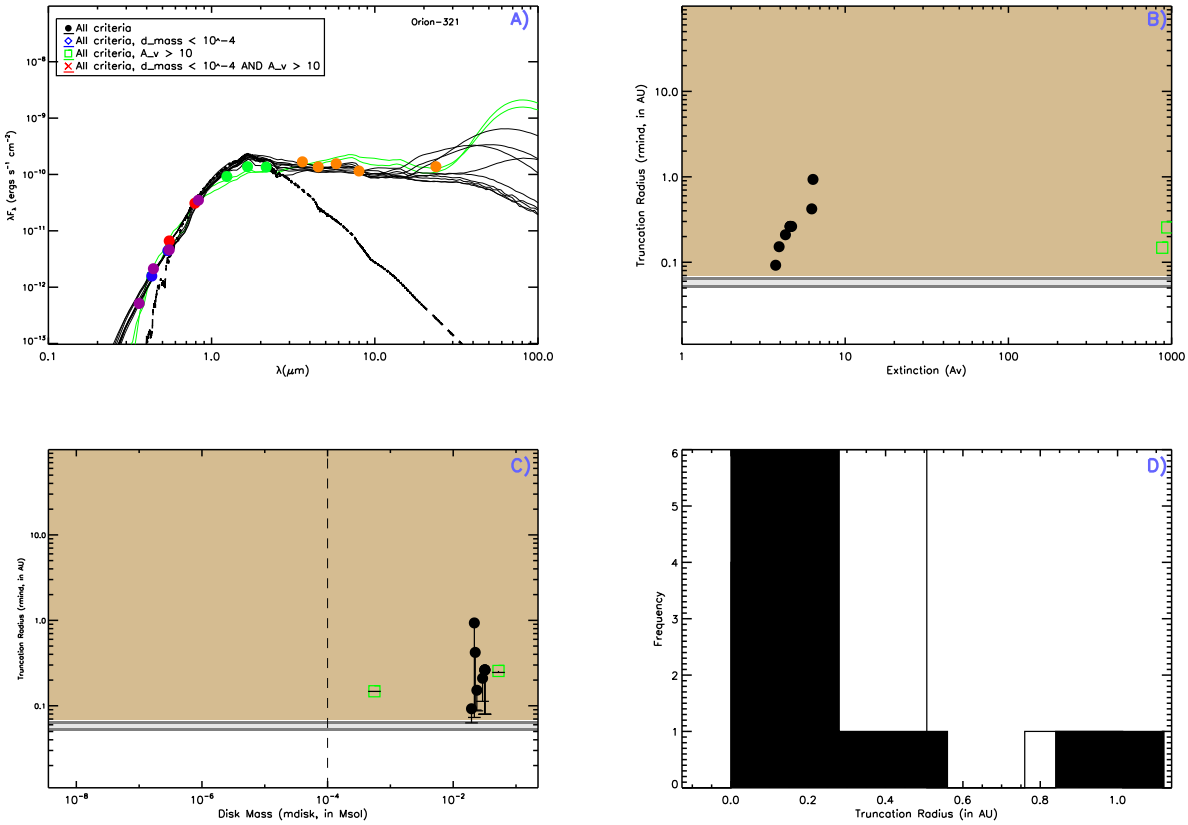

Figure B.48: SED fitting results for ONC #321

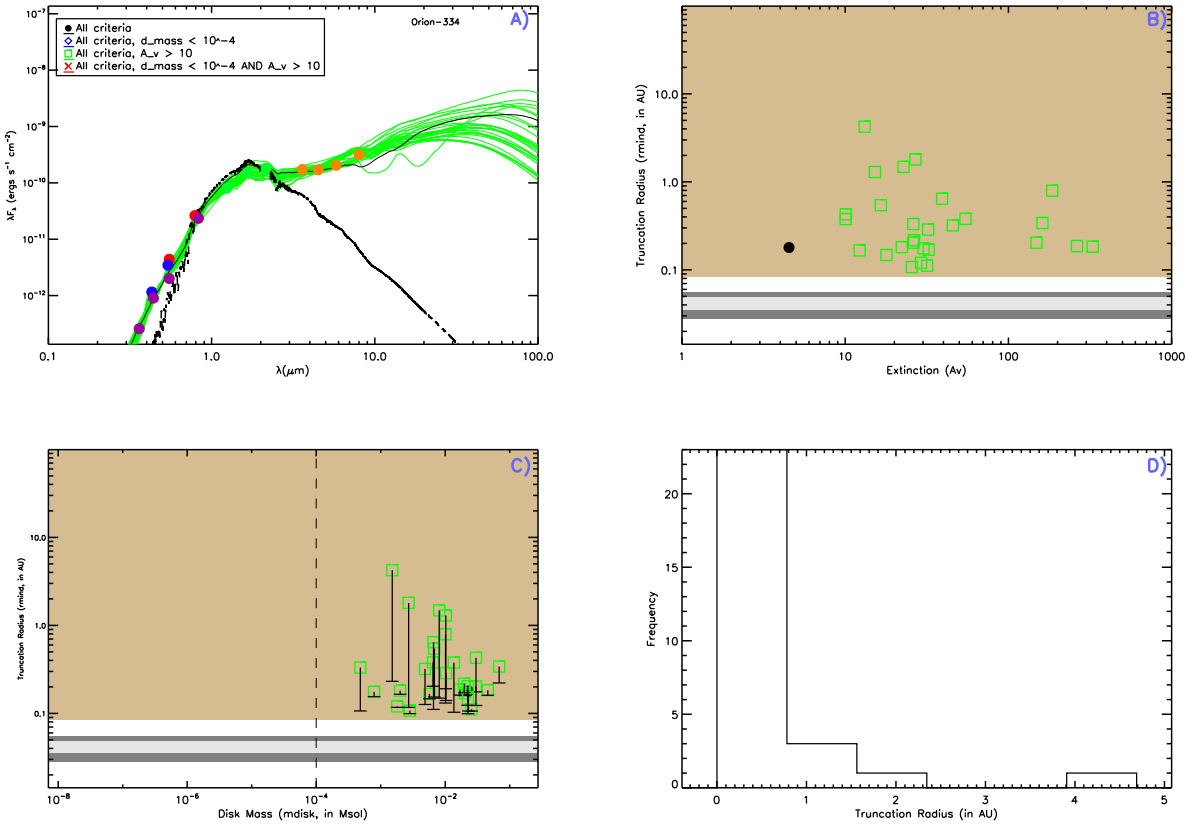

Figure B.49: SED fitting results for ONC #334

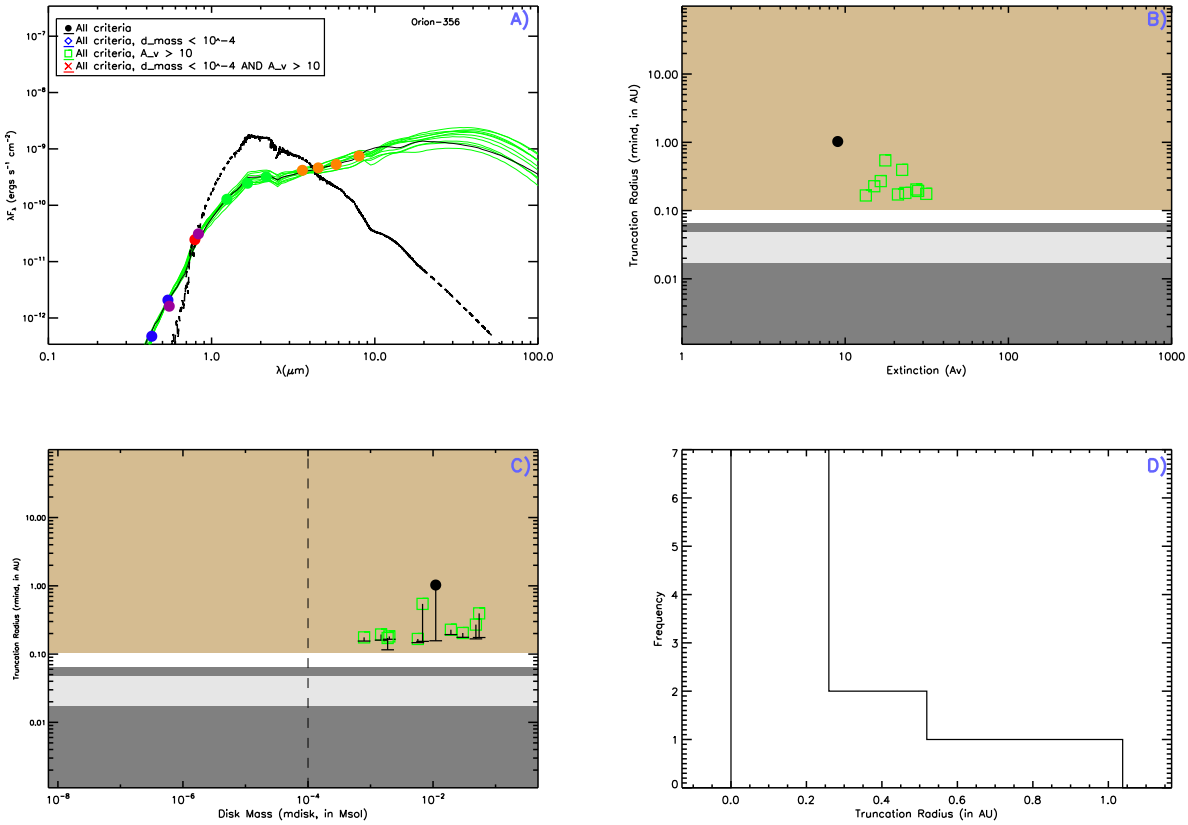

Figure B.50: SED fitting results for ONC #356

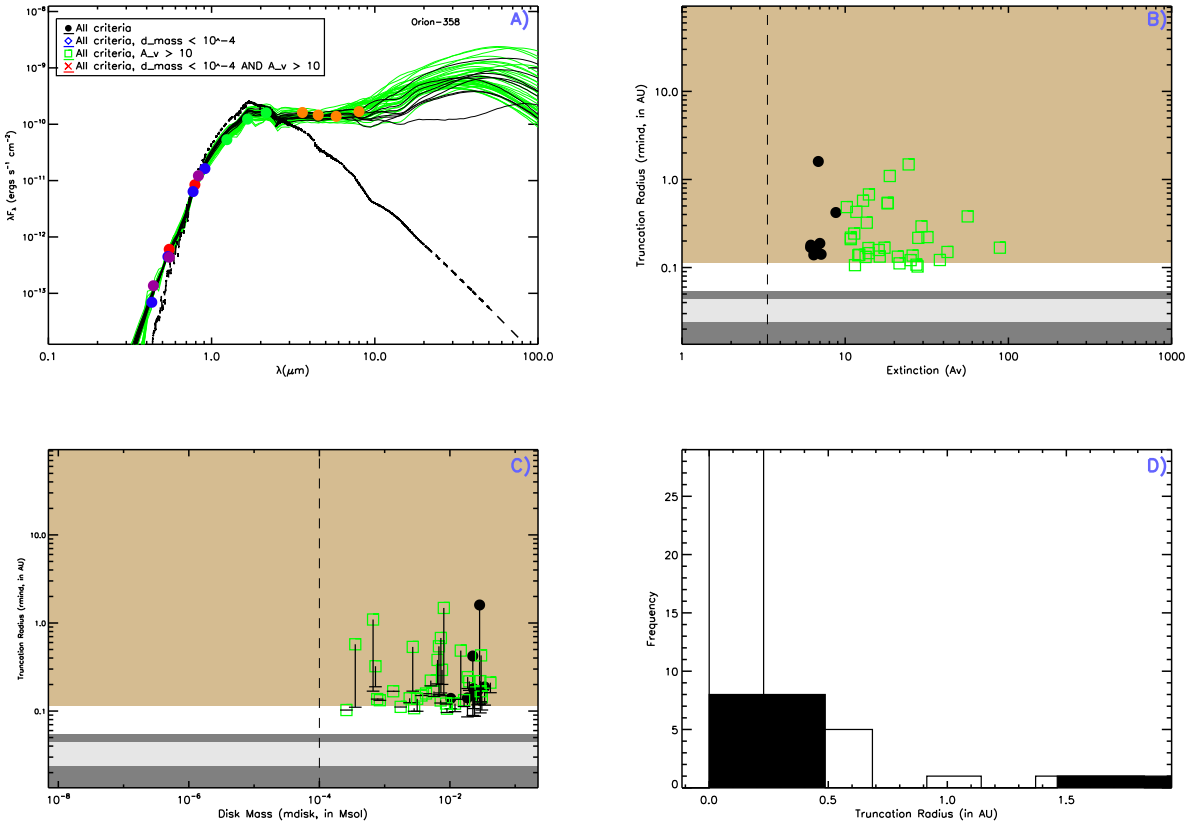

Figure B.51: SED fitting results for ONC #358

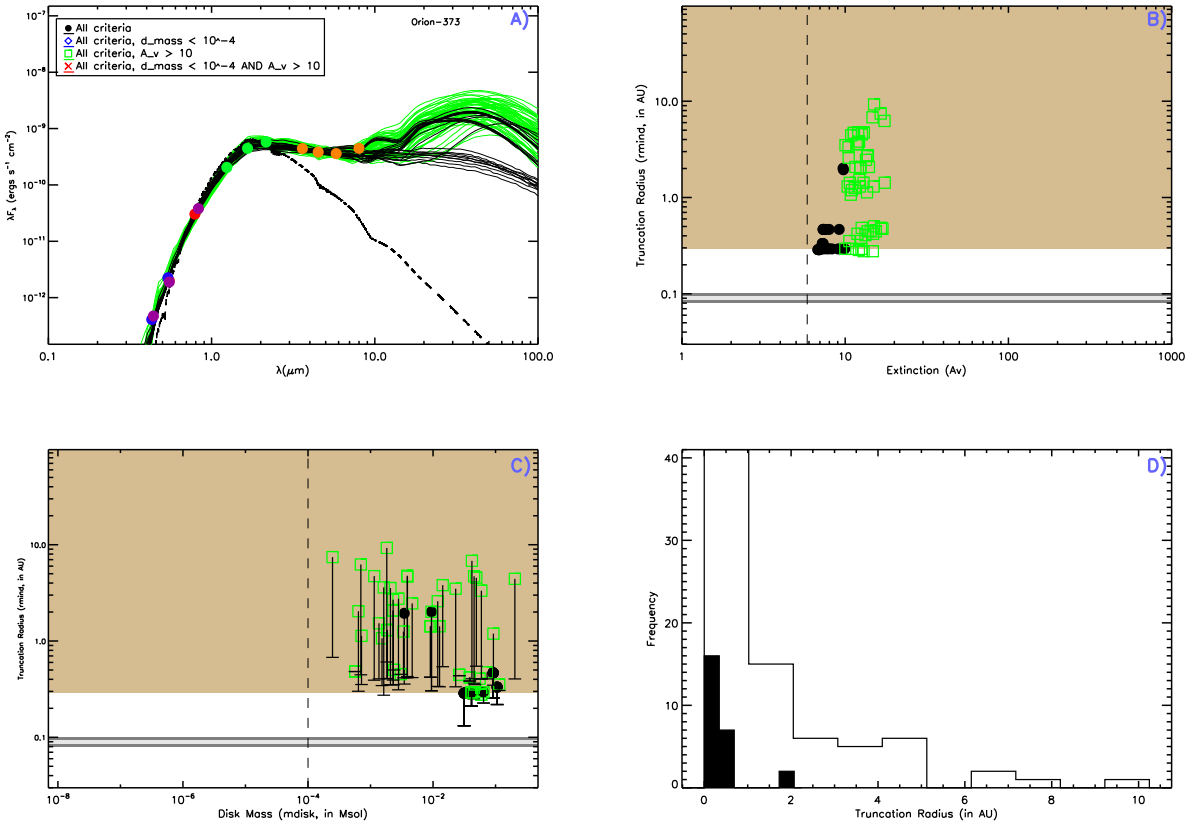

Figure B.52: SED fitting results for ONC #373

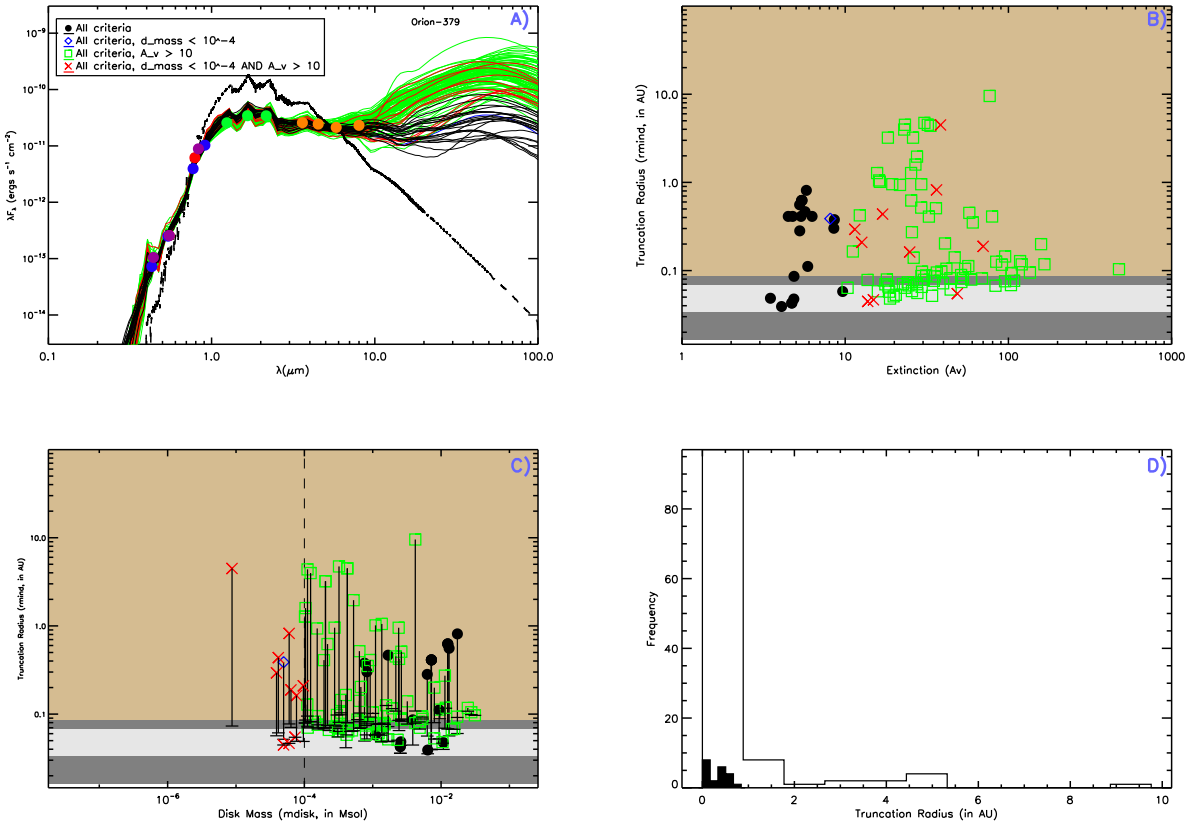

Figure B.53: SED fitting results for ONC #379

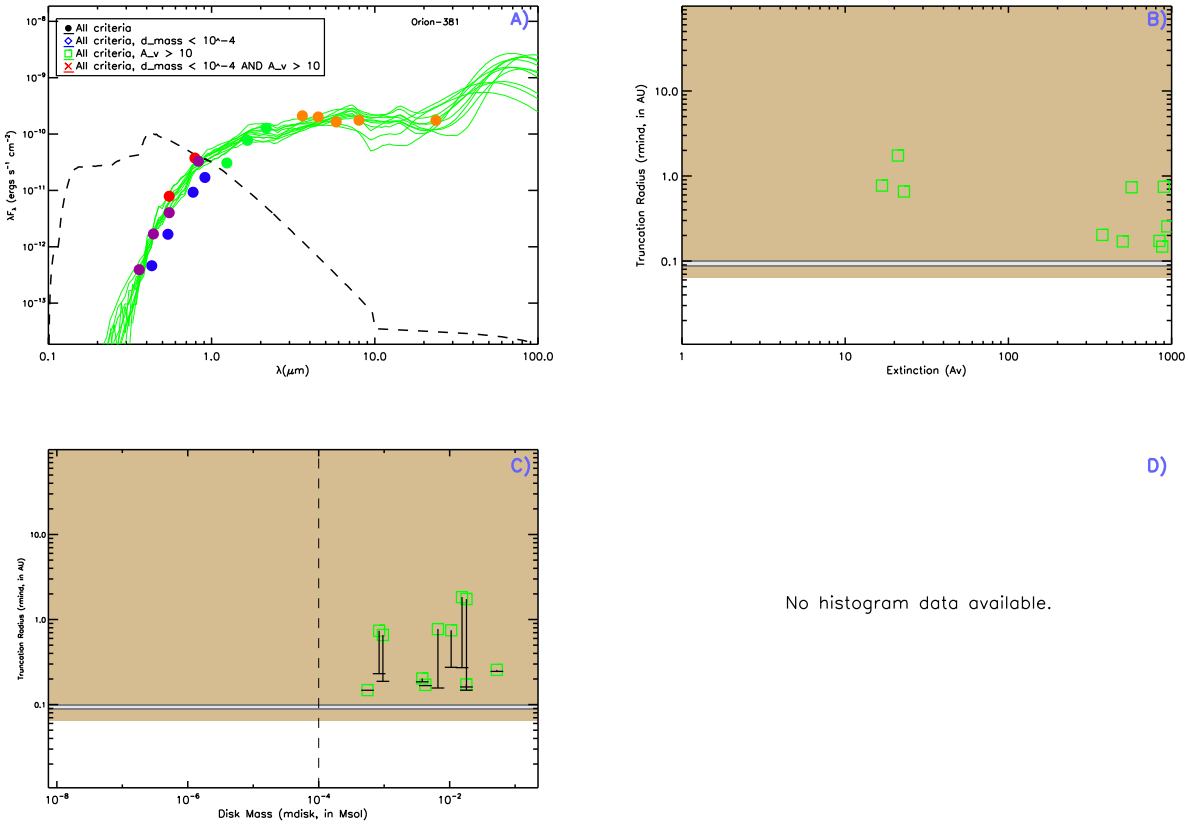

Figure B.54: SED fitting results for ONC #381

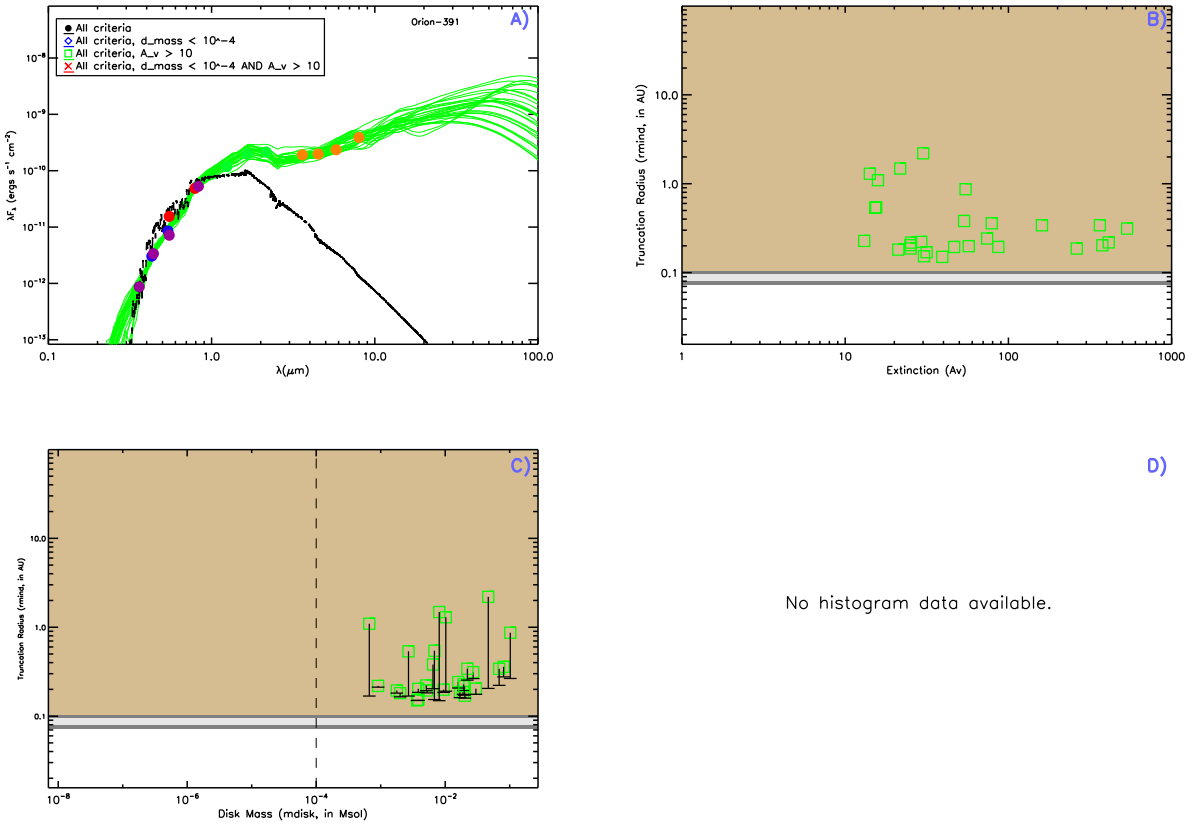

Figure B.55: SED fitting results for ONC #391

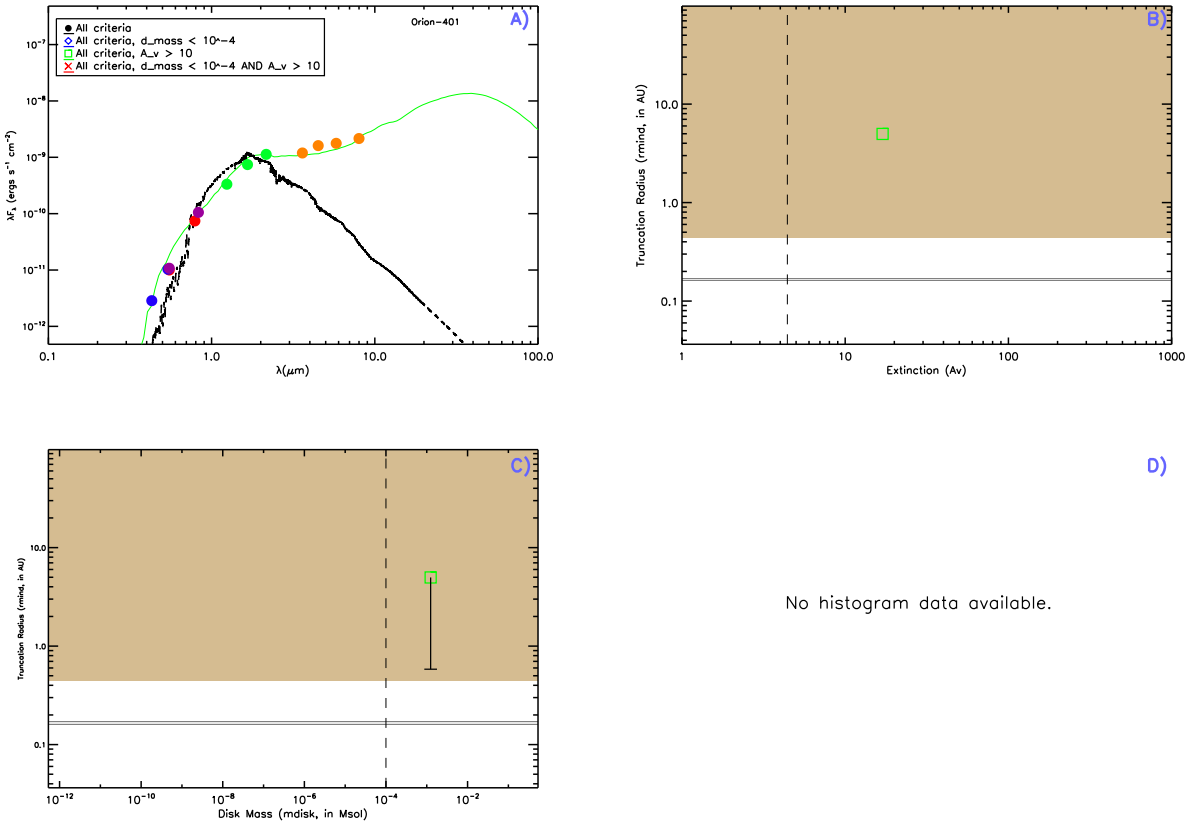

Figure B.56: SED fitting results for ONC #401

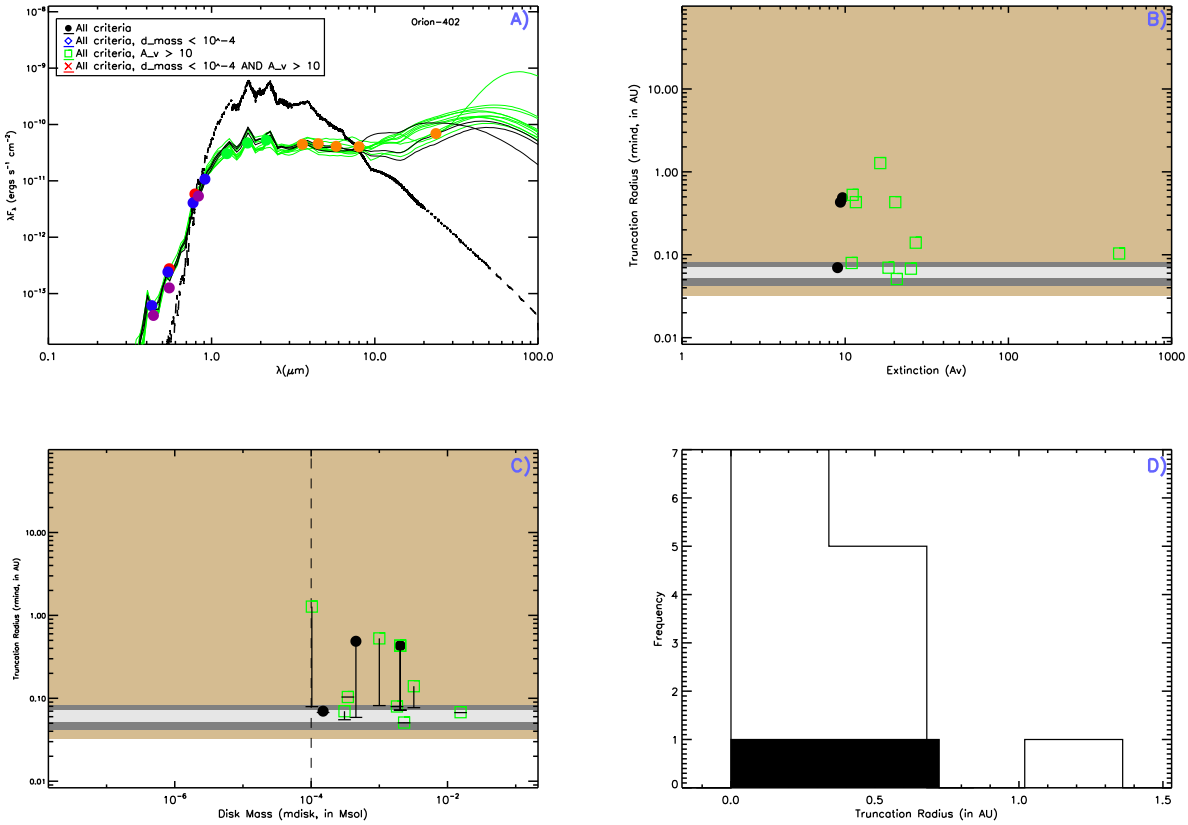

Figure B.57: SED fitting results for ONC #402

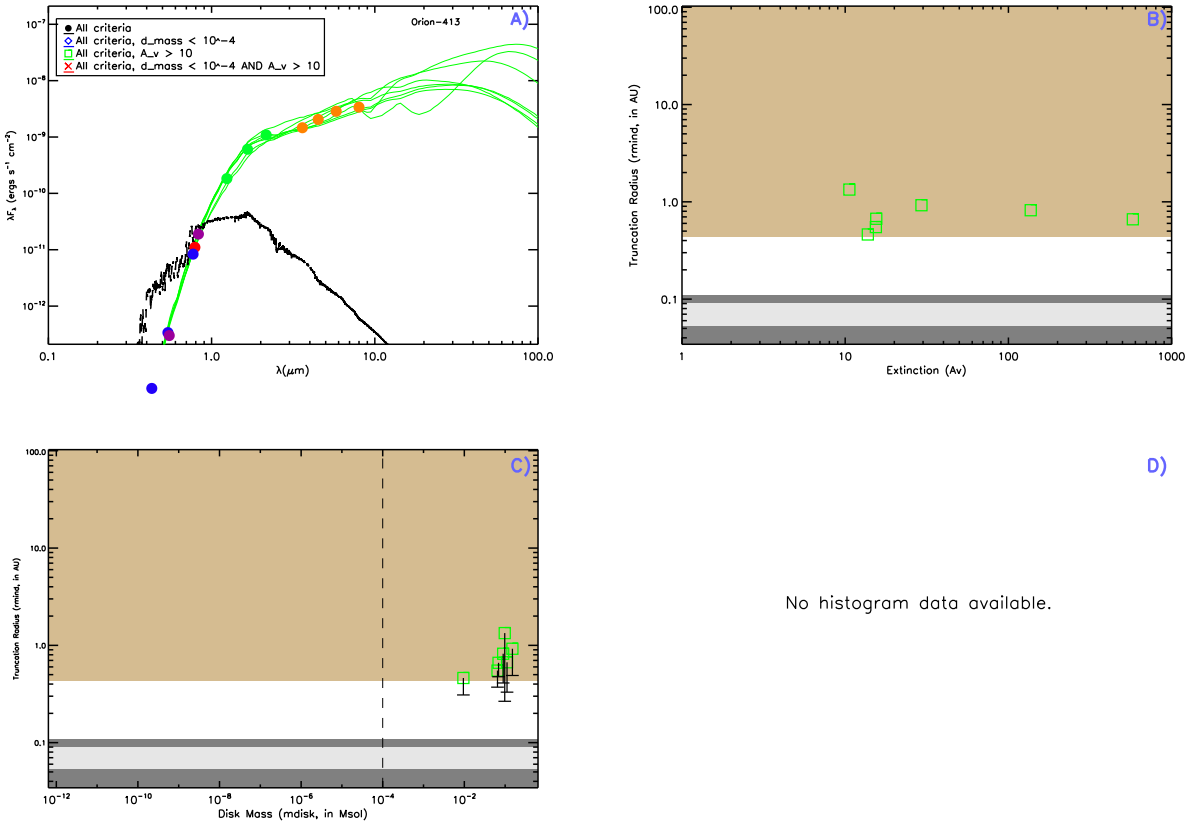

Figure B.58: SED fitting results for ONC #413

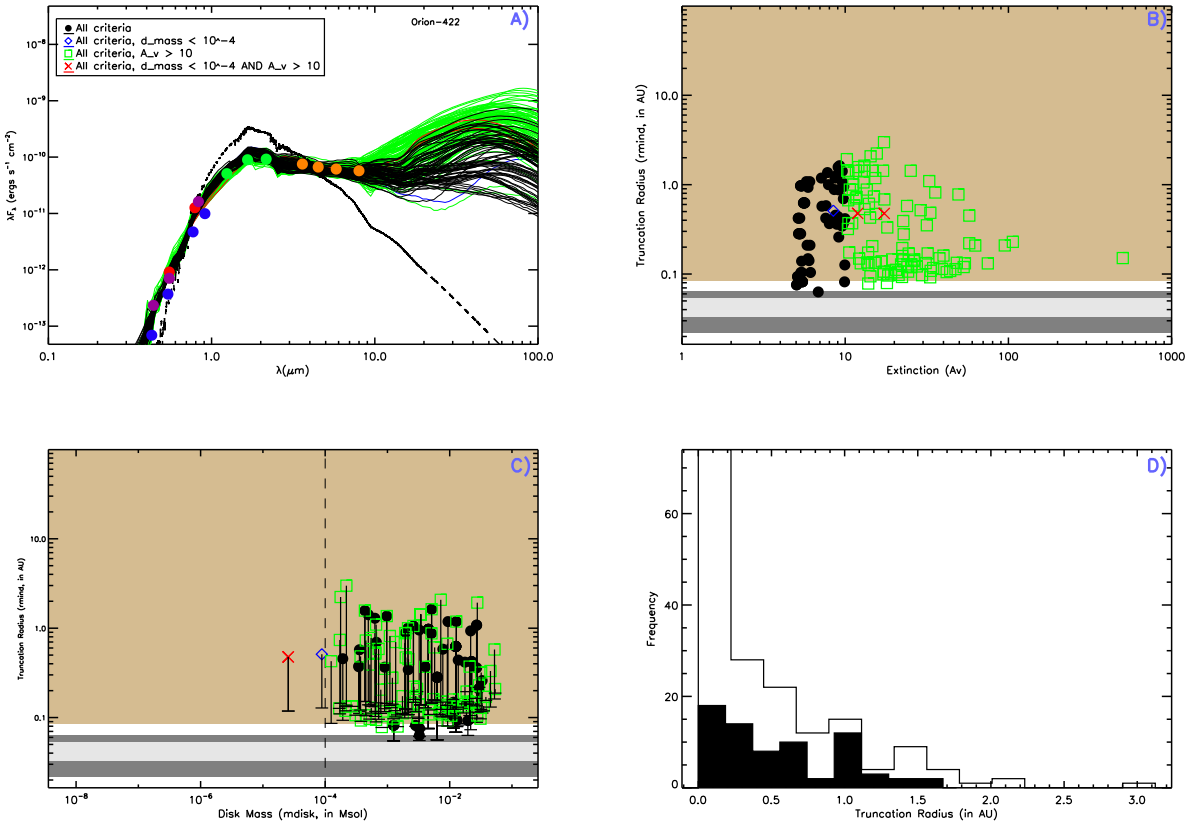

Figure B.59: SED fitting results for ONC #422

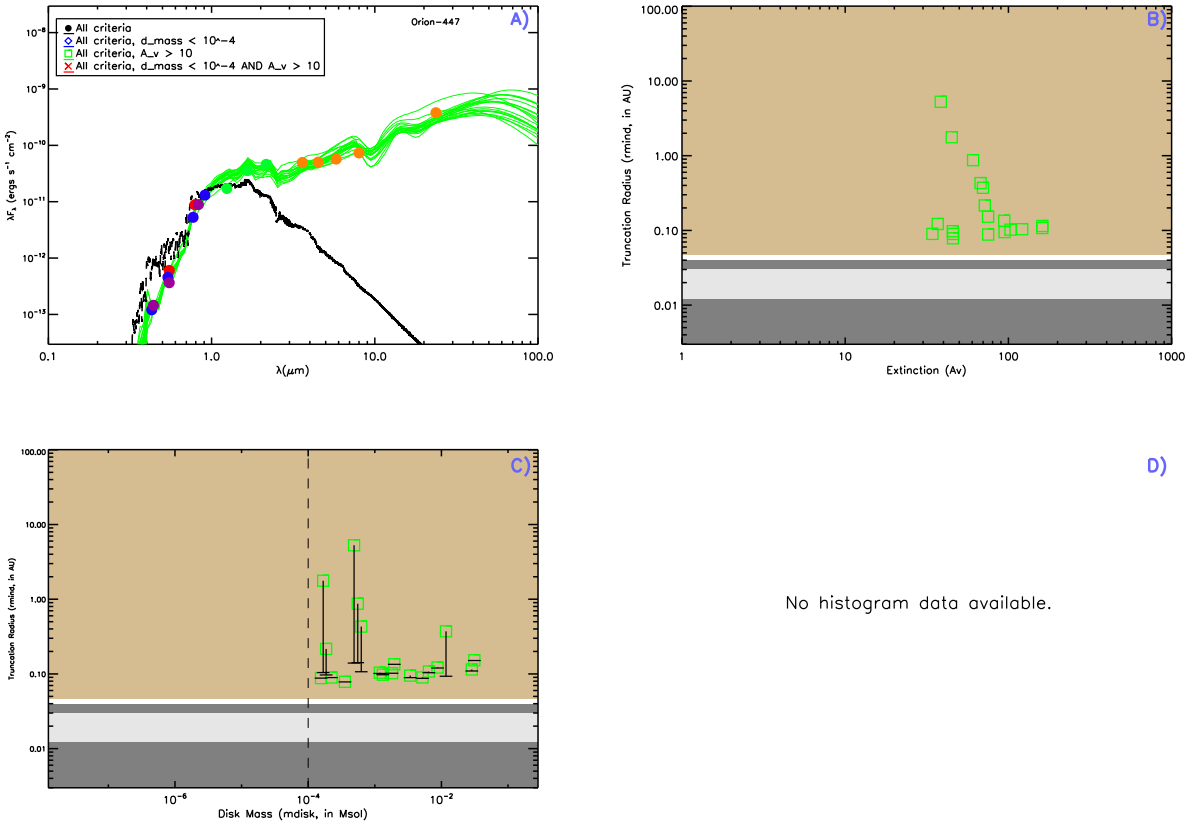

Figure B.60: SED fitting results for ONC #447

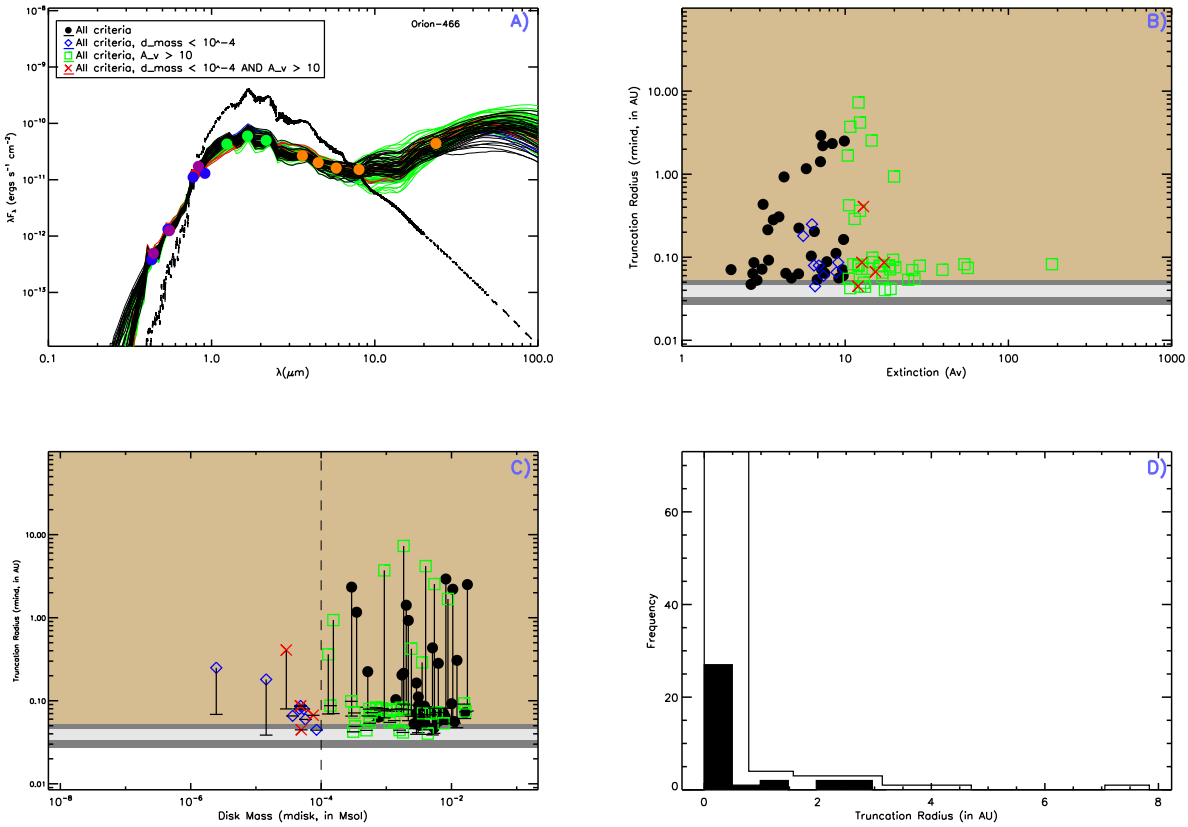

Figure B.61: SED fitting results for ONC #466

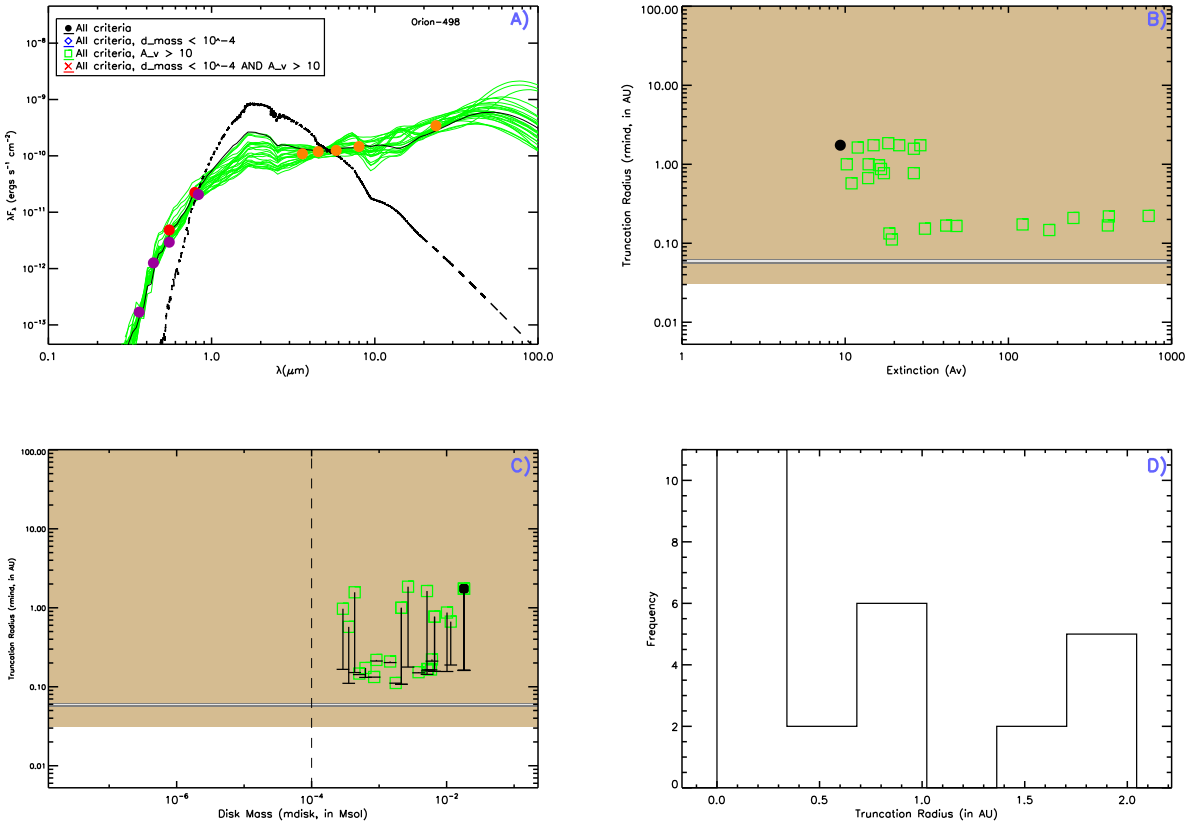

Figure B.62: SED fitting results for ONC #498

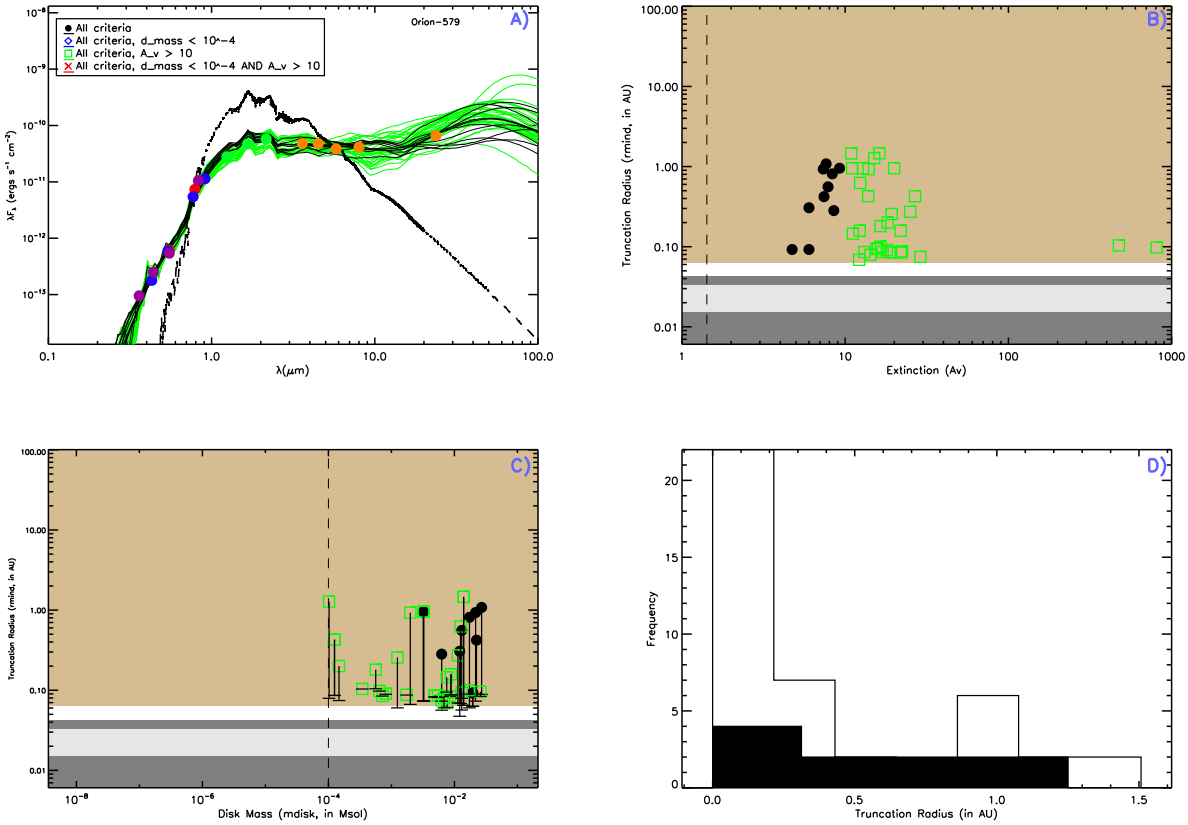

Figure B.63: SED fitting results for ONC #579

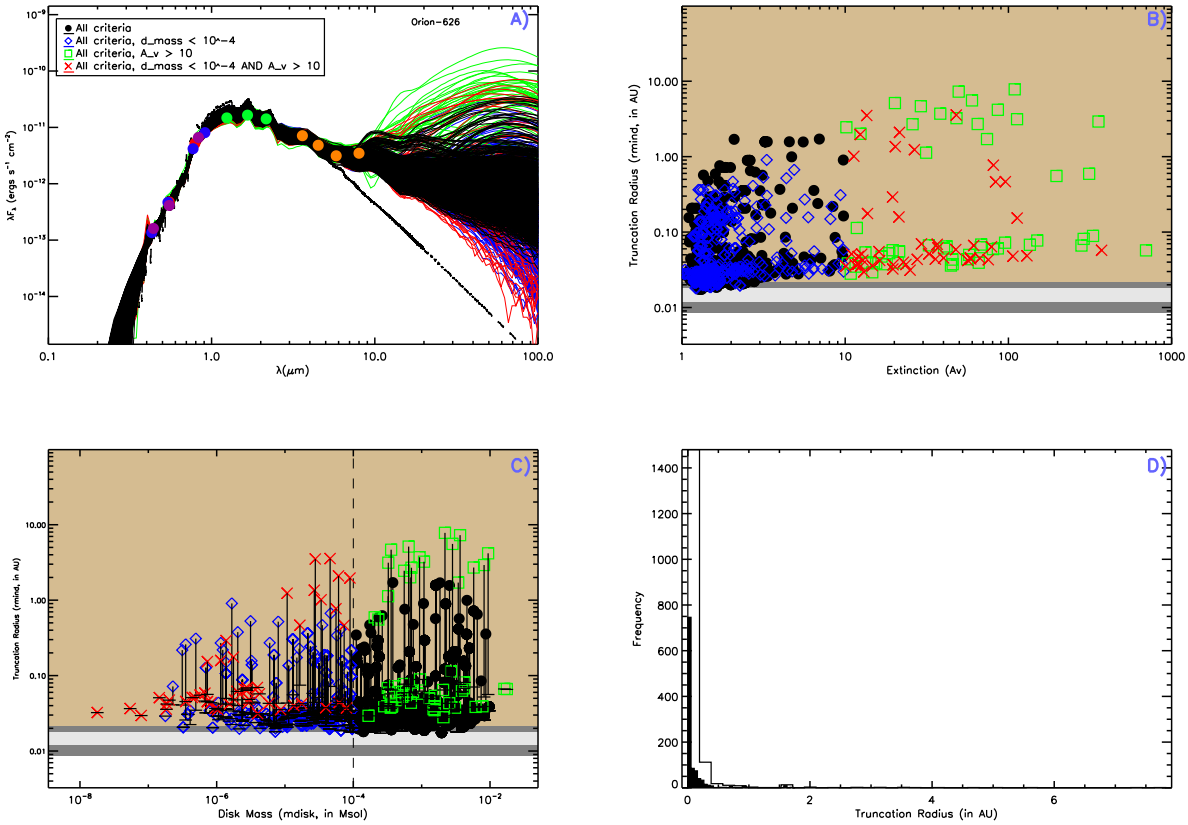

Figure B.64: SED fitting results for ONC #626

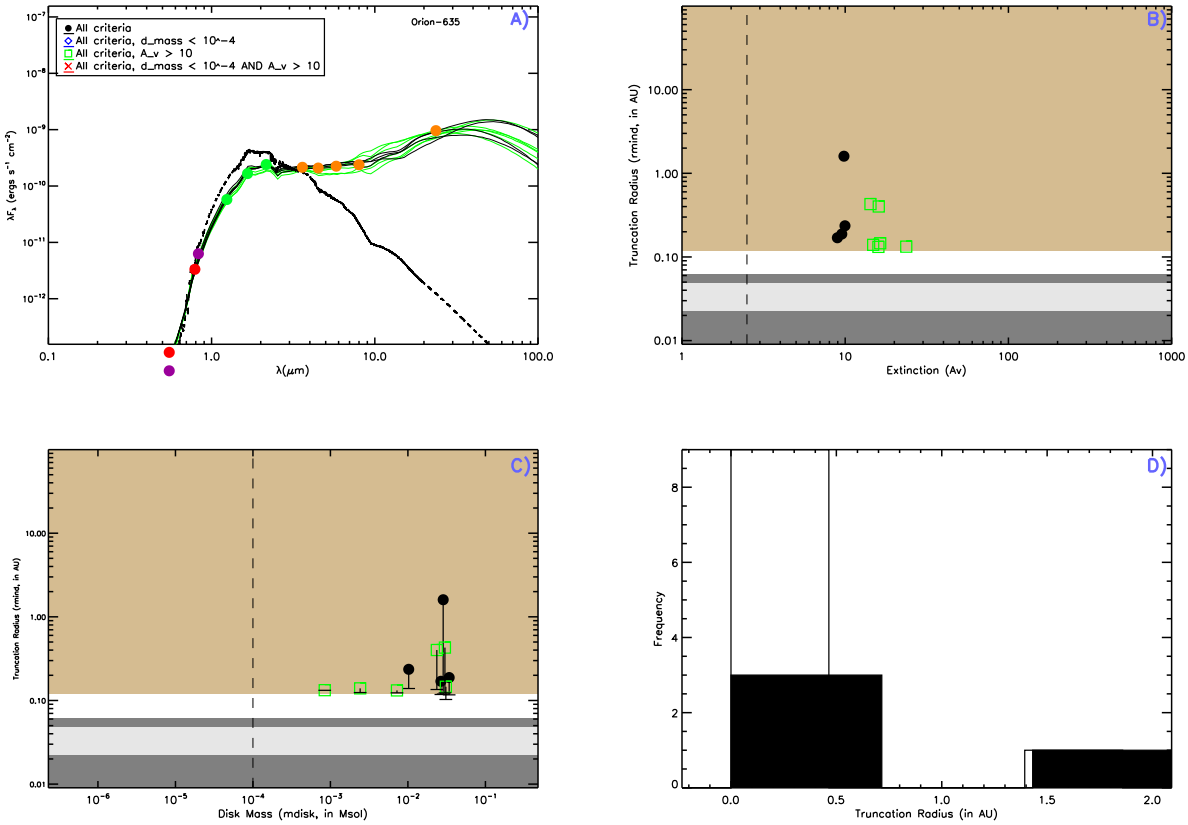

Figure B.65: SED fitting results for ONC #635

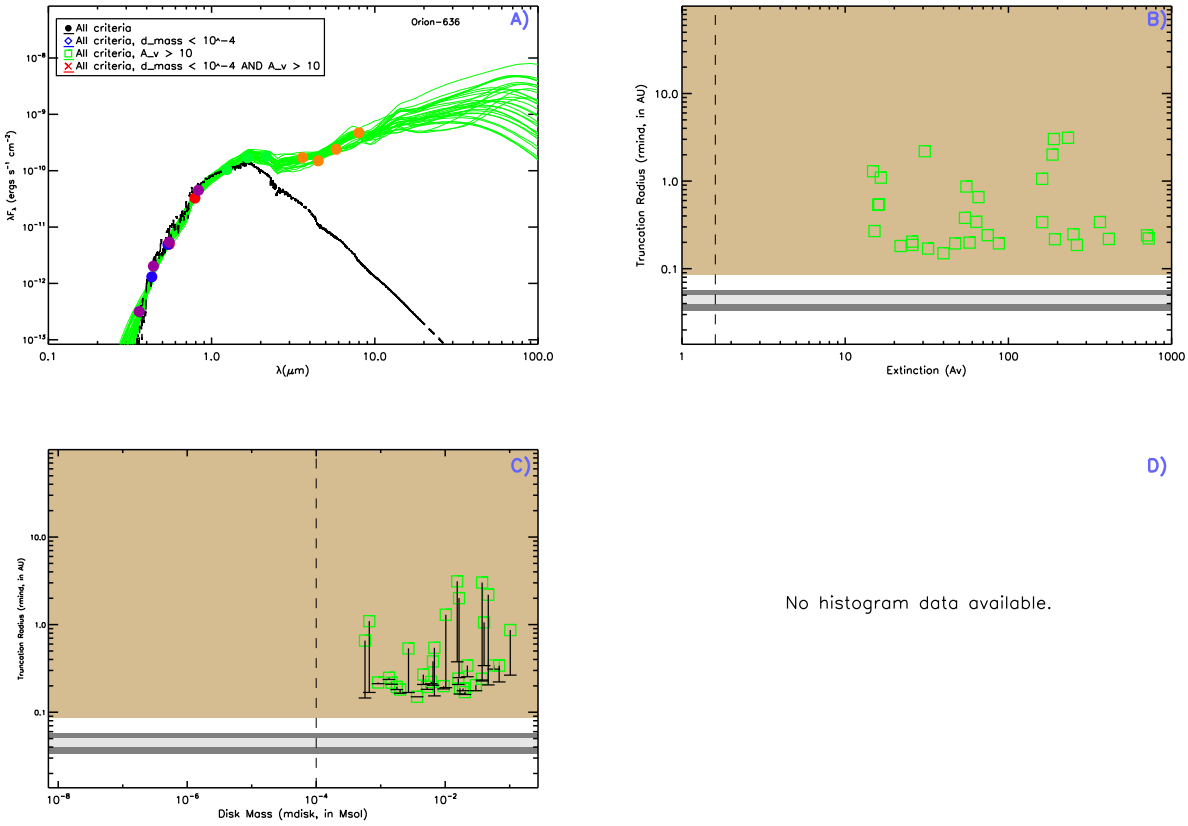

Figure B.66: SED fitting results for ONC #636

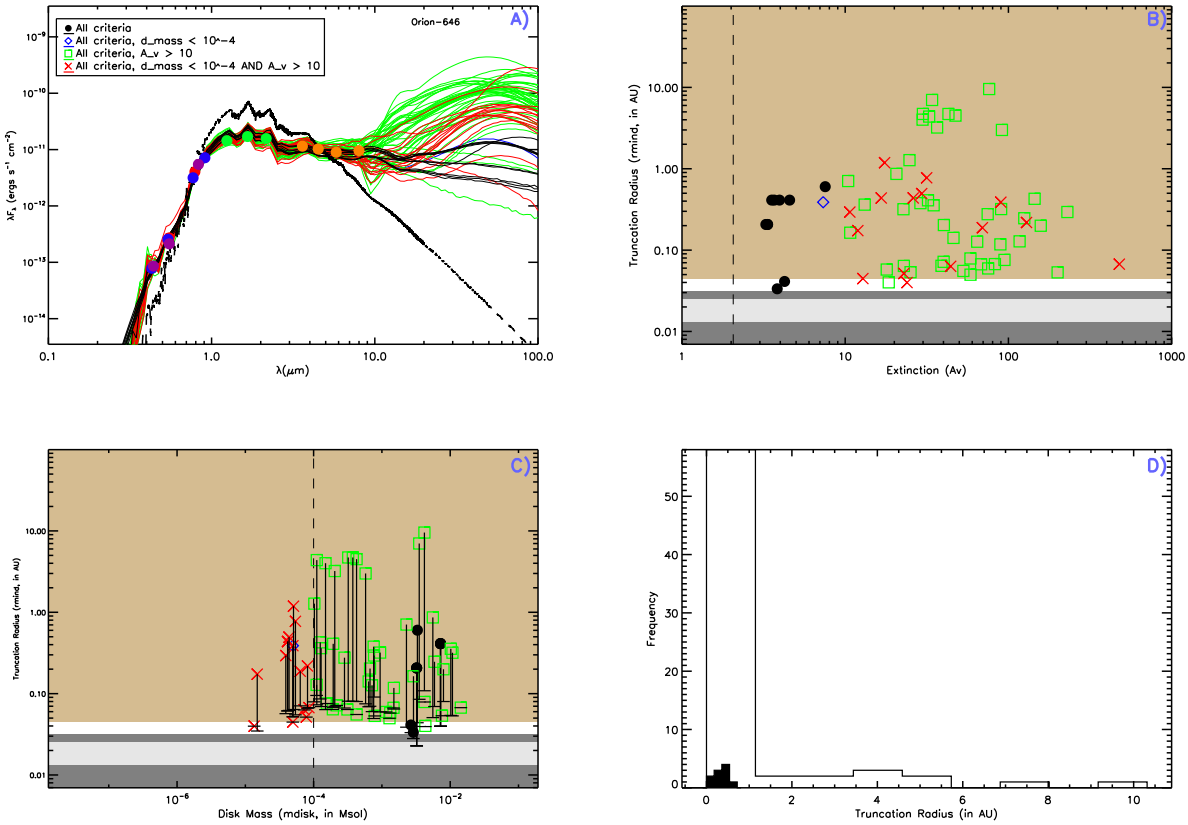

Figure B.67: SED fitting results for ONC #646

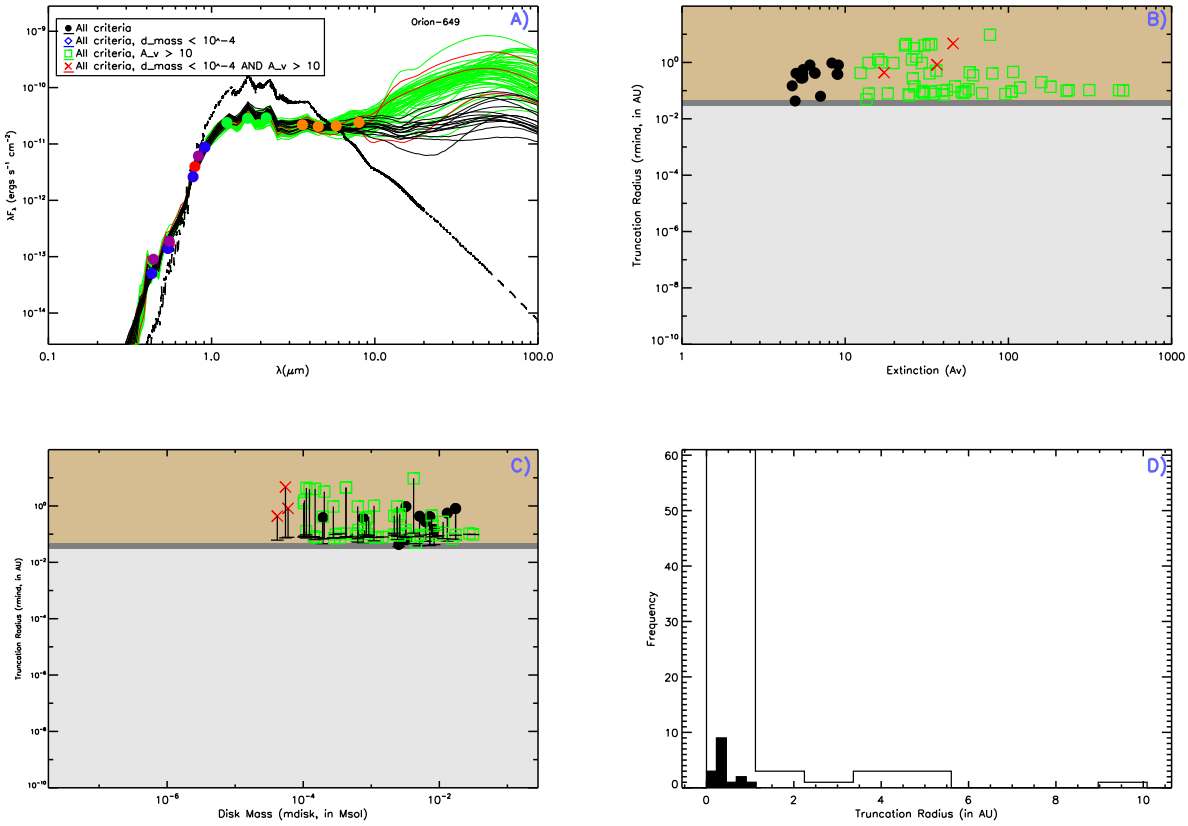

Figure B.68: SED fitting results for ONC #649

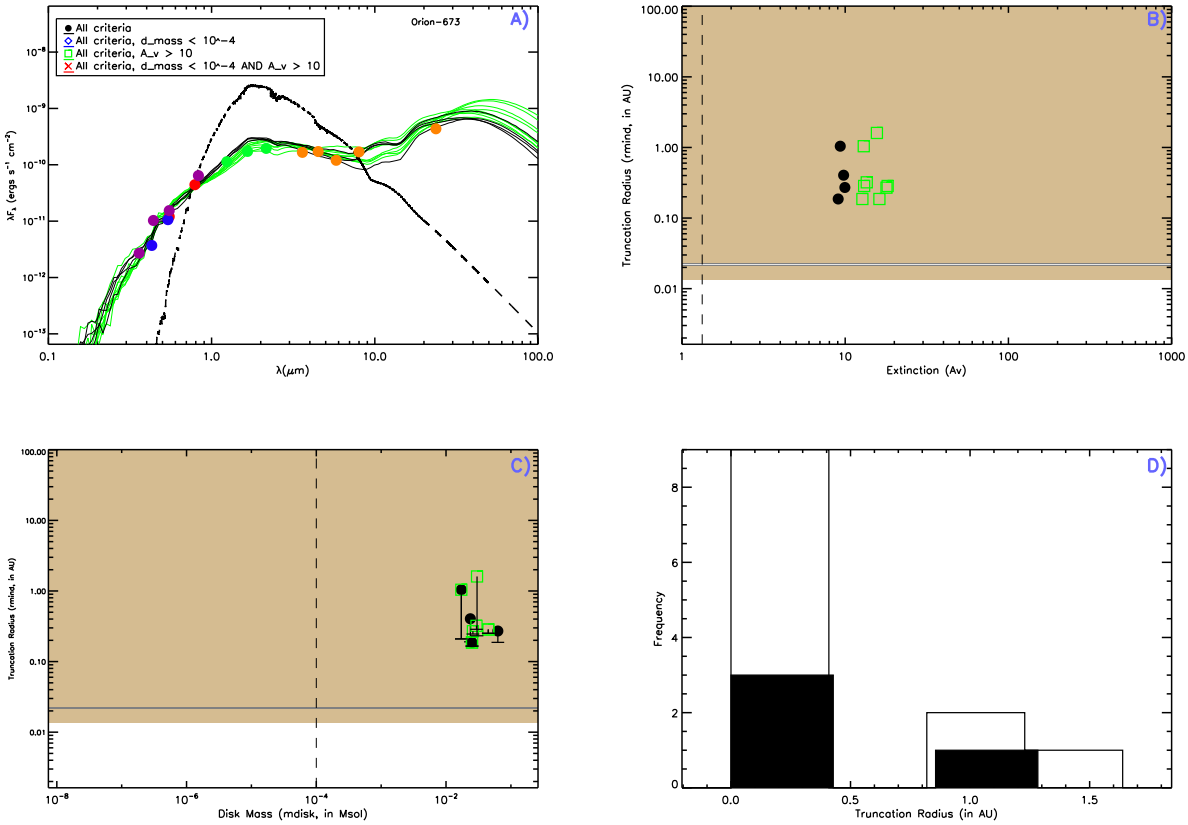

Figure B.69: SED fitting results for ONC #673

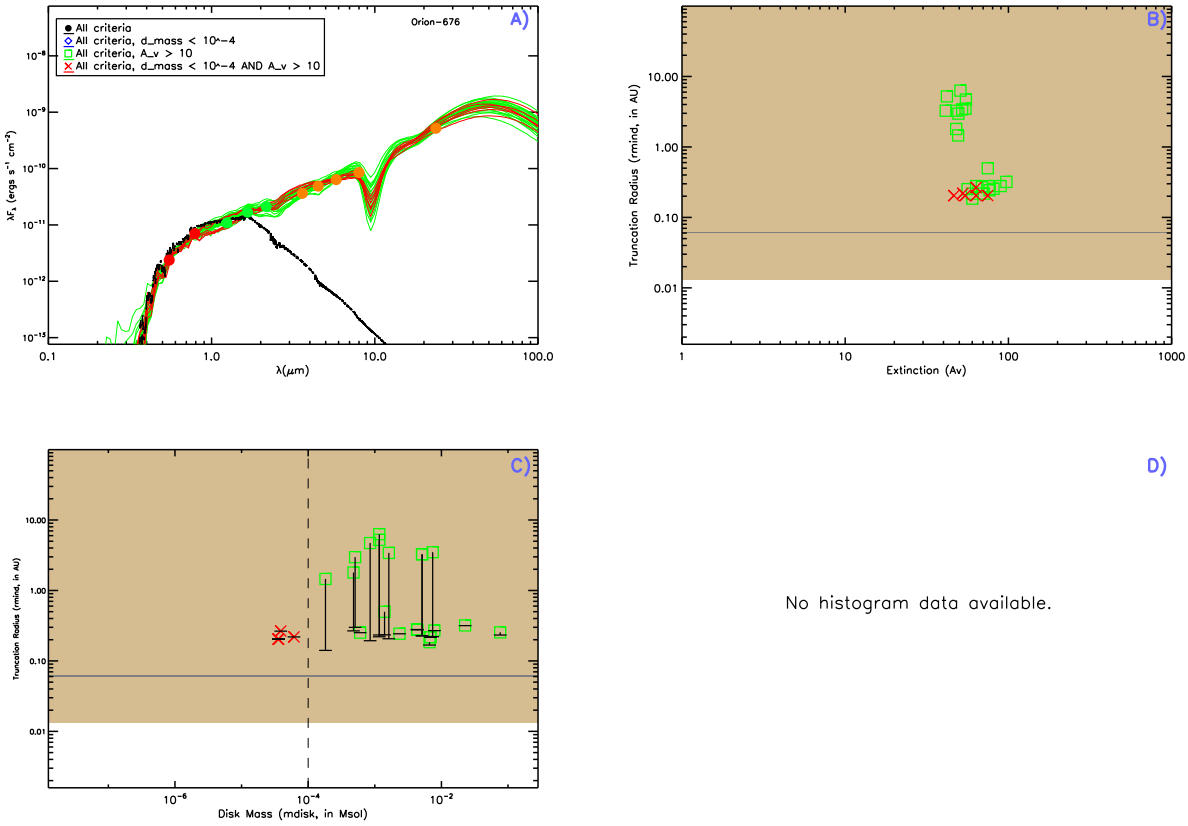

Figure B.70: SED fitting results for ONC #676

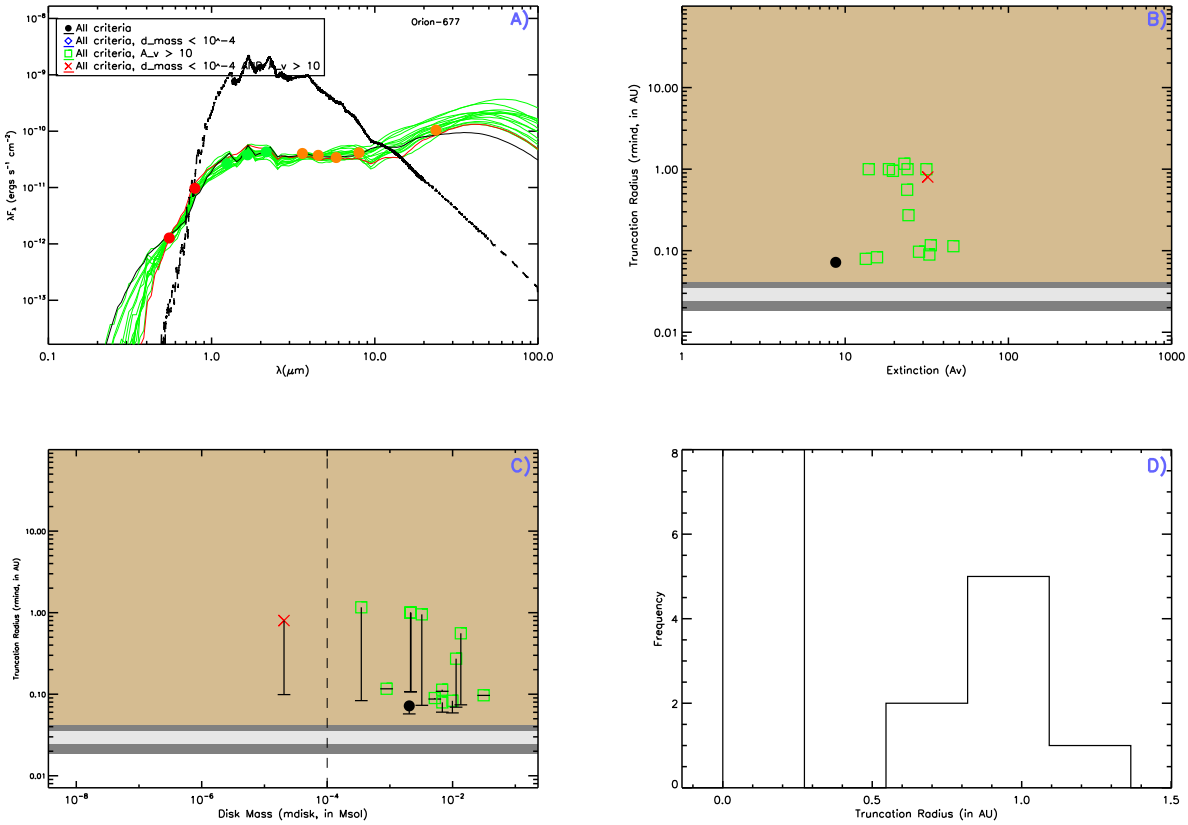

Figure B.71: SED fitting results for ONC #677

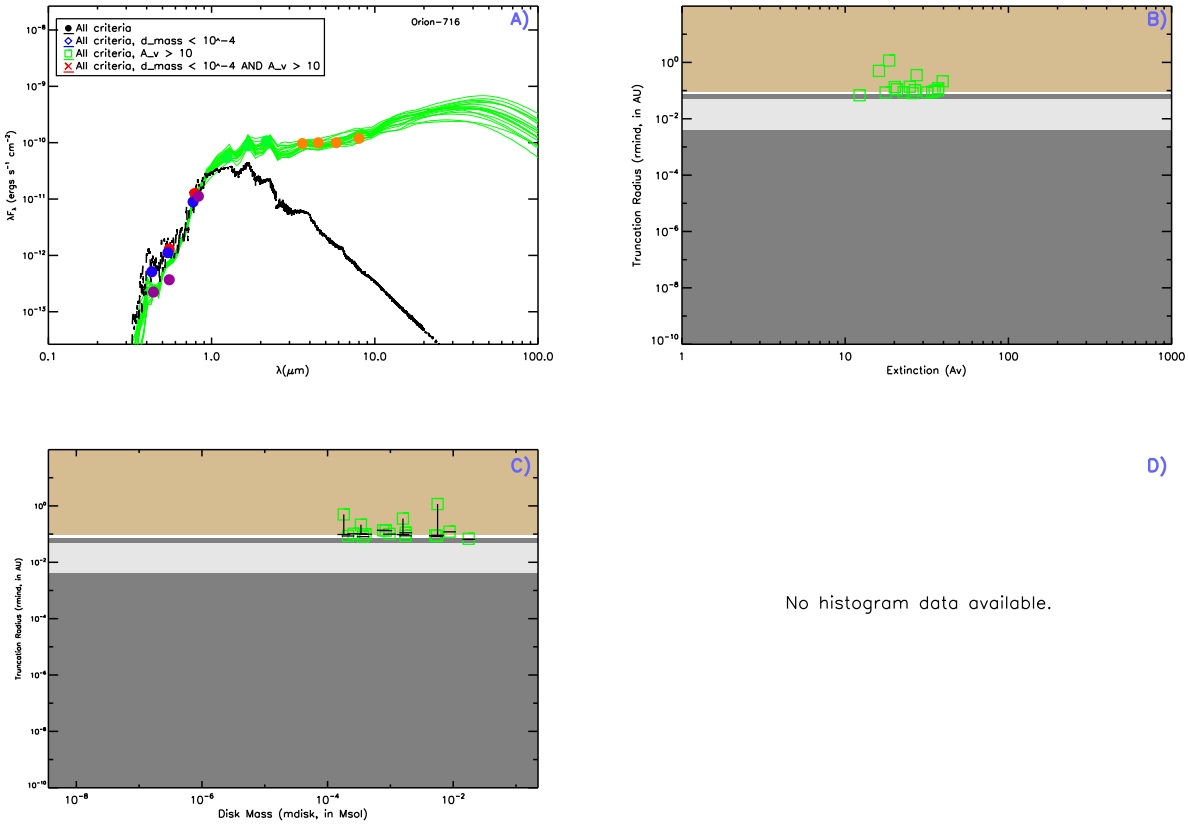

Figure B.72: SED fitting results for ONC #716

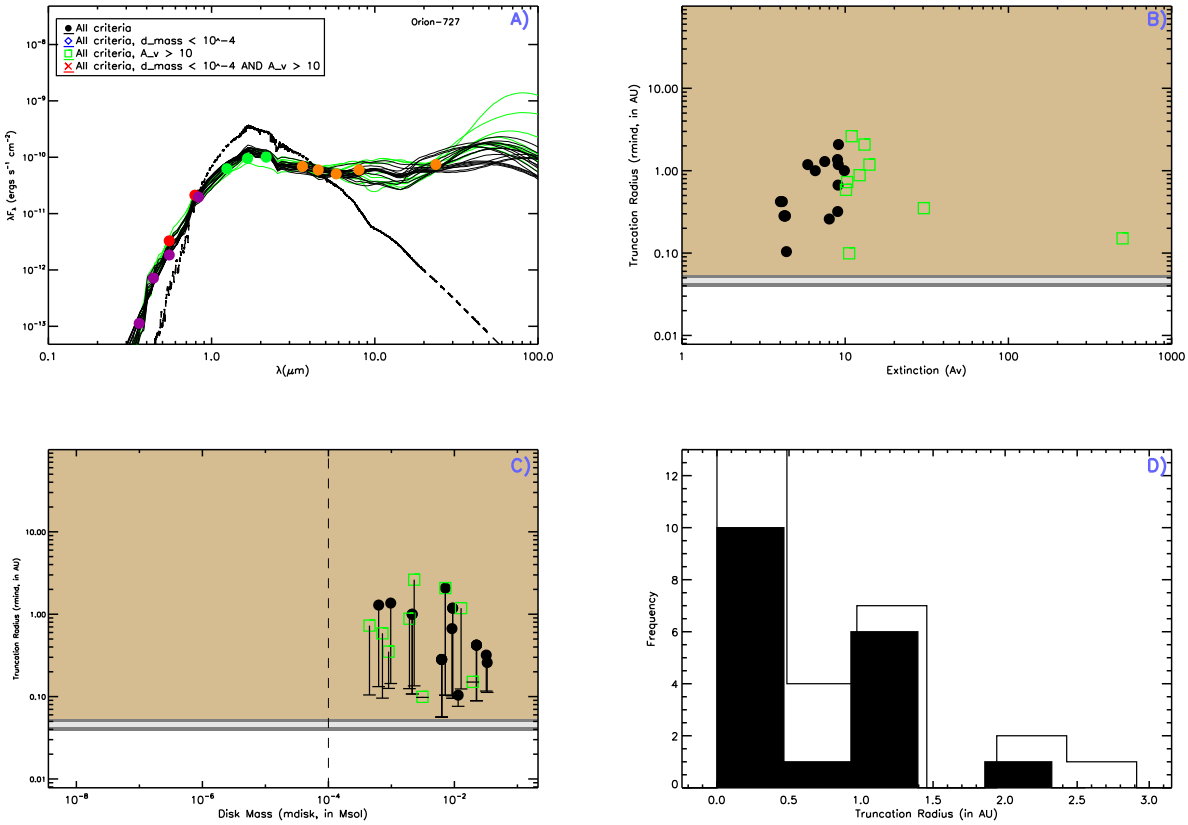

Figure B.73: SED fitting results for ONC #727

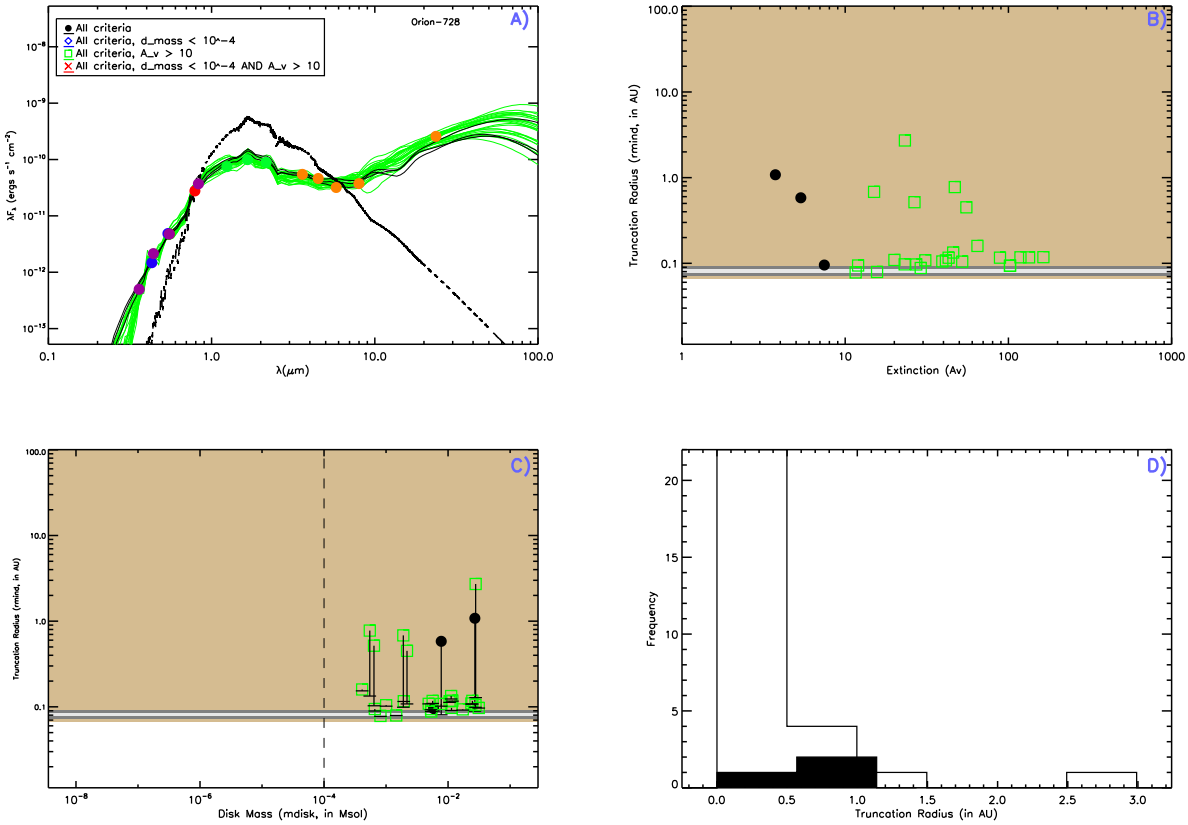

Figure B.74: SED fitting results for ONC #728

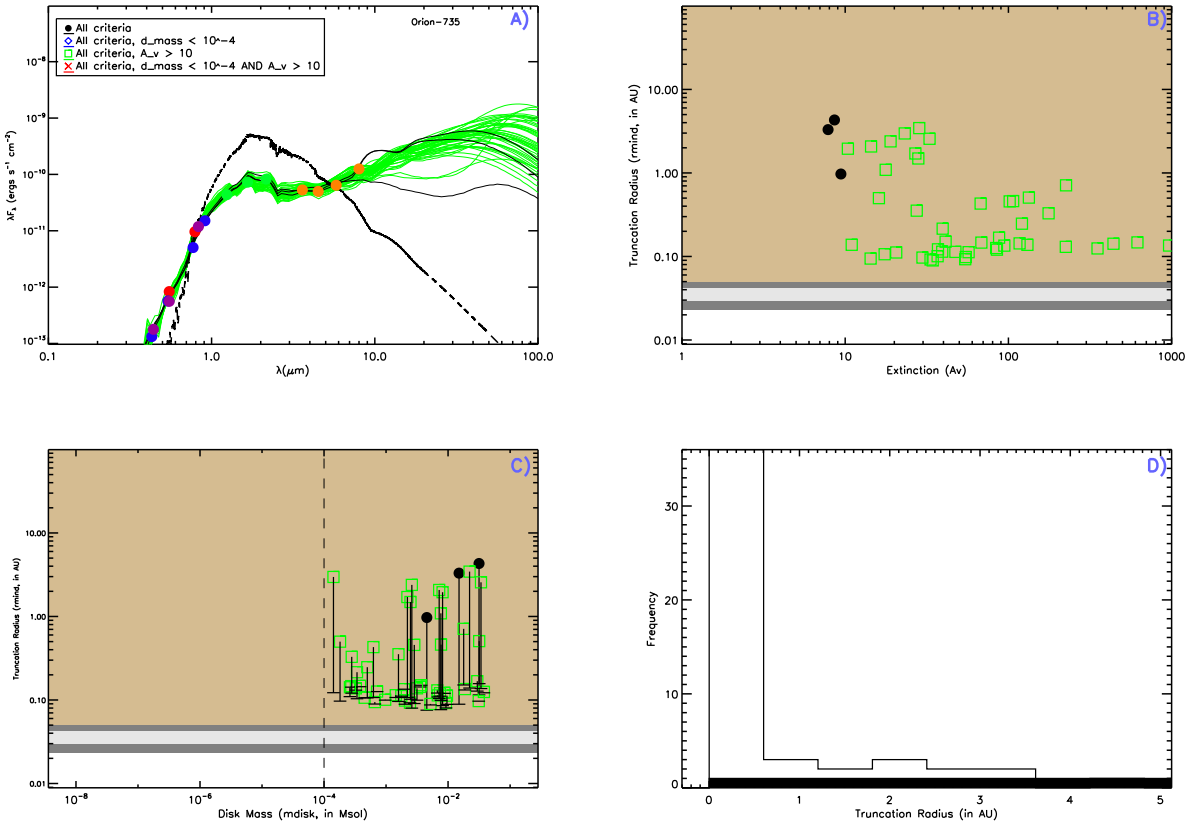

Figure B.75: SED fitting results for ONC #735

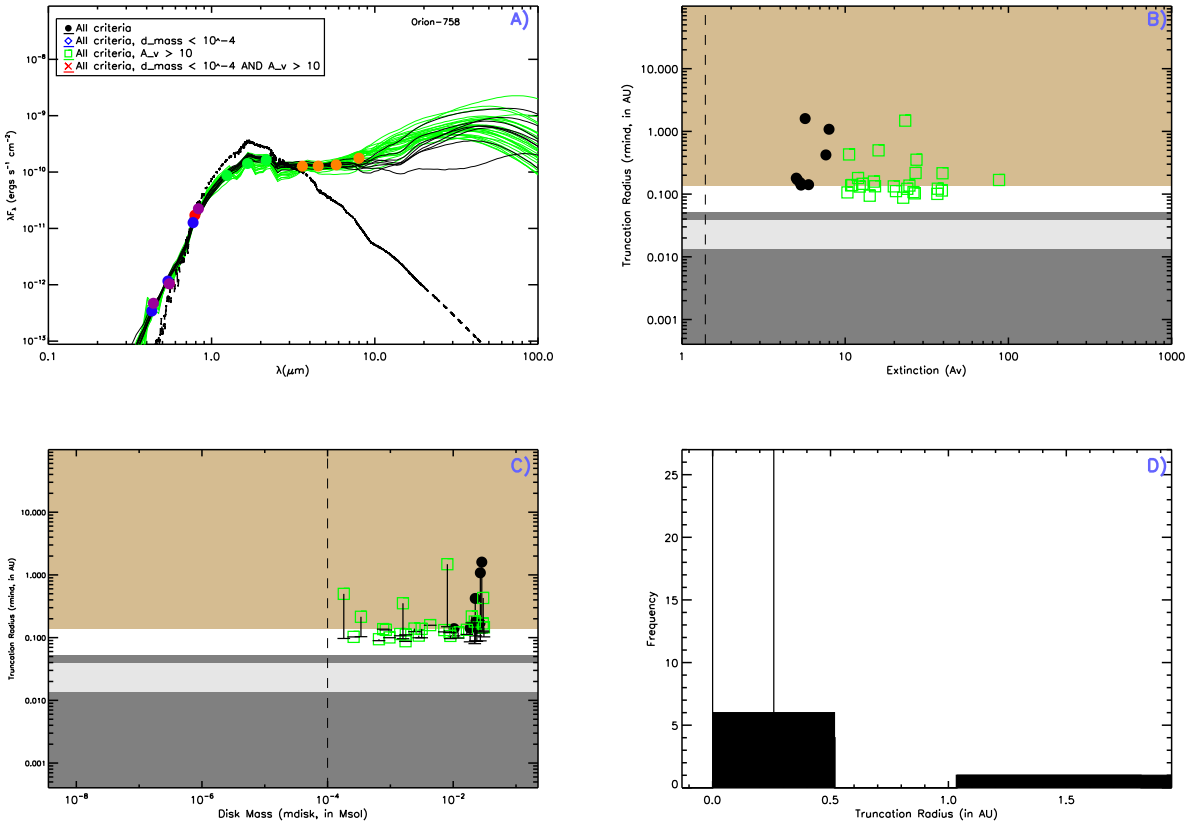

Figure B.76: SED fitting results for ONC #758

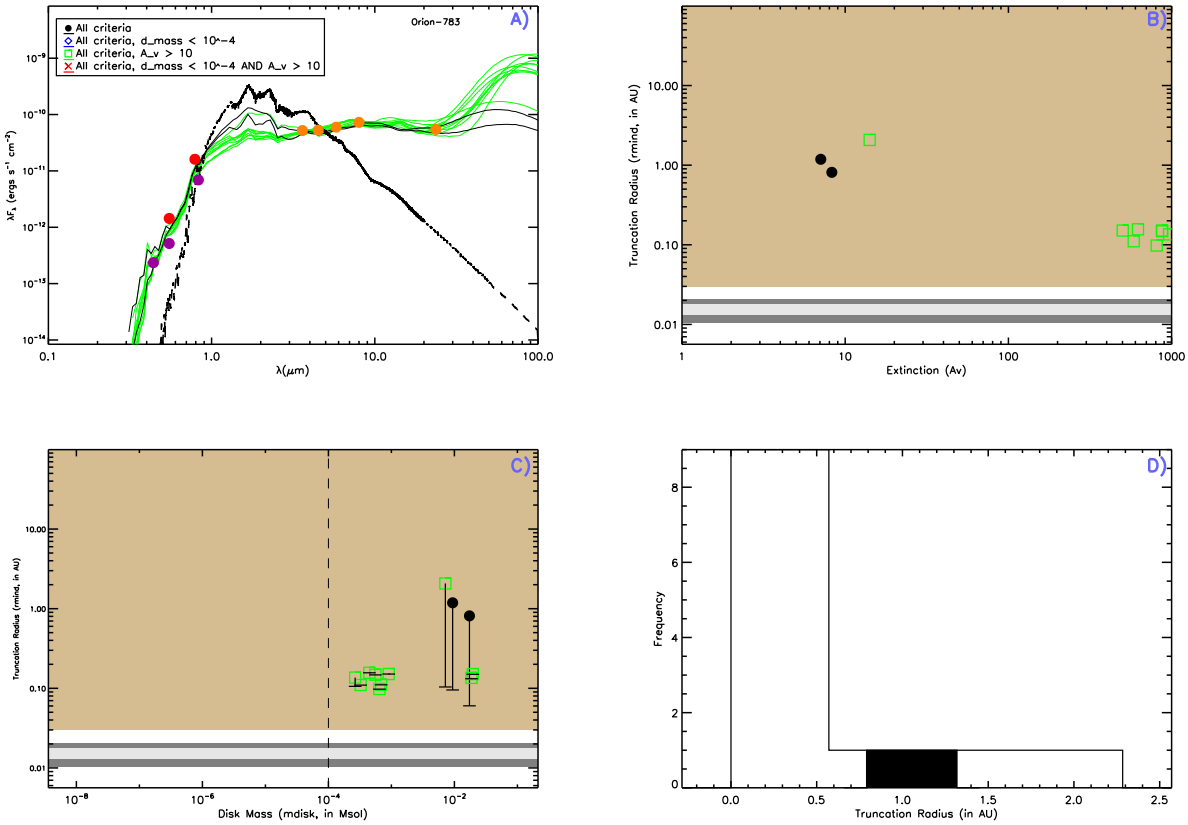

Figure B.77: SED fitting results for ONC #783

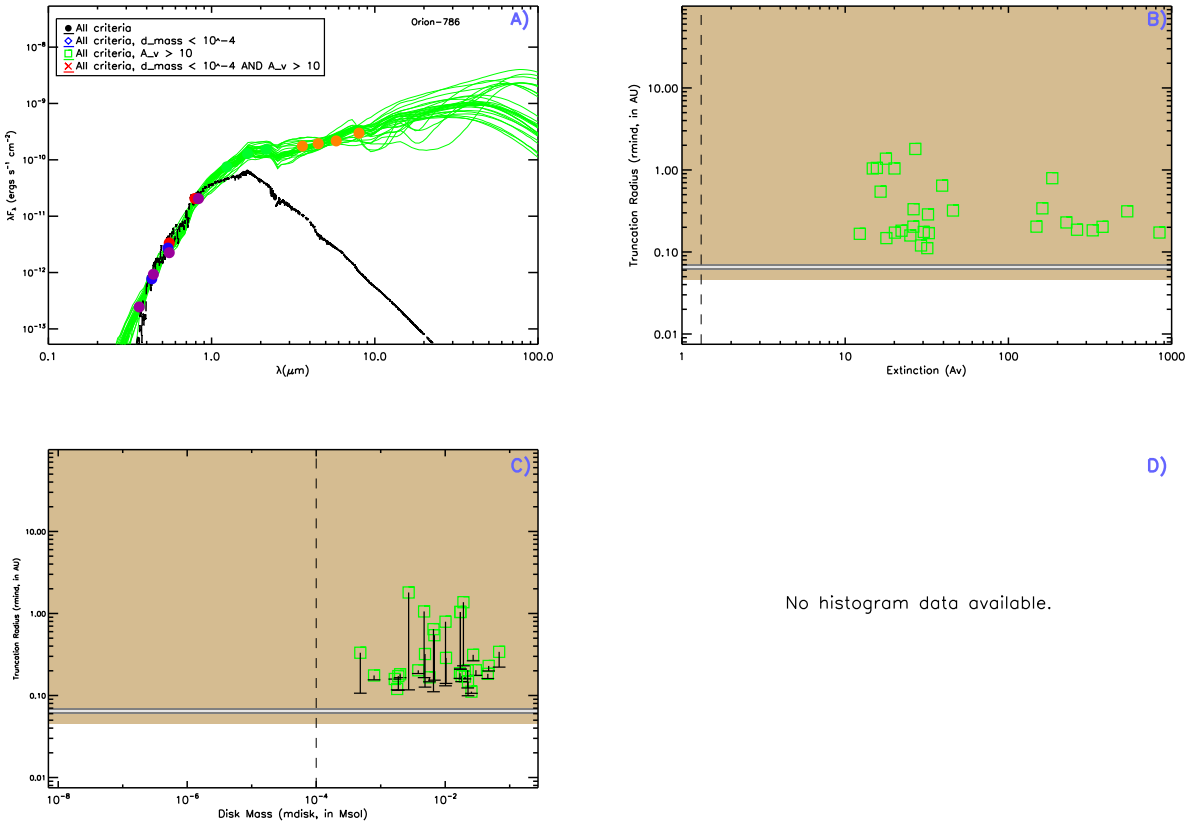

Figure B.78: SED fitting results for ONC #786

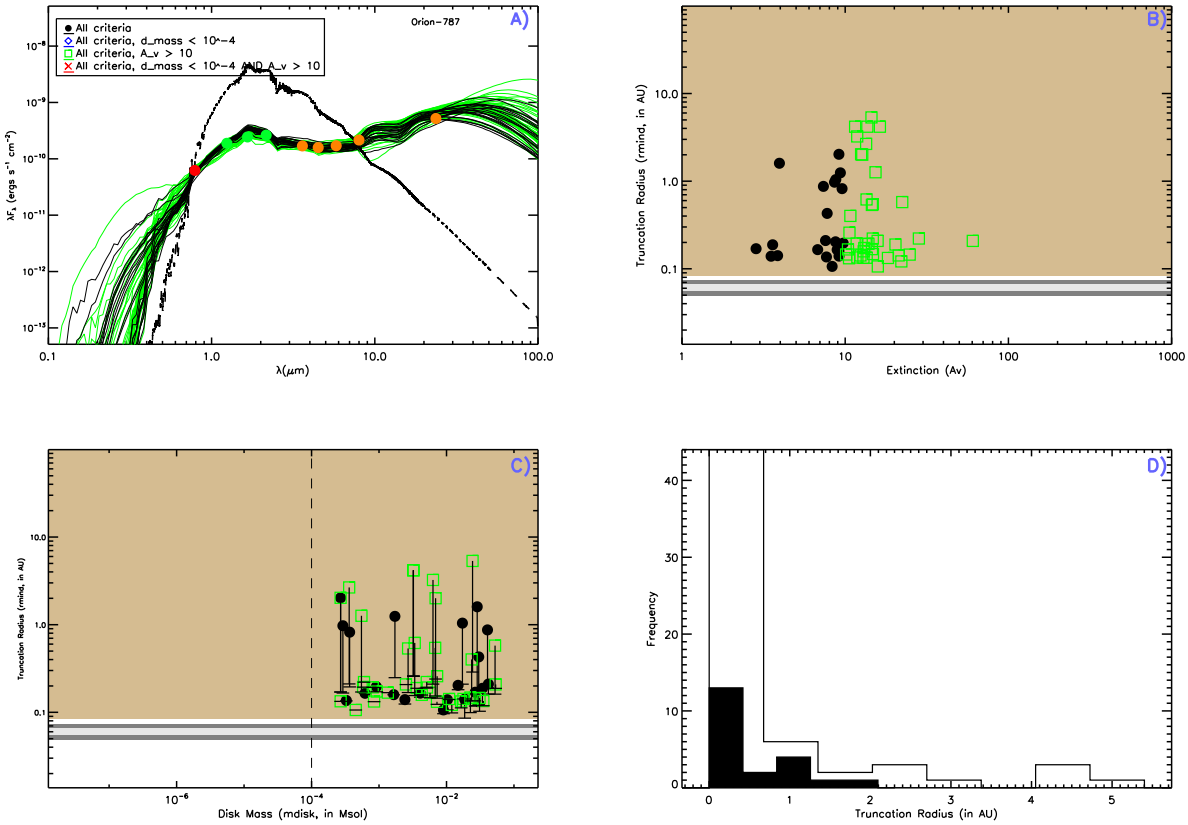

Figure B.79: SED fitting results for ONC #787

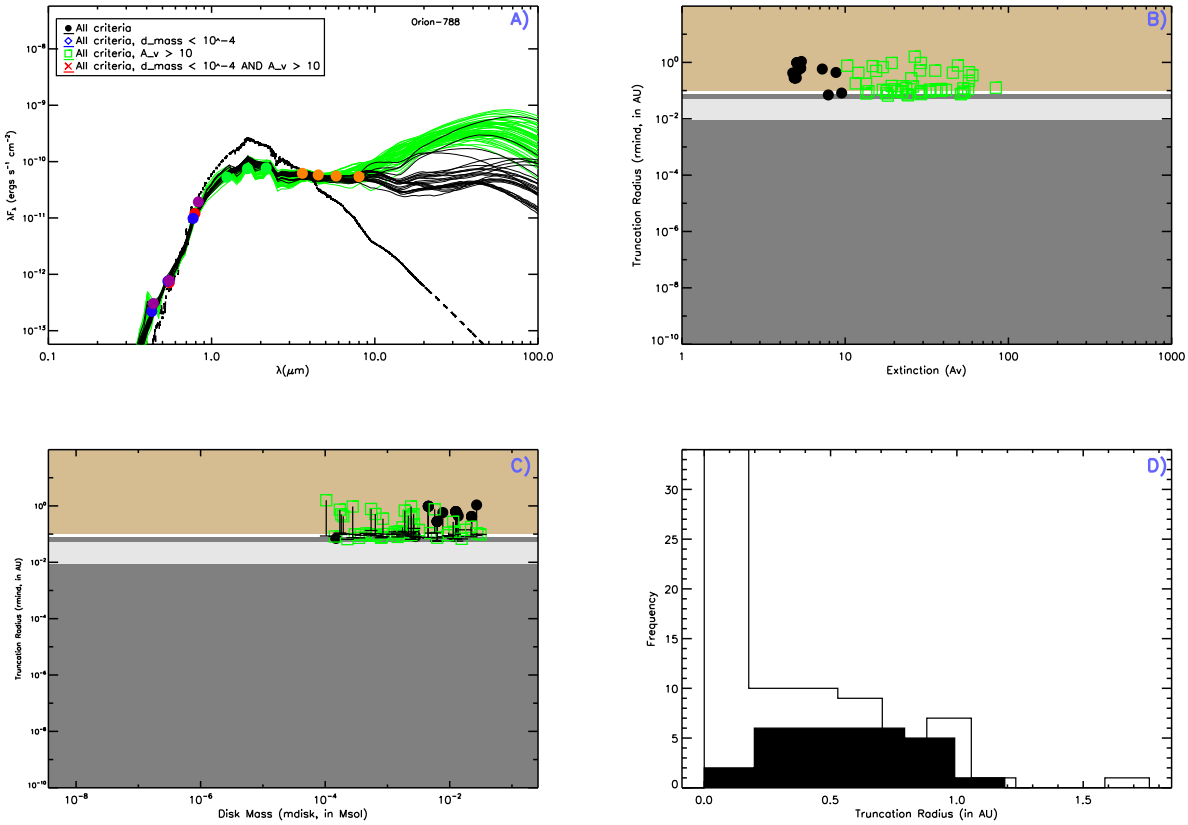

Figure B.80: SED fitting results for ONC #788

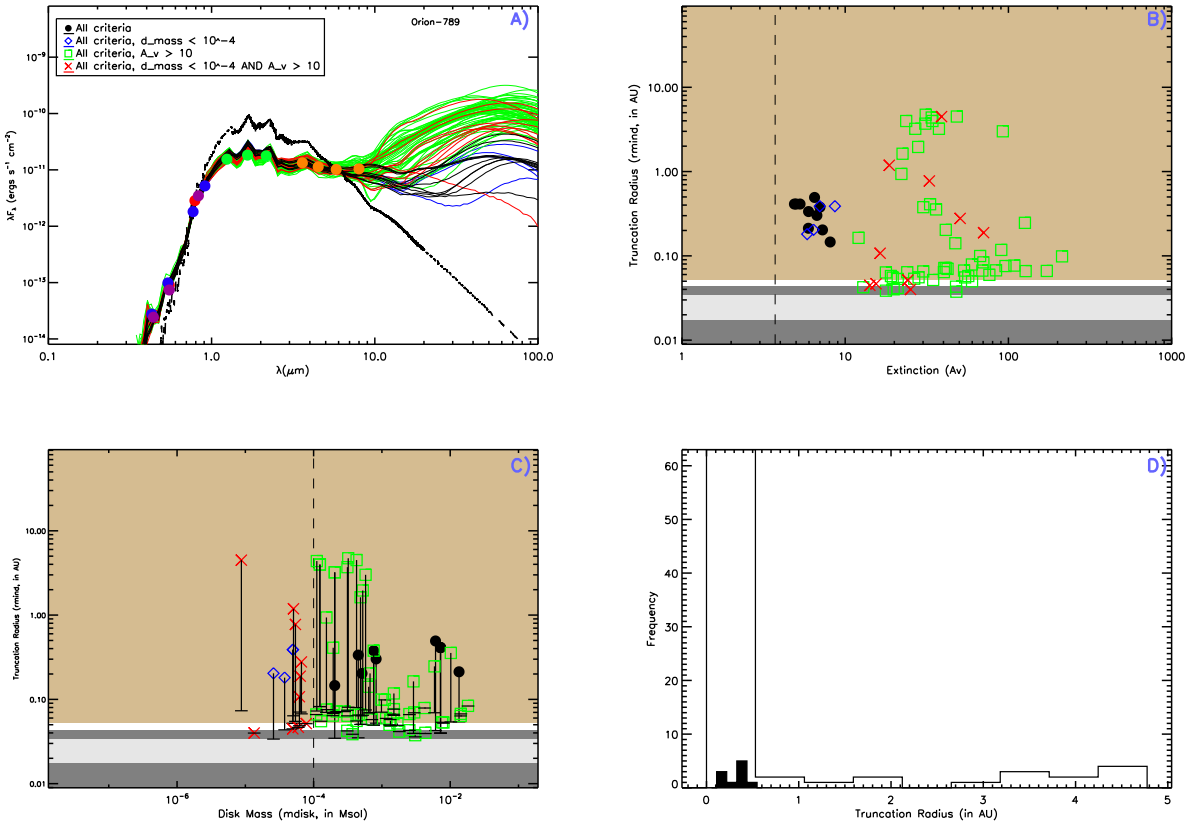

Figure B.81: SED fitting results for ONC #789

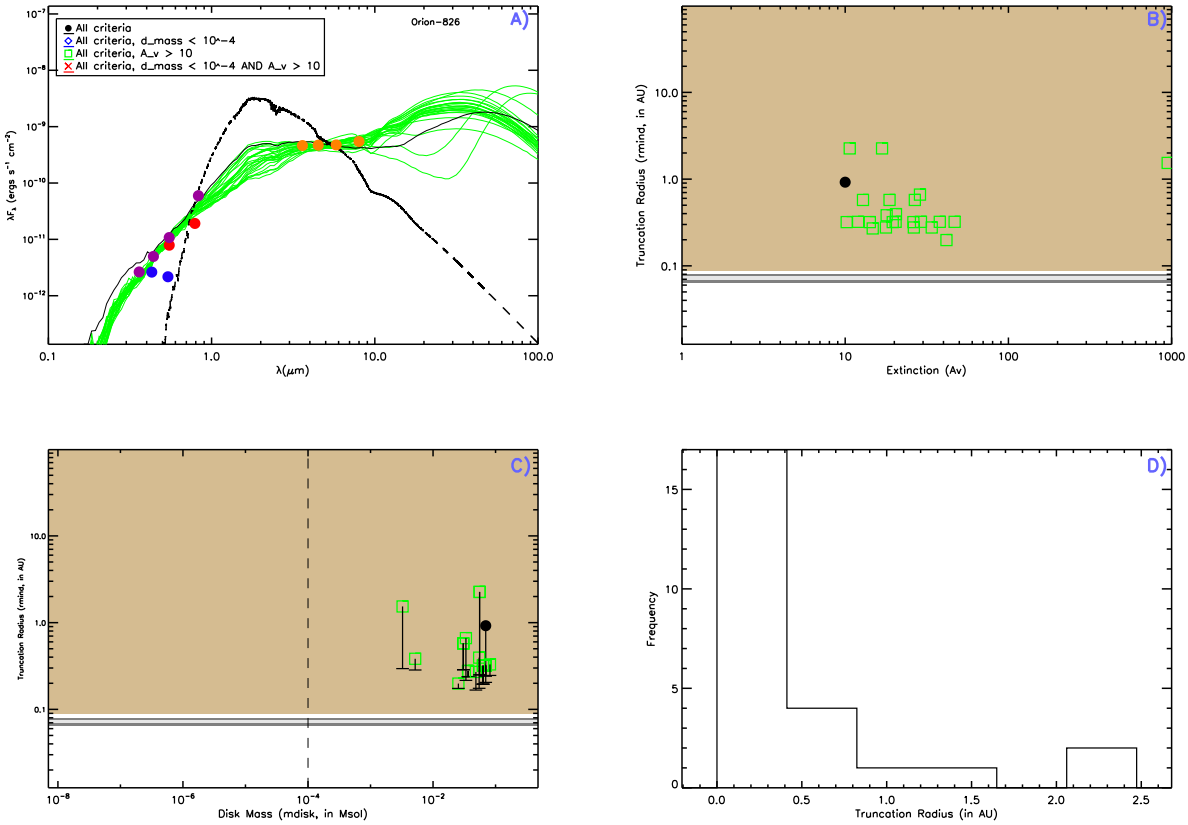

Figure B.82: SED fitting results for ONC #826

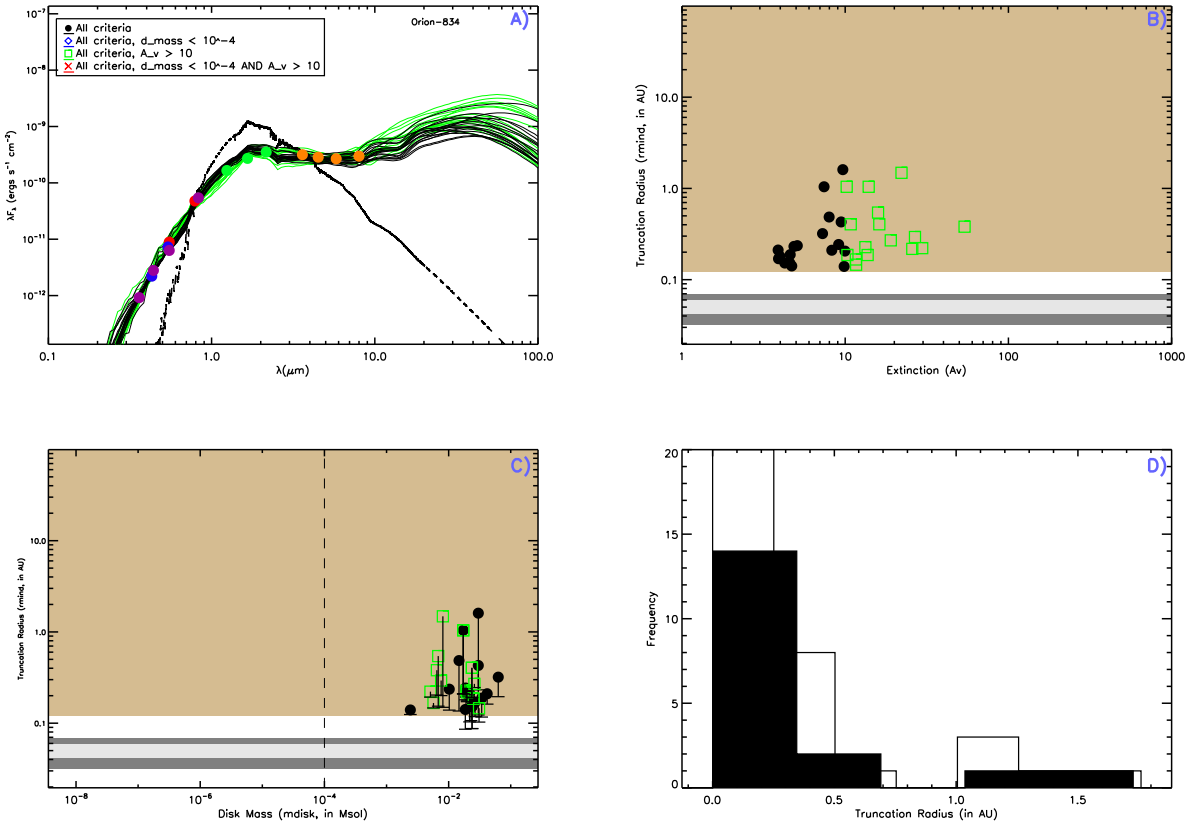

Figure B.83: SED fitting results for ONC #834

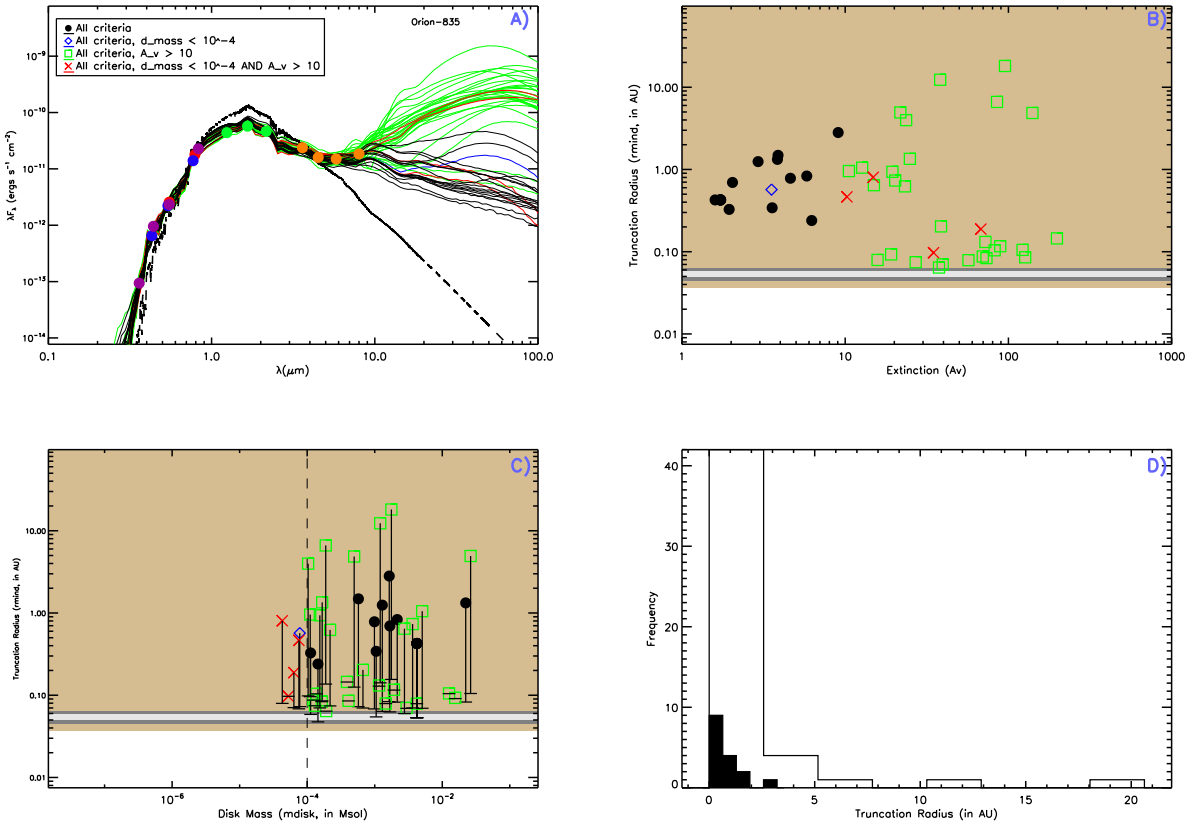

Figure B.84: SED fitting results for ONC #835

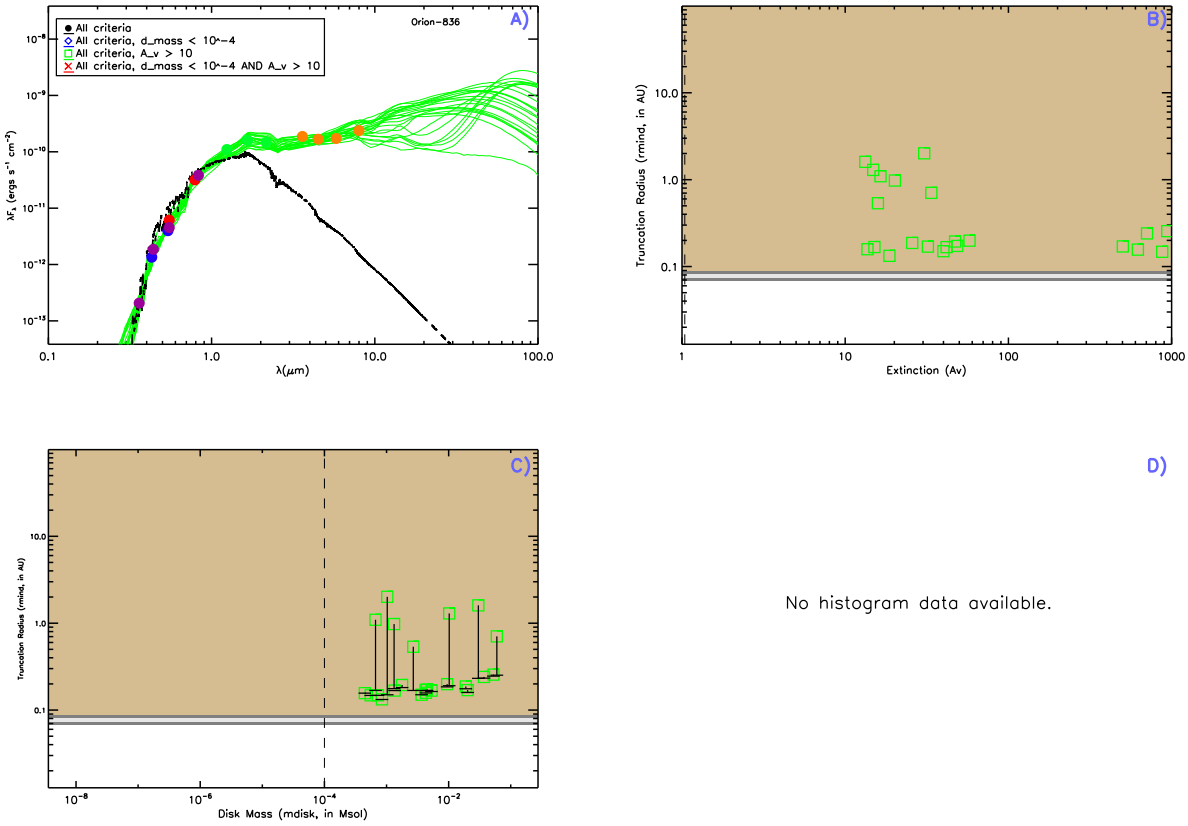

Figure B.85: SED fitting results for ONC #836

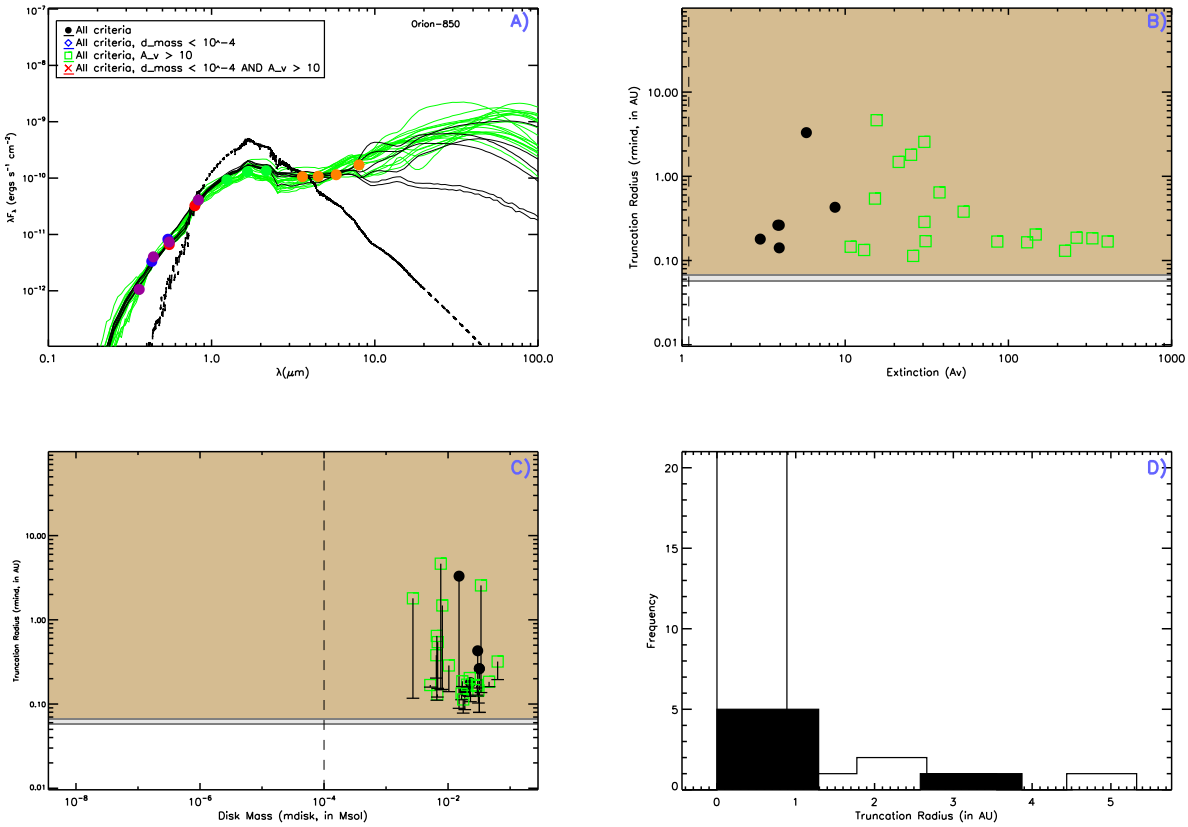

Figure B.86: SED fitting results for ONC #850

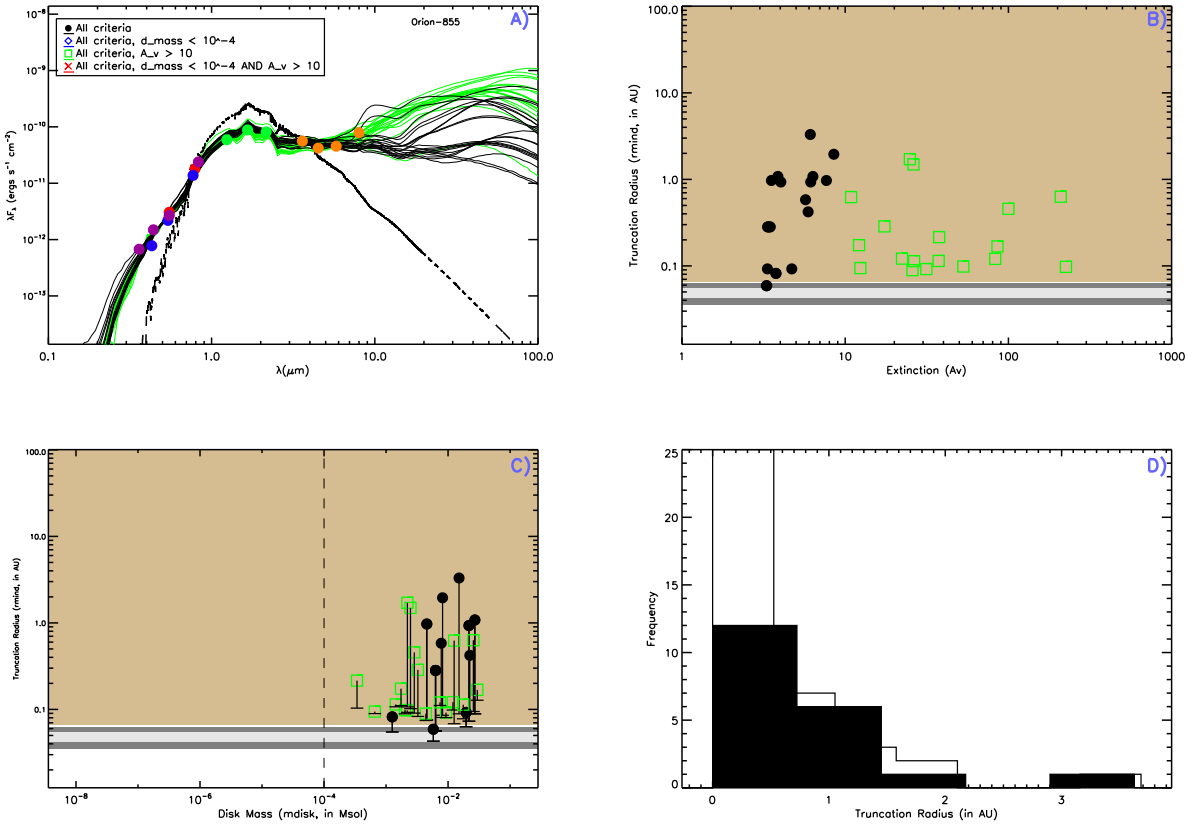

Figure B.87: SED fitting results for ONC #855

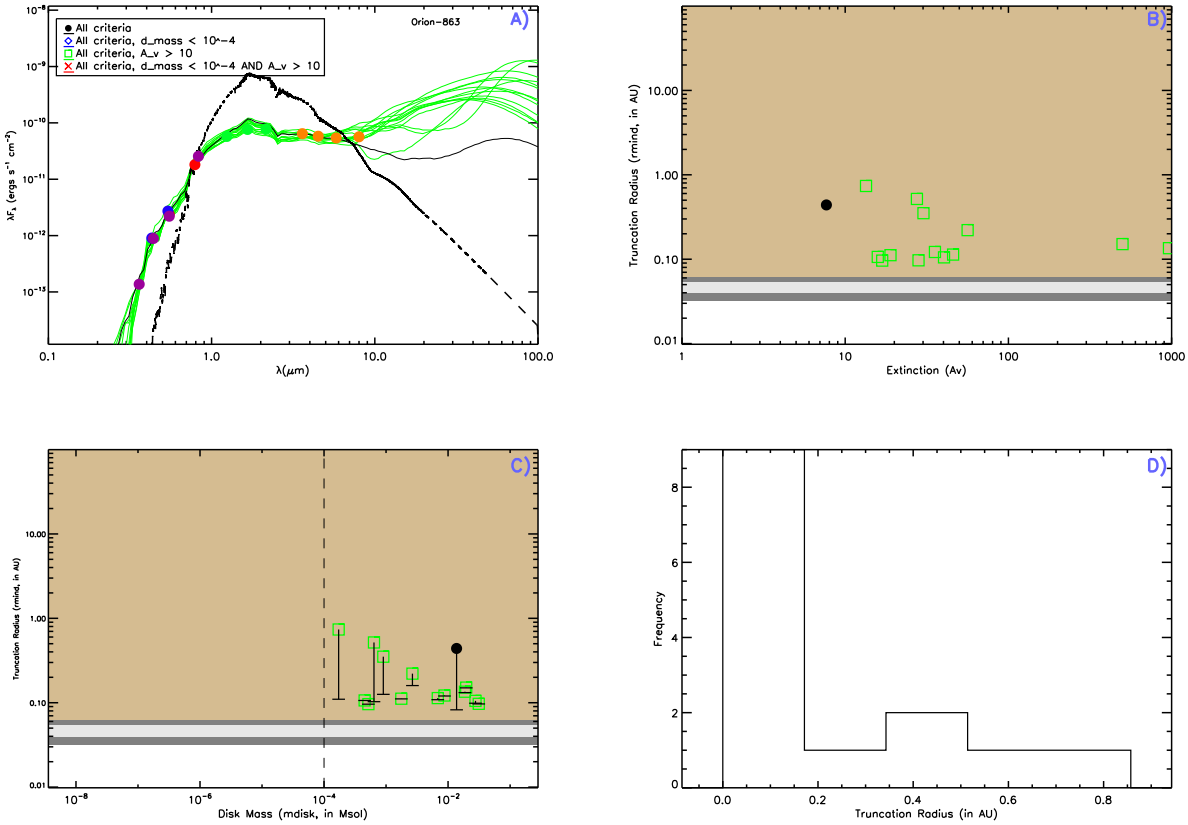

Figure B.88: SED fitting results for ONC #863

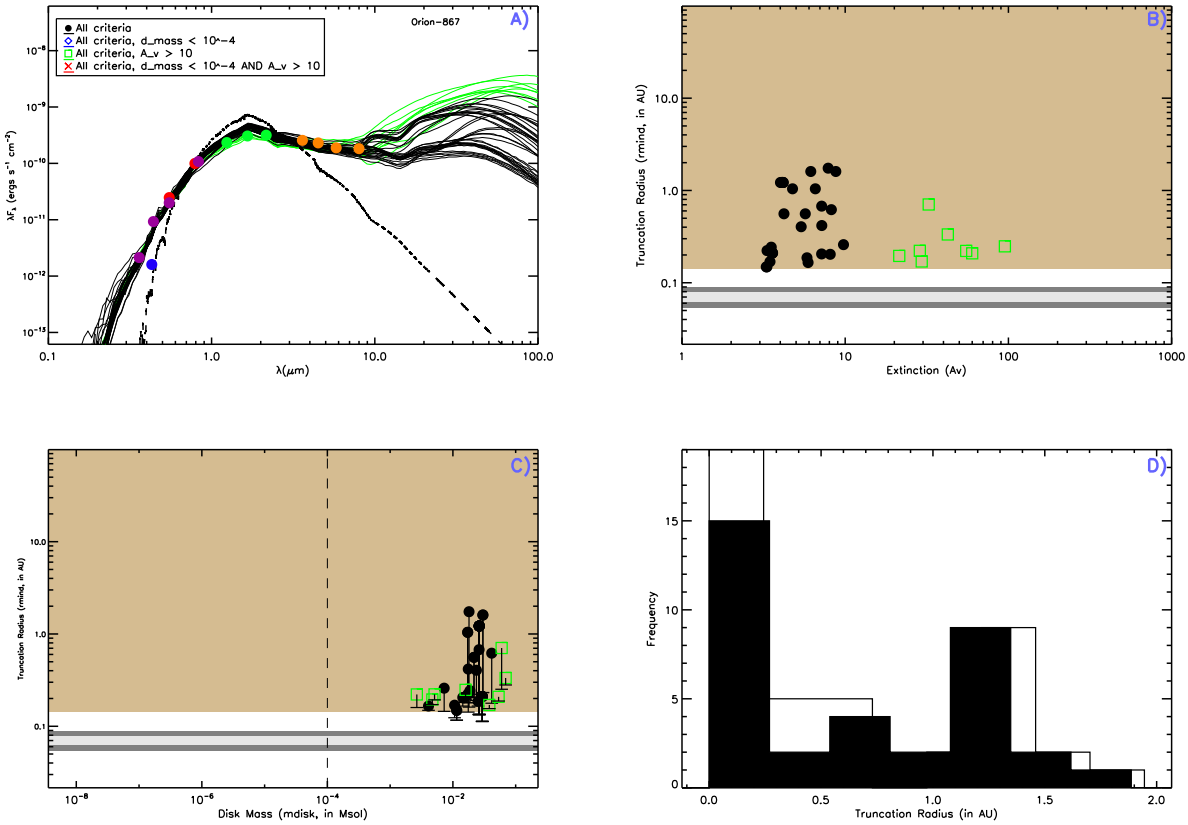

Figure B.89: SED fitting results for ONC #867

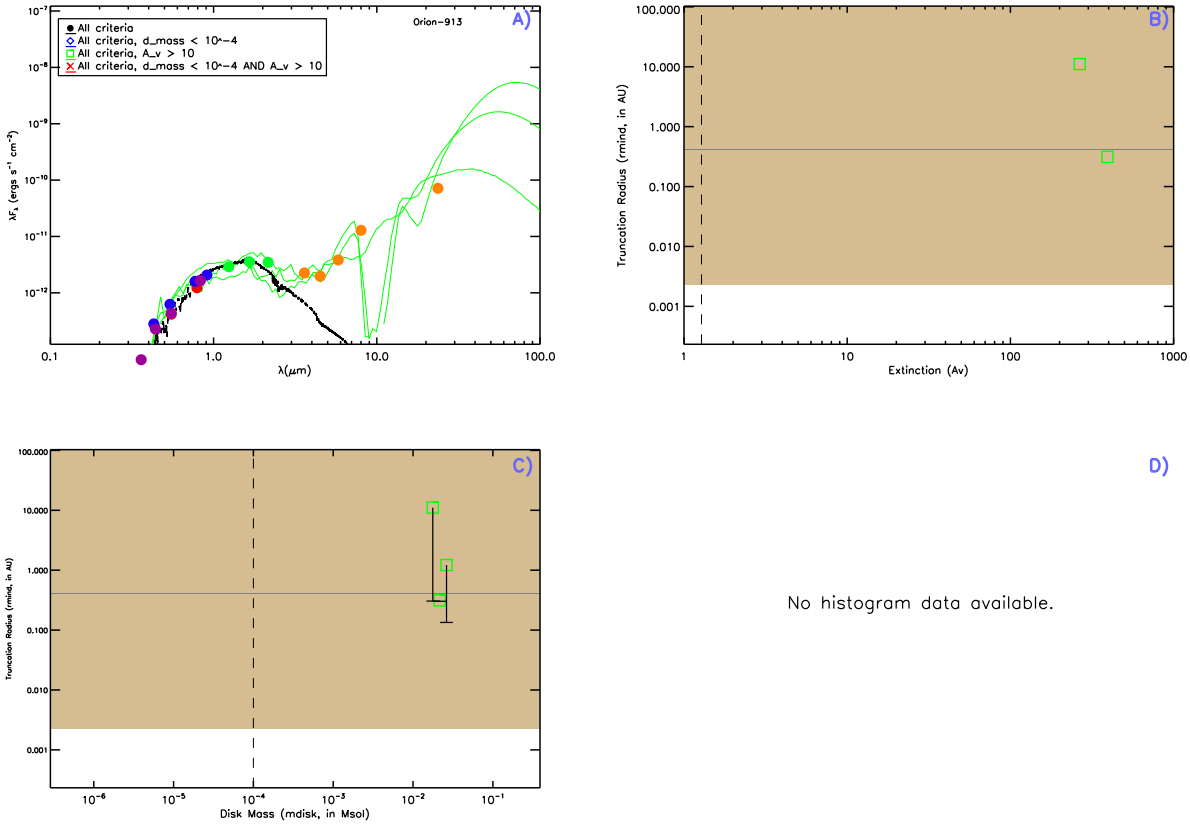

Figure B.90: SED fitting results for ONC #913

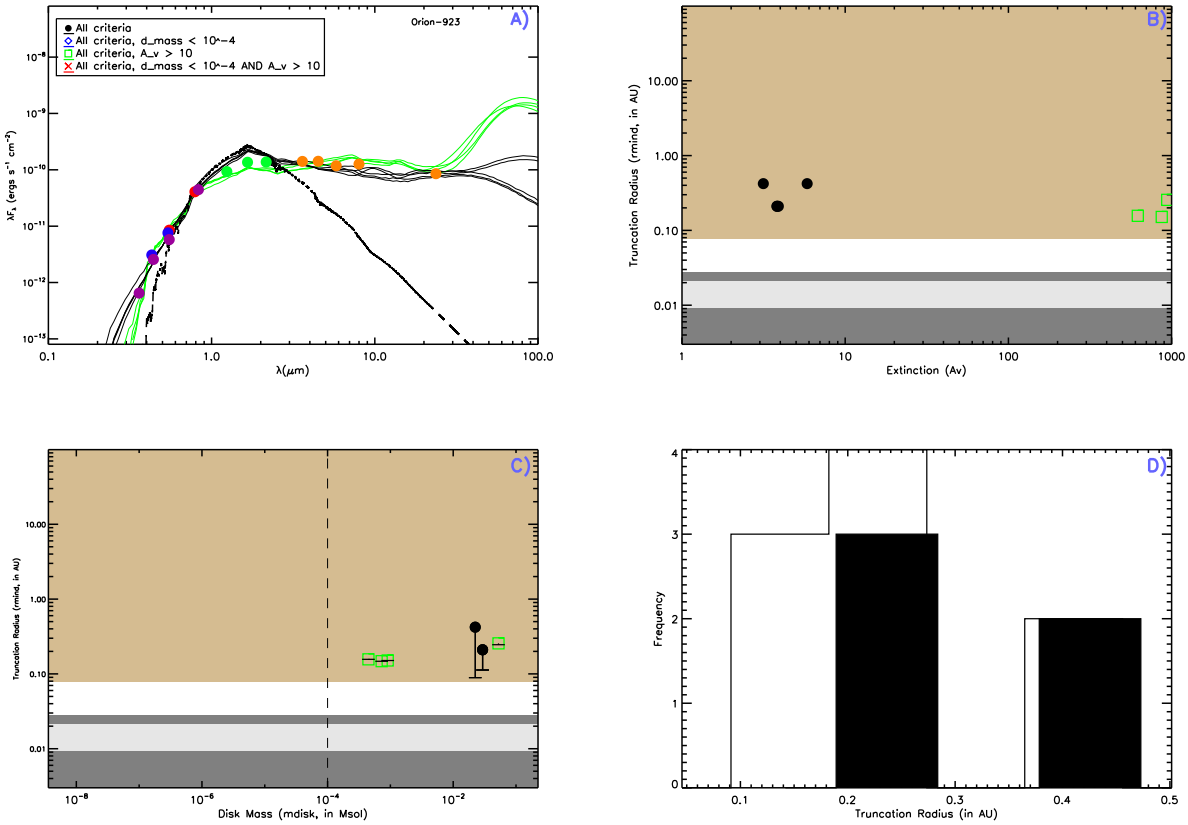

Figure B.91: SED fitting results for ONC #923

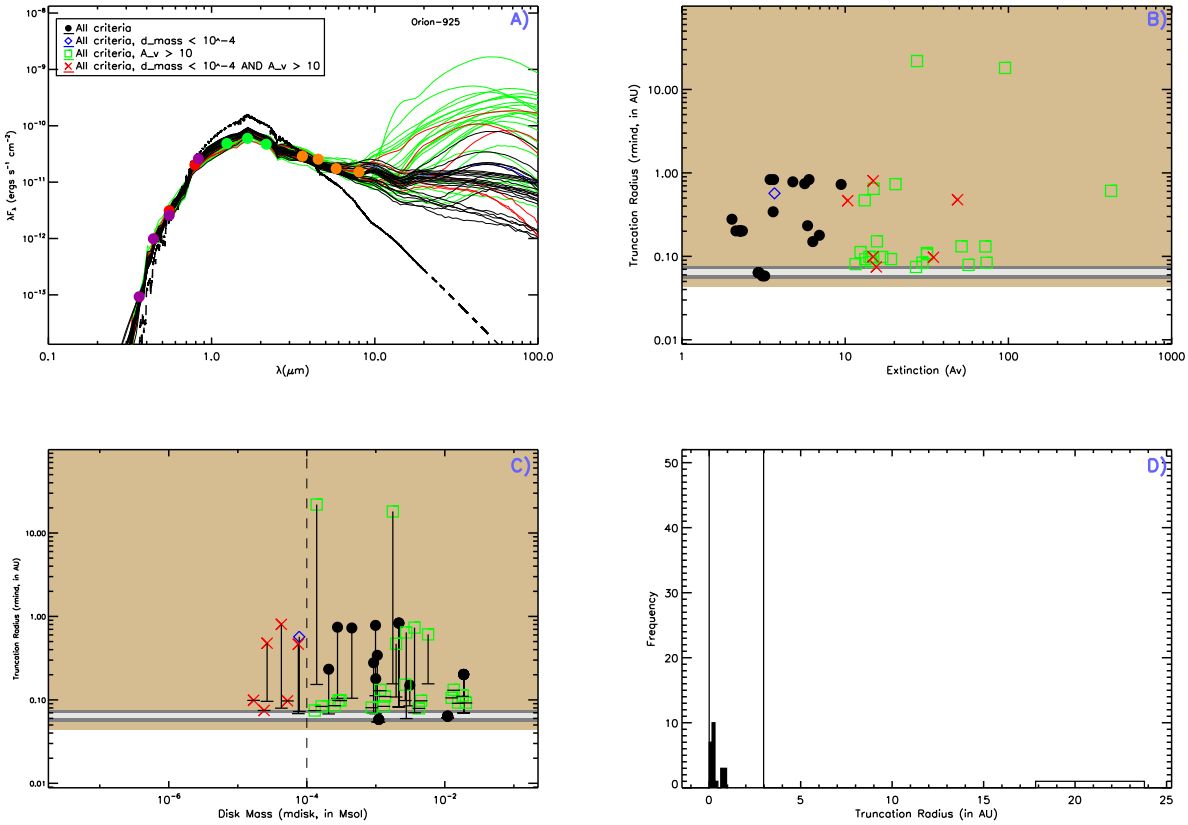

Figure B.92: SED fitting results for ONC #925

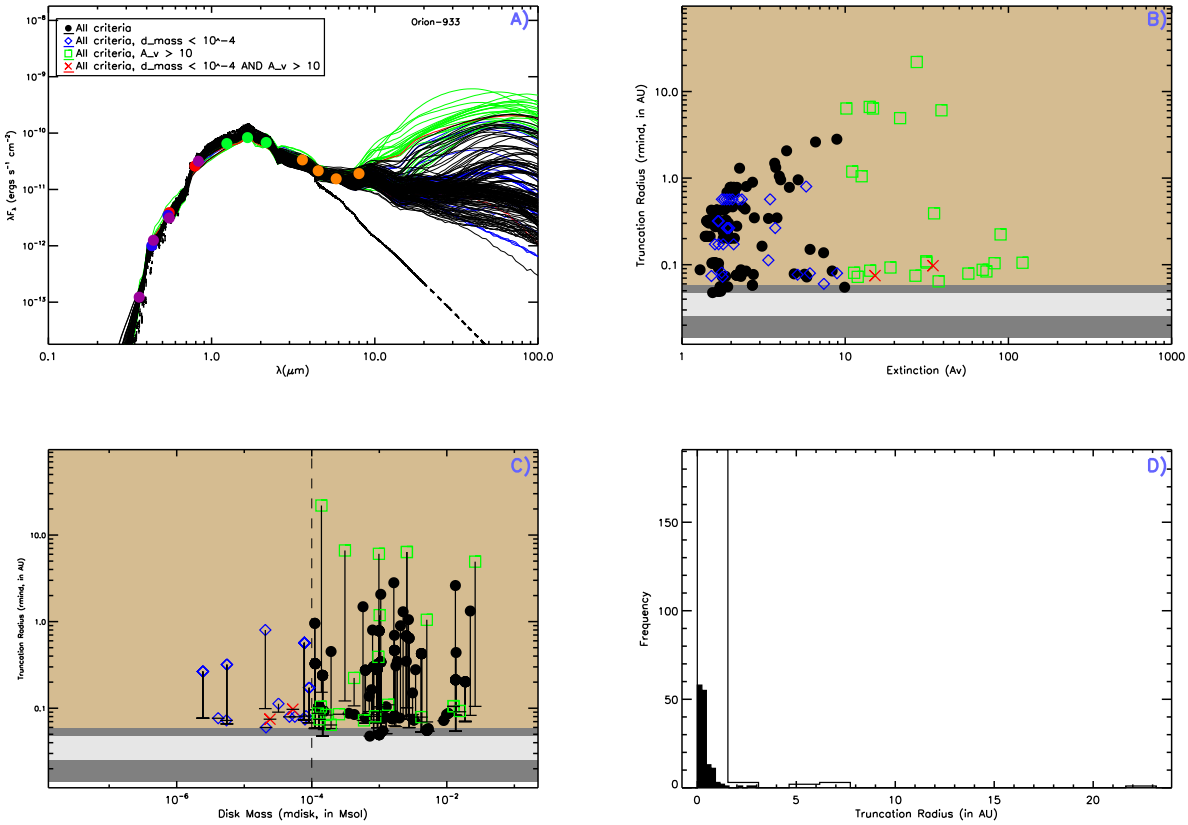

Figure B.93: SED fitting results for ONC #933

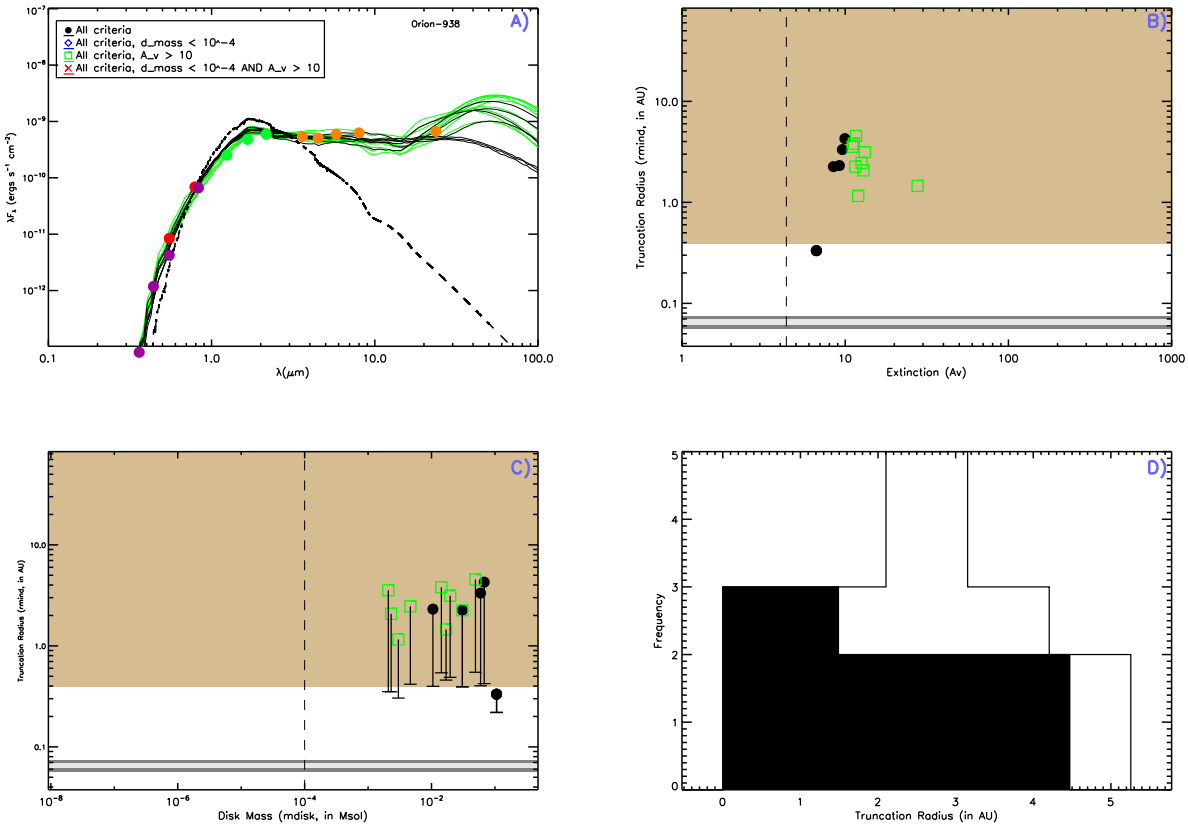

Figure B.94: SED fitting results for ONC #938

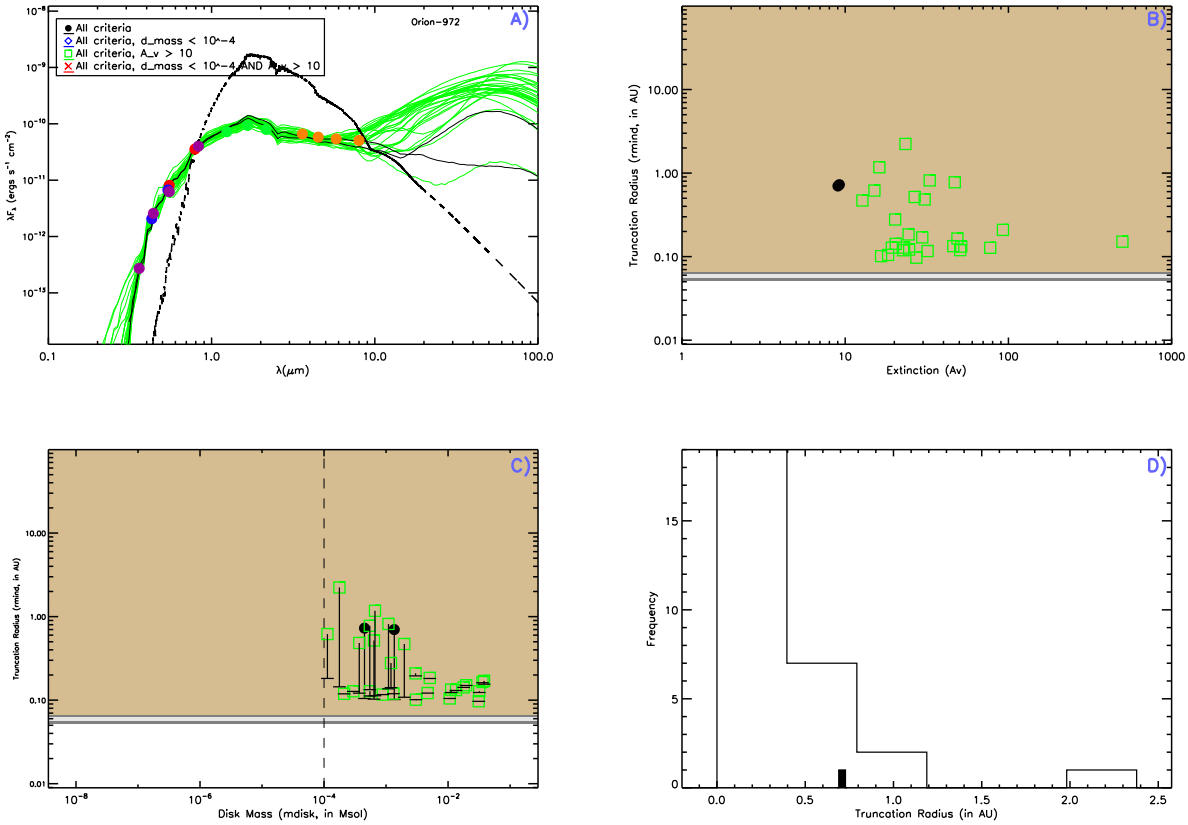

Figure B.95: SED fitting results for ONC #972

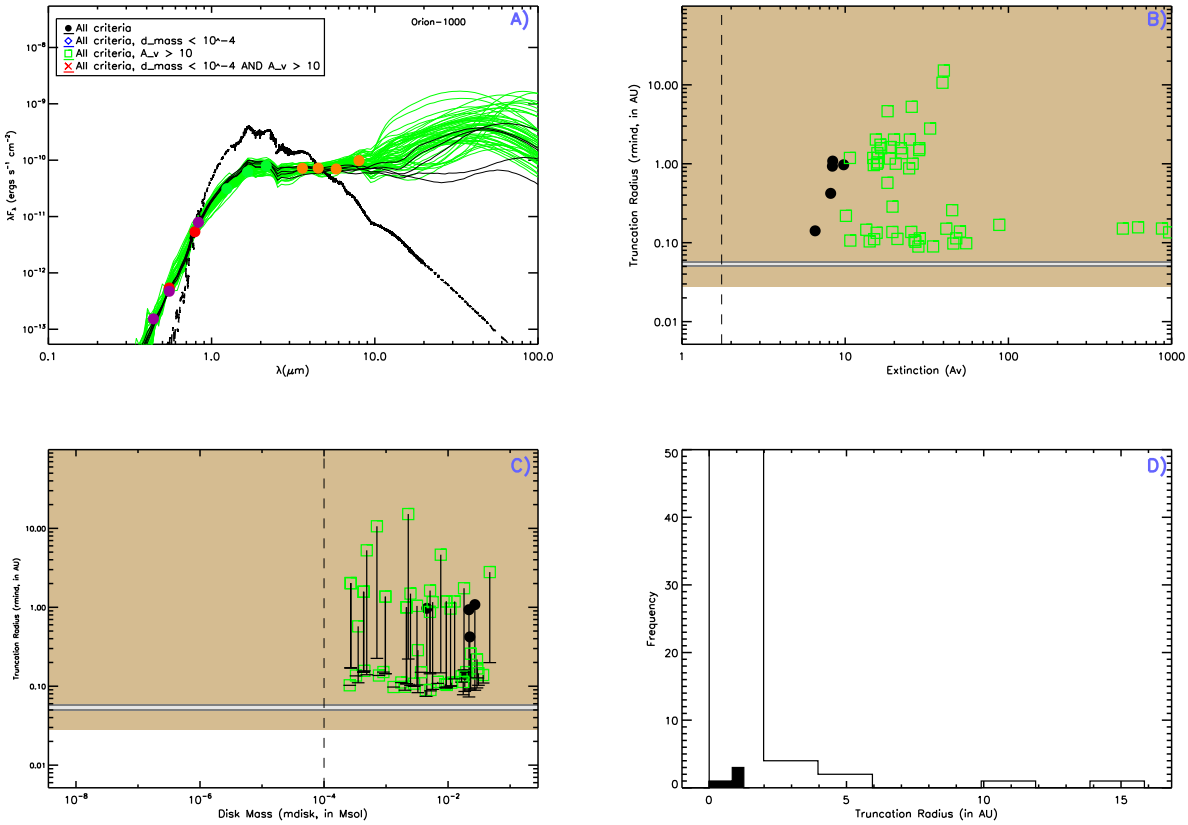

Figure B.96: SED fitting results for ONC #1000

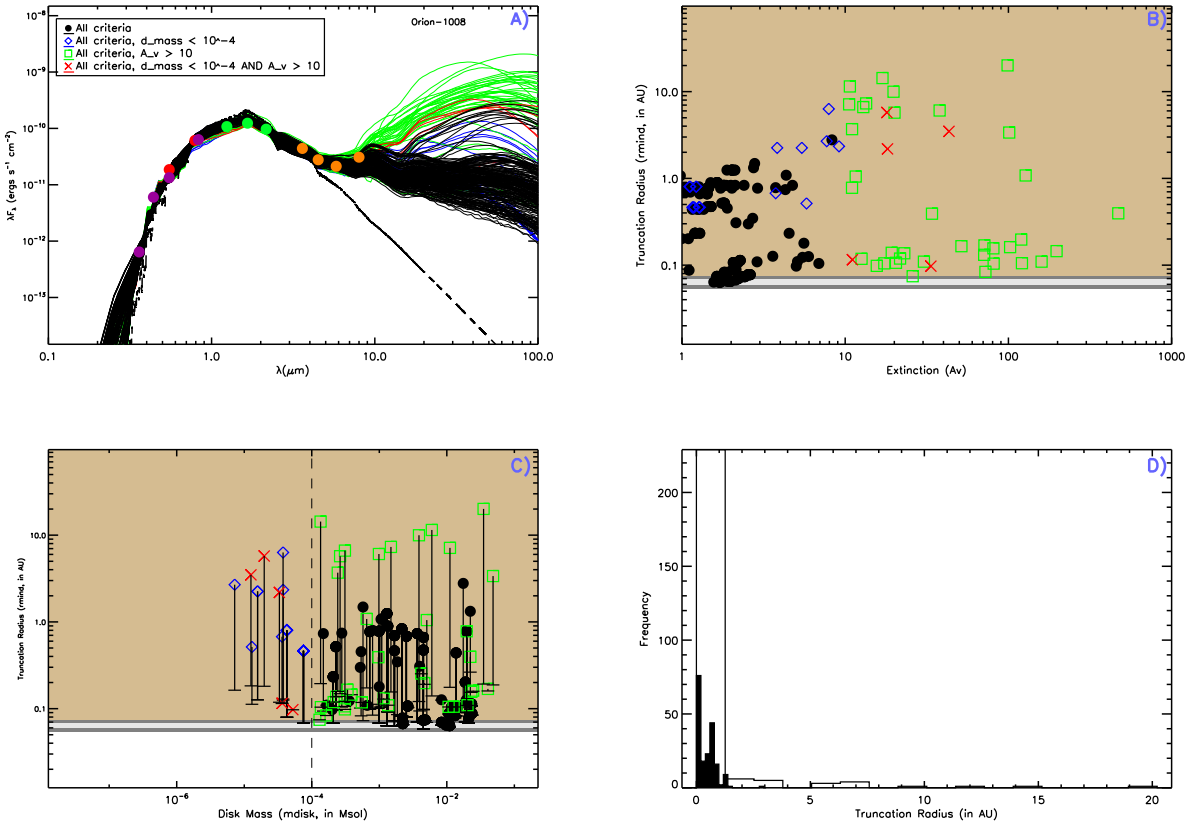

Figure B.97: SED fitting results for ONC #1008

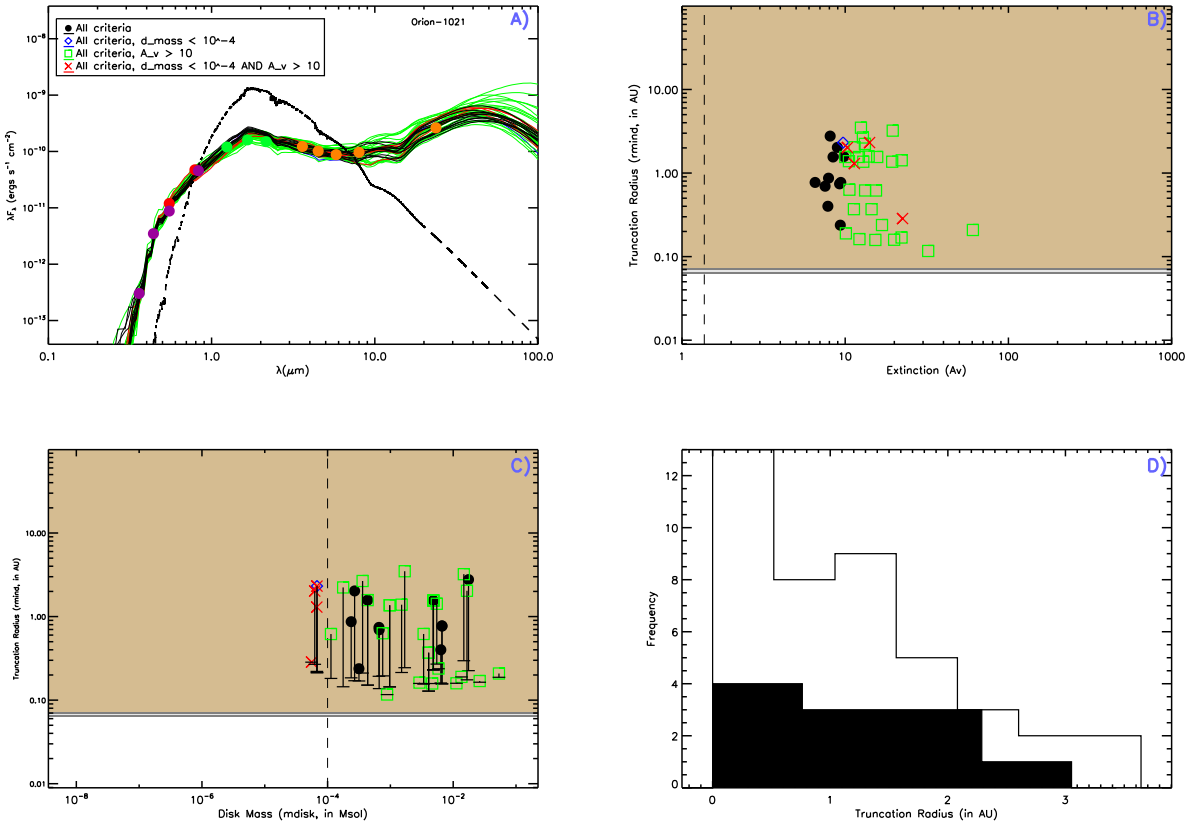

Figure B.98: SED fitting results for ONC #1021

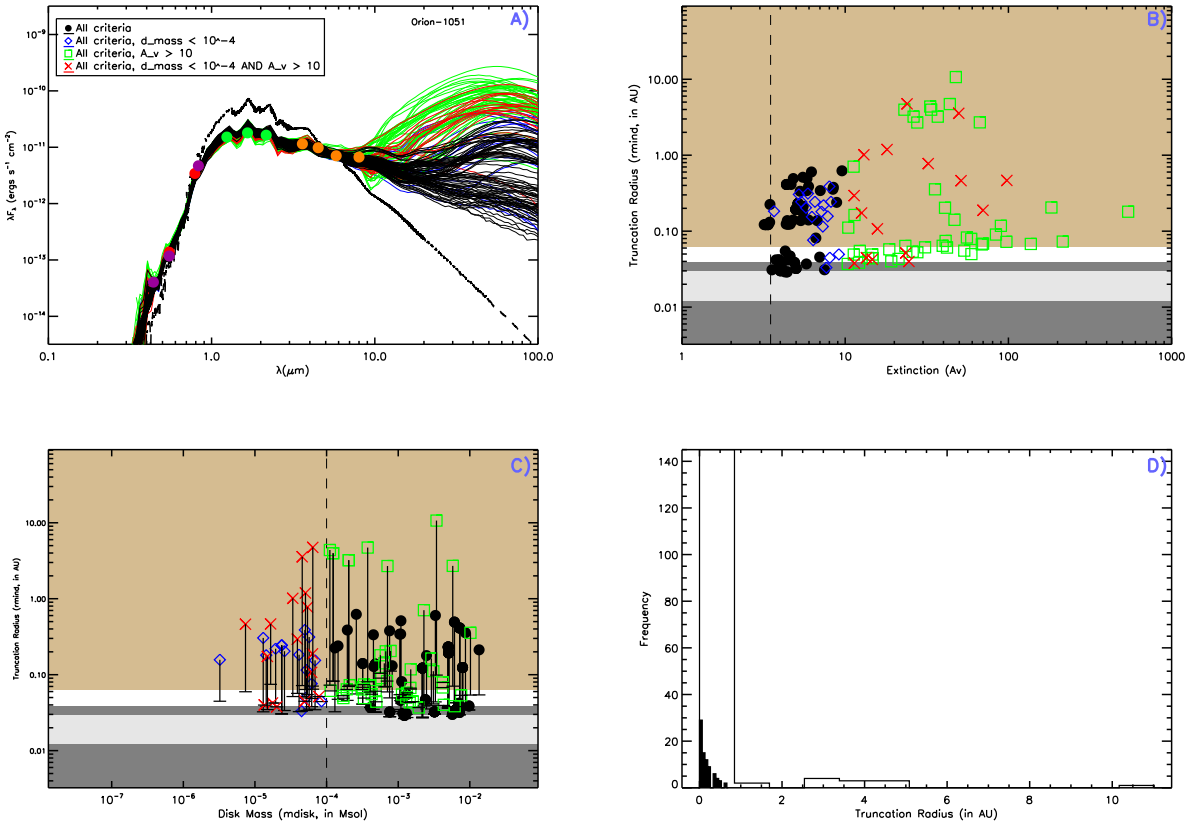

Figure B.99: SED fitting results for ONC #1051

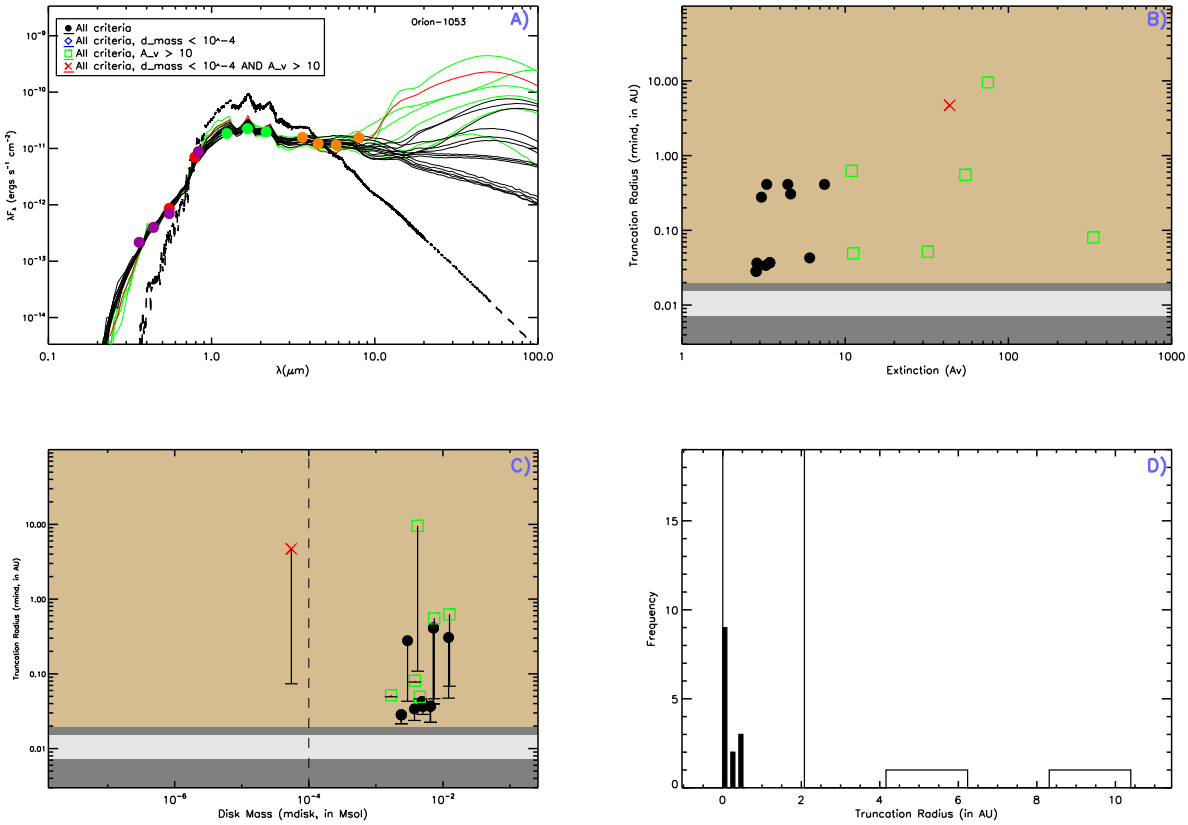

Figure B.100: SED fitting results for ONC #1053

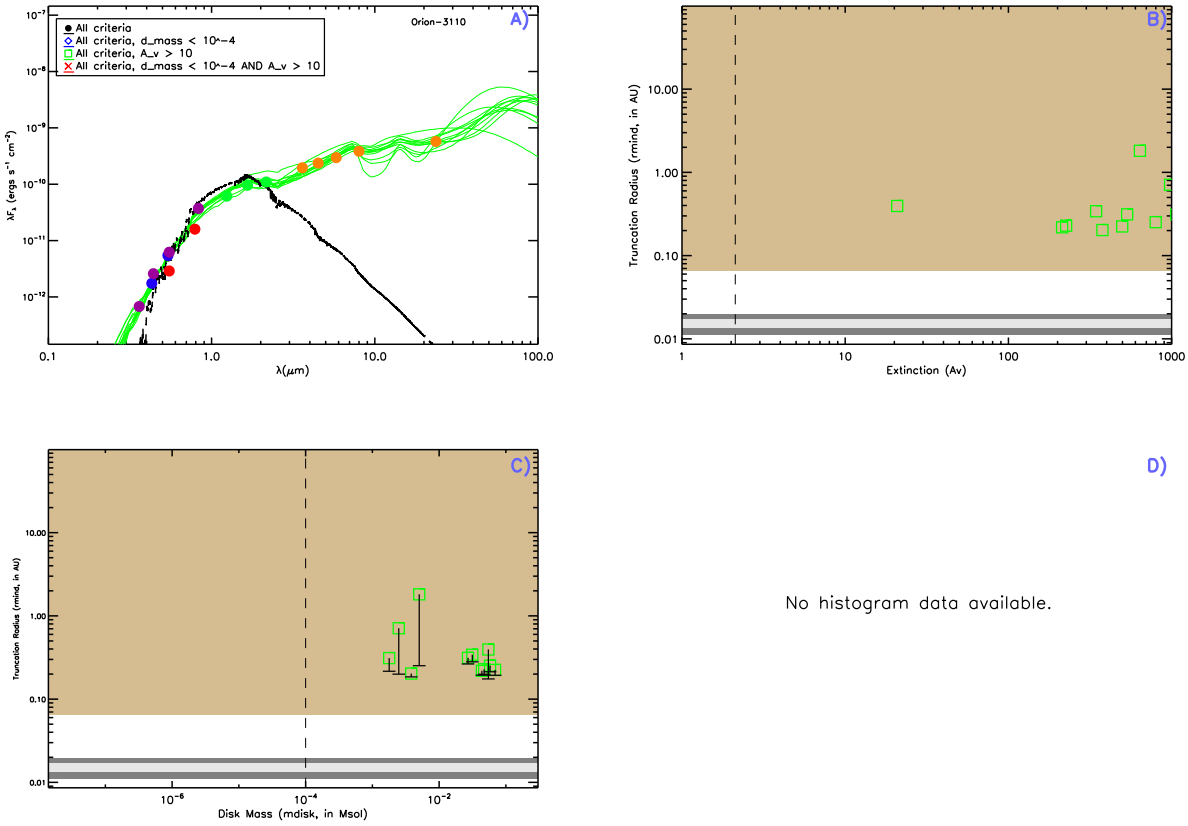

Figure B.101: SED fitting results for ONC #3110

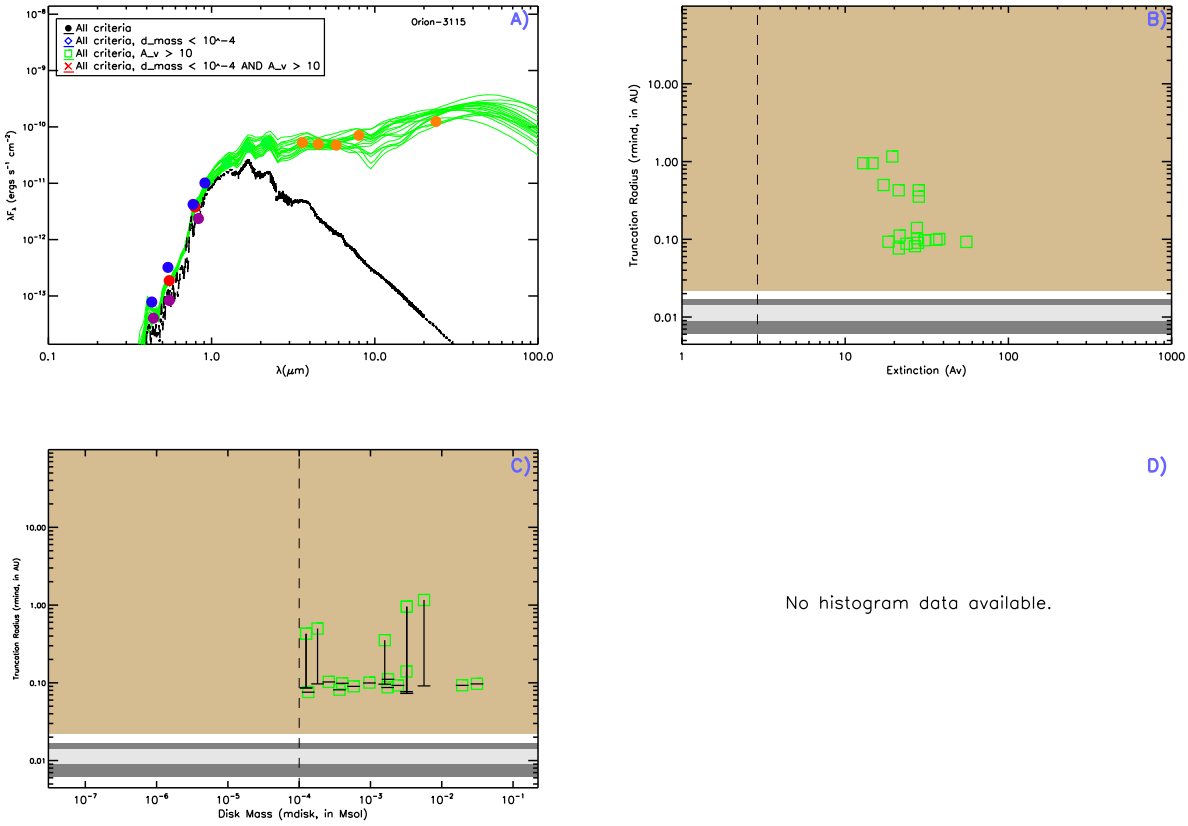

Figure B.102: SED fitting results for ONC #3115

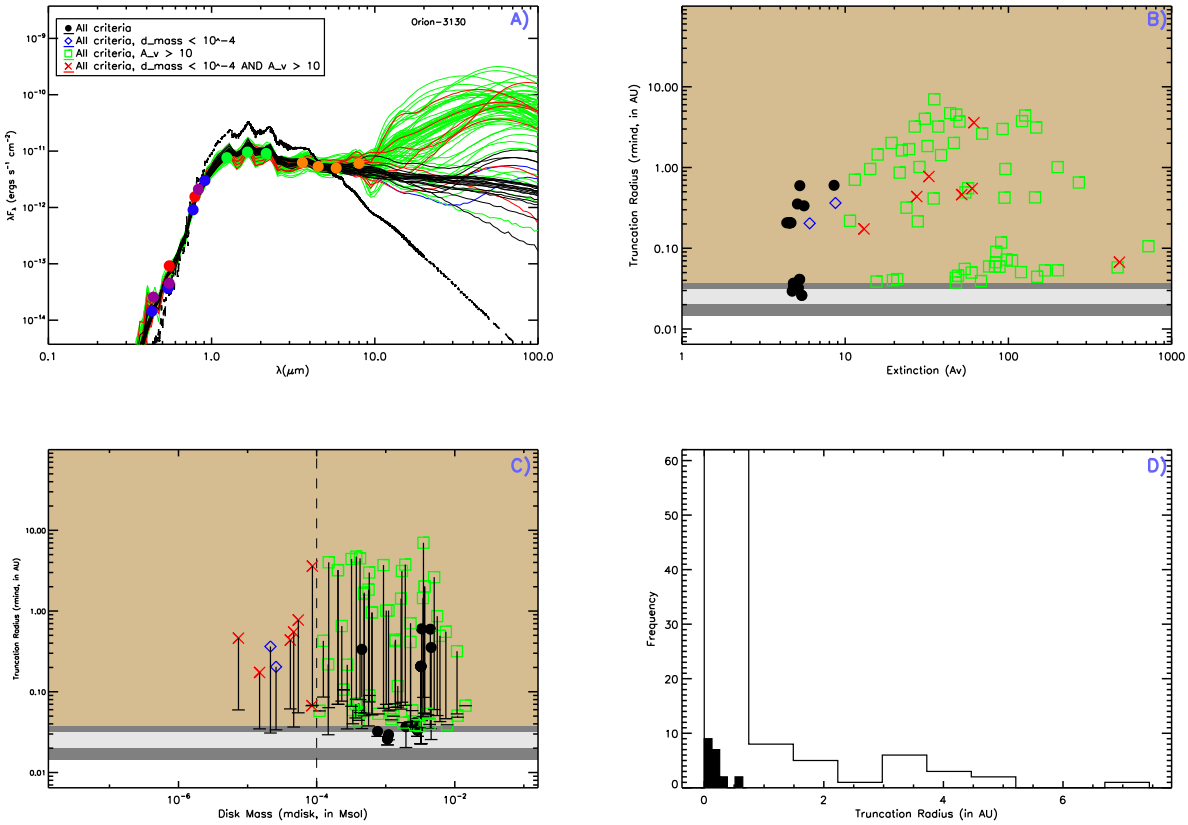

Figure B.103: SED fitting results for ONC #3130

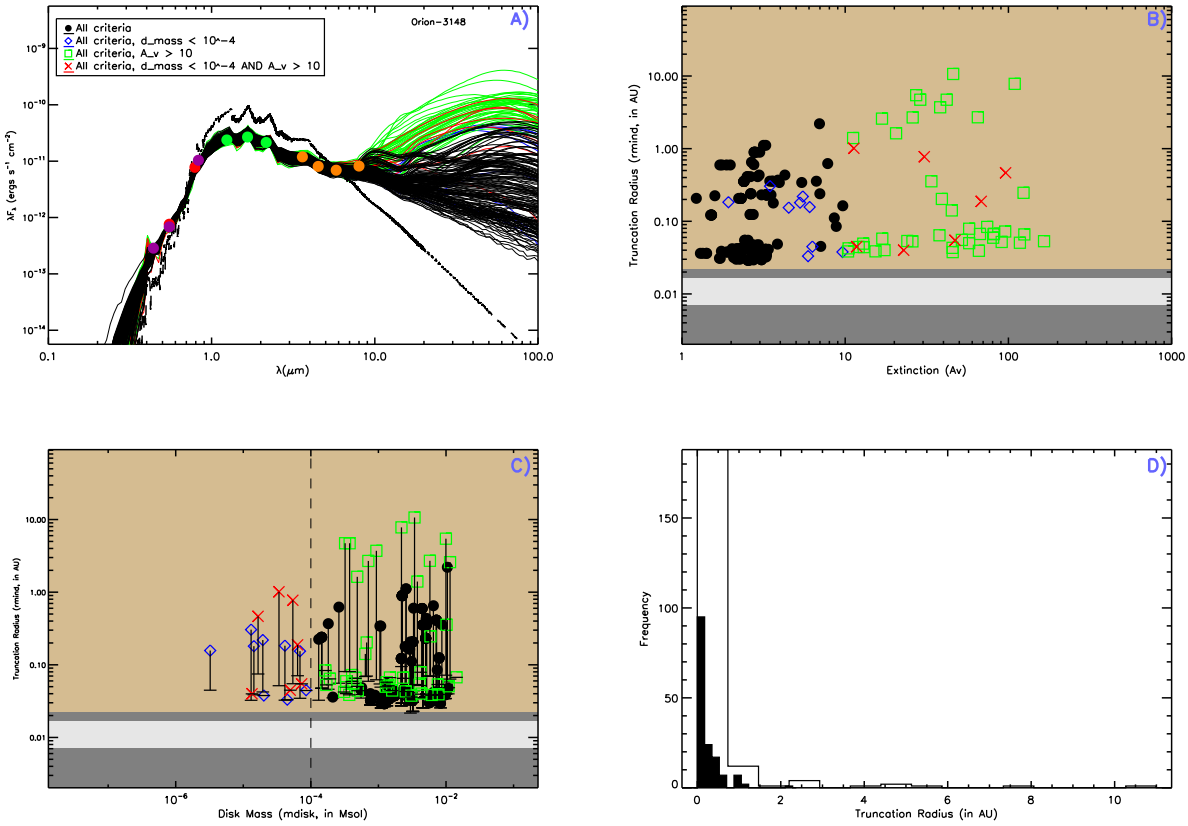

Figure B.104: SED fitting results for ONC #3148

References

Ali, B. & Depoy, D. L. 1995, AJ, 109, 709

Andrews, S. M. & Williams, J. P. 2005, ApJ, 631, 1134

Barsony, M., Ressler, M. E., & Marsh, K. A. 2005, ApJ, 630, 381

Bertoldi, F. 1989, ApJ, 346, 735

Bertout, C., Basri, G., & Bouvier, J. 1988, ApJ, 330, 350

Bjorkman, J. E. & Wood, K. 2001, ApJ, 554, 615

Bouvier, J., Bertout, C., Benz, W., & Mayor, M. 1986, A&A, 165, 110

Carr, J. S. 2007, in IAU Symposium, Vol. 243, IAU Symposium, ed. J. Bouvier & I. Appenzeller, 135–146

Cieza, L. & Baliber, N. 2006, ApJ, 649, 862

—. 2007, ApJ, 671, 605

Cohen, M., Wheaton, W. A., & Megeath, S. T. 2003, AJ, 126, 1090

Cousins, A. W. J. 1976, MmRAS, 81, 25

Covey, K. R., Greene, T. P., Doppmann, G. W., & Lada, C. J. 2005, AJ, 129, 2765

Currie, T., Lada, C. J., Plavchan, P., Robitaille, T. P., Irwin, J., & Kenyon, S. J. 2009, ApJ, 698, 1

Currie, T. & Sicilia-Aguilar, A. 2011, ApJ, 732, 24

Da Rio, N., Robberto, M., Soderblom, D. R., Panagia, N., Hillenbrand, L. A., Palla, F., & Stassun, K. 2009, ApJS, 183, 261

D'Alessio, P., Calvet, N., Hartmann, L., Muzerolle, J., & Sitko, M. 2004, in IAU Symposium, Vol. 221, Star Formation at High Angular Resolution, ed. M. G. Burton, R. Jayawardhana, & T. L. Bourke, 403–+

D'Antona, F. & Mazzitelli, I. 1997, Memorie della Societa Astronomica Italiana, 68, 807

Edwards, S. 1994, Revista Mexicana de Astronomia y Astrofisica, vol. 29, 29, 35

Edwards, S., Strom, S. E., Hartigan, P., Strom, K. M., Hillenbrand, L. A., Herbst, W., Attridge, J., Merrill, K. M., Probst, R., & Gatley, I. 1993, AJ, 106, 372

Eisner, J. A., Hillenbrand, L. A., White, R. J., Akeson, R. L., & Sargent, A. I. 2005, ApJ, 623, 952

Fazio, G. G., Hora, J. L., Allen, L. E., Ashby, M. L. N., Barmby, P., Deutsch, L. K., Huang, J., Kleiner, S., Marengo, M., Megeath, S. T., Melnick, G. J., Pahre, M. A., Patten, B. M., Polizotti, J., Smith, H. A., Taylor, R. S., Wang, Z., Willner, S. P., Hoffmann, W. F., Pipher, J. L., Forrest, W. J., McMurty, C. W., McCreight, C. R., McKelvey, M. E., McMurray, R. E., Koch, D. G., Moseley, S. H., Arendt, R. G., Mentzell, J. E., Marx, C. T., Losch, P., Mayman, P., Eichhorn, W., Krebs, D., Jhabvala, M., Gezari, D. Y., Fixsen, D. J., Flores, J., Shakoorzadeh, K., Jungo, R., Hakun, C., Workman, L., Karpati, G., Kichak, R., Whitley, R., Mann, S., Tollestrup, E. V., Eisenhardt, P., Stern, D., Gorjian, V., Bhattacharya, B., Carey, S., Nelson, B. O., Glaccum, W. J., Lacy, M., Lowrance, P. J., Laine, S., Reach, W. T., Stauffer, J. A., Surace, J. A., Wilson, G., Wright, E. L., Hoffman, A., Domingo, G., & Cohen, M. 2004, ApJS, 154, 10

Ghosh, P. & Lamb, F. K. 1979a, ApJ, 232, 259

—. 1979b, ApJ, 234, 296

Haisch, Jr., K. E., Lada, E. A., & Lada, C. J. 2001, ApJ, 553, L153

Hartigan, P., Edwards, S., & Ghandour, L. 1995, ApJ, 452, 736

Hartigan, P., Heathcote, S., Morse, J. A., Reipurth, B., & Bally, J. 2005, AJ, 130, 2197

Hartmann, L. 2001, Pre-Main Sequence Evolution of Low-Mass Stars

—. 2002, On Disk Braking of T Tauri Rotation

Hartmann, L., Hewett, R., Stahler, S., & Mathieu, R. D. 1986, ApJ, 309, 275

Herbst, W., Bailer-Jones, C. A. L., Mundt, R., Meisenheimer, K., & Wackermann, R. 2002, A&A, 396, 513

Hillenbrand, L. A. 1997, AJ, 113, 1733

Hillenbrand, L. A. & Carpenter, J. M. 2000, ApJ, 540, 236

Hillenbrand, L. A. & Hartmann, L. W. 1998, ApJ, 492, 540

Isella, A., Carpenter, J. M., & Sargent, A. I. 2009, ApJ, 701, 260

Königl, A. 1991, ApJ, 370, L39

Lada, C. J., Muench, A. A., Luhman, K. L., Allen, L., Hartmann, L., Megeath, T., Myers, P., Fazio, G., Wood, K., Muzerolle, J., Rieke, G., Siegler, N., & Young, E. 2006, AJ, 131, 1574

Le Blanc, T. S., Covey, K. R., & Stassun, K. G. 2011, AJ, 142, 55

Luhman, K. L., Rieke, G. H., Young, E. T., Cotera, A. S., Chen, H., Rieke, M. J., Schneider, G., & Thompson, R. I. 2000, ApJ, 540, 1016

Luhman, K. L., Stauffer, J. R., Muench, A. A., Rieke, G. H., Lada, E. A., Bouvier, J., & Lada, C. J. 2003, ApJ, 593, 1093

Matt, S. P., Pinzón, G., de la Reza, R., & Greene, T. P. 2010, ApJ, 714, 989

Mohanty, S. & Shu, F. H. 2008, ApJ, 687, 1323

Mordasini, C., Alibert, Y., & Benz, W. 2009a, A&A, 501, 1139

Mordasini, C., Alibert, Y., Benz, W., & Naef, D. 2009b, A&A, 501, 1161

Muzerolle, J., Allen, L. E., Megeath, S. T., Hernández, J., & Gutermuth, R. A. 2010, ApJ, 708, 1107

Najita, J., Carr, J. S., & Mathieu, R. D. 2003, ApJ, 589, 931

Press, W. H., Teukolsky, S. A., Vetterling, W. T., & Flannery, B. P. 1992, Numerical Recipes In FORTRAN. The Art Of Scientific Computing (Cambridge University Press)

Rebull, L. M., Stauffer, J. R., Megeath, S. T., Hora, J. L., & Hartmann, L. 2006, ApJ, 646, 297

Rebull, L. M., Wolff, S. C., & Strom, S. E. 2004, AJ, 127, 1029

Reipurth, B., Yu, K. C., Rodríguez, L. F., Heathcote, S., & Bally, J. 1999, A&A, 352, L83

Robberto, M., Soderblom, D. R., O'Dell, C. R., Stassun, K. G., Hillenbrand, L. A., Simon, M., Feigelson, E. D., Najita, J., Stauffer, J., Meyer, M., Panagia, N., Romaniello, M., Palla, F., Krist, J., Reid, I. N., McCullough, P., Makidon, R., Bergeron, E., McMaster, M., Kozhurina-Platais, V., Smith, K., & Sherry, W. 2005, in Protostars and Planets V, 8441

Robberto, M., Song, J., Mora Carrillo, G., Beckwith, S. V. W., Makidon, R. B., & Panagia, N. 2004, ApJ, 606, 952

Robitaille, T. P., Whitney, B. A., Indebetouw, R., & Wood, K. 2007, ApJS, 169, 328

Robitaille, T. P., Whitney, B. A., Indebetouw, R., Wood, K., & Denzmore, P. 2006, ApJS, 167, 256

Shu, F., Najita, J., Ostriker, E., Wilkin, F., Ruden, S., & Lizano, S. 1994, ApJ, 429, 781

Stassun, K. G., Mathieu, R. D., Mazeh, T., & Vrba, F. J. 1999, AJ, 117, 2941

Stassun, K. G., Mathieu, R. D., Vrba, F. J., Mazeh, T., & Henden, A. 2001, AJ, 121, 1003

Tuthill, P. G., Monnier, J. D., & Danchi, W. C. 2001, Nature, 409, 1012

Whitney, B. A., Wood, K., Bjorkman, J. E., & Cohen, M. 2003a, ApJ, 598, 1079

Whitney, B. A., Wood, K., Bjorkman, J. E., & Wolff, M. J. 2003b, ApJ, 591, 1049